NUMERICAL STUDY OF TURBULENT SWIRLING FLOWS

Mohammed Abd Al Alah Kadhim

Submitted in accordance with the requirements for the degree of

Doctor of Philosophy

The University of Huddersfield

Mechanical Engineering

School Of Computing and Engineering

July 2021

The candidate confirms that the work submitted is his own, except where work which has formed part of jointly authored publications has been included.

The candidate confirms that appropriate credit has been given within the thesis where reference has been made to the work of others.

Acknowledgements

I would like to sincerely thank Huddersfield University for giving me this opportunity to finish my study by sponsor this research with a fee waiver scholarship.

I would like to sincerely thank my supervisors, Prof. Artur Jaworskiand, Prof. John Chai and Dr. Viacheslav Stetsyuk for their inestimable assistance and patience throughout my PhD journey. Their insights and valuable advice paved the road toward accomplishing the goals of this work. I am grateful to Dr. Viacheslav Stetsyuk for giving me permission to use his experiment's data for my research.

I am indebted to my beloved wife Dhay, my wonderful son Hasan for their everlasting support and love during my PhD.

I wish to express my love and gratitude to all my family, especially my mother, Khaula, and my older brother, Haider, for their support, patience and understanding through all stages of my life and especially during my PhD. I would like to thank all my brothers and my sisters who support me during this study.

Also, for all my friends with special thanks to the Elite – especially Dr. Ahmed Hamood, Dr. Mustafa Ibraheem and all my colleagues at the University of Huddersfiled for their friendship, input and valuable discussions.

Finally, I would like to extend the acknowledgement to Dr. Nihad Malwa, Dr. Salah Alghareeb, Dr. Mustafa Al-Adhami, Dr. Samer Mubarak, Dr. Mohammed Ali, Mr. Moukhalad, Mr. Muhanad and Mr. Gio for their continuous encouragement during my study.

Abstract

The swirling flow plays a decent role in various applications. The interaction between the swirling jet flow phenomena and the CFD numerical modelling is on growing demands for many industrial/non-industrial fields such as combustion chambers and heat exchangers. The purpose of this research is to investigate the applicability of turbulence modelling typically employed in RANS equations to model a non-reacting swirling flow, and to extend the current understanding of turbulence modelling by delivering various range of numerical data to evaluate different types of turbulence models. ANSYS-CFX simulation program is used to model the flow by applying k-ε, RNG k-ε, Shear ST, LRR-IP-RS, SSG-RS and Omega-RS turbulence models at different degrees of swirl intensity. The reason for choosing k-ε, RNG k-ε, Shear ST turbulence models is due to their common use in various published work for various kinds of flow. For instance, standard k-ε turbulence model uses for fully turbulent flows, while RNG k-ε turbulence model is good for strained flows and low Reynolds number flows and Shear Stresses SST is good for transitional, free shear and compressible flows. Besides, RSMs turbulence models are excellent for swirling flow. Thus, indicate the ability of these models to perform the swirling flow at different strength is highly recommended to identify the advantage/disadvantage attached to them. For the planar jet flow, the results show that all the previous models can predict the flow behaviour and have excellent agreement with two cases of the planar jet flow, where the average error percent is 5.33% and 11% for the first and second case, respectively. The results show that all models are recommended to apply for low swirl degree with an approximate average error percent of 16%. The contours results denote a slightly non-symmetric effect due to existence of the swirl and the existence of the screws in the geometry. However, the turbulence models were able to predict the change in the symmetric shape at each location at different level of prediction.

For medium swirl degree, the study has found that the RSM models were preferred to apply because of their ability of showing the influence of swirl degree on the scalar mixing process with a 12% of average error. Additionally, the contours indicate that the non-symmetric form is higher than the first swirling number because of the increasing in the swirl strength. However, the models show different level of computing this feature. For instance, two-equations based turbulence models predict a small non-symmetric shape at the last two locations. Though, the RMS turbulence models predict a large effect of non-symmetric structure. Remarkably, all the models have failed to predict the swirl flow at high swirl strength, apart from the LRR-IP-RS model which show a good agreement with the experiment data by an average error percent of 14.72%. The study concludes that the models based on eddy viscosity method are not ideal for high swirl flow. For instance, the two-equations based turbulence models predict a small non-symmetric shape through the computational domain because these models represent the flow like a planar flow at high velocity. Thus, the related contours of these models show high mixture fraction in all locations. Generally, all the RMS turbulence models predict a huge effect of non-symmetric structure due to the swirl force. However, Methane mass fraction is not correct specially in SSG-RS and Omega-RS turbulence model. Therefore, the RMS turbulence models can predict the high swirl effect on the symmetric structure more than the two-equations based turbulence models. On the other hand, it is also concluded that the diffusion process is dominated the scalar mixing at planar jet flow where the Reynolds number is relatively low. However, the turbulent mixing is the dominant process when the swirl occurred. Finally, the results suggest that the existence of screws have a significate effect on symmetric.

Table of Contents

Acknowledgements iii

Abstract iv

List of Figures x

List of Tables xix

Nomenclature xxi

Chapter 1 1

1.1 Introduction 1

1.2 General review of CFD and modern system development 1

1.3 A brief history of fluid dynamics 4

1.2.1 Steady and unsteady flows. 6

1.2.2 Laminar and turbulent flow. 6

1.2.3 Uniform and non-uniform flow 6

1.2.4 Compressible and in-compressible fluid flow 6

1.2.5 One, two and three-dimensional fluid flow 6

1.2.6 Rotational (swirl) and irrotational flow 6

1.4 Motivation 7

1.5 Research aims and objectives 7

1.6 Description of the thesis 8

Chapter 2 LITERATURE REVIEW 10

2.1 Turbulent jet flow 10

2.1.1 Circular planar jet flow 12

2.1.2 Swirl jet flow 19

2.2 Planar Jet Studies 25

2.2.1 Brief numerical and experimental studies 25

2.2.2 Related experiment review 28

2.2.3 Related numerical review 30

2.3 Swirl jet studies 31
2.3.1 Experiment studies 31
2.3.2 Related experiment review 33
2.3.3 Numerical studies 37
2.3.4 Related numerical review 44
2.4 Gap in knowledge 46
Chapter 3 THEORY OF NUMERICAL METHODOLOGY 48
3.1 Governing equations 48
3.1.1 Continuity equation 48
3.1.2 Momentum equation 48
3.1.3 Energy equation 49
3.1.4 Species transport equation 49
3.2 Numerical modelling 49
3.2.1 Finite Volume Method (FVM) 51
3.2.2 Advantage of finite volume method 52
3.3 Turbulent flow computing methodologies RANS 54
3.4 Closure problem in RANS 55
3.5 Reynolds Averaged Navier-Stokes (RANS) equations 56
3.6 Turbulent fluxes and modelling for RANS scalar transport equation in swirl flow 58
3.7 Computational Fluid Dynamics (CFD) steps 60
3.7.1 Pre-Processor 60
3.7.2 Solver 61
3.7.3 Post-Processor 61
3.8 RANS Turbulence models 62
3.8.1 Eddy viscosity turbulence models 63
3.8.2 Reynolds stress turbulence models 69
3.9 Turbulence models limitations 76

3.10 Numerical errors and uncertainty 77
Chapter 4 VALIDATION STUDY (PLANAR JET NUMERICAL MODELLING) 79
4.1 Planar jet first case study 79
4.1.1 Computational domain 79
4.1.2 Boundary Conditions B.C 84
4.1.3 Mesh sensitivity analysis 85
4.2 Planar jet second case study 91
4.2.1 Computational domain 91
4.2.2 Boundary Conditions B.C 93
4.2.3 Mesh sensitivity analysis 94
4.3 Summery 100
Chapter 5 SWIRL JET NUMERICAL MODELLING 101
5.1 Computational domain 101
5.2 Boundary conditions 104
5.3 Mesh sensitivity analysis 107
5.4 Turbulence models 112
Chapter 6 RESULT & DISCUSSION 114
6.1 Planar jet case study one 114
6.1.1 Effects of mesh quality 114
6.1.2 Self-similar area 118
6.1.3 Turbulence model outcome 122
6.2 Planar jet case study two 125
6.2.1 Effects of mesh quality 125
6.2.2 Turbulence model outcome 130
6.2.3 Effects of diffusivity 132
6.2.4 Symmetric analyses 135
6.3 Swirl jet flow 138

6.4 First swirl number (*S*=0.3) 138
6.4.1 Effects of mesh quality 139
6.4.2 Effects of turbulence modelling 140
6.4.3 Effects of 'zero diffusivity' 148
6.4.4 Symmetric analyses 149
6.5 Second swirl number (*S*=0.58) 156
6.5.1 Effects of turbulence modelling 156
6.5.2 Symmetric analyses 164
6.6 Third swirl number (*S*=1.07) 171
6.6.1 Effects of turbulence modelling 171
6.6.2 Symmetric analyses 179
6.7 Reynolds stress turbulence models review 187
6.8 Effect of screws 189
6.9 Effect of swirl 193
6.10 Effect of ANSYS-CFX 201
Chapter 7 CONCLUSION AND FUTURE WORK 202
7.1 Scope of work 202
7.2 Project's outcome 203
7.2.1 Verification and validation 203
7.2.2 Modelling approach 204
7.3 Limitation 205
7.4 Contributions to knowledge 206
7.5 Conclusion 206
7.6 Recommendations for future work 208
REFERENCES 209

List of Figures

FIGURE 1-1: FLOW DIAGRAM OF THESIS CHAPTERS 9
FIGURE 2-1: WATER JET (COLOURED) EMERGING FROM A NOZZLE INTO UNDISTURBED WATER 10
FIGURE 2-2: JET SPREAD ANGLE. 11
FIGURE 2-3: SCHEMATIC DESCRIPTION OF A FREE JET FLOW 12
FIGURE 2-4: FREE JET FLOW STRUCTURE 13
FIGURE 2-5: FREE VERTICAL JET FLOW STRUCTURE 14
FIGURE 2-6: CIRCULAR JET FLOW STRUCTURE AND CHARACTERISTICS 15
FIGURE 2-7: RADIAL PROFILES OF MEAN AXIAL VELOCITY IN A TURBULENT ROUND JET, RE = 95; 500. THE DASHED LINES INDICATE THE HALF-WIDTH 16
FIGURE 2-8: MEAN AXIAL VELOCITY AGAINST RADIAL DISTANCE IN A TURBULENT ROUND JET, $Re \approx 105$; MEASUREMENTS OF (WYGNANSKI & FIEDLER, 1969). SYMBOLS: ○ $xd = 40$; △, 50; □, 60; ◊, 75; ●, 97.5 16
FIGURE 2-9: WEAK SWIRL DEGREE 20
FIGURE 2-10: STRONG SWIRL DEGREE 20
FIGURE 2-11: FUEL INJECTS INSIDE THE SWIRLING AIRFLOW 21
FIGURE 2-12: EXPERIMENTAL FACILITY SYSTEM 29
FIGURE 2-13: CUT VIEW OF ATMOSPHERIC BURNER 34
FIGURE 2-14: THE LEFT-HAND IMAGE INDICATES THE LASER SHEET POSITIONS DURING PLIF MEASUREMENTS AND THE RIGHT-HAND IMAGE SHOW FLOW ARRANGEMENT 35
FIGURE 2-15: EXPERIMENTAL FACILITY SYSTEM 36
FIGURE 3-1: INTERDISCIPLINARITY OF NUMERICAL SIMULATION OF ENGINEERING PROBLEMS 50
FIGURE 3-2: STANDARDS ASPECTS OF NUMERICAL PREDICTIONS 51
FIGURE 3-3: FVM MESH STRUCTURE TYPES 53
FIGURE 3-4: TURBULENT FLOW COMPUTING METHODOLOGIES 54
FIGURE 3-5: CYLINDRICAL COORDINATE SYSTEM OF THE FREE DEVELOPING SWIRLING JET 58
FIGURE 3-6: RELATION BETWEEN SOLUTIONS, ERRORS, AND PROPERTIES 77
FIGURE 4-1: EXPERIMENT DOMAIN 80

FIGURE 4-2: CORE ANGLE CALCULATION. 81
FIGURE 4-3: 2D EXPERIMENT DOMAIN. 82
FIGURE 4-4: 3D COMPUTATIONAL DOMAIN. 83
FIGURE 4-5: 3D COMPUTATIONAL B.C. 85
FIGURE 4-6: ETHYLENE VOLUME FRACTIONS AND RMSE VALUES FOR ALL MESHES AT DIFFERENT LOCATIONS: A. $20D_E$, B. $40D_E$, C. $60D_E$, AND D. $80D_E$. 88
FIGURE 4-7: RMSE COMPARISON AMONG ALL THE MESHES: A. ALL VALUES AT ALL LOCATIONS, B. AVERAGE RMSE VALUE FOR EACH MESH. 88
FIGURE 4-8: POINT BASED COMPARISON AMONG ALL THE MESHES: A. ALL POINTS VALUES AT ALL LOCATIONS, B. AVERAGE POINTS VALUE FOR EACH MESH. 89
FIGURE 4-9: MESH REFINEMENT DIFFERENCES. A. MESH ONE, B. MESH FIVE. 89
FIGURE 4-10: POINT-BASED COMPARISON OF VOLUME FRACTION VALUE FOR EACH MESH. A. 40DE, B. 80DE. 90
FIGURE 4-11: MESH REFINEMENT DIFFERENCES (CROSS-SECTION). A. MESH ONE, B. MESH FIVE. 90
FIGURE 4-12: 3D COMPUTATIONAL DOMAIN. 92
FIGURE 4-13: THE LEFT-HAND IMAGE SHOWS THE PLANAR BURNER SCHEME. THE RIGHT-HAND SHOWS A SIMPLE DIAGRAM OF THE EXPERIMENT PLANAR JET FLOW 92
FIGURE 4-14: 3D COMPUTATIONAL B.C. 93
FIGURE 4-15: METHANE VOLUME FRACTIONS AND RMSE VALUES FOR ALL MESHES AT DIFFERENT LOCATIONS: A. $1D_F$, B. $3D_F$, C. $5D_F$, AND D. $7D_F$. SECOND CASE STUDY 96
FIGURE 4-16: POINT BASED COMPARISON AMONG ALL THE MESHES: A. ALL POINTS VALUES AT ALL LOCATIONS, B. AVERAGE POINTS VALUE FOR EACH MESH. SECOND CASE STUDY 96
FIGURE 4-17: RMSE COMPARISON AMONG ALL THE MESHES: A. ALL VALUES AT ALL LOCATIONS, B. AVERAGE RMSE VALUE FOR EACH MESH. SECOND CASE STUDY 97
FIGURE 4-18: POINT-BASED COMPARISON OF VOLUME FRACTION VALUE FOR EACH MESH. A. $3D_F$, B. $7D_F$. SECOND CASE STUDY. 97

FIGURE 4-19: MESH REFINEMENT DIFFERENCES. A. MESH ONE, B. MESH FIVE. SECOND CASE STUDY.....98
FIGURE 4-20: MESH REFINEMENT DIFFERENCES (CROSS-SECTION). A. MESH ONE, B. MESH FIVE. SECOND CASE STUDY.....99
FIGURE 5-1: COMPUTATIONAL DOMAIN SCHEME (LEFT). ATMOSPHERIC BURNER (RIGHT).....102
FIGURE 5-2: 3D COMPUTATIONAL NUMERICAL DOMAIN SCHEME. SWIRLING SIMULATION. 103
FIGURE 5-3: COMPUTATIONAL DOMAIN SAMPLES.....103
FIGURE 5-4: 3D COMPUTATIONAL NUMERICAL DOMAIN SCHEME OF THE BURNER CYLINDERS.....104
FIGURE 5-5: 3D COMPUTATIONAL B.C. AT THE BURNER CYLINDERS. 106
FIGURE 5-6: 3D COMPUTATIONAL B.C. SWIRLING SIMULATION.....106
FIGURE 5-7: 3D COMPUTATIONAL B.C. AT DIFFERENT VIEWS. 107
FIGURE 5-8: METHANE VOLUME FRACTIONS AND RMSE VALUES FOR ALL MESHES AT DIFFERENT LOCATIONS: A. $1D_F$, B. $3D_F$, C. $5D_F$, AND D. $7D_F$. SWIRLING SIMULATION.....109
FIGURE 5-9: RMSE COMPARISON AMONG ALL THE MESHES: A. ALL VALUES AT ALL LOCATIONS, B. AVERAGE RMSE VALUE FOR EACH MESH. SWIRLING SIMULATION. 110
FIGURE 5-10: POINT-BASED COMPARISON AMONG ALL THE MESHES: A. ALL POINTS VALUES AT ALL LOCATIONS, B. AVERAGE POINTS VALUE FOR EACH MESH. SWIRLING SIMULATION.....110
FIGURE 5-11: POINT-BASED COMPARISON OF VOLUME FRACTION VALUE FOR EACH MESH. A. $1D_F$, B. $7D_F$. SWIRLING SIMULATION. 111
FIGURE 5-12: MESH REFINEMENT DIFFERENCES. A. MESH ONE, B. MESH FIVE. SWIRLING SIMULATION.....111
FIGURE 5-13: MESH REFINEMENT DIFFERENCES (CROSS-SECTION). A. MESH ONE, B. MESH FIVE. SWIRLING SIMULATION.....112
FIGURE 6-1: CUT-CELL MESHING TECHNIQUE AT DIFFERENT VIEWS.....115
FIGURE 6-2: UNIFORM MESHING TECHNIQUE AT DIFFERENT VIEWS. 116
FIGURE 6-3: MULTI-BODY UNIFORM MESHING TECHNIQUE AT DIFFERENT VIEWS.....117

FIGURE 6-4: MESH QUALITY EFFECTS ON THE RESULTS: A. LOW MESH SIZE. B. HIGH MESH SIZE. 117
FIGURE 6-5: VF OF ETHYLENE AT DIFFERENT LOCATIONS IN THE CHOSEN MESH 119
FIGURE 6-6: VF OF ETHYLENE ALONG THE JET AXIAL AND THE POTENTIAL CORE LENGTH ESTIMATION 119
FIGURE 6-7: MEAN CONCENTRATION PROFILES AT ALL THE COMPUTATIONAL DOMAINS 120
FIGURE 6-8: MEAN CONCENTRATION PROFILES ELIMINATION PROCESS. RMSE PERCENTAGE INCLUDED. 121
FIGURE 6-9: SELF-SIMILAR AREA STARTING LOCATION. RMSE PERCENTAGE INCLUDED. 121
FIGURE 6-10: SELF-SIMILAR AREA AT DIFFERENT LOCATIONS. RMSE PERCENTAGE INCLUDED. 122
FIGURE 6-11: CURVE FITTING TOOL FOR THE MEAN CONCENTRATION PROFILE 123
FIGURE 6-12: HALF-WIDTH INDICATION FOR AN AVERAGE MEAN CONCENTRATION PROFILE. 124
FIGURE 6-13: THE SIMULATION OUTCOME; STANDARD k-ε RESULTS AT DIFFERENT LOCATIONS FOR THE MEAN CONCENTRATION PROFILES, ALONG WITH THE PUBLISHED DNS NUMERICAL METHOD AND THE EXPERIMENT DATA. RMSE PERCENTAGE INCLUDED. 124
FIGURE 6-14: UNIFORM MESH WITH A STRUCTURE INLET AT DIFFERENT VIEWS. 126
FIGURE 6-15: UNIFORM MESH WITH A TETRAHEDRONS INLET AT DIFFERENT VIEWS 127
FIGURE 6-16: A. UNIFORM MESH WITH A STRUCTURE CYLINDER CENTRE AT DIFFERENT VIEWS. 128
FIGURE 6-17: MESH QUALITY EFFECTS ON THE VOLUME FRACTION: 129
FIGURE 6-18: VF OF METHANE AT DIFFERENT LOCATIONS IN THE CHOSEN MESH. 130
FIGURE 6-19: VF OF METHANE AND STETSYUK'S EXPERIMENT AT $1D_F$. k-ε. SECOND CASE PLANAR JET FLOW. 131

FIGURE 6-20: VF OF METHANE AND STETSYUK'S EXPERIMENT AT $3D_F$. k-ε. SECOND CASE PLANAR JET FLOW. 131
FIGURE 6-21: VF OF METHANE AND STETSYUK'S EXPERIMENT AT $5D_F$. k-ε. SECOND CASE PLANAR JET FLOW. 132
FIGURE 6-22: VF OF METHANE AND STETSYUK'S EXPERIMENT AT $7D_F$. k-ε. SECOND CASE PLANAR JET FLOW. 133
FIGURE 6-23: VF OF METHANE AND STETSYUK'S EXPERIMENT AT ALL LOCATIONS. k-ε. SECOND CASE PLANAR JET FLOW. 133
FIGURE 6-24: VF OF METHANE STETSYUK'S EXPERIMENT. A. $1D_F$, B. $3D_F$, C.$5D_F$, D. $7D_F$. k-ε. SECOND CASE PLANAR JET FLOW. 134
FIGURE 6-25: 2D (TOP VIEW) AND 3D VF CONTOURS OF METHANE. A. $1D_F$, B. $3D_F$, C.$5D_F$, D. $7D_F$. k-ε. SECOND CASE PLANAR JET FLOW. 136
FIGURE 6-26: k-ε METHANE VELOCITY 3D STREAMLINE. SECOND CASE PLANAR JET FLOW. 137
FIGURE 6-27: k-ε METHANE VELOCITY PROFILE AND VECTORS. SECOND CASE PLANAR JET FLOW. 137
FIGURE 6-28: MESH QUALITY EFFECTS ON THE VOLUME FRACTION: 139
FIGURE 6-29: METHANE MASS FRACTION AT DIFFERENT LOCATIONS IN THE CHOSEN MESH. 140
FIGURE 6-30: MIXTURE FRACTION OF METHANE AND STETSYUK'S EXPERIMENT. A. $1D_F$, B. $3D_F$, C.$5D_F$, D. $7D_F$. S=0.3, k-ε. 142
FIGURE 6-31: MIXTURE FRACTION AT ALL LOCATIONS FOR METHANE AND STETSYUK'S EXPERIMENT. S=0.3, k-ε. 142
FIGURE 6-32: MIXTURE FRACTION OF METHANE AND STETSYUK'S EXPERIMENT. A. $1D_F$, B. $3D_F$, C.$5D_F$, D. $7D_F$. S=0.3, RNG k-ε. 143
FIGURE 6-33: MIXTURE FRACTION AT ALL LOCATIONS FOR METHANE AND STETSYUK'S EXPERIMENT. S=0.3, RNG k-ε. 143
FIGURE 6-34: MIXTURE FRACTION OF METHANE AND STETSYUK'S EXPERIMENT. A. $1D_F$, B. $3D_F$, C.$5D_F$, D. $7D_F$. S=0.3, SST. 144
FIGURE 6-35: MIXTURE FRACTION AT ALL LOCATIONS FOR METHANE AND STETSYUK'S EXPERIMENT. S=0.3, SST. 144
FIGURE 6-36: MIXTURE FRACTION OF METHANE AND STETSYUK'S EXPERIMENT. A. $1D_F$, B. $3D_F$, C.$5D_F$, D. $7D_F$. S=0.3, LRR-IP-RS. 145

FIGURE 6-37: MIXTURE FRACTION AT ALL LOCATIONS FOR METHANE AND STETSYUK'S EXPERIMENT. S=0.3, LRR-IP-RS.....145
FIGURE 6-38: MIXTURE FRACTION OF METHANE AND STETSYUK'S EXPERIMENT. A. $1D_F$, B. $3D_F$, C.$5D_F$, D. $7D_F$. S=0.3, SSG-RS. 146
FIGURE 6-39: MIXTURE FRACTION AT ALL LOCATIONS FOR METHANE AND STETSYUK'S EXPERIMENT. S=0.3, SSG-RS. 146
FIGURE 6-40: MIXTURE FRACTION OF METHANE AND STETSYUK'S EXPERIMENT. A. $1D_F$, B. $3D_F$, C.$5D_F$, D. $7D_F$. S=0.3, OMEGA-RS. 147
FIGURE 6-41: MIXTURE FRACTION AT ALL LOCATIONS FOR METHANE AND STETSYUK'S EXPERIMENT. S=0.3, OMEGA-RS.....147
FIGURE 6-42: MASS FRACTION OF METHANE AND STETSYUK'S EXPERIMENT AT $7D_F$. k-ε, S=0.3.....148
FIGURE 6-43: 2D (TOP VIEW) AND 3D ωM CONTOURS OF METHANE. A. $1D_F$, B. $3D_F$, C.$5D_F$, D. $7D_F$. k-ε .S=0.3.....150
FIGURE 6-44: 2D (TOP VIEW) AND 3D ωM CONTOURS OF METHANE. A. $1D_F$, B. $3D_F$, C.$5D_F$, D. $7D_F$. RNG k-ε .S=0.3. 151
FIGURE 6-45: 2D (TOP VIEW) AND 3D ωM CONTOURS OF METHANE. A. $1D_F$, B. $3D_F$, C.$5D_F$, D. $7D_F$. SST. S=0.3.....152
FIGURE 6-46: 2D (TOP VIEW) AND 3D ωM CONTOURS OF METHANE. A. $1D_F$, B. $3D_F$, C.$5D_F$, D. $7D_F$. LRR-IP-RS. S=0.3.....153
FIGURE 6-47: 2D (TOP VIEW) AND 3D ωM CONTOURS OF METHANE. A. $1D_F$, B. $3D_F$, C.$5D_F$, D. $7D_F$. SSG-RS. S=0.3. 154
FIGURE 6-48: 2D (TOP VIEW) AND 3D ωM CONTOURS OF METHANE. A. $1D_F$, B. $3D_F$, C.$5D_F$, D. $7D_F$. OMEGA-RS. S=0.3.....155
FIGURE 6-49: MIXTURE FRACTION OF METHANE AND STETSYUK'S EXPERIMENT. A. $1D_F$, B. $3D_F$, C.$5D_F$, D. $7D_F$. S=0.58, k-ε. 158
FIGURE 6-50: MIXTURE FRACTION AT ALL LOCATIONS FOR METHANE AND STETSYUK'S EXPERIMENT. S=0.58, k-ε.....158
FIGURE 6-51: MIXTURE FRACTION OF METHANE AND STETSYUK'S EXPERIMENT. A. $1D_F$, B. $3D_F$, C.$5D_F$, D. $7D_F$. S=0.58, RNG k-ε.....159
FIGURE 6-52: MIXTURE FRACTION AT ALL LOCATIONS FOR METHANE AND STETSYUK'S EXPERIMENT. S=0.58, RNG k-ε. 159

FIGURE 6-53: MIXTURE FRACTION AT ALL LOCATIONS FOR METHANE AND STETSYUK'S EXPERIMENT. S=0.58, SST. 160
FIGURE 6-54: MIXTURE FRACTION OF METHANE AND STETSYUK'S EXPERIMENT. A. $1D_F$, B. $3D_F$, C.$5D_F$, D. $7D_F$. S=0.58, SST. 160
FIGURE 6-55: MIXTURE FRACTION AT ALL LOCATIONS FOR METHANE AND STETSYUK'S EXPERIMENT. S=0.58, LRR-IP-RS.....161
FIGURE 6-56: MIXTURE FRACTION OF METHANE AND STETSYUK'S EXPERIMENT. A. $1D_F$, B. $3D_F$, C.$5D_F$, D. $7D_F$. S=0.58, LRR-IP-RS. 161
FIGURE 6-57: MIXTURE FRACTION AT ALL LOCATIONS FOR METHANE AND STETSYUK'S EXPERIMENT. S=0.58, SSG-RS. 162
FIGURE 6-58: MIXTURE FRACTION OF METHANE AND STETSYUK'S EXPERIMENT. A. $1D_F$, B. $3D_F$, C.$5D_F$, D. $7D_F$. S=0.58, SSG-RS. 162
FIGURE 6-59: MIXTURE FRACTION AT ALL LOCATIONS FOR METHANE AND STETSYUK'S EXPERIMENT. S=0.58, OMEGA-RS. 163
FIGURE 6-60: MIXTURE FRACTION OF METHANE AND STETSYUK'S EXPERIMENT. A. $1D_F$, B. $3D_F$, C.$5D_F$, D. $7D_F$. S=0.58, OMEGA-RS. 163
FIGURE 6-61: 2D (TOP VIEW) AND 3D ωM CONTOURS OF METHANE. A. $1D_F$, B. $3D_F$, C.$5D_F$, D. $7D_F$. k-ε .S=0.58. 165
FIGURE 6-62: 2D (TOP VIEW) AND 3D ωM CONTOURS OF METHANE. A. $1D_F$, B. $3D_F$, C.$5D_F$, D. $7D_F$. RNG k-ε .S=0.58. 166
FIGURE 6-63: 2D (TOP VIEW) AND 3D ωM CONTOURS OF METHANE. A. $1D_F$, B. $3D_F$, C.$5D_F$, D. $7D_F$. SST. S=0.58.....167
FIGURE 6-64: 2D (TOP VIEW) AND 3D ωM CONTOURS OF METHANE. A. $1D_F$, B. $3D_F$, C.$5D_F$, D. $7D_F$. LRR-IP-RS. S=0.58.....168
FIGURE 6-65: 2D (TOP VIEW) AND 3D ωM CONTOURS OF METHANE. A. $1D_F$, B. $3D_F$, C.$5D_F$, D. $7D_F$. SSG-RS. S=0.58. 169
FIGURE 6-66: 2D (TOP VIEW) AND 3D ωM CONTOURS OF METHANE. A. $1D_F$, B. $3D_F$, C.$5D_F$, D. $7D_F$. OMEGA-RS. S=0.58.....170
FIGURE 6-67: MIXTURE FRACTION AT ALL LOCATIONS FOR METHANE AND STETSYUK'S EXPERIMENT. S=1.07, k-ε. 173
FIGURE 6-68: MIXTURE FRACTION OF METHANE AND STETSYUK'S EXPERIMENT. A. $1D_F$, B. $3D_F$, C.$5D_F$, D. $7D_F$. S=1.07, k-ε. 173

FIGURE 6-69: MIXTURE FRACTION AT ALL LOCATIONS FOR METHANE AND STETSYUK'S EXPERIMENT. S=1.07, RNG k-ε. 174
FIGURE 6-70: MIXTURE FRACTION OF METHANE AND STETSYUK'S EXPERIMENT. A. $1D_F$, B. $3D_F$, C.$5D_F$, D. $7D_F$. S=1.07, RNG k-ε.....174
FIGURE 6-71: MIXTURE FRACTION AT ALL LOCATIONS FOR METHANE AND STETSYUK'S EXPERIMENT. S=1.07, SST. 175
FIGURE 6-72: MIXTURE FRACTION OF METHANE AND STETSYUK'S EXPERIMENT. A. $1D_F$, B. $3D_F$, C.$5D_F$, D. $7D_F$. S=1.07, SST.....175
FIGURE 6-73: MIXTURE FRACTION AT ALL LOCATIONS FOR METHANE AND STETSYUK'S EXPERIMENT. S=1.07, LRR-IP-RS.....176
FIGURE 6-74: MIXTURE FRACTION OF METHANE AND STETSYUK'S EXPERIMENT. A. $1D_F$, B. $3D_F$, C.$5D_F$, D.$7D_F$. S=1.07, LRR-IP-RS.....176
FIGURE 6-75: MIXTURE FRACTION AT ALL LOCATIONS FOR METHANE AND STETSYUK'S EXPERIMENT. S=1.07, SSG-RS.....177
FIGURE 6-76: MIXTURE FRACTION OF METHANE AND STETSYUK'S EXPERIMENT. A. $1D_F$, B. $3D_F$, C.$5D_F$, D. $7D_F$. S=1.07, SSG-RS. 177
FIGURE 6-77: MIXTURE FRACTION AT ALL LOCATIONS FOR METHANE AND STETSYUK'S EXPERIMENT. S=1.07, OMEGA-RS. 178
FIGURE 6-78: MIXTURE FRACTION OF METHANE AND STETSYUK'S EXPERIMENT. A. $1D_F$, B. $3D_F$, C.$5D_F$, D. $7D_F$. S=1.07, OMEGA-RS.....178
FIGURE 6-79: 2D (TOP VIEW) AND 3D ωM CONTOURS OF METHANE. A. $1D_F$, B. $3D_F$, C.$5D_F$, D. $7D_F$. k-ε .S=1.07.....181
FIGURE 6-80: 2D (TOP VIEW) AND 3D ωM CONTOURS OF METHANE. A. $1D_F$, B. $3D_F$, C.$5D_F$, D. $7D_F$. RNG k-ε .S=1.07. 182
FIGURE 6-81: 2D (TOP VIEW) AND 3D ωM CONTOURS OF METHANE. A. $1D_F$, B. $3D_F$, C.$5D_F$, D. $7D_F$. SST. S=1.07.....183
FIGURE 6-82: 2D (TOP VIEW) AND 3D ωM CONTOURS OF METHANE. A. $1D_F$, B. $3D_F$, C.$5D_F$, D. $7D_F$. LRR-IP-RS. S=1.07.....184
FIGURE 6-83: 2D (TOP VIEW) AND 3D ωM CONTOURS OF METHANE. A. $1D_F$, B. $3D_F$, C.$5D_F$, D. $7D_F$. SSG-RS. S=1.07.....185
FIGURE 6-84: 2D (TOP VIEW) AND 3D ωM CONTOURS OF METHANE. A. $1D_F$, B. $3D_F$, C.$5D_F$, D. $7D_F$. OMEGA-RS. S=1.07.....186
FIGURE 6-85: 2D (TOP VIEW) AND 3D ωM CONTOURS OF METHANE. 190

FIGURE 6-86: 2D (TOP VIEW) AND 3D ωM CONTOURS OF METHANE. 191
FIGURE 6-87: 2D (TOP VIEW) AND 3D ωM CONTOURS OF METHANE. 192
FIGURE 6-88: 2D (FRONT VIEW) METHANE VF. S=0.3, LRR-IP-RS.....194
FIGURE 6-89: 2D (FRONT VIEW) METHANE VF. S=0.58, LRR-IP-RS.....194
FIGURE 6-90: 2D (FRONT VIEW) METHANE VF. S=1.07, LRR-IP-RS.....195
FIGURE 6-91: 3D METHANE VELOCITY, A. STREAMLINE, B. VECTORS. S=0.3, LRR-IP-RS. 196
FIGURE 6-92: 3D METHANE VELOCITY, A. STREAMLINE, B. VECTORS. S=0.58, LRR-IP-RS. 197
FIGURE 6-93: 3D METHANE VELOCITY, A. STREAMLINE, B. VECTORS. S=1.07, LRR-IP-RS. 198
FIGURE 6-95: 3D AIR VELOCITY VECTORS. S=0.58, LRR-IP-RS. 199
FIGURE 6-94: 3D AIR VELOCITY VECTORS. S=0.3, LRR-IP-RS. 199
FIGURE 6-96: 3D AIR VELOCITY VECTORS. S=1.07, LRR-IP-RS. 200
FIGURE 6-97: 2D AIR VELOCITY VECTORS. A. WITH SCREWS, B. WITHOUT SCREWS, S=0.58, LRR-IP-RS. 200

List of Tables

TABLE 2-1: NON-REACTING BOUNDARY CONDITIONS 35
TABLE 2-2: RELATED NUMERICAL RESEARCH SUMMERY 45
TABLE 3-1: METHODOLOGIES COMPUTATIONAL REQUIREMENT 55
TABLE 3-2: RANS MODELS CLASSIFICATION. RE-PRODUCED FROM (VERSTEEG & MALALASEKERA, 2007) 62
TABLE 3-3: CATEGORIZATION OF TURBULENCE MODELS. RE-PRODUCED FROM (WOELKE, 2007). 62
TABLE 3-4: CLASSIFICATION OF STANDARD REYNOLDS STRESS TURBULENCE MODELS 72
TABLE 3-5: STANDARD REYNOLDS STRESS SUB-MODELS CONSTANTS 74
TABLE 3-6: TURBULENCE MODELS LIMITATIONS 76
TABLE 4-1: COMPUTATIONAL B.C IN ANSYS-CFX 84
TABLE 4-2: MESH ANALYSIS BASED ON RMSE FOR ALL VOLUME FRACTIONS. 87
TABLE 4-3: MESH ANALYSIS BASED ON VOLUME VALUE AT ONE LOCATION.. 87
TABLE 4-4: COMPUTATIONAL B.C IN ANSYS-CFX 93
TABLE 4-5: MESH ANALYSIS BASED ON RMSE FOR ALL VOLUME FRACTIONS. SECOND CASE STUDY 95
TABLE 4-6: MESH ANALYSIS BASED ON VOLUME VALUE AT ONE LOCATION. SECOND CASE STUDY 95
TABLE 5-1: SIMULATION BOUNDARY CONDITIONS. SWIRLING SIMULATION. 105
TABLE 5-2: COMPUTATIONAL B.C IN ANSYS-CFX. SWIRLING SIMULATION..... 105
TABLE 5-3: INITIAL B.C IN ANSYS-CFX. SWIRLING SIMULATION 105
TABLE 5-4: MESH ANALYSIS BASED ON RMSE FOR ALL VOLUME FRACTIONS. SWIRLING SIMULATION 108
TABLE 5-5: MESH ANALYSIS BASED ON VOLUME VALUE AT ONE LOCATION. SWIRLING SIMULATION 109
TABLE 6-1: RMSE PERCENT VALUE AT A SPECIFIC LOCATION. FIRST PLANAR CASE STUDY 125
TABLE 6-2: RMSE PERCENT VALUE AT A SPECIFIC LOCATION. SECOND PLANAR CASE STUDY 134
TABLE 6-3: RMSE PERCENT FOR ALL THE MODELS AT A SPECIFIC LOCATION. S=0.3 149

TABLE 6-4: RMSE PERCENT FOR ALL THE MODELS AT A SPECIFIC LOCATION. S=0.58 164
TABLE 6-5: RMSE PERCENT VALUE FOR ALL THE MODELS AT A SPECIFIC LOCATION. S=1.07 180
TABLE 6-6: AVERAGE RMSE PERCENT FOR ALL THE MODELS AT ALL SWIRLING NUMBER 180
TABLE 6-7: RMSE PERCENT FOR RSMS AT *S*=0.3 187
TABLE 6-8: RMSE PERCENT FOR RSMS AT *S*=0.58 188
TABLE 6-9: RMSE PERCENT FOR RSMS AT *S*=1.07 188

Nomenclature

Symbols	Descriptions	Units
$\overline{R_i}$	Production Rate of Species i	kg/m^3. s
$\overline{S_i}$	Growth Production Rate	kg/m^3. s
$\acute{p}$	Modified Pressure	Pa
$\bar{q}_j$	Time-Averaged Heat Flux	J/m^2. s
$\acute{v}_r, \acute{v}_\emptyset, \acute{v}_z$	Velocity Fluctuations In r, $\emptyset$ And z Directions	m/s
D_i, $D_\circ$	Inner and Outer Jet Diameter	m
$\bar{E}$	Time-Averaged Value of Energy	J/kg
F_1, F_2	Relevant Closure Coefficients	-
G_Z	Axial Flux of Axial Momentum	Kg.m^2/s
G_θ	Axial Flux of Angular Momentum	Kg.m^2/s
K_c	Concentration Spreading Rate	M/s
P_k	Turbulence Creation	m^2/s^2
P_{kb}, $P_{\varepsilon b}$	Influence Of the Buoyancy	N
Pr_t	Turbulent Prandtl Number	m^2/s
R_{ij}	Reynolds Sub-Grid Tensor	-
S_M	Sum Of the Body Forces	N
S_g	Theoretical Or Geometric Swirl Number	-
S_{ij}	Mean Strain Rate Tensor	-
V_D	Fluid Domain Volume	m^3
W_r	Angular Velocity	m/s
a_{ij}	Anisotropy Tensor	-
f_j	j–Coordinate of Force	N
f_η	Turbulence Model Coefficient	-
l_t	Length Scale	mm
$\bar{u}$	Time-Average Velocity	m/s
v_r, $v_\emptyset$, v_z	Mean Velocities In r, $\emptyset$ And z Directions	m/s
δ_{i3}	Kronecker Delta	-
ε_{ij3}	Unit Tensor for Centrifugal Forces	-
μ_{eff}	Effective Viscosity	N.s/m^2

μ_t	Turbulent Or Eddy Viscosity	m^2/s
$\bar{\rho}$	Time-Average Density	Kg/m^3
a	Axial Induction Factor	-
a'	Tangential Induction Factor	-
a_1, a_2, a_3	Semi-Major Axis of The Ellipse	mm
b	Semi-Minor Axis of The Ellipse	mm
C_M	Moment Coefficient	-
C_p	Pressure Coefficient	-
c_p	Specific Heat at Constant Pressure	J/kg. ^oK
D	Diffusion Coefficient, Burner Diameter	m^2/s, mm
d	Orifice Diameter	mm
D_a	Axial Diameter	mm
D_E	Ethylene Diameter	mm
D_f	Fuel Nozzle Diameter	mm
F_n	Normal Force	N
F_t	Tangential Force	N
k	Turbulent Kinetic Energy	J/kg
$\dot{m}$	Mass Flow Rate	Kg/s
p	Pressure	Pa
R	Radius	mm
r	Radial Distance	mm
Re	Reynold Number	-
S	Swirl Number	-
T	Temperature	^oK
t	Time	s
u	X-Velocity Component	m/s
U_m	Mean Velocity	m/s
u_{max}	Maximum Velocity	m/s
v	Y-Velocity Component	m/s
V	Volumetric Flow Rate	m^3/s
w	W-Velocity Component	m/s
U	Axial Velocity	m/s
g	Gravity Acceleration	m/s^2

k	Turbulence Kinetic Energy	m^2/s^2
x	Downstream Distance from the Virtual Source	m
z	Mixture Fraction	-

Greek Symbols

Γ_t	Eddy Diffusivity	m^2/s
Φ_{ij}	Pressure-Strain Tensor	N/m^2
Ω_{ij}	Vorticity Tensor	r.p.m
τ_{ij}	Sub-Grid Tensor	Pa
β	Thermal Expansion	$1/^oK$
γ	Specific Heat Ratio, Azimuth Angle	-, ^{o}
δ	Boundary Layer Thickness	mm
μ	Dynamic Viscosity	$N.s/m^2$
ρ	Density	Kg/m^3
τ_w	Wall Shear Stress	Pa
υ	Kinematic Viscosity	m^2/s
ω_m	Mass Fraction or Mixture Fraction of Methane	-
η	Dimensionless Parameter	-
α	Thermal Diffusivity	W/m.K
ε	Dissipation Rate	m^2/s^3
θ	Cone Angle	^{o}
π	Constant, Equal to 3.14	-
σ	Standard Deviation	mm
ω	Turbulent Frequency	1/s
ϑ	Volume Fraction	-

List of Abbreviations

2D	Two-dimensional	-
3D	Three-dimensional	-
BC	Boundary Conditions	-
CFD	Computational Fluid Dynamics	-
DNS	Direct Numerical Simulation	-

DOES	Delayed-Detached Eddy Simulation	-
DRSM	Differential Reynolds Stress Model	-
FDM	Finite Difference Method	-
FEM	Finite Element Method	-
FVM	Finite Volume Method	-
INS	Indirect Numerical Simulation	-
LDV	Laser Doppler Velocimetry	-
LES	Large Eddy Simulation	-
LRR-IP	Launder, Reece and Rodi Isotropizatio of Production	-
Omega-Rs	Omega-Based Reynolds Stress Model	-
PDES	Partial Differential Equations	-
PTV	Particle Tracking Velocimetry	-
RANS	Reynolds-Averaged Navier-Stokes	-
RCM	Rapid Compression Machine Model	-
RMSE	Root Mean Square Error	-
RSM	Reynolds Stress Model	-
SA	Spalart-Allmaras	-
SIMPLE	Semi Implicit Method for Pressure Linked Equations	-
SOM-MC	Second-Order Moment-Monte Carlo	-
SSG RSM	Speziale, Sarkar and Gatski Reynolds Stress Model	-
SST	Shear Stress Transport	-
TDMA	Tri-Diagonal Matrix Algorithm	-
USM	Unified Second-Order Moment	-

Subscripts

$C_{\varepsilon 1}$, $C_{\varepsilon 2}$, σ_k, σ_ε	Turbulence Model Constant, Equal to 1.44, 1.92, 1.0, 1.3	-
$C_{\varepsilon 2\ RNG}$	Turbulence Model Constant, Equal to 1.68	-
C_μ	Turbulence Model Constant, Equal to 0.09	-
f_μ	Proportionality Constant Equal to 0.01	-
β_{RNG}	Turbulence Model Constant, Equal to 0.012	-
$\sigma_{\varepsilon\ RNG}$	Turbulence Model Constant, Equal to 0.7179	-

Chapter 1

1.1 Introduction

This chapter provide a general introduction of computational fluid dynamics modelling theory. Then, a brief historical study of fluids dynamics phenomena extended with a general outline of fluid flow types. In addition, the motivation of this study is established in section 1.3. The research objective along with the description of the thesis are explained in sections 1.4 and 1.5, respectively.

1.2 General review of CFD and modern system development

Computational Fluid Dynamics (CFD), known as a numerical process, uses generally to predicate fluid flow dynamics and some scientific processes such as "heat transfer, mass transfer, chemical reactions, and related phenomena" by solving governing mathematical equations (Bakker, 2002; Date, 2005). CFD results are used to establish new designs, developments, restructure and troubleshooting (Bakker, 2002). Also, CFD is dealing with fluid dynamics problems by using numerical methods on a computer. Interestingly, CFD relation with these kinds of problems is relatively new compared to fluid dynamics issues which are over three centuries old, while CFD is about five decades old only. In general, all the problems that are associated with CFD involve nonlinear equations, multipart geometries, different sorts of sciences and engineering fields which showed an extraordinary success and raised the demands for CFD. Use of CFD includes the formality of boundary and initial conditions, partial differential equation and subject other conditions (Niyogi et al., 2006). CFD is a computer-based simulation used to analyse many systems including fluid flow, heat transfer and relevant aspects such as chemical reactions and combustion. Likewise, there is a wide range of industrial and non-industrial applications constructed using the CFD technique. For example, the aerodynamics system, hydrodynamics system and the gas turbine engine in power plant and environmental engineering. Furthermore, external and internal fluid flow performances, electrical and electronic engineering, heat transfer, biomedical engineering and others (Versteeg & Malalasekera, 2007).

(Ashgriz & Mostaghimi, 2002) specify that CFD provides a numerical solution to the fluid motion problems by solving the chosen equations through the following steps:

- Indicate the required mathematical equations, differential equations, to represent the fluid flow

• Discretise the equations to create a numerical analogue

• Generate a domain including elements or small grids

• Specify the initial conditions and the boundary conditions of the system

• Specify parameters if needed to solve the problem, either by direct method or iterative method.

Moreover, CFD is considered as a part of classical fluid dynamics and numerical analysis reinforced by vital electronic digital computers with a remarkable contribution that has been done by many researchers, scientists and engineers all over the world. Therefore, CFD able is able to of solve almost all problems of fluid dynamics which increases the passion and confidence of researchers and scientists widely (Niyogi et al., 2006). Some researchers define CFD as a tool that applies to provide a numerical simulation of fluid flows by implementing a sequence of methodologies into a computer where the results can be visualised (Hirsch, 2007; Kinyua Kande, 2017).

Recently, (Sharma, 2016) defines CFD as "a theoretical-method of scientific and engineering investigation, concerned with the development and application of a video-camera like a tool (a software) which used for a unified cause-and-effect based analysis of a fluid-dynamics as well as heat and mass transfer problem. Lastly, One of the researchers defines CFD as a numerical analysis tool with algorithms used to solve fluid mechanics problems (Kinyua Kande, 2017).

Historically,(Emmons, 1944; Richardson, 1911) were recognised as two of the first attempting to establish the uses of CFD. However, the regular study of CFD started in the sixties. CFD developed almost concurrently with electronic digital computers. (Courant et al., 1928) was the first scientist who established the basics of finite difference method for partial differential equations by studying the presence and individuality of solutions of partial differential equations. Meanwhile, the development of powerful electronic digital computers for the past 50 years made CFD progress on very high demands with huge progress outcome, especially for nonlinear problems. Furthermore, the most known methods for this purpose are the finite difference method, finite element method, finite volume method and the spectral method. Remarkably, the use of CFD was led by the governmental and academic institutions since the 1980s, where relevant training was conducted to the researchers and other users.

Nevertheless, until the millennium industry fields were facing difficulties finding professional CFD engineers (Halley & Spall, 2000).

Moreover, the regular study of CFD started in the sixties by the aerospace industry to design, analyse and produce aircraft and jet engines (Date, 2005). Subsequently, this method applied to manufacture internal combustion engines, combustion chambers of gas turbines, predation of drag forces for motor vehicles, and more environmental uses. Gradually, CFD became an energetic component in the design and manufacturing of industrial and non-industrial products and processes (Versteeg & Malalasekera, 2007).

Additionally, it has been indicated that CFD was crucial to the primary desktop software (such as computer codes) being established in the early 1970s and as such, CFD plays an essential role in engineering's industrial development since that time (Date, 2005). Furthermore, the main difference between CFD methods and the approximate methods of standard fluid dynamics is that by using an exact numerical method along with the model implementations such as equations, boundary, and initial conditions. Plus, without presenting any further estimation. On the other hand, the error percent of the approximate methods is much higher than the CFD error percent, which eliminated by improving the mesh quality of the project. Therefore, the computed solutions are predicted to approach the exact solution, while it is not applicable when using a different approximate method (Niyogi et al., 2006).

As it's been mentioned above, CFD is becoming an energetic component in the design and manufacturing of industrial and non-industrial products and processes. Thus, the outcome results need to establish reliability by Verification & Validation. Furthermore, because of its importance, many forums discuss the definition of Verification & Validation such as the American Institute of Aeronautics and Astronautics AIAA (Astronautics, 1998), the ERCOFTAC (Casey et al., 2000) or the ITTC Resistance Committee (Manual, 1999) where different meaning can be found. However, the most definition most straightforward is given by (Roache, 1998) where Verification is a mathematical process that aims to illustrate that the steps of solving the equation are correct. Moreover, Validation is a part of the scientific engineering process which aims to illustrate that the chosen equation is correct “solving the right equations” (Eça & Hoekstra, 2006).

It is known that the cost of CFD facilities is expensive as they use high-performance computers, HPC, along with high technical labs. However, the CFD has many advantages, for instance, it can save time and cost of new system design and it can review extensive systems

where it is impossible to control or accomplish in experiments. Moreover, CFD is safer than experiments and the ability to apply more risks condition to the same project. Finally, the CFD program indicates high quality and different outcome results (Versteeg & Malalasekera, 2007).

Furthermore, the numerical algorithms applied in CFD codes to solve fluid flow phenomena with innovative results contain three main elements. These elements are pre-processor, solver, and post-processor (more details in chapter 3) (Ashgriz & Mostaghimi, 2002; Versteeg & Malalasekera, 2007).

1.3 A brief history of fluid dynamics

Fluids are defined as anything around that can flow and have the ability to rearrange their shapes flexibly without affecting the macroscopic properties of the fluids, such as gases and liquids. Unlike solids, fluid particles can move through pipes at different velocities and accelerations. Fluids are considered as continuous media in which the motion of fluids can be specified according to velocity u, pressure p, and density ρ, etc., (Batchelor & Batchelor, 2000; Pedley, 1997). The fluid flow can be classified into hydraulic which is improved from experimental studies, and hydrodynamic, which is developed from theoretical studies. Interestingly, both classifications have merged into one discipline, which is fluid mechanics (Nakayama, 2018).

The applications of fluid mechanics in human activities and engineering studies are abundant because the earth is covered with 75% water and 100% air. For instance, medical investigations of breathing and blood flow as well as energy generation. Additionally, engineering applications consist of fans, turbans and pumps (Bahrami, 2009). Furthermore, fluid mechanics can cover other applications that occur in nature, such as in biology, and in numerous invented or manufactured situations (Young et al., 2010).

Precisely, then, can fluid flow be considered as an essential discipline in industrial processes; particularly the operations that include the heat transfer process. Examples of applications of fluid flow in transferring the heat are that the cooling water circulated through a gasoline machine, as well as the water stream through the central part of a nuclear reactor and the airflow passing the winds of a motor (Lienhard IV & Lienhard, 2008).

The fluid flow has been discovered in the past when prehistoric relics of irrigation channels had been first found in Egypt and Mesopotamia. This discovery had been proved that the water canals had been created 4000 years B.C. These days, the water city system depends on

transferring clear water from the outlying areas to fountains, baths and public buildings. Although the water city system is very ancient, it has been developed so that the water can be transferred effectively. Also, the size and shape of the water pipe had been designed as well as the supply pressure had been regulated to avoid friction with the wall of the pipe (Nakayama, 2018).

Many researchers have well solved the previous studies of flow problems such as sailing ships and irrigation systems. For example, Archimedes had supposed the parallelogram law for adding vectors as well as the laws of bouncing, applying them to floating and flooded bodies (Rosentrater & Balamuralikrishna, 2005). Moreover, the equation of conservation of mass in one-dimension steady-state flow had been stated by Leonardo da Vinci. Besides, Leonardo da Vinci has made a significant change in the field of hydraulics. Interestingly, he was the first to suppose laws of drag or movement of a jet or falling water. Furthermore, in the period between 1707-1783 the differential and integral equations of motion known as the momentum-flux conservation equations for an inviscid fluid had been developed by Leonhard Euler which known as the Bernoulli equation or Euler's equations. Moreover, the Navier-Stokes equation for a viscous fluid was formed in 1840 when Claude-Louis Navier presented the element of viscosity (Anderson Jr, 2010; Bašić, 2016; Niyogi et al., 2006; Rosentrater & Balamuralikrishna, 2005).

Additionally, the importance of dimensionless Reynolds number has been supposed experimentally by Osborne Reynolds. Ludwig Prandtl had explained that the fluid flow of both water flow and airflow could be divided into two layers. The first layer called the boundary layer, which is considered a thin layer, and it is near the solid surface and interfaces. The other layer patched onto a nearly inviscid outer layer, where Bernoulli and Euler's equations are applied (Bahrami, 2009). In the year 1941, studies were devoted to solving nonlinear equation problems. However, there were no general methods for solving nonlinear problems. Recently, dealing with nonlinear equations have been developed effectively by improving the electronic digital computers and the robust numerical procedures such as finite difference, finite component and their variations (Niyogi et al., 2006). Generally, Fluid flow can be divided into six types as follows:

1.2.1 Steady and unsteady flows.

Steady flows occurs when all fluid properties such as velocity, pressure, and density stay constant with time. Whereas within unsteady flows, all the fluid properties at a specific point can change with time.

1.2.2 Laminar and turbulent flow.

Depending on Reynolds number (Re), laminar flow happens when the fluid particles move in a straight and parallel streamline. This type of flow is known as viscose flow or streamline flow because the fluid particles move in a straight path. On the other hand, turbulent flow is the type of flow when the fluid particle can move in a zig-zag direction. The energy loss in turbulent flow is high because of the eddy's formation.

1.2.3 Uniform and non-uniform flow

The uniform flow can be clarified as the flow that happens when the velocity is constant with the length of flow direction at a specific time. In contrast, non-uniform flow based on changing the velocity with the length of flow direction.

1.2.4 Compressible and in-compressible fluid flow

The difference between the compressible and incompressible flow is the density. The density of the compressible fluid is changing at each point whereas the density of the incompressible fluid is constant at each point.

1.2.5 One, two and three-dimensional fluid flow

One dimensional fluid can be classified as a type of fluid when the flow characteristic such as velocity is a function of time and one space coordinate like x. Two-dimensional fluid flow, the velocity is a function of time, and two spaces coordinate such as x, y. Though, three-dimensional fluid flow is the type of flow when the velocity can be a function of time and three space coordinates x, y, z.

1.2.6 Rotational (swirl) and irrotational flow

Rotational fluid can be known as the kind of fluid in which fluid particles can rotate on their axis whilst they move in a straight path, whereas an irrotational flow means that the fluid particles cannot rotate while they are flowing along streamline (Upp & LaNasa, 2002)

1.4 Motivation

The motivation of the present work initiates from the importance of merging between the swirling jet flow phenomena and the CFD numerical modelling. Furthermore, the importance of swirling jet lies in the fact that a huge range of industrial application rely on this type of flow such as combustion chambers, heat exchangers, internal combustion engines, separators etc. Furthermore, CFD is attractive an energetic component in the design and manufacturing of industrial and non-industrial products and processes. Therefore, applying CFD approach for this type of flow is highly recommended in various industrial/non-industrial fields. The current work also aims to deliver various rang of numerical data to evaluate different types of turbulence models.

Alternatively, understanding the scalar mixing in a non-reacting isothermal flow conditions is also considered in this study. Therefore, the current work provides a comprehensive numerical study of the scalar mixing phenomena in a planar and swirling jet flow via applying ANSYS-CFX simulation program. The swirl flow effect is studied at three degree of swirl levels e.g., low, medium and high at a constant Reynolds number of 28,662 based on the area-averaged velocity of 8.46 m/s at the inlet and the diameter of 50.8mm. Thus, the intention of this study is to evaluate various turbulence models implementing in Workbench programme to simulate an isothermal, non-reacting, and steady state swirling flow.

1.5 Research aims and objectives

The main aim of this research is to investigate the modelling of a non-reacting swirling flows. The present research intentions at extending the current understanding of turbulence modelling employed with the RANS equations. The current and previously published data in open literature are still lacking and discrepancies between different studies exist. The literature review in chapter 2 describes the gaps in knowledge as described in section 2.4 which will be addressed by satisfying the following objectives:

1. Develop a validated approach to modelling the swirling and planar flow phenomena, using ANSYS-CFX. This requires a thorough understanding of prediction approaches and analysis of the discrepancy between the real-life measurements and CFD modelling.
2. Investigate the modelling of the scalar mixing process as a function of swirl number. Hence, three swirling level will be examined i.e., low, medium and high swirling strength.

3. Investigate the effect of using different turbulence models on the swirl. In another words, apply various RANS turbulence models for each swirling level to evaluate them with previously published experimental data.
4. Indicate the best RANS turbulence model among all the applied ones. To specify, establish an overview of error expectation percent of each model when it used to predict the swirling jet flow.
5. Investigate the effect of diffusion and turbulent mixing in the simulation domain. For instance, when the diffusion dominates the flow and when the turbulent is dominated.

1.6 Description of the thesis

This thesis consists of seven chapters. The general background on of CFD and modern system development along with a brief history of fluid dynamics have already been introduced in this chapter. The details and description of each chapter are shown in Figure 1-1 below.

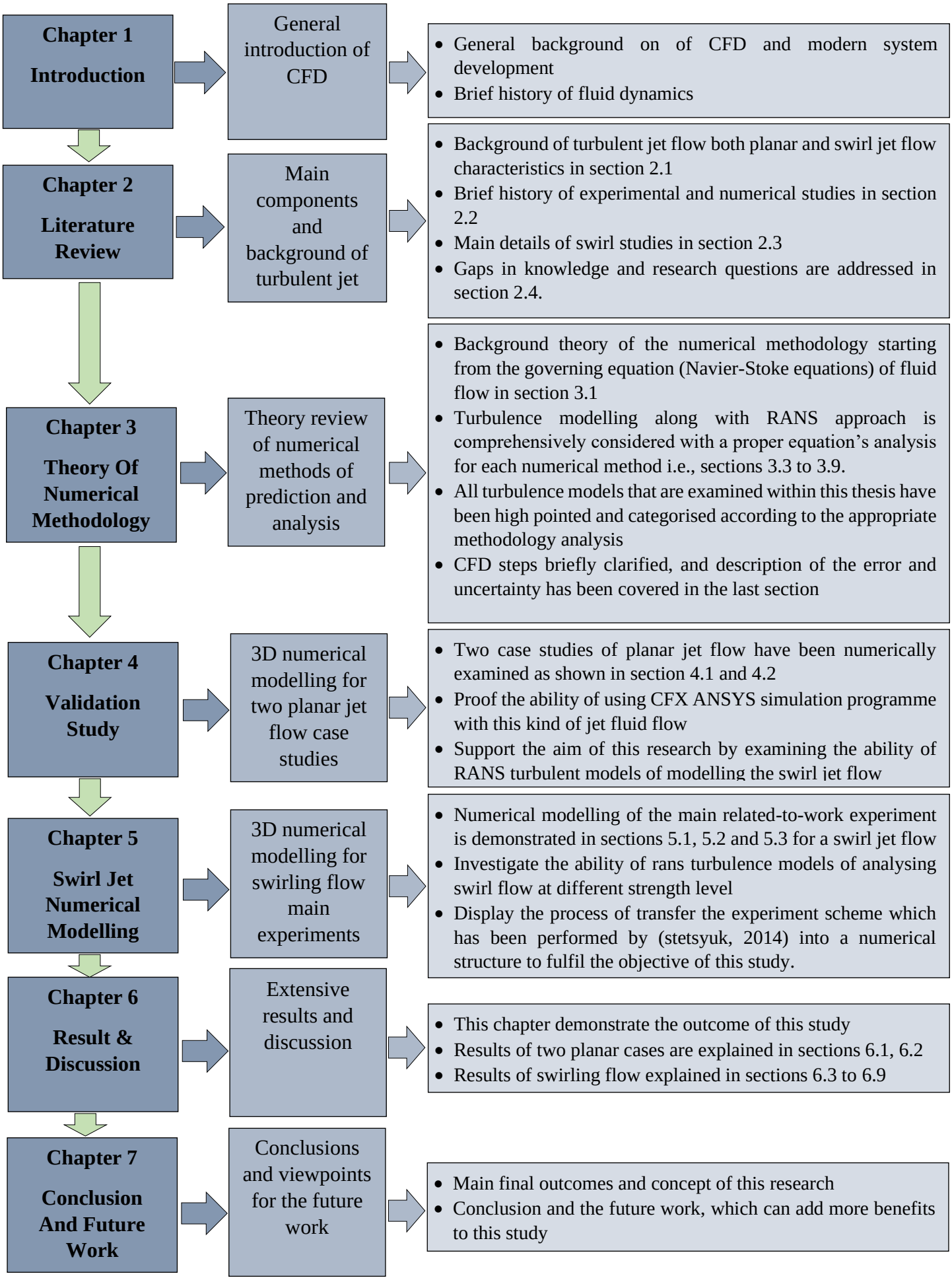

Figure 1-1: Flow Diagram Of Thesis Chapters

Chapter 2 LITERATURE REVIEW

2.1 Turbulent jet flow

Generally, Jet flow is known as any liquid or gas that streams into an environment with the different or same physical and chemical properties, such as flowing of Methane from a jet orifice to the atmospheric air (Golub & Polezhaev, 2008). Conversely, a turbulent jet is creating when a running fluid enters a stationary body of the same fluid, producing a velocity shear layer between the two fluids and causing it to mix with turbulence. Referring to Figure 2-1 which shows a fluid jet starting from its nozzle orifice toward quiescent fluid's environment, though it could be any fluid with the same density. Moreover, the previous figure shows that the continuous turbulence jet flow takes approximately conical shape which means that the radius R to the jet is proportional to the distance x downstream from the inlet place (Mihailovic, 2012).

On the other hand, one of the most important jet principles of free turbulence jet flow is the jet spread angle, which many scientists have a huge interest in studying it as it plays an important role in many applications such as the combustion engineering field. The cone shaped angle as shown in Figure 2-2 is well defined by many experiments and theoretical studies, these methods indicate that the jet half-angle have a limited range of values equals to 7° to 20° (T. Guo et al., 2017).

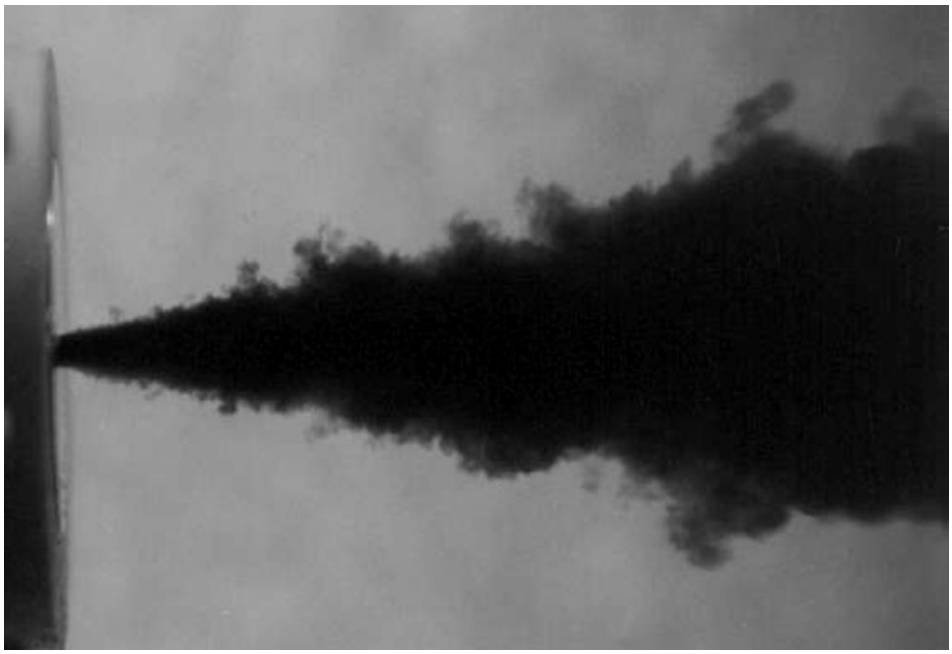

Figure 2-1: Water jet (coloured) emerging from a nozzle into undisturbed water. Modified from (Mihailovic, 2012).

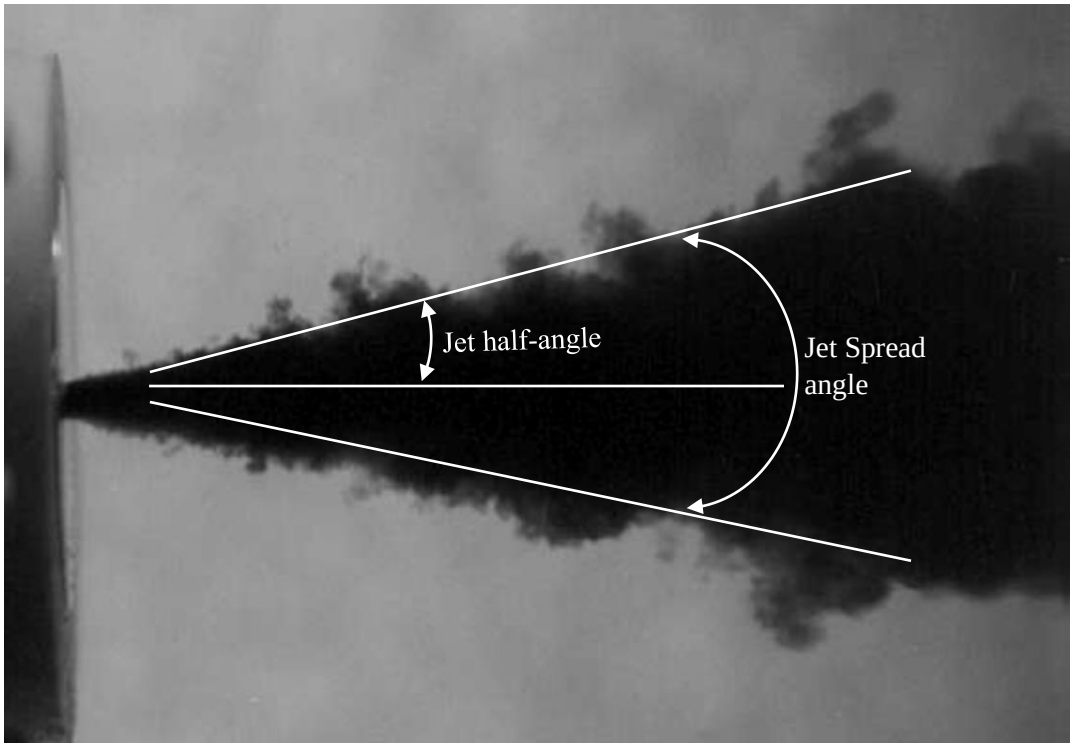

Figure 2-2: Jet Spread Angle. Modified From (Mihailovic, 2012).

Furthermore, it has been agreed that the total spread angle or cone angle has a universal value equal to 24^o or equal to 11.8^o as a half-angle value as in Figure 2-3. This angle remains the same, regardless of the type of fluid and at any different flow conditions such as the orifice diameter or inlet flow velocity. Therefore, the relationship between the downriver distance x and radius R can be indicated as follow (Mihailovic, 2012):

$$\tan 11.8 \approx 1/5 \tag{2-1}$$

$$R(x) = \frac{1}{5} x \tag{2-2}$$

On the other hand, the finite nozzle radius has a value of half the exit diameter d even though the initial jet radius is more than zero. Therefore, the virtual source or potential core has a value of approximately $5d/2$, as shown in Figure 2-3 (Mihailovic, 2012). Many types of research has been applied to study the subject of jets experimentally and numerically over the past seven decades (Ezra, 2018).

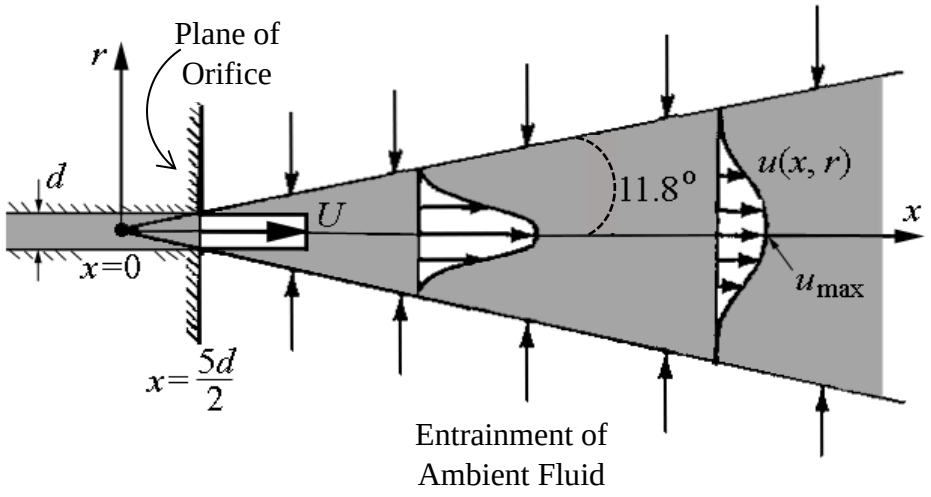

Figure 2-3: Schematic Description Of A Free Jet Flow. Modified From (Mihailovic, 2012).

Commonly, there are many types of turbulent jet flow such as plan turbulent free jet, circular jet flow, radial jet and compound jet (Rajaratnam, 1976). However, this study focuses mainly on turbulent swirling jet flow in a circular geometry burner and one case of planar jet flow. Therefore, the next subheading will include the characterization of planar jet flow and swirling jet flow in a circular jet shape, respectively.

2.1.1 Circular planar jet flow

Circular planar jets can be found in various applications such as heating/ ventilating functions, drying processes, isothermal jets and non-isothermal jets. The efficiency of mixing in this kind of jet flow is dependent upon the jet spread rate and potential core decay. The shear layer is known as the region of interactions – the mixing between the ambient and jet fluids – and it performs an essential factor in the growth of turbulent flow fluctuations in the entrainment of ambient fluid (Ezra, 2018; Sato & Sakao, 1964). Besides, a free jet is occurring when a fluid penetrates a quiescent environment by a pressure drove force only and there is no effect of the wall ceiling or barrier on the flow, while a confined jet flow created by the influence of reverse flows originated from the same jet entraining ambient material. Furthermore, the static pressure is constant in the free shear layer for the subsonic jet flow because the fluid boundary cannot maintain a pressure difference across it. Then, the outlet boundary layer grows as a mixed free shear layer and entraining the

ambient fluid in the jet flow. Therefore, the mass flow increases with jet spread along the downstream direction while the centreline velocity decreases to conserve momentum (Ezra, 2018; Rajaratnam, 1976). Many researchers have studied the flow structure of free jet flow and four different zones based on centreline velocity decay has been established from these studies as shown in Figures 2-4 and 2-5 (Yue, 1999).

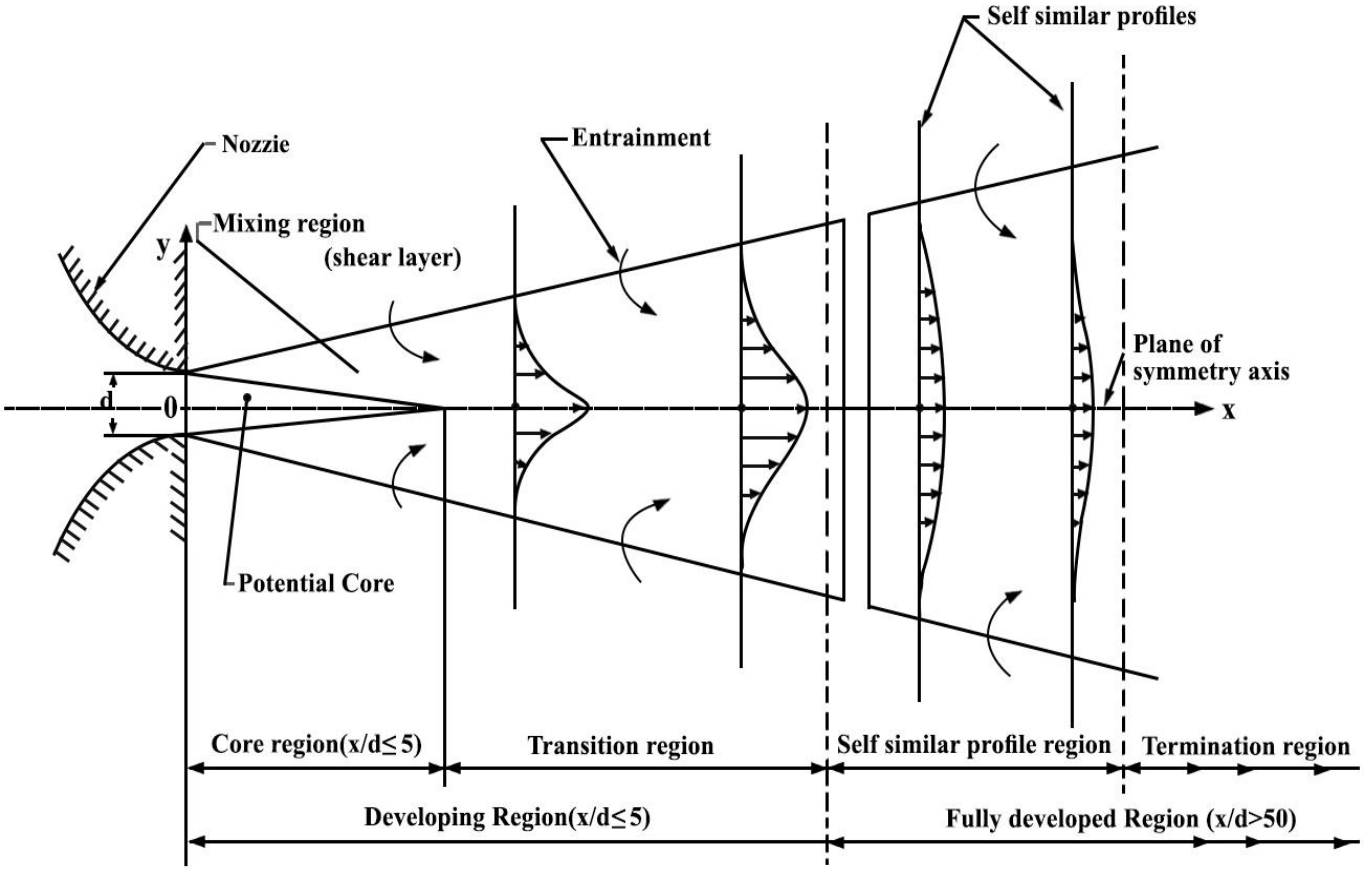

Figure 2-4: Free Jet Flow Structure. Modified From (Yue, 1999).

The first zone, which is called the convergent zone, is the place of the potential core which is the area where the centreline quantity or maximum quantity such as velocity, concentration and volume is equal to the nozzle outlet quantity and it usually expands up to $4d$ to $6d$, where d is the diameter of the nozzle exit and it is in the form of a cone. Subsequently, the second zone, which is called transition zone or interaction region, is the area where centreline quantity begins to decay and shear layers from both sides merge. This zone normally take place at the region from $6d$ to $20d$ and the quantity decay is proportional to $x^{-0.5}$ where x is the axial distance. Then, the third zone, which is called the self-similar

area, is the area where the quantity profiles such as transverse velocity profiles are similar at different values of x, the decay at this area is proportional to x^{-1}. Finally, the fourth zone, called the termination zone, is the area where the centreline quantity starts to decay quickly and it is been studied by various researchers (Yue, 1999). Moreover, diffusion plays as the main force of moving at the first two zones in the axial jet flow while the third and fourth zones are only the developed and termination jet respectively, and most engineering applications are applying at the first three zones. Alternatively, large eddies are formed because of the huge velocity difference at the surface between the outlet jet fluid velocity and the static ambient fluid which leads to lateral mixing. Then, the mixing will slow down the fluid jet flow velocity while it increases the surrounding fluid velocity and the width of the jet increases as a result of fluids interfering (Ezra, 2018; Rajaratnam, 1976).

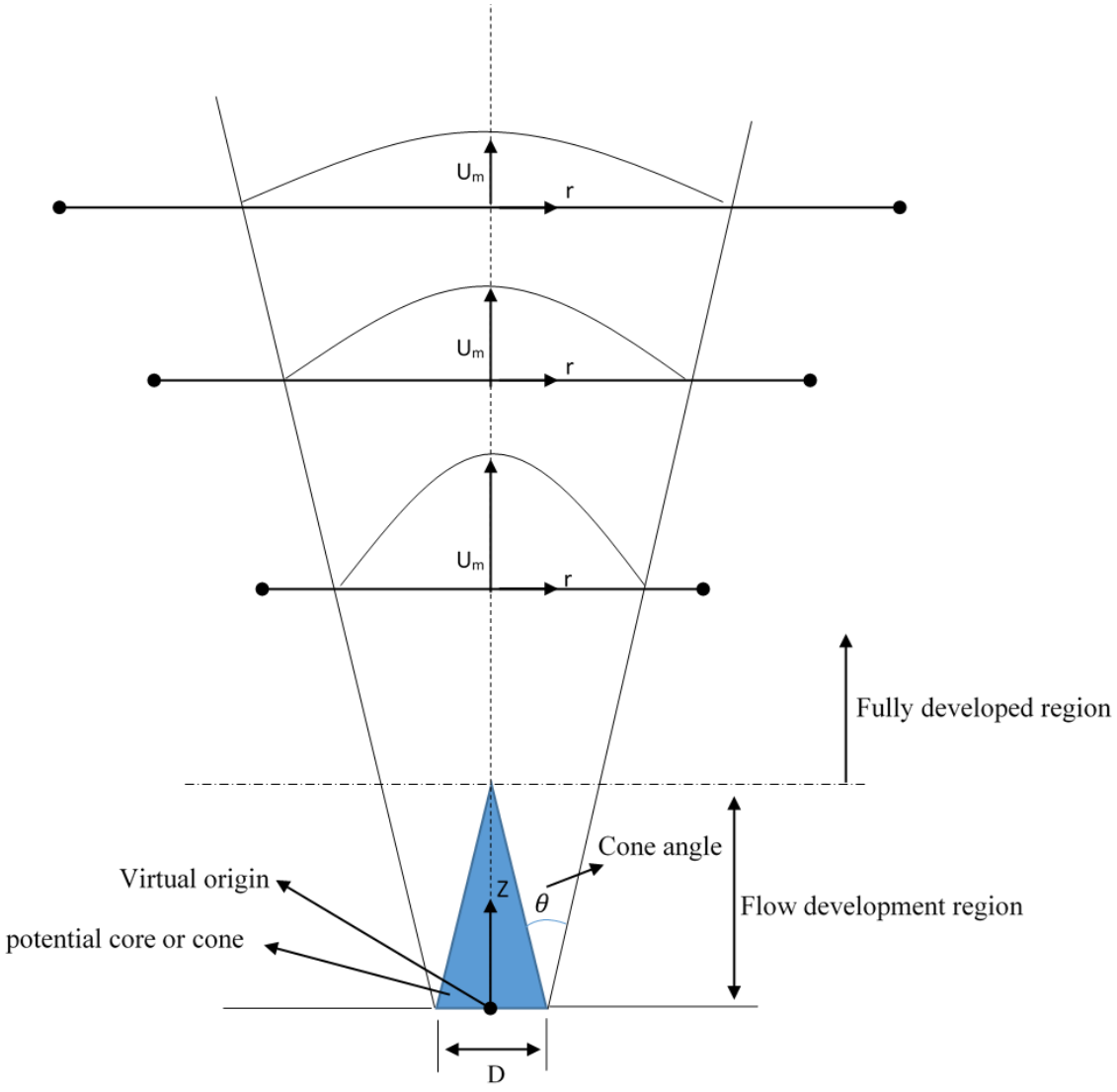

Figure 2-5: Free Vertical Jet Flow Structure

I. Characterization of circular planar jet flow

$$u(x,r) = u_{\max} \exp\left(-\frac{r^2}{2\sigma^2}\right) \quad (2\text{-}3)$$

Figure 2-6 illustrates the main fundamentals of circular jet flow where the diameter d develops from a jet nozzle with a uniform velocity of U, into a significant static quantity of the same liquid. As has been previously explained, the size of the jet increases gradually as it moves away from the nozzle. Moreover, the description of jets growth is explained in the same Figure by using a time-mean velocity measuring device such as pitot-tube to calculate the deviation of the axial velocity u with the radial distance r at different axial sections. A potential core zone can be indicated by the section up to 1-1 where the not diminished velocity equal to U, after this area the generated turbulence at the boundaries begins to penetrate to the axis and the mean velocity U_m on the axis starts to decay with x (Rajaratnam, 1976). Many other factors affect the jet spread such as Reynolds number, nozzle geometry, inlet velocity profile, fluid temperature and aspect ratio (Ezra, 2018)..

Furthermore, many numerical experiments and studies indicate the self-similar area by computing the average turbulent fluctuations, such as the work done by (Pope, 2000; Wygnanski & Fiedler, 1969), in order to calculate the velocity profiles as shown in Figures 2-7 and 2-8, the results show that velocity shape through the jet flow is a practically similar to bell curve which is fitting to Gaussian equation. Similar profiles can be seen in Figures 2-3, 2-4, 2-5 and 2-6. Therefore, the velocity can be written as follows:

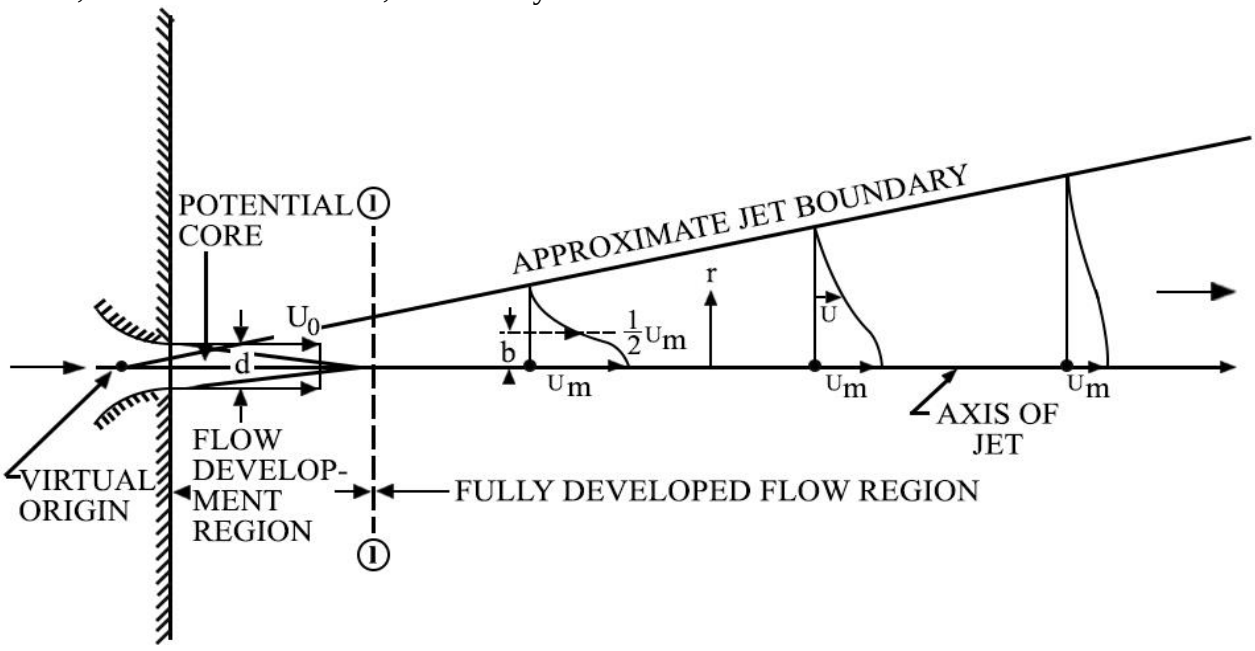

Figure 2-6: Circular Jet Flow Structure And Characteristics. Modified From (Rajaratnam, 1976).

Where x refers to the downriver distance from the virtual source along with the jet, r is the cross-jet radiating distance measured from jet centreline, $u_{\max}$ known as the maximum velocity which is normally at the centreline of the jet. Finally, σ is the standard deviation associated with the spread rate of the profile across the centreline.

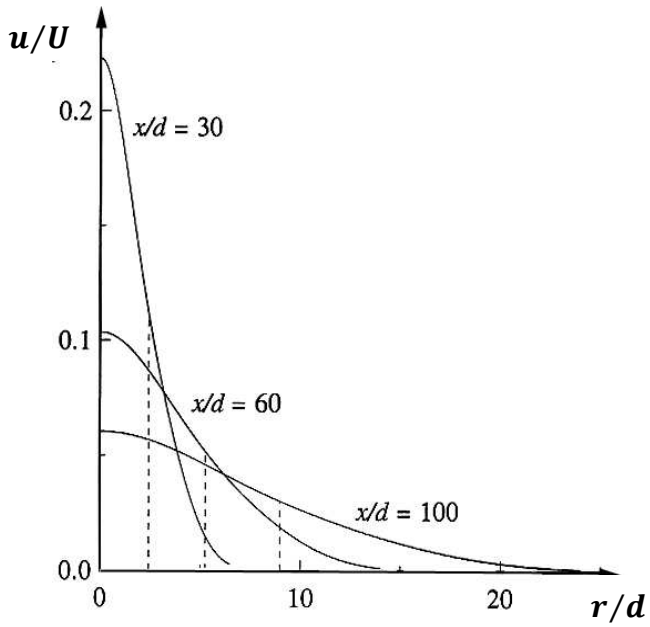

Figure 2-7: Radial Profiles Of Mean Axial Velocity In A Turbulent Round Jet, Re = 95; 500. The Dashed Lines Indicate The Half-Width. Adapted From (Mihailovic, 2012; Pope, 2000)

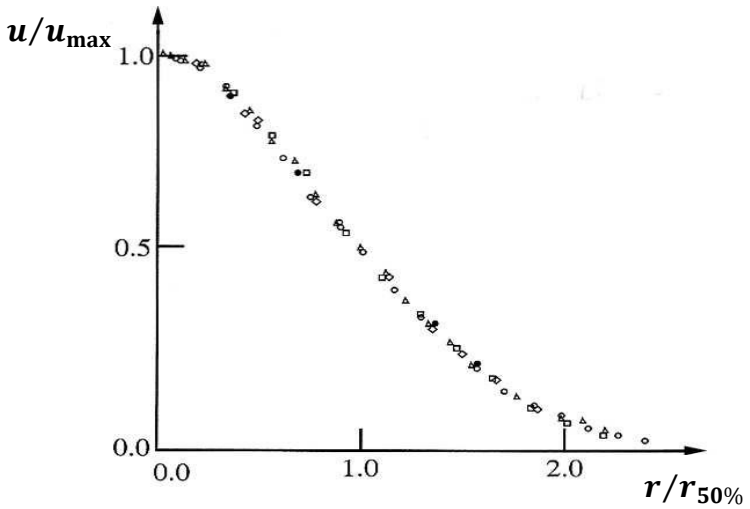

Figure 2-8: Mean AXIAL VELOCITY AGAINST RADIAL DISTANCE IN A TURBULENT ROUND JET, $Re \approx 10^5$; MEASUREMENTS OF (Wygnanski & Fiedler, 1969). Symbols: ○ $x/d = 40$; △, 50; □, 60; ◇, 75; ●, 97.5. Adapted FROM (Mihailovic, 2012; Pope, 2000).

II. Equation of motion

The circular jet equation of motion can be derived by using Reynolds equations in the cylindrical system $r, \emptyset, z$, since the jet dominates only a small width in the transverse direction then the boundary layer of the jet will be approximated. The Reynolds equations in the cylindrical system for steady axisymmetric flow is written as follow (Loitsyanskii, 1966; Rajaratnam, 1976; Schlichting, 1968):

$$v_r \frac{\partial v_r}{\partial r} + v_z \frac{\partial v_r}{\partial z} - \frac{v_\emptyset^2}{r} = -\frac{1}{\rho}\frac{\partial p}{\partial r} + v\left(\frac{\partial^2 v_r}{\partial r^2} + \frac{1}{r}\frac{\partial v_r}{\partial r} - \frac{v_r}{r^2} + \frac{\partial^2 v_r}{\partial z^2}\right) - \left(\frac{\partial}{\partial r}\overline{\acute{v}_r^2} + \frac{\partial}{\partial z}\overline{\acute{v}_r \acute{v}_z} + \frac{\overline{\acute{v}_r^2}}{r} - \frac{\overline{\acute{v}_\emptyset^2}}{r}\right) \quad (2\text{-}4)$$

$$v_r \frac{\partial v_\emptyset}{\partial r} + v_z \frac{\partial v_\emptyset}{\partial z} + \frac{v_r v_\emptyset}{r} = v\left(\frac{\partial^2 v_\emptyset}{\partial r^2} + \frac{1}{r}\frac{\partial v_\emptyset}{\partial r} - \frac{v_\emptyset}{r^2} + \frac{\partial^2 v_\emptyset}{\partial z^2}\right) - \left(\frac{\partial}{\partial r}\overline{\acute{v}_r \acute{v}_\emptyset} + \frac{\partial}{\partial z}\overline{\acute{v}_\emptyset \acute{v}_z} + 2\frac{\overline{\acute{v}_r \acute{v}_\emptyset}}{r}\right) \quad (2\text{-}5)$$

$$v_r \frac{\partial v_z}{\partial r} + v_z \frac{\partial v_z}{\partial z} = -\frac{1}{\rho}\frac{\partial p}{\partial z} + v\left(\frac{\partial^2 v_z}{\partial r^2} + \frac{1}{r}\frac{\partial v_z}{\partial r} + \frac{\partial^2 v_z}{\partial z^2}\right) - \left(\frac{\partial}{\partial r}\overline{\acute{v}_r \acute{v}_z} + \frac{\partial}{\partial z}\overline{\acute{v}_z^2} + \frac{\acute{v}_r \acute{v}_z}{r}\right) \quad (2\text{-}6)$$

$$\frac{\partial}{\partial r} r v_r + \frac{\partial}{\partial z} r v_z = 0 \quad (2\text{-}7)$$

Where v_r, $v_\emptyset$, v_z are referring to mean velocities in r, $\emptyset$ and z directions while $\acute{v}_r$, $\acute{v}_\emptyset$ and $\acute{v}_z$ are the velocity fluctuations. As in a planar circular jet there is no swirl, which means that $v_\emptyset$ is equal to 0 and all the terms containing $v_\emptyset$ and its derivatives disappear from the above equations. On the other hand, radial gradient directions are much higher than those in the axial direction $v_z \gg v_r$. It has been assumed that when the nozzle Reynolds number is greater than a few thousand, the corresponding turbulent shear stresses will be much larger than viscous stresses which can be neglected. Moreover, the turbulent normal stresses can be assumed to be equal in both radial and peripheral directions. Therefore, the equations of motion turn into (Loitsyanskii, 1966; Rajaratnam, 1976; Schlichting, 1968):

$$\frac{1}{\rho}\frac{\partial p}{\partial r} = -\frac{\partial}{\partial r}\overline{\acute{v}_r^2} \quad (2\text{-}8)$$

$$v_r \frac{\partial v_z}{\partial r} + v_z \frac{\partial v_z}{\partial z} = -\frac{1}{\rho}\frac{\partial p}{\partial z} - \left(\frac{\partial}{\partial r}\overline{\acute{v}_r \acute{v}_z} + \frac{\overline{\acute{v}_r \acute{v}_z}}{r} + \frac{\partial}{\partial z}\overline{\acute{v}_z^2}\right) \quad (2\text{-}9)$$

$$\frac{\partial}{\partial r}\, r v_r + \frac{\partial}{\partial z}\, r v_z = 0 \tag{2-10}$$

By Integrating Equation 2-8 and substituting in 2-9 simplifying like that of the plane jet, Equation 2-9 converts to:

$$v_r \frac{\partial v_z}{\partial r} + v_z \frac{\partial v_z}{\partial z} = -\frac{1}{\rho}\frac{\partial p}{\partial z} - \frac{1}{r}\frac{\partial}{\partial r}\,(\overline{r \acute{v}_r \acute{v}_z}) \tag{2-11}$$

Where: p is the outside pressure of the jet. Assuming that u, v refer to velocity in axial and radial directions respectively, x is the axial distance downstream the jet and $\tau = -\rho\overline{\acute{v}_r \acute{v}_z}$. With these substitutions, the equations of motion become:

$$u\,\frac{\partial u}{\partial x} + v\frac{\partial u}{\partial r} = -\frac{1}{\rho}\frac{\partial p}{\partial x} + \frac{1}{\rho r}\frac{\partial r\tau}{\partial r} \tag{2-12}$$

$$\frac{\partial}{\partial x}\, ru + \frac{\partial}{\partial r}\, rv = 0 \tag{2-13}$$

Furthermore, in most of the practical cases, it has been assumed that $\partial p/\partial x$ is approximately zero, therefore Equation 2-12 become:

$$u\frac{\partial u}{\partial x} + v\frac{\partial u}{\partial r} = \frac{1}{\rho}\frac{1}{r}\frac{\partial r\tau}{\partial r} \tag{2-14}$$

Finally, Equations 2-13 and 2-14 are representing the simplified equations of motion for a planar circular jet (Loitsyanskii, 1966; Rajaratnam, 1976; Schlichting, 1968).

III. Equation of momentum

The momentum flux of a circular jet flow in the axial direction is conserved due to a zero-pressure gradient as the jet diffusing into a static atmosphere of the same fluid type. Therefore, the development of this equation based on this criterion starts with multiply Equation 2-14 by ρr and integrate with respect to r from $r = 0$ to $r = \infty$. So (Rajaratnam, 1976):

$$\int_0^\infty \rho u r\, \frac{\partial u}{\partial x}\, \mathrm{d}r + \int_0^\infty \rho v r\, \frac{\partial u}{\partial r}\, \mathrm{d}r = \int_0^\infty \frac{\partial r\tau}{\partial r}\, \mathrm{d}r \tag{2-15}$$

$$\int_0^\infty \rho u r\, \frac{\partial u}{\partial x}\, \mathrm{d}r = \frac{1}{4\pi}\frac{d}{dx}\int_0^\infty 2\pi\rho u^2\, r\mathrm{d}r \tag{2-16}$$

$$\begin{aligned}\int_0^\infty \rho v r\, \frac{\partial u}{\partial r}\, \mathrm{d}r &= |\rho u v r|_0^\infty - \int_0^\infty \rho u\, \frac{\partial r v}{\partial r}\, \mathrm{d}r = \int_0^\infty \rho u\, \frac{\partial r u}{\partial r}\, \mathrm{d}r \\ &= \frac{1}{4\pi}\frac{\mathrm{d}}{\mathrm{d}x}\int_0^\infty 2\pi\rho u^2\, r\mathrm{d}r\end{aligned} \tag{2-17}$$

$$\int_0^\infty \frac{\partial r\tau}{\partial r}\, \mathrm{d}r = |r\tau|_0^\infty = 0 \tag{2-18}$$

Consequently, Equation 2-15 will be:

$$\frac{d}{dx}\int_0^\infty 2\pi r dr \rho u^2 = 0 \tag{2-19}$$

Importantly, Equation 2-19 declares the previous assumption that where the momentum flux in the axial direction is conserved, the rate of change of the axial momentum flux in the axial direction is equal to zero.

Moreover, Equation 2-19 can be used to develop velocity and length scales equations as

$$u/u_m = f(r/b) = f(\eta) \tag{2-20}$$

$$u_m \propto x^p \tag{2-21}$$

$$b \propto x^q \tag{2-22}$$

follow:

$$\frac{d}{dx}\,\rho u_m^2 b^2 \int_0^\infty 2\pi\eta r f^2 d\eta = 0 \tag{2-23}$$

With these substitutions, Equation 2-19 turns to:

$$u_m^2 b^2 \propto x^o \tag{2-24}$$

$$2p + 2q = 0 \tag{2-25}$$

$$p + q = 0 \tag{2-26}$$

Because the value of the definite integral in Equation 2-23 is a constant, therefore:

2.1.2 Swirl jet flow

Swirling flows as shown in Figures 2-9 and 2-10 are very common in natural phenomena such as tornadoes, hurricane, and whirlpools as well as in industrial applications such as the combustion chambers, heat exchangers, internal combustion engines, separators etc. (A. K. Gupta et al., 1984; Gursul, 2004; L. N. Jones, 2004). There is much published research that has been done on this kind of flow where a high level of turbulence occurs. The uses of a swirling jet flow will create a low-pressure region in the swirling core centre because of the axial, radial and tangential velocity components that generate the pressure gradients to create re-circulation zone as shown in Figure 2-10. Besides, a reversal flow and vortex breakdown take place when the rotating momentum of fluid is able to resist the pressure gradient created by the swirling components at a certain degree of swirl flows. Interestingly, the reversal flow area, which can also call the recirculation zone, is the source of the flame stabilization because of mixing among the reactants, subsequent ignition and the burnt products, the vortex core zone created by the

solid body rotation in the central region. Moreover, swirl flows can be generated by three methods such as tangential entry e.g. axial-plus-tangential, navigable vanes and by rotating pipe (A. K. Gupta et al., 1984).

In addition, the uses of swirling flow will control the combustion procedure as it can stabilize and anchor the flam inside the combustion system of liquid fuel diffusion flams. As shown in Figure 2-11, the fuel injects inside the swirling airflow known as combustion chamber in a form of spreading droplets. Then, the creation of a recirculation zone will deliver a hot reaction result to the flame and increase the mixing between air and fuel. As mentioned before, swirling flow is the source of the flame stabilization by fitting the flame front velocity to the velocity of the recirculated results. Therefore, adjusting the speed of swirling flow is very important and balancing between the flame speed and fuel/air stream speed is mandatory to avoid extinction of the flame or causing jet blowing-off (A. K. Gupta et al., 1984; L. N. Jones, 2004).

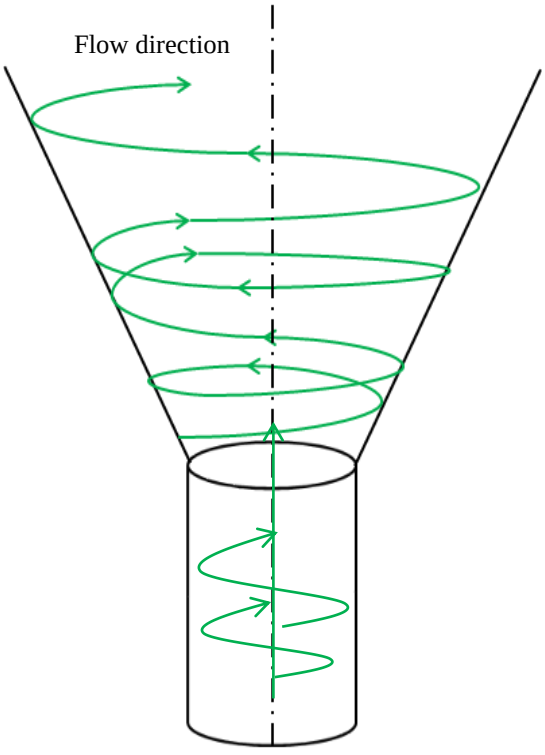

Figure 2-9: Weak Swirl Degree. Re-Produced From (A. K. Gupta Et Al., 1984).

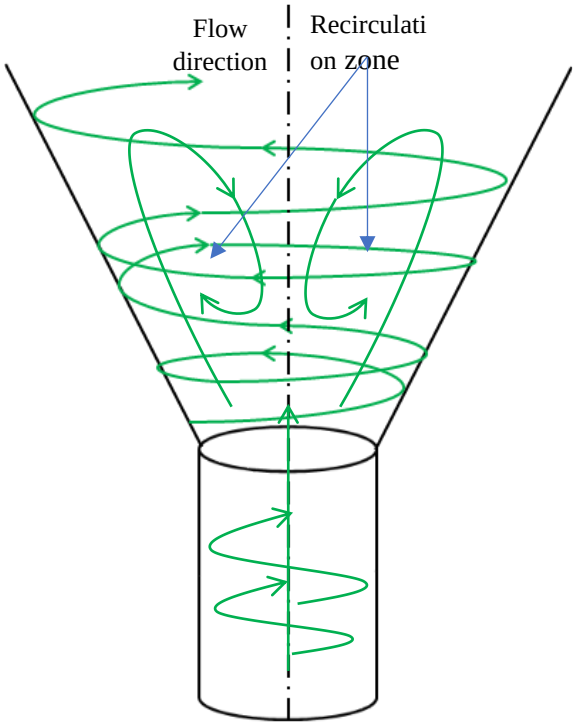

Figure 2-10: Strong Swirl Degree. Re-Produced From (A. K. Gupta Et Al., 1984).

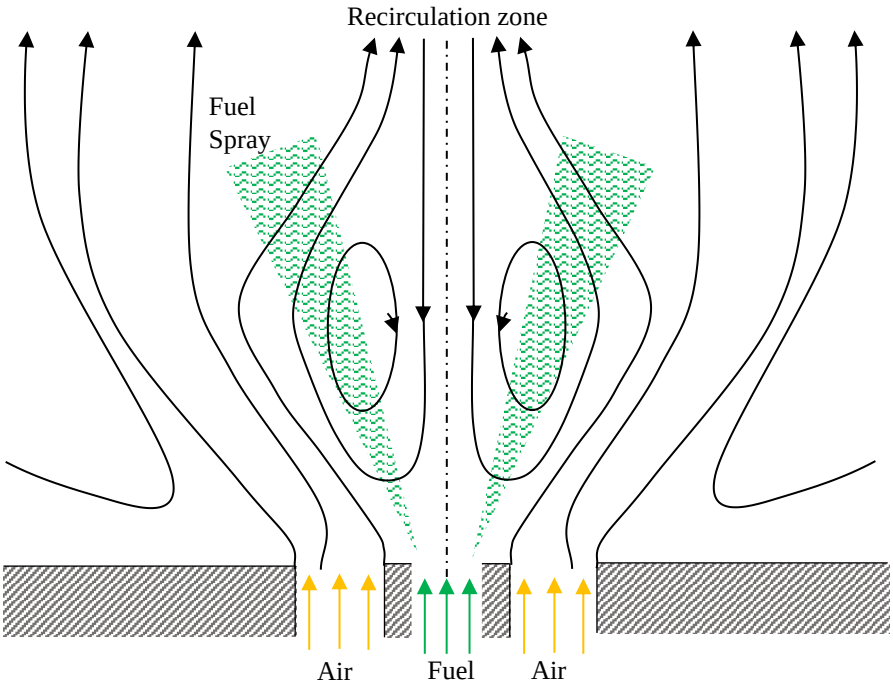

Figure 2-11: Fuel Injects Inside The Swirling Airflow. Re-Produced From (L. N. Jones, 2004).

Defined as the ratio of the axial flux of angular momentum to the axial flux of axial momentum multiplied with the equivalent exit radius, the swirl number S known as the main parameter to define the swirl flows strength. As shown in the equation below (A. K. Gupta et al., 1984):

$$S = \frac{2G_\theta}{G_Z D} \tag{2-27}$$

Where, G_θ is the axial flux of angular momentum, G_Z is the axial flux of axial momentum and D represent the existing diameter of the burner. In addition, a researcher indicates that the swirl number is depending on the velocity profile which is not always constant but depending on downstream axial locations. Therefore, The axial fluxes can be defined as (Milosavljevic, 1993):

$$G_\theta = 2\pi\rho \int_{r=r_i}^{R} UW_r r dr \tag{2-28}$$

$$G_Z = 2\pi \int_{r=r_i}^{R} (\rho U^2 + p) r dr \Rightarrow G_Z = 2\pi\rho \int_{r=r_i}^{R} UUr dr \tag{2-29}$$

Where: ρ density, Uaxial velocity, W_r angular velocity and r is the radial. Furthermore, the swirl number can be defined by the geometry shape of the device, which knows in this case as the theoretical or geometric swirl S_g, written as follows:

$$S_g = \frac{2}{3}\frac{[-(D_i - D_\circ)^3]}{[-(D_i - D_\circ)^2]}\tan\gamma \tag{2-30}$$

Where: D_i, $D_\circ$ are the inner and outer jet diameter respectively and refer to γ azimuth angle. Generally, there are two groups of swirling flows depending on the swirl number as follow (A. K. Gupta et al., 1984; Stetsyuk, 2014):

A. Weak swirl flow $S < 0.6$, Figure 2-9

B. Strong swirl flow $S > 0.6$, Figure 2-10

Furthermore, many experimental studies indicate that for $S < 0.5$, the flow called 'solid body' rotation will demonstrate as a result of flow patterns. For $S > 0.5$, the flow will quickly rotate at the core zone to grow a structure enclosed by an annulus of short vorticity (Steenbergen, 1995).

I. Equation of motion and momentum

While the previous equations were based on the Navier-Stokes approach, the following equations are representing the basic formula of swirl flow motion and momentum equations. Starting from general equations of circular jet flow with the existence of swirl power, as follows:

For the axial direction:

$$u\,\frac{\partial u}{\partial x} + v\frac{\partial u}{\partial r} = -\frac{1}{\rho}\frac{\partial p}{\partial x} - \frac{\partial \overline{\acute{u}\acute{v}}}{\partial r} - \frac{\overline{\acute{u}\acute{v}}}{r} - \frac{\partial \overline{\acute{u}^2}}{\partial x} \tag{2-31}$$

For the radial direction:

$$-\frac{w^2}{r} = -\frac{1}{\rho}\frac{\partial p}{\partial r} - \frac{\partial \overline{\acute{v}^2}}{\partial r} - \frac{\overline{\acute{v}^2}}{r} - \frac{\overline{\acute{w}^2}}{r} \tag{2-32}$$

For the peripheral direction:

$$u\,\frac{\partial w}{\partial x} + v\frac{\partial w}{\partial r} + \frac{vw}{r} = -\frac{\partial \overline{\acute{v}\acute{w}}}{\partial r} - \frac{2\,\overline{\acute{v}\acute{w}}}{r} - r\frac{\partial}{\partial r}\frac{\overline{\acute{v}\acute{w}}}{r} - \frac{\overline{\acute{v}\acute{w}}}{r} \tag{2-33}$$

And the continuity equations:

$$\frac{\partial ru}{\partial x} + \frac{\partial rv}{\partial r} = 0 \tag{2-34}$$

Where: u, v and w are the turbulent mean velocity in the axial, radial and peripheral directions. While $\acute{u}$, $\acute{v}$ and $\acute{w}$ represent the identical velocity fluctuations in the same directions. As been mentioned before, the turbulent normal stresses, their derivatives and boundary-layer Where: u, v and w are the turbulent mean velocity in the axial, radial and peripheral directions. While $\acute{u}$, $\acute{v}$ and $\acute{w}$ represent the identical velocity fluctuations in the same directions. As been mentioned before, the turbulent normal stresses, their derivatives and boundary-layer approximations will be neglected. Then the equations of motion shortened to this formation:

$$u\,\frac{\partial u}{\partial x}+v\frac{\partial u}{\partial r}=-\frac{1}{\rho}\,\frac{\partial p}{\partial x}+\frac{1}{\rho r}\,\frac{\partial r\tau_x}{\partial r} \tag{2-35}$$

$$\frac{w^2}{r}=-\frac{1}{\rho}\,\frac{\partial p}{\partial r} \tag{2-36}$$

$$u\,\frac{\partial w}{\partial x}+v\frac{\partial w}{\partial r}+\frac{vw}{r}=-\frac{1}{\rho}\frac{\partial}{\partial r}\tau_{\emptyset}+\frac{2}{\rho}\,\frac{\tau_{\emptyset}}{r} \tag{2-37}$$

$$\frac{\partial ru}{\partial x}+\frac{\partial rv}{\partial r}=\ 0 \tag{2-38}$$

By integrating Equation 2-35 with respect to r after multiplying it by ρr. Will get:

$$\int_0^{\infty}\rho ur\,\frac{\partial u}{\partial x}\,r\mathrm{d}r\ +\ \int_0^{\infty}\rho vr\,\frac{\partial u}{\partial r}\,\mathrm{d}r=-\int_0^{\infty}\frac{\partial p}{\partial x}\,r\mathrm{d}r+\ \int_0^{\infty}\frac{\partial r\tau_x}{\partial r}\,\mathrm{d}r \tag{2-39}$$

$$\int_0^{\infty}\rho u\,\frac{\partial u}{\partial x}\,r\mathrm{d}r\ =\frac{1}{2}\,\frac{\mathrm{d}}{\mathrm{d}x}\int_0^{\infty}\rho u^2\,r\mathrm{d}r \tag{2-40}$$

$$\int_0^{\infty}\rho vr\,\frac{\partial u}{\partial r}\,\mathrm{d}r=\ |\rho uvr|_0^{\infty}-\int_0^{\infty}\rho u\,\frac{\partial rv}{\partial r}\,\mathrm{d}r=\frac{1}{2}\,\frac{\mathrm{d}}{\mathrm{d}x}\int_0^{\infty}\rho u^2\,r\mathrm{d}r \tag{2-41}$$

$$\int_0^{\infty}\frac{\partial p}{\partial x}\,r\mathrm{d}r=\frac{\mathrm{d}}{\mathrm{d}x}\int_0^{\infty}\rho r\mathrm{d}r \tag{2-42}$$

$$\int_0^{\infty}\frac{\partial r\tau_x}{\partial r}\,\mathrm{d}r=|r\tau_x|_0^{\infty}=0 \tag{2-43}$$

Therefore, Equation 2-39 will turn to:

$$\frac{\mathrm{d}}{\mathrm{d}x}\int_0^{\infty}(p+\rho u^2)\,r\mathrm{d}r=0 \tag{2-44}$$

Equation 2-44 indicate that the adding of axial momentum and pressure is conserved in the x-direction. However, for more confident way, this equation can be established as follow:

$$\begin{aligned}\int_0^\infty \frac{\partial p}{\partial x}\, r dr &= \left|\frac{r^2}{2}\frac{\partial p}{\partial x}\right|_0^\infty - \int_0^\infty \frac{r^2}{2}\frac{\partial}{\partial r}\left(\frac{\partial p}{\partial x}\right) dr \\ &= -\int_0^\infty \frac{r^2}{2}\frac{\partial}{\partial x}\left(\frac{\partial p}{\partial r}\right) dr \\ &= -\int_0^\infty \frac{r^2}{2}\frac{\partial}{\partial x}\left(\frac{\rho w^2}{r}\right) dr \\ &= -\frac{1}{2}\frac{\mathrm{d}}{\mathrm{d}x}\int_0^\infty \rho w^2\, r\mathrm{d}r\end{aligned} \tag{2-45}$$

Hence, the integral equation turns to:

$$\frac{\mathrm{d}}{\mathrm{d}x}\int_0^\infty \rho\left(u^2 - \frac{w^2}{2}\right) r\mathrm{d}r = 0 \tag{2-46}$$

Moreover, by using as same as the above procedure, the equation of motion in the peripheral direction can be computed by multiplying Equation 2-37 by $\rho r^2$and integrating with respect to r, the final equation will be:

$$\frac{\mathrm{d}}{\mathrm{d}x}\int_0^\infty r^2 \rho u w dr = 0 \tag{2-47}$$

Finally, Equation 2-47 indicate that the moment of the peripheral momentum flux or the angular momentum is conserved in the x-direction (Rajaratnam, 1976).

2.2 Planar Jet Studies

2.2.1 Brief numerical and experimental studies

As has been previously discussed, the main research of this thesis is about swirling flow modelling. However, to cover this subject a planar case study has been examined for validation and comparison purpose. Therefore, this section includes a brief review of numerical and experimental studies that have been performed by scientists on a round planar jet flow.

One of the earliest experiments was conducted by (R A Antonia & Bilger, 1973), whereby analysing the flow progress of an axisymmetric jet draining into a running air stream which has various values of the ratio of external air velocity to jet velocity. Surprisingly, the results such as the dissipation length scales, u-component turbulence intensity and Reynolds shear stress values denote that the turbulence similarity presumptions are incorrect for the current flow situation. Moreover, the experiment found that the mean velocity profiles are not affected by the flow development along with the downstream flow, and the turbulence structure of the flow is not self-similar. Another experiment has been done via using three circular and turbulent plane jets to compute the mean dissipation rate along with the downstream axes distance and in a range of Re. The results of this experiment confirm that there is a mutual relationship for both jets between the dissipation rate and axial distance such as the local Re is related to turbulence Re by a derived equation for either type of jet (Robert A Antonia et al., 1980). Furthermore, (Chambers et al., 1985) have investigated the root mean square r.m.s and mean values for both temperature and velocity at the beginning of the interaction area of a plane jet flow with two different sets of conditions. The results have been published by using schlieren photography and a spectral coherence method for both cases, and its shows a significate explanation and analysing for the fluid features at the above-mentioned area. However, the same previous study has been published once again by (Chua & Antonia, 1986) which explain more details about the interaction region for laminar flow only such as the development of the probability density function of the temperature fluctuation.

Alternatively, numerical research has been carried out via employing k-ε turbulent model to examine the steady free turbulent jet flow and combustion. The study includes using a multi-grid solver along with a SIMPLE approach and a pressure boundary condition for the isothermal jet flow, combusting jet flows and partially premixed flame simulation process. In the end, the simulation results of diffusion jet flame and isothermal jet flow shows good agreement with several pieces of experimental data. However, the partial premixed jet flames

outcome reveals a particular error percentage with Eddy-Dissipation-Concept (EDC) modulation (X. Zhou et al., 1999). Besides, a direct numerical simulation has been used to study the mechanisms of two distinct types of bifurcating jets by applying bi-modal perturbation at the nozzle. The results indicate a good agreement with experimental data of various features such as bifurcating excitation which is able to lead large-spreading jets (Danaila & Boersma, 2000). Conversely, (Robert A Antonia & Zhao, 2001) experimentally investigate the effect of initial conditions on two types of circular jets where the first jet create by a shrinkage with a laminar top-hat velocity profile while the second one leaves from a pipe with a fully developed turbulent mean velocity profile. The results imply that the large-scale anisotropy remains the same between the two flows in the far-field position (usually $x \gtrsim 30$ of the jet diameter).

Interestingly, one of the earliest pieces of numerical research uses a three-dimensional DNS model to investigate the flow of the planar jet (Stanley et al., 2002). The investigation of this study includes comparing experimental data with various subjects such as jet growth rates, mean profiles of the scalar mixing, Reynolds stress and velocity along with a discussion of the large-scale and small-scale anisotropies in the jet and some other fluids features. Following from these findings, another numerical study uses the DNS method to examine a passive scalar transport in a spatially evolving turbulent jet at Schmidt number equal to 1 and Reynolds number of 2400. Moreover, many jet flow characteristics have been examined with various experiments such as mean scalar concentration, mean velocity, fluctuations of velocity, fluctuations of scalar and finally the instantaneous radial profiles of velocity and passive scalar. It has been found that the velocity and scalar profiles are fairly similar, having a Gaussian mean profile. Also, the instantaneous diffusive and convective terms in the passive scalar transport equation are studied, and diffusion-dominated regions are recognized (Babu & Mahesh, 2005). Later, some researchers numerically explore the characteristics of single-phase turbulent confined jets via utilizing the CFD program and compare them with some experiment's parameters from the literature. The above study is based on analysing the effect of the existence of the draft tube and the effect of enclosure size in order to examine the jet expansion and hydrodynamics in confinement status. The results indicate that the size of the draft tube has a significant responsibility in determining the degree of entrainment and the amount of mixing between the surrounding fluid and the jet fluid (Kandakure et al., 2008). Interestingly, large-eddy simulations (LES) method with proper near-wall modelling has been employed by (S. Zhang et al., 2015) to study the flow and mixing features such as the scalar distributions and

velocity, rates of velocity and scalar decay, turbulence intensities in various directions and variations of characteristic length scales in a turbulent circular wall jet. These features have been compared with other results from existing experimental data as well as from standard k-ε and standard k–ω turbulence models. The outcome indicates that LES are able to predicate the mixing characteristics and the kinematic of the turbulent wall jet and it's more accurate than the RANS models with enhanced wall functions. Furthermore, (Qu et al., 2015, 2016) examines via experimental methods and a 3D numerical method the air–steam jet flow, in order to study the mixture condensation specifications in stationary cool water with a steam mass fraction above 0.5. The numerical model is based on the volume of fluid (VOF) and Euler–Euler two-fluid method along with species model to simulate the bubble condensation, and the results which have been compared with the experimental data indicate the ability to use the CFD model to predict the steam–air-jet condensation process. On the other hand, (Mossad & Ravinesh, 2015) use the Standard k-ε, Realizable, k-ω and SST turbulent models implemented in the ANSYS-Fluent CFD software to investigate the ability of these models to predict the mean velocity distribution of a plane air jet issuing into the quiescent environment. The numerical modelling involves a range of Reynolds number based on the bulk mean velocity (1500-10000) and a range of meshes size (8000-5,000,000) grid points. Curiously, the simulation results which have been contrasted with a published experimental data suggest that the standard k-ε turbulence model has a good agreement with the published data. However, the accuracy of SST turbulent model is better than k-ε turbulence when it uses at Re equal to 1500. Later, some researchers use a 3D LES method to numerically investigate spatially developing planar turbulent jet at Re of 4000. In Addition, various flow features have been indicated such as the transition from laminar to turbulent, evolution of vortex, coherent structures in a turbulent planar, self-similar performance of mean velocity and energy spectra (Bisoi et al., 2017).

Recently, many investigations have been done on planar jet flow via applying Reynolds Averaged Navier Stokes (RANS) turbulence models which implemented in the ANSYS-CFD programme to study various fluid features. For instance, (Gopalakrishnan & Disimile, 2018) examine the velocity and jet growth characteristics via applying SST k-ω turbulence model, while (Li et al., 2019) use the standard k-ε turbulence model with volume-of-fluid (VOF) method to study the velocity decay of offset jet in a narrow and deep pool with a circular and rectangular jet exit zone. Lastly, (Yan et al., 2020) utilises the standard k-ε, renormalization group (RNG) k-ε, standard k-ω, and k-ω shear stress transport (SST) turbulence models to study in 3D form the mixing and dilution qualities of vertical buoyant jets released from

multiport diffusers, the results, having been compared to sets of experimental data, show that the RNG k-ε turbulence model has the most accurate values among all the other models.

2.2.2 Related experiment review

The following experimental research was based on the work done by some scientists to study and investigate some fluid features in a planar jet flow. Therefore, it has been taken as a case study in this research for validation study purposes.

The main work was to examine and investigate the fluid mixing procedure as well as Reynolds number-independent/dependent similarities and the turbulent concentration fields of a gas fluid flow. The experiments were established on using a round free turbulent jet i.e., momentum-driven, co-flow system flow and then mixed with the existence of static quiescent reservoir fluid. Also, a non-intrusive laser-Rayleigh scattering method was implemented to solve the full range of temporal and spatial concentration levels. Moreover, the determination of the measurements of axial concentrations fields has been taken at $20D_E$, $40D_E$, $60D_E$ and $80D_E$, where D_E is the Ethylene inlet diameter at a Reynolds number of 5000.

Figure 2-12 illustrates the main dimensions and the gas phase jet mixing equipment. The total internal volume of the enclosure system is nearly $3.4m^3$, the gas phase is vertically produced from a 0.02m jet nozzle which has an 11 to 1 reduction ratio, and the exit turbulence level is below 0.2%. Generally, to provide the entrainment needs of the jet, the system produces a volume flux of uniform co-flow gas with a velocity equal to approximately 0.006 of the main jet velocities. For the experiment's purpose, Ethylene C_2H_4 has been used as the main gas flow with a jet velocity up to 4.04m/s and the flow rate is set as a single-stage mechanism and a metering valve. Nevertheless, by adjusting the pressure of a specific distribution manifold, Nitrogen N_2 has been produced as the uniform co-flow reservoir fluid flow with a jet velocity equivalent to 0.024m/s and the density ratio between the Ethylene and Nitrogen is 1.0015.

The outcome of the experiments showed that computed mean and root mean square r.m.s values of the fluid features such as concentration and mean scalar dissipation rate is found to obey the law of jet similarity. Likewise, the concentration fluctuation power spectra and probability density function for the concentration have been discovered to have self-similar profiles along the path originating from the virtual origin of the jet towards the end of the reservoir. On the other side, the scaled probability density function of jet fluid concentration is indicated to be approximately independent of the Reynolds number at the centreline of the jet

flow (D. Dowling & Dimotakis, 1988; D. R. Dowling, 1988; D. R. Dowling & Dimotakis, 1990).

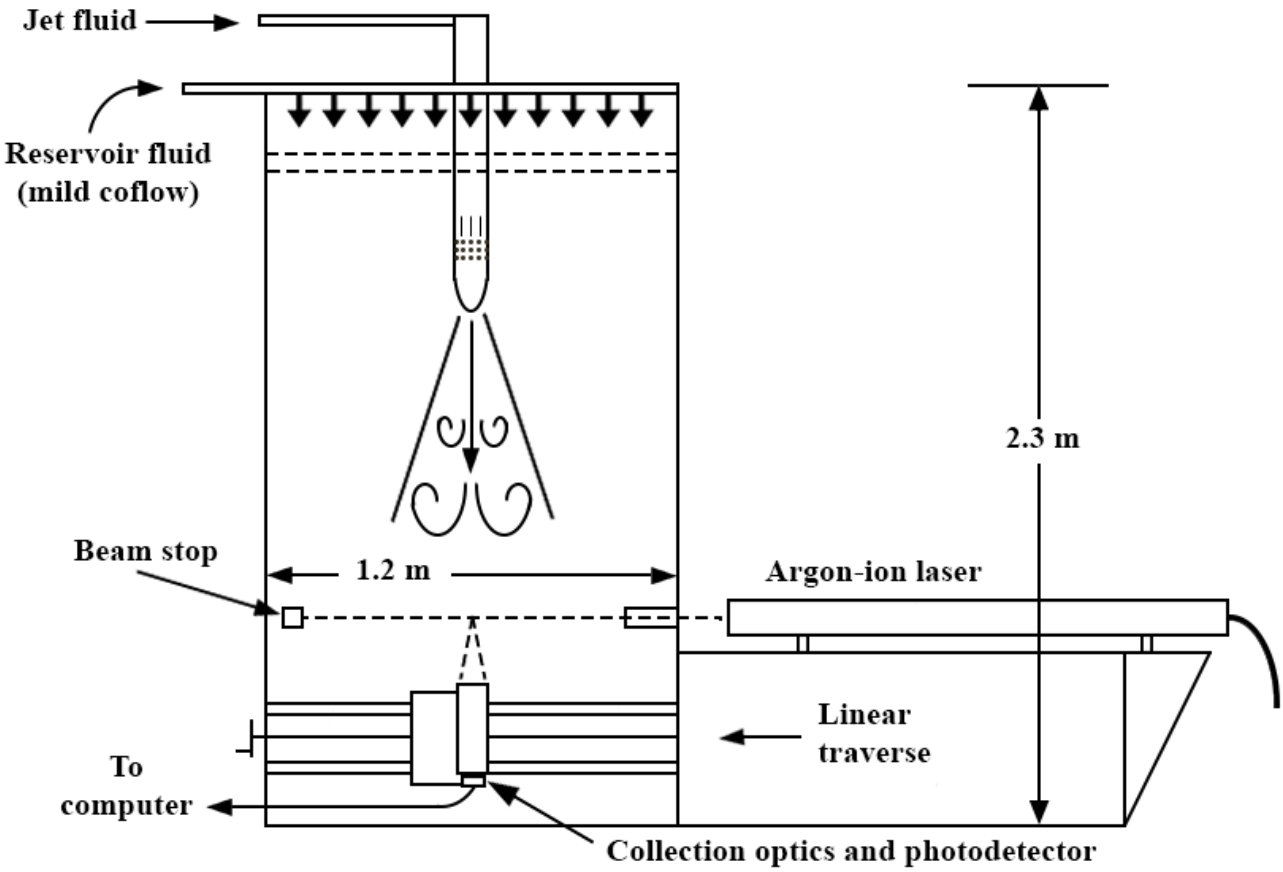

Figure 2-12: Experimental Facility System. Re-Produced From (D. R. Dowling, 1988).

Moreover, many studies based on the previous experiment have been implemented via validating the outcomes among them. For instance, (Gazzah et al., 2004) used the first and second order turbulent closure models to investigate the effect of co-flow on a turbulent binary gas mixing round jet, and the main purpose is to achieve a better knowledge of the flow structure and mixing process in turbulent variable-density jets. The outcome of the previous study indicate that co-flow increased the efficiency of the mixing while it reduced the jet spreading rate. On the other hand, based on the (D. R. Dowling, 1988) experiment's outcomes, an investigation of small-scale unintended releases of hydrogen were performed to predict the performance of small-scale hydrogen releases via using experimental and modelling program (Schefer et al., 2008).

In addition, (Ball et al., 2012) published an essential study review on the flow field in turbulent round free jets which led to indicate that the related experiment work has and

significate outcomes in turbulent jet studies. Thus, the experiment done by (D. R. Dowling, 1988) determined the effect of Reynolds number was depending on the root mean square radial distribution of the concentration fluctuations as well as the decay rate of the mean concentration field.

Following many studies, (Ishay et al., 2017) carried out the affection of nozzle geometry on stratified layer corrosion by vertical turbulent jet in the nuclear power plants. The research aim was to improve the efficiency of turbulent jet behaviour of containment flows to correctly predict various effects. The modelling outcomes showed that the jet behaviour was strongly depends on the nozzle geometry.

In addition, one of the most recent studies has been carried out by (Sahebjam et al., 2022) to examine the dynamics of an axisymmetric turbulent jet in existence of homogeneous isotropic turbulence along with passive scalar field at different Reynolds number. The study was based on utilizing the classical Eulerian averages method as well as two-region model for the jet structure in the environmental turbulence. Last but not least, an Lagrangian experimental investigation was applied to investigate many flow properties such diffusion, entrainment and effective compressibility in a self-similar turbulent jet. Generally, the outcomes of this study found an improved comprehension of turbulent entrainment and diffusion in turbulent jets (Basset et al., 2022).

2.2.3 Related numerical review

Following the previous experiment work and along with other experiments related to the same subject. (Lubbers et al., 2001) numerically investigated the mixing of a passive scalar in a spatially developing free round turbulent jet flow by using the Direct Numerical Simulation (DNS). Moreover, the Reynolds number was depending on the orifice diameter and has a velocity equivalent to $2x10^3$, while the Schmidt number used in the simulations was equal to 1.0. The main purpose of this research was to study the far-field self-similar area of the concentration of the passive scalar in jet flow. Therefore, the distribution of concentration probability density functions together with concentration fluctuations and therefore, mean concentration profiles have been analysed. The results have been compared with the literature of much previously published experimental data. Generally, the DNS outcome showed a good agreement with the experimental data by indicating that the mean concentration profiles in the far-field area have self-similar profiles. However, the root mean square of the concentration fluctuations profiles were not self-similar which disagree with findings by (D. R. Dowling &

Dimotakis, 1990). Finally, the turbulent Schmidt number was equal to 0.74, which fairly agrees with experiments ones.

2.3 Swirl jet studies

2.3.1 Experiment studies

This section is focusing on some experimental work that is related to the main subjects of this thesis. The following section will cover the numerical studies on swirling flow, though this will include some experiment work as well.

Interestingly, many researchers have investigated swirling jet flow via experiments. One of the important experiment done by (Samet & Einav, 1988) carried out via using of tangential injection method to generate a swirl flow with a range of 0-0.49 swirling strength. The purpose of the previous experiment is to indicate the mean velocity and mass flow rate with a range of 2-20 x/d by using an impact probe device.

Alternatively, another experiment uses a passive vanes technique to create a swirl flow with a range of 0-0.42 swirling number, a domain of 1-15 x/d, and a Reynolds number is $80x10^3$. The study uses many types of procedures, such as cold-wire, hot-wire and single hot-wire, in order to investigate and compute the axial, radial and tangential mean velocity along with statistics fluxes (Elsner & Kurzak, 1989).

Moreover, many researchers describe the pressure and all directions mean velocity at swirling number equal to 0.48 and Reynolds number value $375x10^3$ in a tangential nozzles swirl flow generation, and the results have been published in a range of 0-6 x/d by using impact probe device and a Single hot-wire method (Farokhi et al., 1989).

On the other hand, (Mehta et al., 1991) uses a rotating honeycomb method to generate a swirling flow with a strength of 0-0.2 to indicate the blow-out limits alongside the mean velocity and flow rate in a range of 0-2.31 x/d by implementing of hot wire technique.

However, (Milosavljevic, 1993) applies a tangential injection swirl burner which works by using coal, gas and kerosene fuel. The target of the study is to evaluate major species concentration as well as the mean velocity and blow-out limits for a range of swirl numbers such as 0.3, 0.5 and 1.07 and Reynolds number value $29x10^3$ via utilizing a laser doppler velocimetry and Pitot probe at a domain up to 1.9 x/d.

Meanwhile, another swirl burner has been used to investigate and analyse the outcome of the experiment in a form of pictures by using schlieren visualization system for a range of Re 13 $x10^3$ to $20.5x10^3$, swirl number 0-1.87 and 0-5 x/d (Park & Shin, 1993).

Yet another experiment has been conducted by using a tangential injection method to create swirl flow for a selection of swirl number 0-0.52 at Re equal to $18x10^3$ and a domain of 0.14-32 x/d. This experiment applies a 3D- Laser doppler velocimetry method to analyse the results such as mean velocity and statistics of the flow (Feyedelem & Sarpkaya, 1998).

Simultaneously, (Oljaca et al., 1998) use ultrasound scattering and hot-wire techniques to study the mean velocity and flow rate of swirl flow which is generated via a rotating paddle at a Re equal to $10x10^3$, a swirl number domain 0-0.24 and a range of 0.25-3 x/d.

Subsequently, (Gilchrist & Naughton, 2005) conducted an experiment in order to analyse the mean velocity in tangential injection swirl generator at Re $100x10^3$ and range of 0-0.23 swirl number for incompressible fluid flow, the results have been taken at the domain of 0-20 x/d and by using an impact probe method.

Concurrently, (Toh et al., 2005) use the same previous method to generate the swirl flow at Re equivalent to $3.9x10^3$ and range of 0.06-0.15 swirl number. However, this experiment employs particle image velocimetry along with planar laser-induced fluorescence approaches to indicate the flow features in a form of pictures for a domain of 0-5.8 x/d.

Later, (Örlü, 2006) conducted an experiment to study the mixing of a passive scalar in swirl jet flow where the swirl creates by using a rotating pipe. The swirl number range of the above experiment is about 0-0.5, Re is equal to $24x10^3$ and the results have been indicated via using hot-wire and cold-wire techniques with a domain of 0-6 x/d.

Furthermore, (Facciolo, 2006) uses an axially rotating pipe method to generate a swirl flow in the experiment with a swirl number range of 0-0.5, Re is approximately 12-$33.5x10^3$. The results have been carried out by using some essential techniques such as hot-wire, 2D-Laser doppler velocimetry and 2D-Particle image velocimetry to signify the mean velocities alongside mixing features in a domain of 0-8 x/d.

The next section will explain the related experiments which have been used to compare the author numerical study with its results.

2.3.2 Related experiment review

Studying and examining the applicability of prediction of the swirling flow by employing the turbulence models implemented in the ANSYS CFD programme to imperatives the use of a detailed experiment to fulfil the purpose of this work. Therefore, one of the essential parts of this work is based on the results of the experiment done by (Stetsyuk, 2014) which can be briefly detailed as follows:

I. Atmospheric Burner and the Flow configuration

The main part of the experiment is the atmospheric burner which can be involved in a reacting flow study by operating it with a mixture of $CH_4/H_2/N_2$ or in a non-reacting flow study by operating it with a single type of gas, such as air, seeded with methane or acetone vapour. Moreover, to create the swirl flow, this burner contains a built-in swirl generator by using six side slots to obtain swirling flow with different levels of swirling numbers as shown in Figure 2-13. Furthermore, the experiment includes using reacting fluid flow at different swirling flow levels by applying a mixture of $CH_4/H_2/N_2$ as well as a non-reacting fluid flow at a planar and swirl jet flow by applying Acetone vapour gaseous. The burner shown in Figures 2-13, 2-14 and 2-15 has been first design by (Dixon et al., 1983) and reproduced in the study of (Milosavljevic, 1993) for its ability to produce different flow characteristics (planar or swirl) simultaneously with a burning mixture of pure gaseous fuel. The design of the burner shown in the previous figures is made of two main cylindrical bodies for the axial and swirl airflow along with a central pipe for the fuel (Stetsyuk, 2014).

Furthermore, the internal diameter D of the first internal pipe is 50.8mm and it's concentric with the fuel orifice and the airflow creating within this annulus for 264mm. Likewise, the fuel such as acetone vapour is injecting through the fuel pipe which has an internal diameter D_f of 15mm and long of 0.75m and centred within the surrounding circular duct by three locking screws at 25mm upstream ends of the burner tube. The air can enter the burner through two places, namely the axial and the swirl. However, when the air enters the axial orifice only in the case of planar jet flow is it an un-swirled stream and through axial along with the swirl slots in case of swirl jet flow is namely a swirling stream. Moreover, the tangential velocity

components are generating due to six tangential slots milled into the outer wall of the burner pipe (Stetsyuk, 2014).

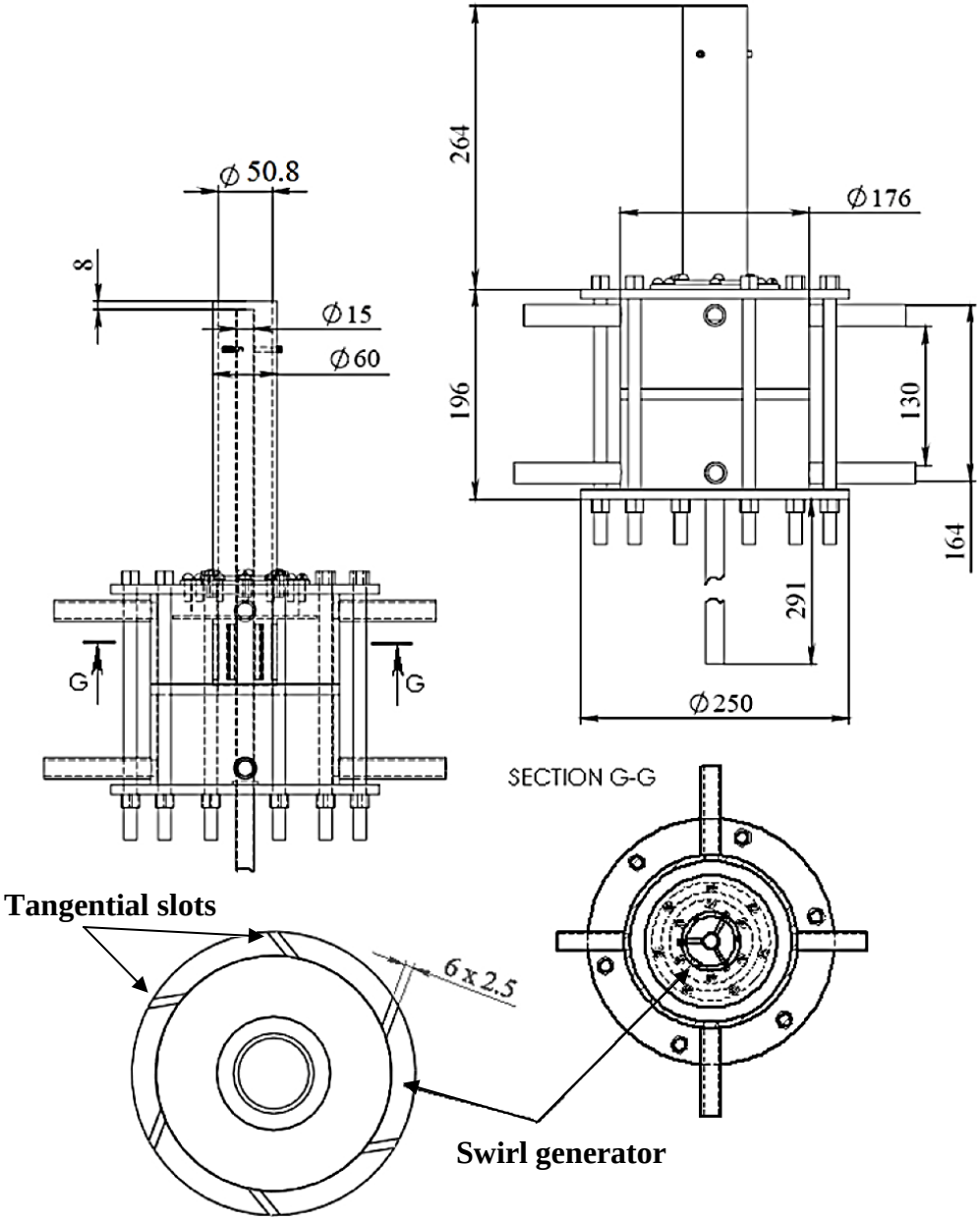

Figure 2-13: Cut View Of Atmospheric Burner Used In The Experiment. All Units In Mm. Modified From (Stetsyuk, 2014).

In addition, this study is on an isothermal and non-reacting fluid flow only, therefore the non-reacting flow boundary conditions of a range of swirl numbers 0.3-1.07 in this experiment are stated by (Dixon et al., 1983) and can be viewed in Table 2.1 where the scalar part refers to the fuel and the swirl and axial parts refer to airflow. In addition, the scalar mixing field same as mixture fraction is considered to have a vital role in isothermal non-reacting swirling flow, thus a planar laser-induced fluorescence PLIF technique is used to compute it. This method can be qualitative as well as a quantitative categorization of the flow fields, as it's

considered to have non-invasive measurements and it's ideal for this type of flow conditions (Stetsyuk, 2014).

Table 2-1: Non-Reacting Boundary Conditions

S	Axial	Swirl	Axial & Swirl	Scalar	
	V l/min	V l/min	Re	V l/min	Re
0.3	500	400	28662	40	3770
0.58	350	550			
1.07	150	750			

Where V is the volumetric flow rate, the results have been taken at a certain location as shown in Figure 2-14 where the x refer to the radial direction, perpendicular to the jet propagation and y refer to the axial direction, parallel to the flow propagation.

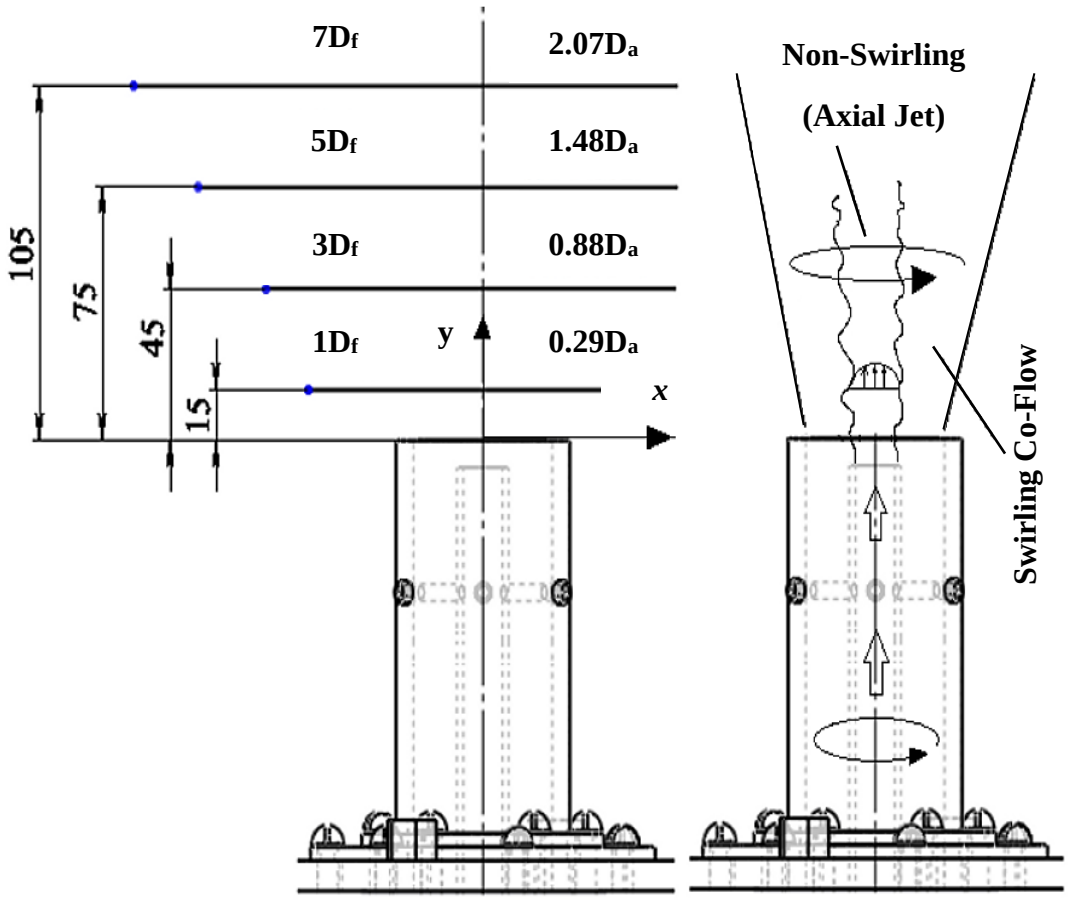

Figure 2-14: The Left-Hand Image Indicates The Laser Sheet Positions During Plif Measurements And The Right-Hand Image Show Flow Arrangement. Modified From (Stetsyuk, 2014).

Lastly, Figure 2-15 shows a three-dimensional plot of the experiment setup (Stetsyuk, 2014). The definition of each device in the figure is assigned as a number, in which (1) refers to the cylindrical positive lens, (2) a dichroic mirror, (3) frequency-doubled, (4) a beam damper, (5) a mechanism and the traverse handle, (6) the ruler, (7) the thermometer, (8) an electrical hob, (9) a water bath, (10) an Acetone feeder, (11) a thermocouple, (12) CCD camera Imager Intense, (13) a filter, (14) a swirl-stabilized burner and (15) the fluid flow test section (Stetsyuk, 2014).

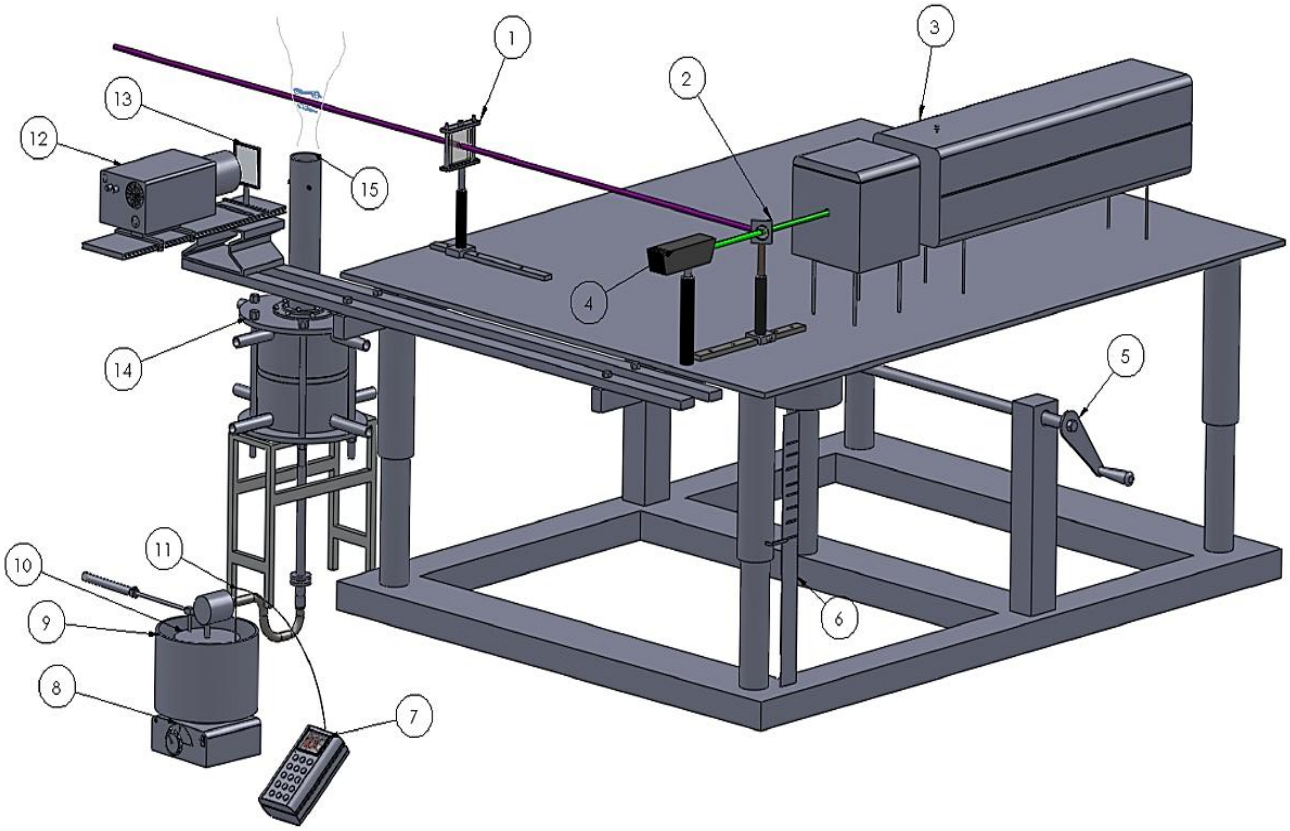

Figure 2-15: Experimental Facility System (Stetsyuk, 2014).

2.3.3 Numerical studies

Swirling flows have been numerically investigated for the last five decades. One of the earliest studies was conducted by (Lilley, 1976) where non-isotropic turbulence in swirling flows numerically examined by some simple turbulent models. The study showed that there is a solid connection among the local swirl number, the swirl number, the Richardson number and the effect of the swirl on turbulent stress and viscosity which need to be included in the turbulent models' phenomena. Before long an axisymmetric incompressible turbulent swirling jet flow was investigated via using space marching integration methods where a k-ε turbulence model applied to solve the governing Reynolds equations. Many properties such as Reynolds stresses, turbulent kinetic energy and dissipation rate were achieved and were in agreement with the experimental data with the assumption of isotropic turbulent viscosity (Naji, 1986). Meanwhile, (Morsi & Clayton, 1986) used a Prandtl mixing length hypothesis and k-ε model to analyse turbulent swirling flow (assumed fully developed) in axisymmetric annulus coaxial tubes. High and low swirl components were deemed, and the analyses were based on Navier-Stokes equations in cylindrical coordinates to account for the velocity components. The turbulence models result showed good agreement with the experimental velocity profiles with significant success and amelioration in predictions. Subsequently, the Reynolds stress transport model used to indicate enclosed axisymmetric flow in helium jet consisted of an outer strongly swirling annular air stream and an inner non-swirling flow. The results indicated that the model outcome was in good agreement by showing some characteristics such as the interaction between swirl, density gradients and turbulence. However, poor predictions of radial mixing between the helium and air streams (Hogg & Leschziner, 1989).

Curiously, experimental and numerical investigations were carried out by (Sommerfeld & Qiu, 1993) to study particle distribution characteristics in a confined swirling flow with a swirl number of 0.5. The numerical method used k-ε turbulence model with isotropic turbulence assumption to predict the mean velocity profiles and mass flux which fit well the measured gas characteristics, contrariwise to gas-phase turbulent kinetic energy where underpredicted. Moreover, a standard k-ε turbulence model was employed to investigate both three-dimensional, turbulent flow in a multichannel swirler and axisymmetric, isothermal, turbulent flow in combustion chambers. The velocity profiles of both air and gas at the swirler outlets were derived. The sensitivity of swirling flow inside the chamber to the inlet and outlet boundary conditions were employed. The results showed that the flow behaviour in the chamber is not very sensitive to the actual shape of the inlet velocity profiles provided the

averages of the inlet axial, radial and azimuthal velocity components are separately preserved (Xia et al., 1997).

On the other hand, the dissipation rate model has been improved by an empirical strategy as well as pressure and the velocity gradients terms were well proposed in the transport equations for the Reynolds stresses. The potential improvements were confirmed by the calculations of a turbulent boundary layer over a smooth wall (Djenidi & Antonia, 1997). Additionally, (de Parias Neto et al., 1998) investigated the numerical modelling of the hydrodynamics of an annular swirling decaying flow generated by a single tangential inlet in the laminar flow system. In addition, the FIDAP package has been used to solve Complete Navier-Stokes equations. The results appeared that a correct numerical modelling was strongly linked to the mesh generation. Some researchers studied swirling flow experimentally and numerically in a water model combustion chamber. The turbulence models for the numerical calculations applied are k-ε turbulence model, the RNG k-ε turbulence and a differential Reynolds stress model (DRSM). It is been found that there was a corner circulation zone and toroidal circulation zone attached to a central reverse zone which extends all the way to the exit of the combustion chamber (Xia et al., 1998). A few researchers deal with the construction of a mathematical model of growth of free swirling turbulent flow. The calculations have been made by some semiempirical models of turbulence and compared with experimental data (Chernykh et al., 1998). Moreover, (Pinton et al., 1998) analysed the statistical properties of velocity and temperature fluctuation in a turbulent flow created in the gap between coaxial disks. The study obtained temperature-velocity colourations and found that the velocity field characteristics were unbiased on the large scale anisotropy. (Ahmed, 1998) measured the flow of a confined, isothermal, swirling flow field in an axisymmetric sudden expansion research combustor using Doppler velocimeter. The swirling streamline data was compared with the simple dump flow, and it was revealed that the swirl reduces the size of the corner recirculation region and produces a toroidal recirculation region. In addition, swirling improves the production and distribution of turbulence energy in the combustion chamber. Meanwhile, (Reynier & Minh, 1998) applied a finite volume scheme and a two-equation turbulence model to simulate compressible and turbulent air-air coaxial jets. The calculations showed that the flow near the inlet was strongly unstable, also in the outer mixing layer, there were coherent structures developed as in a simple round jet. Whereas, in the inner mixing layer there was a recirculation region found on the jet axis.

Later, (Jakirlić et al., 2000) investigated the swirl and turbulence flow experimentally, using a cylinder of single stroke Rapid Compression Machine (RCM) model and Reynolds Averaged Navier Stokes (RANS) model. Direct Numerical Simulations (DNS) have been applied on RCM modes which are steady rotation, transient spin down without compression and transient spin down with compression. The results from DNS were validated with experimental results which showed a good agreement. On the other hand, (De Farias Neto et al., 2001) applied numerical modelling of mass transfer on an annular cell subjected to swirling laminar decaying flow. The results showed that correct mass transfer coefficients in such a flow were directly linked to a sufficient mesh generation. Also, the numerical results showed a good agreement with the experimental data obtained. A researcher studied numerically the dynamic of a three-dimensional vortex sheet of swirl flow. Fast summation and vortex methods were applied on a parallel computer. The evolution of the vortex sheet was then computed and the complex dynamics of the sheet was described (Sakajo, 2001). Furthermore, some researchers suggested two models, a Second-Order Moment (SOM) model and a Monte Carlo (MC) simulation of stochastic particle motion to simulate the gas velocity seen by particles. They compared the results with PDPA measurement data which showed that SOM-MC models gave a good agreement with the measured data (Liu et al., 2001). However, (Lebarbier et al., 2001) suggested a hydraulic model of an industrial dryer in order to investigate the precession of the central jet. The experiment predicted that the flow was mainly time dependent.

Next, (L. X. Zhou et al., 2003) made a simulation on methane-air swirling combustion and NO formation for different swirl numbers using a Unified Second-Order Moment (USM) turbulence chemistry model. The simulation results compared with the results obtained by applying E-A Archimedes combustion model indicated that the results by USM model were better than that by E-A Archimedes model. Some researchers studied swirling flow in a coaxial jet combustor using a Large Eddy Simulation (LES) model of particle laden and Navier stocks equation. The results by LES proved more accurate than the Navier stocks equation for the same problem (Apte et al., 2003). However, (Yang et al., 2003) utilized a three-dimensional flow field simulation with Reynolds Stress Turbulence Model (RSTM). The RSTM model results showed a good level of agreement with the experimental data and the RSTM model suggested the velocity and recirculation gradients were better than the k-ε turbulence model results. Soon after, a numerical study had been made on an open swirl-stabilized turbulent premixed flame. Flame properties have been well explained by simulating the flow field, combustion and heat transfer. The results showed that the flame zone was free of swirl. The

simulation exposed that flame stabilization depended on flow divergence instead of zone recirculation (Zhao et al., 2004). Moreover, an evaluation study has been published on the performance of Unsteady Reynolds-Averaged Navier-Stocks (RANS) (U-RANS) method in predicting the processing vortex core phenomenon. The results showed that the U-RANS method was able to capture the processing vortex core both qualitatively and in parts quantitatively (Wegner et al., 2004).

Furthermore, a non-premixed combusting swirling flow analysed by using Reynolds-stress and k-ε turbulence model, the results for both models such as gas temperatures, mean axial and tangential velocities were compared to experimental data. Interestingly, the predicted results for both models were relatively good for the flame properties but for different properties related to isothermal features, combusting flow fields and some properties inside the recirculation zone were better for the Reynolds-stress turbulence model than k-ε turbulence model (German & Mahmud, 2005). Meanwhile, a range of swirl number S= 0 to 1.2 numerically investigated using a Large Eddy Simulation (LES) method in unconfined annular jet, the results showed the increasing of swirl leads to a stronger effect near the axis (García-Villalba & Fröhlich, 2005). Some researchers utilized an experiment and Three-dimensional 3D RANS computations models to study the mixing between a swirling annular jet (primary air) and the non-swirling inner jet (fuel) for different swirling number. The numerical method carried out by commercial CFD-software FLUENT, the velocity results from the programme showed acceptable agreement with experimental data, also Large Eddy Simulations were compared to Fluent method for equilibrium, fully-developed swirling flow (Palm et al., 2006). Concurrently, (Freitag et al., 2006) used DNS and based on Laser Doppler Velocimetry (LDV) experiment to study the recirculation area in a swirling flow by computing velocity and scalar concentration. The results showed that the processing vortex core has high effects on the mixing process leading to a recessing scalar concentration field because of the reverse flow zone. Also, the numerical method was in strong agreement with the experiment. Curiously, both RANS and LES techniques were applied to examine the flow patterns in an axisymmetric swirl combustor structure and unsteady nonreactive swirl flow dynamics downstream (Grinstein & Young, 2006).

Moreover, (Oefelein et al., 2007) studied swirling particle-laden flow via using LES in a combustion chamber where many features were computed and compared directly with comprehensive experimental measurements. The outcomes indicated that by using the accurate

mesh, grid resolution, well-defined boundary conditions and suitable numeric steps led to the ability to use LES for this kind of combustor. However, the Sydney Swirl Flame series was examined by LES for the flow and mixing in a selected non-premixed state where a mixture fraction with a certain condition was used to predict the chemical state in the flame. The result showed that vortex and non-vortex breakdowns were sensitive to both the swirl amount and the ability of LES in combustion were in good agreement with experimental data (Stein & Kempf, 2007). Additionally, (Murphy et al., 2007) employed a Differential Reynolds Stress Model with default constants for the turbulence closure in two commercial CFD codes to investigate a highly swirling single-phase flow with core recirculation. The effect of omitting wall reflection terms was well-predicted by the numerical method, however, the velocity profile prediction between the two codes was not identified because of pressure–strain and turbulent diffusion terms. Meanwhile, an RNG k-ε turbulence model was utilised in order to research the dynamics of three-dimensional flow in a cyclone with tangential inlet and tangential exit, the results found the model was capable of predicting the tangential velocities and it was in good agreement with the results published by using Particle Tracking Velocimetry (PTV) of the same case (A. Gupta & Kumar, 2007). (Eldrainy et al., 2009) used a k-ε turbulence module implemented in the CFD Fluent programme and a novel swirler concept to explain how the flow dynamics inside the gas turbine combustors at different swirl number. The outcomes of the simulations required a discussion of some features such as turbulence intensity, pressure drop, and central recirculation zone at different swirl numbers. Alternatively, (H. F. Guo et al., 2009) investigated a swirling air-jet spinning nozzle for compressible fluid via using a realisable k-ε turbulence model, also, the effects of nozzle geometric parameters such as the injection angle, diameter, chamber diameter and others on the flow and some properties explored. Many factors were concluded via simulation, such as the relation between velocity distribution, reverse flow and vortex breakdown caused by the nozzle geometric modification, were considerably related to fluid flow and yarn properties.

Moreover, (Qi et al., 2010) applied the Speziale, Sarkar and Gatski Reynolds Stress Model (SSG RSM) to simulate the fluid dynamics in a full baffled stirred tank with a Rushton turbine impeller. The results from the work were compared with published experimental results which showed that the SSG RSM model captured the global fluid dynamics and the local types of trailing vortices. The simulation by using SSG RSM and MRF impeller rotational model together could perfectly shape turbulent fluid flow in the stirred tank, and it could approach an alternative method for design and optimisation of stirred tanks. Some research developed a

numerical code to solve the unsteady RANS equations based on three k-ε turbulence model knows as the standard k-ε turbulence model, the $v^2 - f$ model, and the nonlinear k-ε turbulence model. The study carried out the performance of simple and complex jet flows from a turbulent free jet, a turbulent jet impinging on a flat plate, and a turbulent wall jet. The numerical results were compared to experimental data and it showed that the linear turbulence model was in good agreement with simple jet flows, but for complex flows such models, it wasn't able to predict an accurate results (Balabel & El-Askary, 2011). Simultaneously, (Moureau et al., 2011) studied the ability to use LES and DNS to the analysis of a swirl burner run with a lean methane-air mixture, whereby a different mesh approach took place at each numerical method. Generally, both methods showed good potential to catch some features of flame in swirling flows burner. Furthermore, the LES numerical method used by many researchers to analyse and study various combustions burner is based on swirling flows. For instance, (Xiouris & Koutmos, 2012) studied a partially premixed propane-air burner known as stratified disk burner, while (W. P. Jones et al., 2012) simulated a two-phase flow in a swirl-stabilized burner and (Zheng et al., 2013) examined a premixed swirling combustor in both non-reacting and reacting cases.

Generally, the LES method showed a good agreement with the experiments used by the researcher. Nevertheless, (Kim et al., 2015) used the Shear Stress Transport (SST) turbulence model to determine the location of vortex generation and swirl angle in the pump sump station. The model showed very good agreement with experimental values, for instance the predicted swirling angle degree was 11.3 while it was 10.9 degree in the experiment. Some researchers numerically studied the propane turbulent premixed flames in an atmospheric lean-premixed swirl-stabilized burner. The research was based on the RANS technique, three turbulence models were used (standard k-ε, Realizable k-ε and SST k-ω) and five swirl numbers S = 0, 0.35, 0.75, 1.05 and 1.4 with a validation of experimental data. Surprisingly, axial and radial velocity profiles, temperature and propane concentration profiles for the models showed a good agreement with experimental data (Z. M. Mansouri et al., 2016). However, (Benim et al., 2017) used a gas turbine combustor to investigate turbulent swirling flames via CFD code OpenFOAM, LES and unsteady RANS numerical methods where SST turbulence module applied as the turbulence model. The results indicated that using unsteady RANS in CFD code would take a shorter period than the LES method, however, the accuracy of LES was greatly better compared to unsteady RANS such as mixture fraction and the scalar dissipation rate. Similarly, (Pampaloni et al., 2017) used LES and RANS as an assessment to predict the

turbulent combustion process in methane swirl-stabilized lean-burn flames. In line with the findings of other researchers, the outcome indicated that LES is able to compute turbulent mixing between swirling flow and co-flow whilst RANS can compute the main features of the reacting flow field and elements concentrations. (Z. Mansouri & Boushaki, 2018) carried out a numerical and experimental investigation of methane/air swirled burner at a non-reacting and reacting swirling jet flows conditions, and the non-premixed flame was stabilized and studied at high swirl number S = 1.4. The numerical method included a combination of RANS and Delayed-Detached Eddy Simulation (DOES) for non-reacting and reacting swirling flows, many features indicated numerically and compared to the ones from the experiment and showed the good potential of agreement between both methods. Once again, a combination of unsteady RANS and LES numerical methods were employed to investigate turbulent swirling reacting and aimed to reduce computational costs by assessing the possibility of unsteady RANS for the computations of turbulent reacting flows. Despite the low cost of the unsteady RANS approach, the study suggested that the simulation of turbulent combustion accuracy of LES was much higher than the unsteady RANS numerical method (Ilie, 2018). Though (Chen & Zhao, 2018) operated only RANS with three-dimensional Reynolds stress models to study a non-reacting flow fields of swirling trapped vortex ramjet combustor which worked in different swirling flow conditions, the model showed a good agreement of computing at range of swirl number up to 0.98. Some researchers used LES methods with a Smagorinsky sub-grid scale model to configure a premixed methane-air swirl in an ignition process, many features computed such as non-reacting mean, tangential and radial velocity profiles which showed a good agreement with the experimental results (EidiAttarZade et al., 2019).

On the other hand, a few researchers examined three RANS turbulence models placed in the CFD programme to study the combustion characteristics of non-premixed swirling burners. The results showed that the Reynolds stress turbulence model is more than 50% accurate among the spectral turbulence model and Re-normalization model by compared it with experimentally measured data (Khodabandeh et al., 2020). Furthermore, the annular swirling combustor model investigated via using the DNS method in turbulent swirling kerosene/air premixed flames at different Reynolds numbers (Xiao et al., 2020). Another study based on the RANS method was carried out by using SST k-ω and Reynolds stress turbulence model, as established by (Morrall et al., 2020), the research dedicated to analysing fluid mechanic and performance of a one-phase swirling flows in a multi-nozzle annular jet pump. Also, different swirl strength carried out numerically and experimentally to compute the static pressure fields

for three regimes. Although both models showed good agreement with the experiment at low swirling flow, the high level of swirling flow showed that the models result disagree more and the Reynolds stress model was in better agreement.

Recently, some researchers investigated the ability to use unsteady RANS via using the SSG Reynolds stress model (RSM) of obtaining some properties such as the helical structures and vortex breakdown by using a three-dimensional, incompressible and isothermal annular bluff-body swirling jet at Reynolds number Re = 8500 and swirl number S = 0.39. The study mentioned above showed an acceptable precision between RSM and experimental data (Y. Zhang & Vanierschot, 2021).

2.3.4 Related numerical review

As described in the previous section, many scientists have carried out studies on numerical modelling of swirling jet flow. However, the main studies which are more closely aligned to the present study, are described here and showed in Table 2-2.

Three decades ago, some researchers studied the modelling of swirling flow via employing k-ε turbulence model, Reynold stress transport model and Algebraic stress model to evaluate the applicability of models in swirling and recirculating flows for different cases. The modelling assumed that the isotropic eddy viscosity and the modified Boussinesq hypothesis explain the stress distributions, and the redistribution of the stress magnitudes was necessary. The results showed that the k-ε turbulence model is poorly applicable for high swirling flow and a slight improvement for the other models (Sloan et al., 1986)

Posteriorly, (Shamami & Birouk, 2008) published assessment research using different RANS turbulence models for simulating turbulent swirling can-combustor flows at two swirling number such as S =0.4 and S =0.81. The models result compared to experimental data and indicated that the Reynolds stress and Eddy-viscosity models were able to compute weakly swirling flow features such as central recirculation zone. However, Eddy-viscosity models, realizable k-ε module and SST k-ε module were unable to be used with high swirling flow, but Reynolds stress models showed better prediction at same conditions.

Remarkably, the RNG k-ε turbulence model and Reynolds stress model applied in a Two-dimensional CFD simulation for a swirling flow inside a straight pipe. The main purpose of the simulation was to evaluate the ability of these models to predict the swirling flow at various swirl numbers, the results showed that both models were not appropriate to predict the

decay of the turbulence quantities. However, both models demonstrated good agreement with other features at different swirling flow as showed in below:

A. For low swirling flows: the velocity profiles of the RNG k-ε turbulence model was in better agreement with experimental results than the Reynolds stress model.

B. For high swirling flows: Reynolds stress model overpass RNG k-ε turbulence and it was more fitting for high swirling flows (Escue & Cui, 2010).

Finally, (Miltner et al., 2015) examined a flow field of the turbulent free jet by implemented a CFD program with various RANS turbulence models at very low swirl flow and straight flow. For the swirling flow part, the results showed that the Reynolds stress model and to a slight extent SST k-ω turbulence models were in better agreement with experimental data than standard k-ε, Spalart-Allmaras, Realizable k-ε, standard k-ω and RNG k-ε turbulence models.

Table 2-2: Related Numerical Research Summery

#	Author/ Year	Turbulence model	Swirling strength	Outcome
1	Sloan et al., 1986	Standard k-ε Reynolds stress Algebraic stress	Low & High	• k-ε turbulence model applicable for low swirling flow only. • Other models slightly better for high swirling flow.
2	Shamami & Birouk, 2008	Reynolds stress Eddy-viscosity realizable k-ε Shear Stresses SST k-ε	S = 0.4 S = 0.81	• Reynolds stress model good for both swirling number • All other models good for S=0.4 only
3	Escue & Cui, 2010	RNG k-ε Reynolds stress	Low & High	• RNG k-ε is good for low swirling flow • Reynolds stress is more fitting for high swirling flows
4	Miltner et al., 2015	Reynolds stress Standard k-ω SST k-ω Standard k-ε Realizable k-ε RNG k-ε Spalart-Allmaras	Very low swirling flow	• Reynolds stress & SST k-ω are slightly better than the other models

2.4 Gap in knowledge

Following the conduction of the literature review, it can be explained that there are various research projects which focus upon the swirling jet flow. Moreover, many types of research have been carried out to discuss the phenomena of using RANS and LES numerical turbulence modelling to compute swirling jet flows. Most of the numerical work relies on one turbulence model to carry out the results and compare it with different researchers work. However, only a few researchers use the swirling flow experiment to evaluate different turbulence model which employed in RANS equations to indicate the limitation and drawbacks of them.

Therefore, there is a clear need to do more research into using a wider range of swirling jet flows with a wide range of numerical turbulence model to define the ability of these models of predicting the swirl flow behaviour and validate the turbulence models with experiment data. The present research aims at extending the current understanding of turbulence modelling employed with the RANS equations. The current and previously published data in the open literature remains lacking essential details and enables discrepancies between different studies to be surfaced.

Commonly, the priority of swirling flow relies on the wide range of applications that this type of flow can be used such as cyclone separators, turbomachines and combustion chambers. Therefore, the contribution of this research is to expand the knowledge of the swirling flow implemented in a burner via using different types of turbulence models. In addition, the novelty of this work is to establish the applicability of turbulence modelling typically employed in RANS equations e.g., six models to model swirling flows by using the ANSYS-CFX simulation program, and to specify the most suitable turbulence module to use in swirling jet flow by comparing them with the previously published experimental data. In addition, to study the effect of swirling flow number on the turbulence level. Last but not least, the effect of diffusion (for the scalar mixing) will be examined. Finally. The effect of screws along with the swirl degree on the self-symmetric structure will be performed.

One the other hand, Ansys CFX will be implemented in this study for its ability of operation turbomachinery applications at high performance rate such as aeromechanics, blade design and optimization, industry leading turbulence and advanced material modelling. Moreover, CFX known as the standard CFD software to solve turbomachinery studies where both models and solver are connected in an innovative, spontaneous and adaptable Graphical User interface (GUI). Therefore, CFX have a wide ability for customization and automation

via applying scripting, session files and a strong expression language. In other words, the capability of this software relays on providing accurate results that will save time and money for various complicated challenges in turbomachinery applications. Finally, CFX software is extensively validated for this type of study for its robustness and accuracy which applied by numerous researchers now days (CFX, 2018).

Chapter 3 THEORY OF NUMERICAL METHODOLOGY

3.1 Governing equations

The governing equations of fluid flow are known as a mathematical expression of the essential conservation laws of physical science. These equations are known as the Navier-Stokes equations which are a combination of Partial-Differential Equations (PDEs) based on the conservation of mass, momentum and energy fundamentals. These equations define the relationship between the velocity, pressure, density, and temperature of a moving fluid. Therefore, based on the law of the conservation of mass, whereby the fluid mass is conserved as it can be neither created nor destroyed, a continuity equation is established. Moreover, the momentum equation represents Newton's 2nd law of motion where the rate of change in momentum is equal to the sum of forces that act on the fluid practical. These forces are mainly due to gravity, pressure difference and viscosity of the fluid. On the other side, the energy equation represents the 1st law of thermodynamic where the rate of change of the energy is equal to the sum of the rate of heat added to the rate of work done on a fluid particle (Pope, 2000; Zavila, 2012). Mathematical expressions for continuity and momentum equations are shown and explained in the following sub-sections by applying the Eulerian approach.

3.1.1 Continuity equation

The continuity equation characterises the conservation of mass, for unsteady and compressible fluid flow is written as follows:

$$\frac{\partial \rho}{\partial t} + \frac{\partial (\rho . \bar{u}_j)}{\partial x_j} = 0 \qquad (3\text{-}1)$$

where: ρ is the fluid density [kg/m3], t is time [s], $\bar{u}_j$ is the time-averaged j coordinate of the fluid flow velocity [m/s], and x_j is a coordinate of the Cartesian coordinate system (Zavila, 2012).

3.1.2 Momentum equation

For compressible fluids, momentum equation in form of Navier-Stokes equation to calculate turbulent flow, time-averaged value is written as follows:

$$\frac{\partial (\rho . \bar{u}_i)}{\partial t} + \frac{\partial (\rho \bar{u}_i . \bar{u}_j)}{\partial x_j} = -\frac{\partial \bar{p}}{\partial x_i} + \frac{\partial}{\partial x_j} . \tau_{ij} + \rho . \delta_{i3} . g + \rho . f_c . \varepsilon_{ij3} . \bar{u}_j + \rho . f_j \qquad (3\text{-}2)$$

where: $\bar{\rho}$ is the time-averaged value of pressure [Pa], $\tau_{ji}$is the tensor of viscous stress [Pa], $\delta_{i3}$is the Kronecker delta, $\varepsilon_{ij3}$is the unit tensor for centrifugal forces, f_j is the j–coordinate of force [N], and g is the gravity acceleration [m/s2] (Zavila, 2012).

3.1.3 Energy equation

This equation is used in case of combustions problem and for variable-density flow. For compressible fluids, energy equation in form of Navier-Stokes equation to calculate the fluid energy and it is written as follows:

$$\frac{\partial}{\partial t}.[\rho.\bar{E}] + \frac{\partial}{\partial x_j}.\left[\rho.\bar{u}_j.\bar{E}\right] = \rho.\bar{u}_j.f_i - \frac{\partial\left(p\bar{u}_j\right)}{\partial x_j} + \frac{\partial\left(\tau_{ij}.\bar{u}_j\right)}{\partial x_j} - \frac{\partial\bar{q}_j}{\partial x_j} \quad (3\text{-}3)$$

where: $\bar{E}$ is the time-averaged value of energy [J/kg] and $\bar{q}_j$ is the time-averaged heat flux [J/(m2.s)] (Zavila, 2012).

3.1.4 Species transport equation

This equation is used in case of a combustions problem and for chemical reaction existence. This equation represents the time-average values of the local species mass fraction, which simplifies to $\bar{\gamma}_i$, the equation is written as follows:

$$\frac{\partial}{\partial t}(\rho.\bar{\gamma}_i) + \frac{\partial}{\partial x_j}.\left(\rho.\bar{u}_j.\bar{\gamma}_i\right) = -\frac{\partial}{\partial x_i}J_{j,i} + R_i + S_i \quad (3\text{-}4)$$

where: $\bar{R}_i$ is the production rate of species i [kg/(m3.s)], $\bar{S}_i$ is the growth production rate from distributed species [kg/(m3.s)] (Zavila, 2012).

3.2 Numerical modelling

Numerical modelling is an extensively employed technique in various scientific studies as shown in Figures 3-1 and 3-2. It works by applying many mathematical models to describe a certain physical condition. This technique includes the use of a different kind of equations whereas some of them very difficult to solve directly such as Navier-Stokes equations or any partial differential equations. Therefore, several methods such as Finite Difference Methods (FDM), Finite Element Methods (FEM) and Finite Volume Method (FVM) have been created to solve and eliminate the error percent for much difficult research. These methods are used to indicate approximate solutions and they have many procedures depending on the used method (Ismail-Zadeh & Tackley, 2010; Schäfer, 2006).

Furthermore, this research is based on using ANSYS-CFX simulation programme which is based on Finite Volume Method (FVM); hence the next sub-section includes an explanation of this numerical method.

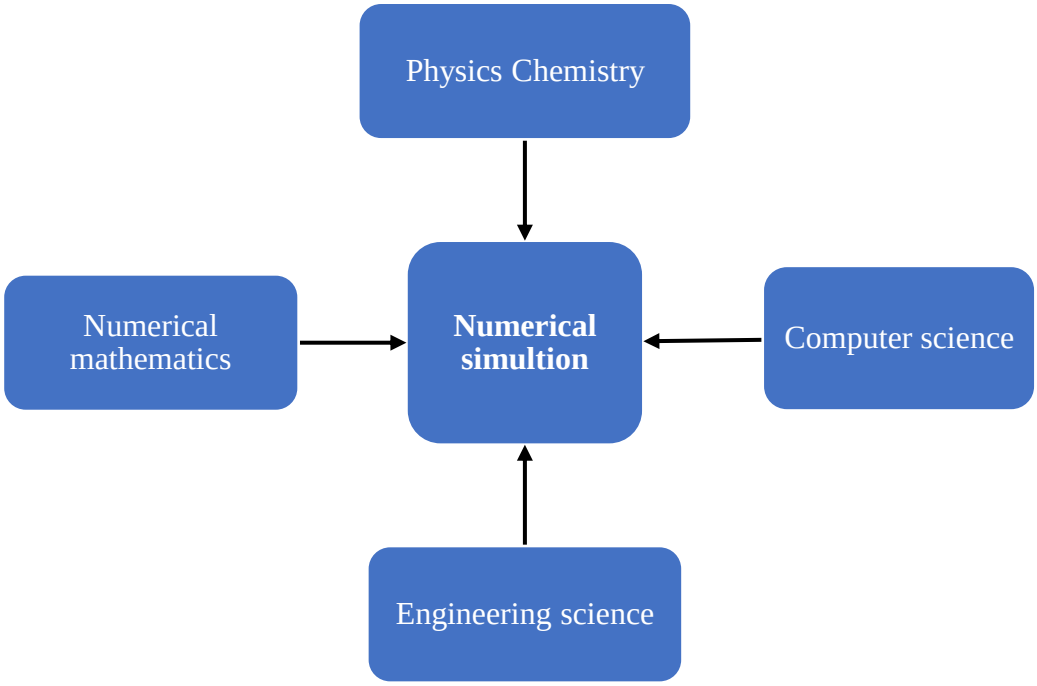

Figure 3-1: Interdisciplinarity Of Numerical Simulation Of Engineering Problems. Re-Produced From (Schäfer, 2006).

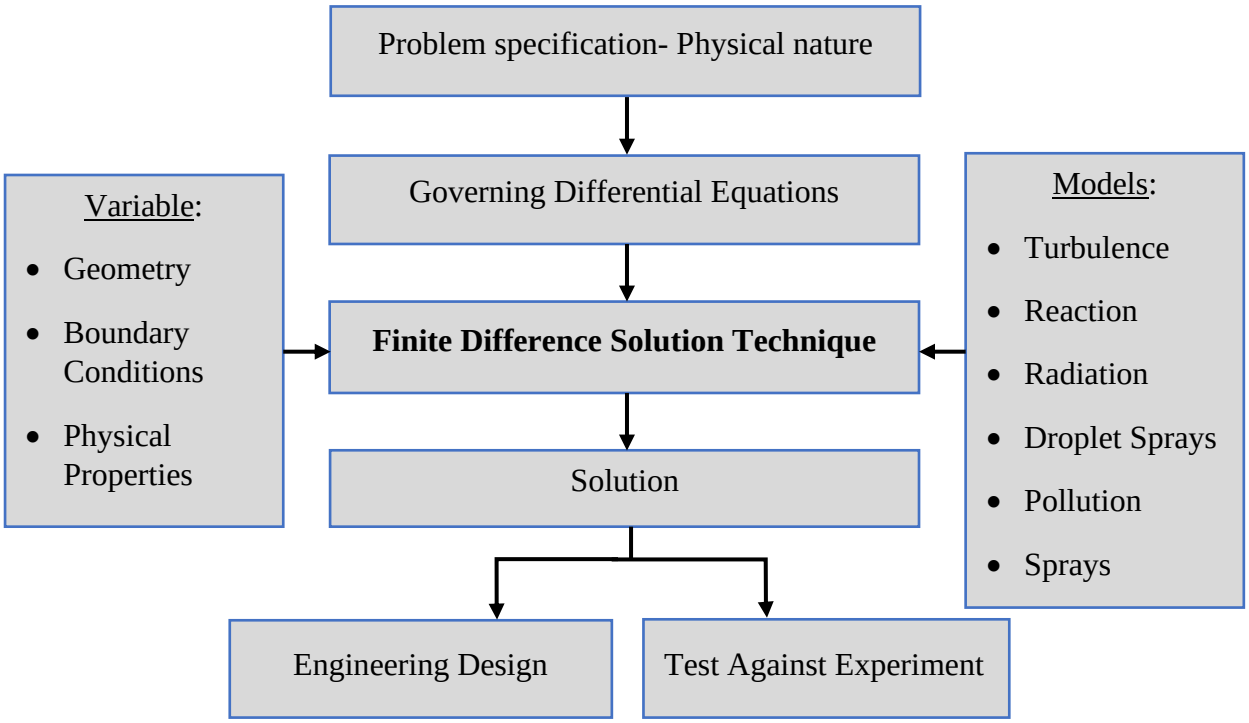

Figure 3-2: Standards Aspects Of Numerical Predictions. Re-Drawing From (A. K. Gupta Et Al., 1984; Lilley, 1976).

3.2.1 Finite Volume Method (FVM)

Known as box methods, finite volume methods first introduced by McDonald, MacCormack, and Paullay in the 1970s to examine the numerical solution of problems in fluid mechanics and non-fluid applications (Schäfer, 2006). Moreover, FVM is a "discretization method for the approximation of a single or a system of partial differential equations expressing the conservation, or balance, of one or more quantities". Generally, conservation laws is another representation of the partial differential equations (PDEs) which have various natures such as elliptic, parabolic or hyperbolic (Eymard & Gallouët, 2010). One of the most important properties of this method is the balance principles as it plays the main role in the mathematical modelling of continuum mechanical problems and the conservativity in the discrete equations (Schäfer, 2006). In another meaning, the constructed mesh in FVM contains a partition of the domain where the space variable exists to format mesh elements which are called control volumes where PDEs integrated take place in a balanced equation (Eymard & Gallouët, 2010).

Generally, using FVM when conducting research has various procedure steps, starting with the breakdown of the problem field into control volumes, then formularization of integral balance equations for each control volume following by numerical integration to

estimate the integrals, an interpolation with nodal values take place to approximate the function values and derivatives respectively. The last stage occurs by assembling the discrete algebraic system to find the final solution (Schäfer, 2006). However, one of the major problems is the discretization of the fluxes at the boundaries of each control volume, this issue can be solved by making the numerical fluxes conservative (the flux incoming a control volume from its neighbour require to be the opposite of the one incoming the neighbour from the control volume) and consistent (as the mesh size vanishes, the numerical flux tends to be continuous flux).

3.2.2 Advantage of finite volume method

Commonly, FEM and FDM have been used many years before FVM, nevertheless, FVM shows an exceptionally outstanding role in the simulation of fluid flow problems and linked transport phenomena. Therefore, FVM is a very popular technique implemented in various simulation programmes such as in Computational Fluid Dynamics (CFD) as it offers a high discretization flexibility process (Moukalled et al., 2015). Also, the most known advantages of FVM are listed below (Bjorn, 2016; Margolin & Plesko, 2019; Moukalled et al., 2015):

1. The discretization is carried out directly in the physical space, which means no need for any alteration between the physical and the computational system.
2. The ability to solve complex/ simple geometries due to the flexibility of adoption of many kinds of mesh structure as shown in Figure 3-2. For instance, the ability to create any uniform and non-uniform/unstructured grid (Margolin & Plesko, 2019; Moukalled et al., 2015).
3. The applicability to comprise a wide range of research applications while maintaining the simplicity of its mathematical formation.
4. The ability to represent the physics and the conservation principles accurately, such as the integral property of the governing equations, and the physical characteristics of the terms.
5. FVM based on conservation laws. Thus, it is a genuine choice for CFD problems since it deals with partial differential equations (Bjorn, 2016).

6. Very strong for robust handling of conservation laws occurring in transport problems because it only requires performing flux evaluation for the cell boundaries (Bjorn, 2016).

7. The accuracy of FVM is highly accepted and can be increased by improving the mesh around that corner of the subject (Bjorn, 2016).

8. FVM is based on cell-average volume values for two- or three-dimension geometries, in other meaning, the variable values are calculated around each node of the mesh, which allows the model to combine different geometry properties such as different kinds of swirl flows.

9. FVM provides an easy method to discretise the governing equations such as continue, momentum and energy equations.

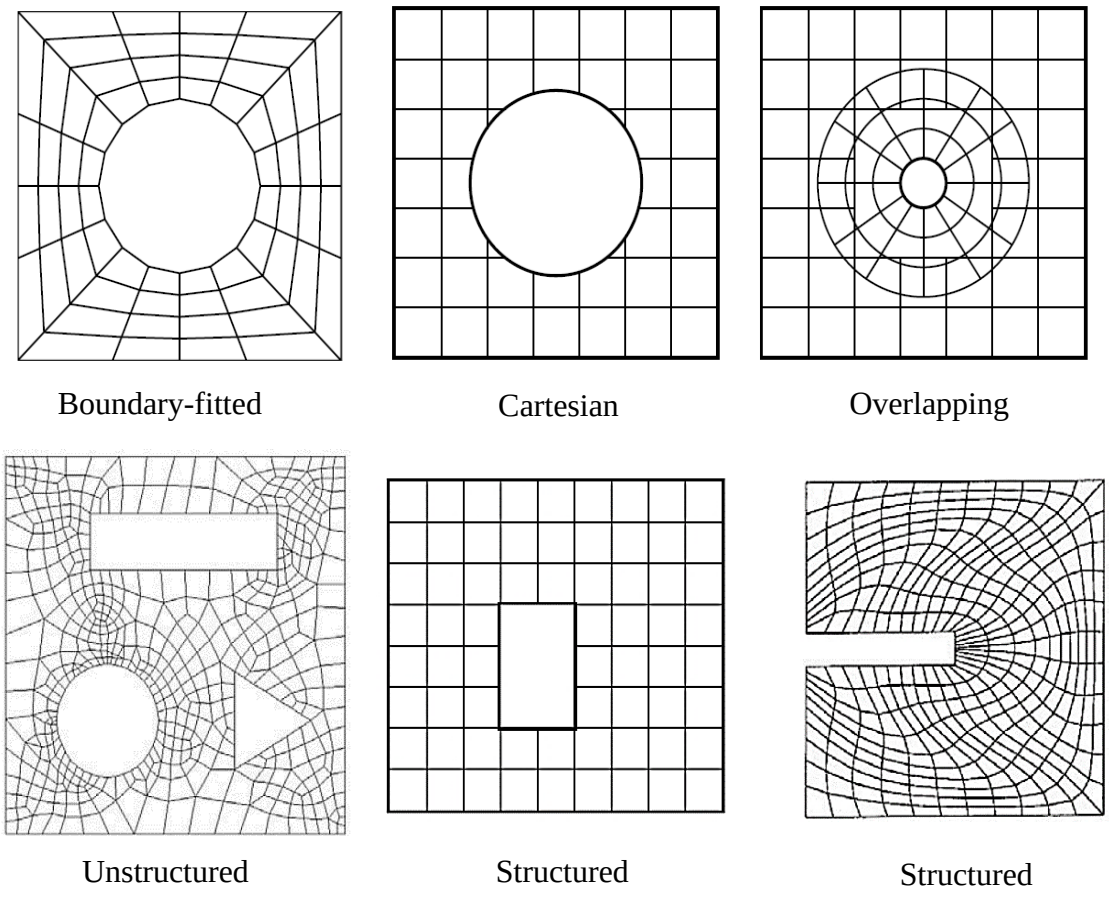

Figure 3-3: FVM Mesh Structure Types. Re-Produced From (Schäfer, 2006)

3.3 Turbulent flow computing methodologies RANS

According to (Pope, 2000; Qi et al., 2010; Versteeg & Malalasekera, 2007) there are three methodologies for turbulent flow computing prediction known as Direct numerical simulation (DNS), Large-eddy simulation (LES) and Reynolds Averaged Navier-Stokes (RANS). Generally, each approach of these methodologies has a different complexity process and accuracy depending on the domain and time scales required to be studied as shown in Figure 3-3.

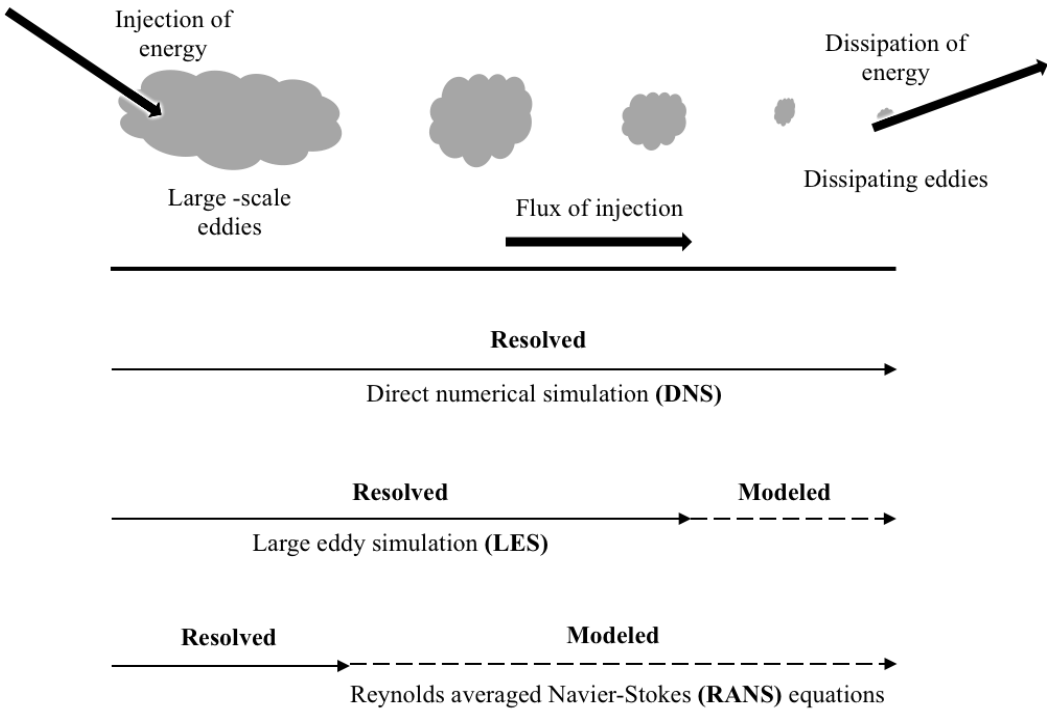

Figure 3-4: Turbulent Flow Computing Methodologies. Re-Produced From (Wu & Porté-Agel, 2012).

In Large Eddy Simulation (LES), (Chivaee, 2014) indicates that this method is able to process larger time-steps and coarser meshes compared with DNS which leads to modelling small-scale motion with a revolving of large-scale motion. Moreover, the LES approach is applicable to use at unsteady flow state which makes it more appropriate than other methods to study unsteady aerodynamic loads on structures, the generation of sound and more complex turbulent-flow experiments, such as reacting flows and high-speed compressible flows.

However, in Direct Numerical Simulation (DNS), the composition of the turbulence from the biggest eddies to the lowest eddies are calculated because of the ability of this method to compute the length and time scales entirely, along with a high level of accuracy and flow description. Therefore, this method needs huge computational energy to operate at the

significant domain of the largest eddies and extremely fine grids, which make this method appropriate for small-scale flow problems and flows with low-to-moderate Reynolds number (Pope, 2000; Qi et al., 2010). On the other hand, Reynolds Averaged Navier-Stokes (RANS) needs the minimum computational energy requirement along with the lowest cost. This method works by indicating the averaged flow motion and the effect of turbulent fluctuations.

Commonly, LES and DNS are less desirable in several industrial applications due to the high-level computational demands, although they offer more accurate results than RANS (Stergiannis et al., 2016). In addition, each approach of these three methodologies has different computational requirements such as the number of iterations needed for convergence, the running time and grid size as being shown in Table 3-1 below (Kolmogorov, 1991; Sanderse et al., 2011). Although, LES and DNS are capable of implementing and solving swirling flow, as has been shown in the literature review, this research investigates the ability of the RANS method to describe and examine the swirling jet flow by using different turbulence flow. Therefore, the next section highlights the RANS method background, CFD steps and turbulence models.

Table 3-1: Methodologies Computational Requirement

Approach	Grid size	Cycles to convergence	Normalized Running time
Reynolds Averaged Navier-Stokes (RANS)	10^6 - 10^7	10^3	10^2
Large Eddy Simulation (LES)	10^9 – 0^{11}	10^6	10^8
Direct Numerical Simulation (DNS)	10^{14}- 10^{16}	10^8	10^{10}

3.4 Closure problem in RANS

The velocity, pressure and any other fluid quantities of a fluid flow can be represented by using certain mathematical equations, namely the Navier–Stokes equations a mentioned in section 3.2. Moreover, each quantity may be decomposed into a fluctuating component and a mean component of a turbulent flow. Therefore, Reynolds Averaged Navier-Stokes (RANS) takes the average value of these quantities which governing the mean flow. However, velocity (or any other quantity) fluctuations still exist in the RANS equations due to the nonlinearity of

the Navier–Stokes equations, which presented as $\overline{-pv_i'v_j'}$ from the convective acceleration part in Equation 3-8b. This term called Reynolds stress R_{ij}; hence, closure means the removal of any cause to the fluctuating part of the fluids quantity via modelling the Reynolds stress term R_{ij} as a function of the mean flow to close the RANS equations with mean values only (Lilley, 1976). Moreover, this method was established to resolve ensemble-averaged equation of fluid flow motions and for many years it has been considered as a traditional approach to model many problems. Conversely, in the RANS modelling, it is very hard to achieve the mean chemical source term in the averaged species transport equation and thus conserved scalar techniques used in several applications and the most known models based on non-reactive scalars, which later became a standard tool in modelling non-premixed combustion. Likewise, the most important advantage of using the RANS equation method is to predict practically any model flow configurations and operating conditions such as the flame temperature, mixture fraction and species mass fractions by corresponding to ensemble-averaged quantities. However, this technique has some disadvantage such as a lack of ability to predict instantaneous flow structures.

3.5 Reynolds Averaged Navier-Stokes (RANS) equations

The previous section signifies that the flow features fluctuate in time and space due to the irregular non-periodic performance of the turbulent flow. Likewise, RANS hypothesis that a flow variable at a known spatial place and instant in time can be symbolized as the sum of the random fluctuations $\acute{u}$ about the mean value and mean value $\bar{u}$. Therefore, the Reynolds-Averaging process and Reynolds decomposition hypothesis along with the spatial-temporal variation for velocity, u, is stated as (Ben-Artzi et al., 2013; Pope, 2000):

$$u = \bar{u} + \acute{u} \tag{3-5}$$

and the pressure is given by:

$$p = \bar{p} + \acute{p} \tag{3-6}$$

The Equations 3-5 and 3-6 have applied for an incompressible fluid when the viscosity μ is constant. The Equations 3-1 and 3-2 which are called Navier-Stokes equations have been applied with the following rules averaging Equations 3-7 to produce the Reynolds-Averaged Navier-Stokes (RANS) Equations 3.8 (Ben-Artzi et al., 2013; Celik, 1999; Pope, 2000).

$$
\begin{aligned}
\overline{\bar{u}_i} &= \bar{u}_i \\
\overline{\acute{u}_i} &= 0 \\
\overline{\bar{u}_i + \acute{u}_i} &= \bar{u}_i + \overline{\acute{u}_i} = \bar{u}_i \\
\overline{\bar{u}_i \acute{u}_i} &= 0 \\
\overline{\acute{u}_i \acute{u}_j} &< 0 \\
\overline{\bar{u}_i^{\,2}} &= \bar{u}_i^{\,2} \\
\overline{\frac{\partial u_i}{\partial x_j}} &= \frac{\partial \bar{u}_i}{\partial x_j}
\end{aligned}
\qquad (3\text{-}7)
$$

$$
\frac{\partial \bar{u}_i}{\partial x_i} = 0 \qquad (3\text{-}8a)
$$

$$
\frac{\partial \bar{u}_i}{\partial t} + \bar{u}_j \frac{\partial \bar{u}_i}{\partial x_j} = -\frac{1}{\rho}\frac{\partial \bar{p}}{\partial x_i} + \frac{1}{\rho}\frac{\partial}{\partial x_j}\left[\mu \frac{\partial \bar{u}_i}{\partial x_j} - \rho \overline{u_i' u_j'}\right] \qquad (3\text{-}8b)
$$

The momentum Equation 3-8b has been compared with NS Equations 3-2 which showed that there is an additional stress term on the left side. The term $-\rho \overline{u_i' u_j'}$ is equal to R_{ij} that refers to Reynolds stress tensor and it is considered as a function of the fluctuating velocity components as well as it can be written as follow:

$$
R_{ij} = \overline{u_i' u_j'} = \begin{pmatrix} \overline{u_1'^2} & \overline{u_1' u_2'} & \overline{u_1' u_3'} \\ \overline{u_2' u_1'} & \overline{u_2'^2} & \overline{u_2' u_2'} \\ \overline{u_3' u_1'} & \overline{u_3' u_2'} & \overline{u_3'^2} \end{pmatrix} \qquad (3\text{-}9)
$$

Furthermore, Equation 3-8b has six unknown terms because of the symmetry of $\overline{u_1' u_2'}$ $=\overline{u_2' u_1'}$. This means that the RANS system is not closed because there are more unknown terms than equations. Therefore, the closure problem can be solved by replacing the unknown variables in term of known ones. This process comes after turbulence modelling, and it requires additional modelling to close the RANS equation for solving. Lastly, the procedure had led to the formation of many different turbulence models. According to (Pope, 2000) Boussinesq approximation suggests that the turbulent shear stresses could be proportional to the mean strain rate with a turbulent eddy viscosity μ_t, as follows:

$$
R_{ij} = -\rho \overline{u_i' u_j'} = \left[\mu_t \left(\frac{\partial u_i}{\partial x_j} + \frac{\partial u_j}{\partial x_i}\right) - \frac{2}{3}\rho\, k\, \delta_{ij}\right] \qquad (3\text{-}10)
$$

In which μ_t represents the eddy turbulent viscosity and it can be calculated by applying a turbulence model. The symbol *k* in the equation above represents the turbulent kinetic energy and $\delta ij = 1$ for i=j and =0 for i≠j which identified as the Kronecker delta.

3.6 Turbulent fluxes and modelling for RANS scalar transport equation in swirl flow

Figure 3-4 shows the main developing components of free swirling jet flow, swirling flow considered as a mixture of a free vortex where the tangential velocity ***W*** "is inversely proportional to the radius and a forced vortex in which the tangential velocity is proportional to the radius" (A. K. Gupta et al., 1984; Örlü, 2006). Generally, the turbulence levels are relating to the swirling flow degree and influence the mixing process. Moreover, the turbulent mixing process is one of the main considerable points in the design process in many applications.

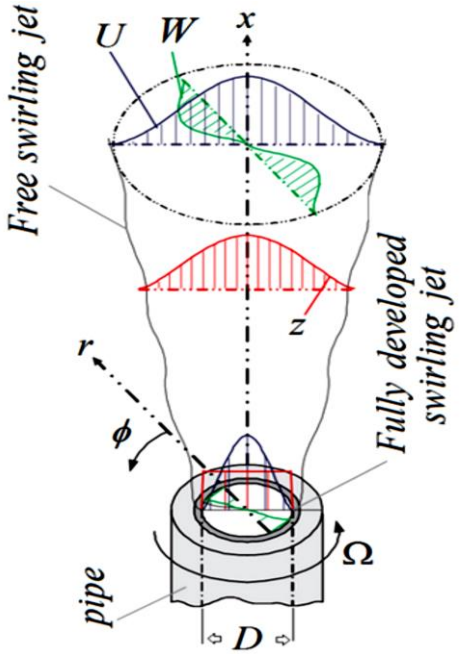

Figure 3-5: Cylindrical Coordinate System Of The Free Developing Swirling Jet. Adopted From (Örlü, 2006).

The following equations represent the flow motion description in polar coordinates. Whereas, the axial, radial and azimuthal velocity components called the swirling component are decomposed into their three cylindrical components u, v, w. Therefore, the continuity and Navier-Stokes equations become as (Stetsyuk, 2014) denotes:

$$\frac{1}{r}\frac{\partial}{\partial r}(r\omega)+\frac{1}{r}\frac{\partial \vartheta}{\partial \emptyset}+\frac{\partial u}{\partial x}=0 \tag{3-11}$$

$$\frac{\partial w}{\partial t}+w\frac{\partial w}{\partial r}+\frac{\vartheta}{r}\frac{\partial w}{\partial \emptyset}+u\frac{\partial w}{\partial x}-\frac{\vartheta^2}{r}=-\frac{1}{\rho}\frac{\partial p}{\partial r}+\vartheta(\nabla^2 w-\frac{w}{r^2}-\frac{2}{r^2}\frac{\partial \vartheta}{\partial \emptyset}) \tag{3-12}$$

$$\frac{\partial \vartheta}{\partial t}+w\frac{\partial \vartheta}{\partial r}+\frac{\vartheta}{r}\frac{\partial \vartheta}{\partial \emptyset}+u\frac{\partial \vartheta}{\partial x}-\frac{w\vartheta}{r}=-\frac{1}{\rho r}\frac{\partial p}{\partial \emptyset}+\vartheta(\nabla^2 \vartheta-\frac{\vartheta}{r^2}-\frac{2}{r^2}\frac{\partial w}{\partial \emptyset}) \tag{3-13}$$

$$\frac{\partial u}{\partial t}+w\frac{\partial u}{\partial r}+\frac{\vartheta}{r}\frac{\partial u}{\partial \emptyset}+u\frac{\partial u}{\partial x}=-\frac{1}{\rho}\frac{\partial p}{\partial x}+\vartheta\nabla^2 u \tag{3-14}$$

$$\nabla^2=\frac{1}{r}\frac{\partial}{\partial r}\left(r\frac{\partial}{\partial r}\right)+\frac{1}{r^2}\frac{\partial^2}{\partial \emptyset^2}+\frac{\partial^2}{\partial x^2} \tag{3-15}$$

However, the above equations cannot be solved as they describe the instantaneous flow field. Nevertheless, when the mean or time-dependent and fluctuating parts or time-independent introduced in the Reynolds decomposition, also, assume a steady-state and axisymmetric mean flow, then the time-averaged flow field equations in polar coordinates will be (Pope, 2000; Stetsyuk, 2014):

$$u=U+\acute{u} \tag{3-16}$$

$$\vartheta=V+\acute{\vartheta} \tag{3-17}$$

$$w=W+\acute{w} \tag{3-18}$$

$$p=P+\acute{p} \tag{3-19}$$

$$\frac{\partial}{\partial t}=0,\qquad \frac{\partial}{\partial \emptyset}=0 \tag{3-20}$$

$$\begin{aligned} W\frac{\partial W}{\partial r}+U\frac{\partial W}{\partial x}-\frac{\partial \overline{\acute{w}^2}}{\partial r}+\frac{\partial \overline{\acute{u}\acute{w}}}{\partial x}-\frac{1}{r}(V^2+\overline{\acute{\vartheta}^2}-\overline{\acute{w}^2}) \\ =-\frac{1}{\rho}\frac{\partial P}{\partial r}+\vartheta(\nabla^2 W-\frac{W}{r^2}) \end{aligned} \tag{3-21}$$

$$W\frac{\partial V}{\partial r}+U\frac{\partial V}{\partial x}+\frac{VW}{r}+\frac{\partial \acute{u}\acute{w}}{\partial x}+\frac{1}{r^2}\frac{\partial}{\partial r}(r^2\overline{\acute{\vartheta}\acute{w}})\ =\vartheta(\nabla^2 V-\frac{V}{r^2}) \tag{3-22}$$

$$W\frac{\partial U}{\partial r}+U\frac{\partial U}{\partial x}+\frac{\partial \overline{\acute{u}^2}}{\partial x}+\frac{1}{r}\frac{\partial(r\overline{\acute{u}\acute{w}})}{\partial r}=-\frac{1}{\rho}\frac{\partial P}{\partial x}+\vartheta\nabla^2 U \quad (3\text{-}23)$$

Furthermore, the passive scalar transport equation mixture fraction will be composed as follows:

$$\frac{\partial z}{\partial t}+w\frac{\partial z}{\partial r}+\frac{\vartheta}{r}\frac{\partial z}{\partial \emptyset}+u\frac{\partial z}{\partial x}=D\nabla^2 z \quad (3\text{-}24)$$

Where z is mixture fraction, by applying the Reynolds decomposition, the transport equation (time-averaged) for the passive scalar is written as follows:

$$W\frac{\partial \bar{z}}{\partial r}+U\frac{\partial \bar{z}}{\partial x}+\frac{\partial \overline{uz}}{\partial x}+\frac{1}{r}\frac{\partial(r\overline{wz})}{\partial r}=D\nabla^2\bar{z} \quad (3\text{-}25)$$

In Equation 3-22 the passive scalar represents the diffusivity, however, to change the scalar to a different parameter such as temperature, then the thermal diffusivity α should replace the diffusivity D. Additionally, the equation is for constant density flows where the temperature varsity is very low, which makes the fluid flow not affected (Pope, 2000; Stetsyuk, 2014).

3.7 Computational Fluid Dynamics (CFD) steps

As has been explained in section 1.1, CFD is a numerical procedure employed to predicate fluid flow dynamics and some scientific processes such as “heat transfer, mass transfer, chemical reactions, and related phenomena” by solving governing scientific equalities (Bakker, 2002; Date, 2005).

Furthermore, the numerical algorithms applied in CFD codes to solve fluid flow phenomena with innovative results contain three main elements. These elements are outlined by (Ashgriz & Mostaghimi, 2002; Versteeg & Malalasekera, 2007) as follows:

3.7.1 Pre-Processor

The pre-processor step applies to define the boundary conditions, problem geometry, generate the grid and the flow parameter. This stage involves the input of the flow problem to a CFD program and the consequent transformation of this input into a type appropriate so that it can be used by the solver. The pre- processing stage can consist of several activities. For example, a description of the geometric zone of interest such as the computational domain. Furthermore, grid generation which includes the sub-division of the domain into a smaller number and non-overlapping sub domains such as grid of cells. Also, the pre-processing can include selection of the physical and chemical phenomena that require to be developed.

Additionally, the definition of fluid properties is one of the pre-processing activities. Finally, pre-processing activities includes specification of suitable boundary conditions at cells in which it overlaps with or touch the domain boundary.

Generally, the accuracy of CFD solution can rely upon the number of cells in which the higher the number of cells the better the solution accuracy. Interestingly, the solution of a flow problem such as velocity, pressure and temperature can be defined at nodes inside each cell. The accuracy of CFD solutions and its cost depend on the intricacy of the grid in terms of necessary computer hardware and calculation time. Additionally, it is considered that the best meshes should be non-homogeneous. However, efforts are devoted in order to develop CFD codes with a self-adaptive meshing ability.

3.7.2 Solver

The second CFD codes element is known as solver which consists of three numerical solution techniques: finite difference, finite element and spectral methods. In addition, the numerical algorithm solution can be highlighted to three steps: the first step refers to the integration of the governing equation of the fluid flow which can distinguish the finite volume from all other CFD techniques.

The second step of the numerical algorithm is called the discretisation technique which can covert the results of integral equations into algebraic equations. This technique is important in the process of key transport phenomena, convection and diffusion.

The final step is the solution of an algebraic equation by an iterative solution method. The iterative solution is required for the complex and non-linear algebraic equations. Furthermore, the most common procedure for these types of equations is by a method know as Tri-Diagonal Matrix Algorithm (TDMA).

3.7.3 Post-Processor

Post-processor employed to transfer and show the data/results in a graphical and simple and readable format. Interestingly, many processes are taking place in the post-processing field and because of the attractiveness of engineering workspaces, led to provide CFD packages with adaptable data visualization. These steps include domain geometry and grid display, vector plots, line and shaded contour plots, 2D and 3D surface plots, particle tracking, view manipulation translation, rotation, scaling etc. and colour PostScript output.

3.8 RANS Turbulence models

RANS turbulence models are mainly used to produce a solvable closed equation via utilising the Boussinesq eddy viscosity assumption within the mathematical equations for each different model. Moreover, turbulence modelling is a very complex process due to the fluctuations in the flow field in space, time, three dimensional, unsteady and consists of numerous scales. Therefore, a huge quantity of CFD investigation has focussed on methods that make use of turbulence models. Moreover, RANS turbulence models have been precisely developed for many decades to solve NS equations in affordable, inexpensive methods in order to explain the effects of turbulence without the need for very fine mesh and direct numerical simulation DNS. Generally, RANS models are categorized based on the number of extra transport equations that need to be resolved along with the RANS flow equations as shown in Table 3-2, while Table 3-3 shows the turbulence models classification (Woelke, 2007). The mathematical illustration of each model uses in this research area in the following sections (C. F. X. Ansys, 2010; Bakker, 2003; Cao, 2011; Versteeg & Malalasekera, 2007).

Table 3-2: RANS Models Classification. Re-Produced From (Versteeg & Malalasekera, 2007)

No. of extra transport equations	Model Name
Zero	Mixing length model
One	Spalart–Allmaras model
Two	k-ε Model
	k-ω Model
	Algebraic stress model
Seven	Reynolds stress model

Table 3-3: Categorization Of Turbulence Models. Re-Produced From (Woelke, 2007).

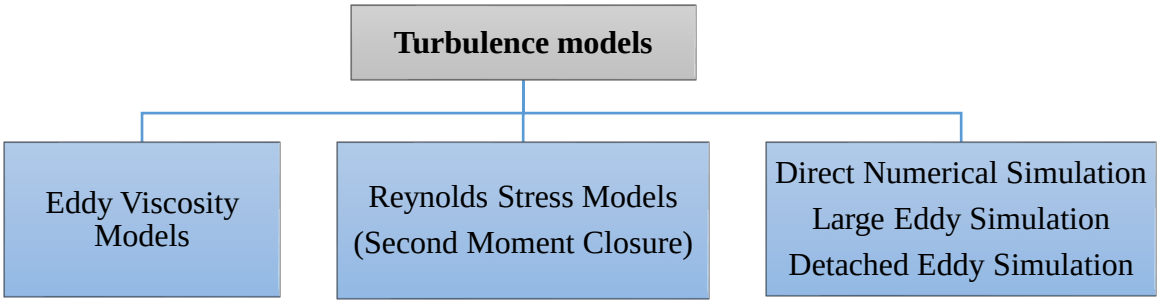

3.8.1 Eddy viscosity turbulence models

This method assumes that the Reynolds stresses are proportional to mean velocity gradients. This assumption is based on the small eddies that exist in the turbulence which are continuously forming and dissipating. In other words, the eddy viscosity hypothesis suggests that the eddy (turbulent) viscosity and velocity gradients are related to Reynolds stresses by the gradient diffusion theory. In laminar Newtonian flow, the relationship between the strain tensors and the stress is as follows:

$$-\rho\overline{u_i'u_j'} = \mu_t\left(\frac{\partial U_i}{\partial x_j}+\frac{\partial \mathrm{U_j}}{\partial x_i}\right)-\frac{2}{3}\,\delta_{ij}\left(\rho k+\mu_t\frac{\partial U_k}{\partial x_k}\right) \qquad (3\text{-}26)$$

Thus, Turbulent or eddy viscosity μ_t needs to be modelled. The eddy diffusivity (which declares that the mean scalar gradient is linearly related to the Reynolds fluxes of a scalar) hypothesis is similar to the eddy viscosity hypothesis:

$$-\rho\overline{u_i\varphi} = \Gamma_t\,\frac{\partial \Phi}{\partial x_i} \qquad (3\text{-}27)$$

Where Γ_t refer to eddy diffusivity which has to be specified, written as:

$$\Gamma_t = \frac{\mu_t}{Pr_t} \qquad (3\text{-}28)$$

In the above equation, Pr_t is the turbulent Prandtl number which is used to prescribe the eddy diffusivities. Moreover, when the turbulent viscosity is identified the previous equations can express the turbulent fluctuations in terms of functions of the mean variables. On the other hand, this variable has been used by k-ε and k-ω two-equations turbulence models as will be discussed in the next sections. According to the previous hypotheses, the Reynolds averaged momentum and scalar transport equations turn out to be:

$$\frac{\partial \rho U_i}{\partial t}+\frac{\partial}{\partial x_j}(\rho U_i U_j) = -\frac{\partial \acute{p}}{\partial x_i}+\frac{\partial}{\partial x_j}\left[\mu_{eff}\left(\frac{\partial U_i}{\partial x_j}+\frac{\partial U_j}{\partial x_i}\right)\right]+S_M \qquad (3\text{-}29)$$

In which, S_M is the sum of the body forces. Also, μ_{eff} is the effective viscosity and $\acute{p}$ is a modified pressure and they both specified as:

$$\mu_{eff} = \mu+\mu_t \qquad (3\text{-}30)$$

$$\acute{p} = p + \frac{2}{3}\rho k + \frac{2}{3}\mu_{eff}\frac{\partial U_k}{\partial x_k} \quad (3\text{-}31)$$

For incompressible fluids, the last term in Equation 3-31 is neglected in the ANSYS CFX programme due to the divergence of velocity. While the second term is depending on the expert parameter pressure value which holds many values depending on the specific situation. Thus, the final shape of Reynolds averaged transport equation for any variables for non-reacting scalars written as (C. F. X. Ansys, 2010; Bakker, 2003; Brian Edward Launder & Spalding, 1983; Versteeg & Malalasekera, 2007):

$$\frac{\partial \rho \Phi}{\partial t} + \frac{\partial}{\partial x_j}(\rho U_j \Phi) = \frac{\partial}{\partial x_j}\left[\left(\Gamma_\Phi + \frac{\mu_t}{\sigma_\Phi}\right)\frac{\partial \Phi}{\partial x_j}\right] + S_\Phi \quad (3\text{-}32)$$

I. Zero equation model

The zero-equation model has no additional transport equations to be determined and it identifies as the simplest version among RANS turbulence models. In addition, the eddy viscosity μ_t have a global value depending on the mean velocity and a geometric length scale by applying a practical formula. ANSYS CFX utilizes an algebraic equation of this model to compute the viscous contribution from turbulent eddies by calculating a constant turbulent eddy viscosity for the entire flow field. This model has not a lot of physical groundwork and is not advised for many types of research. Furthermore, Prandtl and Kolmogorov suggested that the turbulence viscosity is modelled as the result of a turbulence length l_t and a turbulent velocity scale U_t as follow:

$$\mu_t = \rho f_\mu U_t l_t \quad (3\text{-}33)$$

Where, f_μ is a proportionality constant equal to (0.01). The length scale l_t is obtained using the equation:

$$l_t = \left(V_D^{\frac{1}{3}}\right)/7 \quad (3\text{-}34)$$

In the Equation 3-34, V_D is the fluid domain volume (C. F. X. Ansys, 2010; Bakker, 2003; Brian Edward Launder & Spalding, 1983; Versteeg & Malalasekera, 2007).

II. Two equation turbulence models

These types of RANS turbulence models are offering a great agreement between computational accuracy and numerical effort which make them very popular nowadays. The term 'two-equation' refers to employing two separate transport equations for the velocity and length scale in the solving process, which make it more advanced than the zero equation models. The procedure of two-equation models is represented by computing the turbulence velocity scale the turbulent kinetic energy, which is supplied from the solution of its transport equation. Furthermore, turbulent kinetic energy and its dissipation rate are normally used to approximate the turbulent length scale. However, the solution of the dissipation rate transport equation provides the value of the turbulent kinetic energy. The following models are the most common versions of RANS turbulence models (C. F. X. Ansys, 2010; Bakker, 2003; Brian Edward Launder & Spalding, 1983; Versteeg & Malalasekera, 2007).

A. Standard k-epsilon model k-ε

(Brian Edward Launder & Spalding, 1983) proposed the Standard k-epsilon model, which is built on two transport equations, namely turbulence kinetic energy k equation which defined as the variance of the fluctuations in velocity and based on the exact equation and its dissipation rate ε equation known as the ratio whereon the variations of velocity are disperse and based on physical analysis. Moreover, this model is appropriate for practical engineering flow calculations because of the ability to utilize the slant diffusion assumption to convey the Reynolds stresses to the turbulent viscosity as well as mean velocity rises. The mathematical equation of the model introduces two new variables into the system. Thus, the momentum and continuity equations are (C. F. X. Ansys, 2010; Versteeg & Malalasekera, 2007):

$$\frac{\partial \rho}{\partial t} + \frac{\partial (\rho . U_j)}{\partial x_j} = 0 \tag{3-35}$$

$$\frac{\partial \rho U_i}{\partial t} + \frac{\partial}{\partial x_j}(\rho U_i U_j) = -\frac{\partial \acute{p}}{\partial x_i} + \frac{\partial}{\partial x_j}\left[\mu_{eff}\left(\frac{\partial U_i}{\partial x_j} + \frac{\partial U_j}{\partial x_i}\right)\right] + S_M \tag{3-36}$$

However, turbulence kinetic energy and dissipation rate are linked with the turbulence viscosity as shown:

$$\mu_t = C_\mu \, \rho \, \frac{K^2}{\varepsilon} \tag{3-37}$$

Where: C_μ is a turbulence model constant that is equal to 0.09. Besides, k and ε values are determined precisely from the differential transport equations for the turbulence kinetic energy and turbulence dissipation rate as follows:

$$\frac{\partial\,(\rho k)}{\partial t}+\frac{\partial}{\partial x_j}(\rho U_j k)=\frac{\partial}{\partial x_j}\left[\left(\mu+\frac{\mu_t}{\sigma_k}\right)\frac{\partial\,k}{\partial x_j}\right]+P_k+\rho\varepsilon+P_{kb} \tag{3-38}$$

$$\frac{\partial\,(\rho\varepsilon)}{\partial t}+\frac{\partial}{\partial x_j}(\rho U_j \varepsilon)=\frac{\partial}{\partial x_j}\left[\left(\mu+\frac{\mu_t}{\sigma_\varepsilon}\right)\frac{\partial\,\varepsilon}{\partial x_j}\right]+\frac{\varepsilon}{k}(C_{\varepsilon 1}P_k-C_{\varepsilon 2}\rho\varepsilon+C_{\varepsilon 1}P_{\varepsilon b}) \tag{3-39}$$

The first term ($\frac{\partial\,(\rho\varepsilon)}{\partial t}$) in Eq. 3-39 refer to the rate of change of k or ε, and $\frac{\partial}{\partial x_j}(\rho U_j \varepsilon)$ is the Transport of k or ε by convection. In addition, the Transport of k or ε by diffusion is written as $\frac{\partial}{\partial x_j}\left[\left(\mu+\frac{\mu_t}{\sigma_\varepsilon}\right)\frac{\partial\,\varepsilon}{\partial x_j}\right]$ and the rate of production/ destruction is indicated by $\frac{\varepsilon}{k}(C_{\varepsilon 1}P_k-C_{\varepsilon 2}\rho\varepsilon+C_{\varepsilon 1}P_{\varepsilon b})$.

Hence, $C_{\varepsilon 1}$, $C_{\varepsilon 2}$, σ_k and σ_ε are turbulence model constant, their values are 1.44, 1.92, 1.0 and 1.3, respectively. Additionally, the influence of the buoyancy forces is symbolled as P_{kb} and $P_{\varepsilon b}$. However, the turbulence creation due to viscous forces is shorted as P_k as showing in the below equation:

$$P_k=\mu_t\left(\frac{\partial U_i}{\partial x_j}+\frac{\partial \mathrm{U_j}}{\partial x_i}\right)\frac{\partial U_i}{\partial x_j}-\frac{2}{3}\frac{\partial U_k}{\partial x_k}\left(3\mu_t\frac{\partial U_k}{\partial x_k}+\rho k\right) \tag{3-40}$$

Finally, $\partial U_k/\partial x_k$ can be discarded for incompressible fluid flow because of the small value. Therefore, it is unable to significantly contribute to the production. However, it has a large value for compressible fluid flow in areas with high-velocity divergences, such as at shocks (C. F. X. Ansys, 2010; Versteeg & Malalasekera, 2007).

B. RNG *k*-epsilon model

The RNG k-ε model shares the same transport equations for turbulent kinetic energy and dissipation rate as the standard k-ε model, and it is established on the renormalization group study of the Navier-Stokes equations to examine the low Reynolds number. However, the major difference between the two models is the model constants as shown below equations:

$$\begin{aligned}&\frac{\partial\,(\rho\varepsilon)}{\partial t}+\frac{\partial}{\partial x_j}(\rho U_j \varepsilon)\\&=\frac{\partial}{\partial x_j}\left[\left(\mu+\frac{\mu_t}{\sigma_{\varepsilon\,RNG}}\right)\frac{\partial\,\varepsilon}{\partial x_j}\right]+\frac{\varepsilon}{k}(C_{\varepsilon 1\,RNG}P_k-C_{\varepsilon 2\,RNG}\rho\varepsilon+C_{\varepsilon 1\,RNG}P_{\varepsilon b})\end{aligned} \tag{3-41}$$

Where:

$$C_{\varepsilon 1\,RNG} = 1.42 - f_{\eta} \tag{3-42}$$

Also, $C_{\varepsilon 2\,RNG}$ is equal to (1.68), $\sigma_{\varepsilon\,RNG}$ = 0.7179. And:

$$f_{\eta} = \frac{\eta\left(1 - \frac{\eta}{4.38}\right)}{(1 + \beta_{RNG}\,\eta^{3})} \tag{3-43}$$

$$\eta = \sqrt{\frac{P_k}{\rho C_{\mu\,RNG} \in}} \tag{3-44}$$

Where: f_{η} is the turbulence model coefficient, β_{RNG} is the turbulence model constant 0.012 (C. F. X. Ansys, 2010; Versteeg & Malalasekera, 2007).

C. Realizable *k*-epsilon model

Realizable $k - \varepsilon$ models are another version of $k - \varepsilon$ model which has the same transports equations. However, the process of calculating turbulent viscosity is different as it solves the eddy viscosity as a function of the turbulent dissipation rate and turbulent kinetic energy as in Equation 3-37, the model's equations are as follows (Shih et al., 1995):

The turbulent kinetic energy equation and its dissipation rate:

$$\frac{\partial k}{\partial t} + U_j \frac{\partial k}{\partial x_j} = \tau ij \frac{\partial U_i}{\partial x_j} - \varepsilon + \frac{\partial}{\partial x_j}\left[(v + v_T/\sigma_k)\frac{\partial k}{\partial x_j}\right] \tag{3-45}$$

$$\frac{\partial \varepsilon}{\partial t} + U_j \frac{\partial \varepsilon}{\partial x_j} = C_{\varepsilon 1}\frac{\varepsilon}{k}\tau ij \frac{\partial U_i}{\partial x_j} - C_{\varepsilon 2}\frac{\varepsilon^{2}}{k} + \frac{\partial}{\partial x_j}\left[(v + v_T/\sigma_{\varepsilon})\frac{\partial \varepsilon}{\partial x_j}\right] \tag{3-46}$$

Relevant closure coefficients and relations are provided by:

$$C_{\mu} = \frac{1}{A_o + A_s U^{*}\frac{k}{\varepsilon}} \tag{3-47}$$

Where C_{μ} is constant in k−ε model. But:

$$A_o = 4.04,\ A_s = \sqrt{6}\cos\vartheta,\ \vartheta = \left(\frac{1}{3}\right)\cos^{-1}(\sqrt{6}\,W)\ ,$$

$$W = \frac{S_{ij}S_{jl}S_{ik}}{\tilde{S}},\ \tilde{S} = \sqrt{S_{ij}S_{ij}}$$

$C_{\varepsilon 1}$= max (0.43 , $\frac{\eta}{\eta+5}$) , $C_{\varepsilon 2}$ =1.9, σ_k=1.0, σ_{ε}=1.2 and $\eta = \frac{Sk}{\varepsilon}$

$$U^* \equiv \sqrt{S_{ij}S_{ij+}\widetilde{\Omega}_{ij}\widetilde{\Omega}_{ij}} \tag{3-48}$$

$$\tilde{\Omega}_{ij} = \bar{\Omega}_{ij} - \varepsilon ijk\ \omega k \tag{3-49}$$

where $\overline{\Omega}_{ij}$ is the mean rate-of-rotation tensor in a moving reference frame with an angular velocity ω_k.

D. *k*-omega model

(Wilcox, 1998) suggested the k-ω turbulence model as another two-equation RANS turbulence model. Furthermore, the main advantage of the model is the near-wall processing for low-Reynolds number computations, and it does not need the complex nonlinear damping functions as the $k-\varepsilon$ model. Therefore, this model has better accuracy and more robust results than the $k-\varepsilon$ model which needs at least near-wall resolution $y^+ < 0.2$ while for k-ω model needs at least near-wall resolution $y^+ < 2$ for low Reynolds number. In this model, it's been assumed that the turbulence viscosity is related to the turbulence kinetic energy and turbulent frequency by relation (C. F. X. Ansys, 2010; Versteeg & Malalasekera, 2007):

$$\mu_t = \rho\ \frac{k}{\omega} \tag{3-50}$$

Moreover, the model's transport equations for the turbulent kinetic energy k and turbulent frequency ω is as follow:

$$\frac{\partial\ (\rho k)}{\partial t} + \frac{\partial}{\partial x_j}(\rho U_j k) = \frac{\partial}{\partial x_j}\left[\left(\mu + \frac{\mu_t}{\sigma_k}\right)\frac{\partial\ k}{\partial x_j}\right] + P_k + \acute{\beta}\rho k\omega + P_{kb} \tag{3-51}$$

$$\frac{\partial\ (\rho\omega)}{\partial t} + \frac{\partial}{\partial x_j}(\rho U_j \omega) = \frac{\partial}{\partial x_j}\left[\left(\mu + \frac{\mu_t}{\sigma_\omega}\right)\frac{\partial\ \omega}{\partial x_j}\right] + \alpha\frac{\omega}{k}P_k - \beta\rho\omega^2 + P_{\omega b} \tag{3-52}$$

The model's constants are: $\acute{\beta}$ = 0.09, β = 0.075, α = 5/9, σ_k = 2 and σ_ω = 2

E. Shear-stress transport (SST) model

The Shear-Stress Transport (SST) model is a modified version of the k-ω model which provides very accurate predictions of the onset and the quantity of flow separation beneath adverse pressure gradients. Also, the turbulent eddy viscosity in the standard form of the k-ω model is showed in Equation 3-50. However, for the (SST) k - ω model is:

$$\mu_t = \frac{\rho\alpha_1 k}{max(\alpha_1\omega, SF_2)} \tag{3-53}$$

Moreover, the model's transport equations for the turbulent kinetic energy k and turbulent dissipation rate is as follows:

$$\frac{\partial k}{\partial t} + U_j \frac{\partial k}{\partial x_j} = P_k - \beta^* k\omega + \frac{\partial}{\partial x_j}\left[(v + v_T/\sigma_k)\frac{\partial k}{\partial x_j}\right] \tag{3-54}$$

$$\frac{\partial \omega}{\partial t} + U_j \frac{\partial \varepsilon}{\partial x_j} = \alpha S^2 - \beta\omega^2 + \frac{\partial}{\partial x_j}\left[(v + v_T/\sigma_\omega)\frac{\partial \varepsilon}{\partial x_j}\right] + 1(1 - F_1)\sigma_{\omega 2}\frac{1}{\omega}\frac{\partial k}{\partial x_j}\frac{\partial \omega}{\partial x_i} \tag{3-55}$$

Plus, the relevant closure coefficients and relations are given by:

$$F_2 = tanh\left[max\left(\frac{2\sqrt{k}}{\beta^*\omega y}, \frac{500v}{y^2\omega}\right)^2\right] \tag{3-56}$$

$$P_k = min\left(\tau ij \frac{\partial U_i}{\partial x_j}, 10\,\beta^* k\,\omega\right) \tag{3-57}$$

$$F_1 = tanh\left\{min\left[max\left(\frac{\sqrt{k}}{\beta^*\omega y}, \frac{500v}{y^2\omega}\right), \frac{4\,\sigma_{\omega 2}\,k}{CD_{kw}y^2}\right]^4\right\} \tag{3-58}$$

$$CD_{kw} = max\left(2\,\rho\sigma_{\omega 2}\,\frac{1}{\omega}\frac{\partial k}{\partial x_j}\frac{\partial \omega}{\partial x_i}, 10^{-20}\right) \tag{3-59}$$

3.8.2 Reynolds stress turbulence models

Reynolds Stress Equation Model (RSM) which is also called the second-order or second-moment closure model does not rely on the eddy viscosity hypothesis. Nevertheless, RSM closes the Reynolds-averaged Navier-Stokes equations via computing the transport equations for all the individual stress components of the Reynolds stress tensor and the dissipation rate in the fluid. Although, Algebraic Reynolds stress model computes algebraic equations for the Reynolds stresses terms the differential Reynolds stress models calculate differential transport equations independently for each Reynolds stress component. On the other side, RSM implemented scale equations of ω or ε which led to inherent weaknesses resulting from the basic hypotheses in these equations, but the results outstanding the simpler models in all cases of flows. In contrast, a general drawback of the two-equations models, such as the $k - \varepsilon$ model, are the efforts to calculate flows with significant body forces or complex strain fields. In this instance, RSM shows that they are superior to two-equation models.

Nerveless, RSM is used to model the exact production term and the inherent modelling of stress anisotropies of the flow features. Therefore, RSM is considered as the finest RANS approach along with it being better equipped to give accurate predictions to model many fluids flow phenomena such as swirling flows, cyclone flows, rotating flow passages and complex flows. Moreover, modelling of the pressure-strain and dissipation-rate terms is exceptionally difficult and frequently considered to be accountable for compromising the accuracy of RSM calculations. But the reliability of RSM predictions is restricted by the closure hypothesis utilized to model several terms in the transport equations for the Reynolds stresses.

The Reynolds averaged momentum equations for the mean velocity are derived by taking moments of the exact momentum equation as follow (C. F. X. Ansys, 2010; Gibson & Launder, 1978; Brian E Launder, 1989; Brian Edward Launder et al., 1975; Versteeg & Malalasekera, 2007):

$$\frac{\partial \rho U_i}{\partial t} + \frac{\partial}{\partial x_j}(\rho U_i U_j) - \frac{\partial}{\partial x_j}\left[\mu\left(\frac{\partial U_i}{\partial x_j} + \frac{\partial U_j}{\partial x_i}\right)\right] = -\frac{\partial \acute{p}}{\partial x_i} - \frac{\partial}{\partial x_j}(\rho\overline{u_i' u_j'}) + S_{Mi} \quad (3\text{-}60)$$

Where, $\acute{p}$ refers to modified pressure - which has no turbulence contribution and is related to the static (thermodynamic) pressure as in the below equation - S_{Mi} is the sum of body forces and $\rho\overline{u_i' u_j'}$ is the fluctuating Reynolds stress contribution.

$$\acute{p} = p + \frac{2}{3}\mu\frac{\partial U_k}{\partial x_k} \quad (3\text{-}61)$$

Also, $\rho\overline{u_i' u_j'}$ is known as the differential stress model which is used to satisfy a transport equation. However, another transport equation should compute for every one of the six Reynolds stress components of $\rho\overline{u_i' u_j'}$ as shown below:

$$\frac{\partial \rho\overline{u_i' u_j'}}{\partial t} + \frac{\partial}{\partial x_k}(U_k \rho\overline{u_i' u_j'}) - \frac{\partial}{\partial x_k}\left[\left(\delta_{kl\mu} + \rho C_s \frac{k}{\varepsilon}\overline{u_k u_l}\right)\frac{\partial \overline{u_\iota u_j}}{\partial x_l}\right] = P_{ij} - \frac{2}{3}\delta_{ij}\rho\varepsilon + \Phi_{ij} + P_{ij,b} \quad (3\text{-}62)$$

Where, Φ_{ij} is the pressure-strain tensor (correlation), C is constant, $P_{ij,b}$ and P_{ij} are buoyancy turbulence term and shear production of the Reynolds stresses, respectively.

I. The Standard Reynolds Stress Model

The Standard Reynolds Stress Model SRSM uses in the ANSYS CFX programme is originated from the ε-equation as shown below (C. F. X. Ansys, 2010):

$$\frac{\partial \rho \overline{u_\iota u_J}}{\partial t} + \frac{\partial}{\partial x_k}\left(U_k \rho \overline{u_\iota u_J}\right) - \frac{\partial}{\partial x_k}\left[\left(\mu + \frac{2}{3}\rho C_s \frac{k^2}{\varepsilon}\right)\frac{\partial \overline{u_\iota u_J}}{\partial x_k}\right] = P_{ij} - \frac{2}{3}\delta_{ij}\rho\varepsilon + \Phi_{ij} + P_{ij,b} \tag{3-63}$$

$$P_{ij} = -\rho\overline{u_\iota u_k}\frac{\partial U_j}{\partial x_k} - \rho\overline{u_J u_k}\frac{\partial U_i}{\partial x_k} \tag{3-64}$$

$$P_{ij,b} = B_{ij} - C_{buo}\left(B_{ij} - \frac{1}{3}B_{kk}\delta_{ij}\right) \tag{3-65}$$

Moreover, the buoyancy contribution is characterised by the second term of the pressure strain equation. Besides, B_{ij} is written as:

$$B_{ij} = \mathrm{g}_i b_j - \mathrm{g}_j b_i \tag{3-66}$$

Here, b_i is modelled only when the Boussinesq buoyancy is applied, where:

$$b_i = -\frac{\mu_t}{\sigma_\rho}\beta\frac{\partial T}{\partial x_i} \tag{3-67}$$

The thermal expansion coefficient is noted as β. For the complete buoyancy model, which is established on density differences, b_i is written as:

$$b_i = -\frac{\mu_t}{\rho\sigma_\rho}\frac{\partial \rho}{\partial x_i} \tag{3-68}$$

And the equation for the ε is:

$$\frac{\partial(\rho\varepsilon)}{\partial t} + \frac{\partial}{\partial x_k}(\rho\varepsilon U_k) = \frac{\varepsilon}{k}(C_{\varepsilon 1}P_k - C_{\varepsilon 2}\rho\varepsilon + C_{\varepsilon 1}\rho_{\varepsilon b}) + \frac{\partial}{\partial x_k}\left[\left(\mu + \frac{\mu_t}{\sigma_{\varepsilon RS}}\right)\frac{\partial \varepsilon}{\partial x_k}\right] \tag{3-69}$$

In the above equations, the isotropic formulation has replaced the anisotropic diffusion coefficients of the authentic models, which raises the strength of the Reynolds stress model.

Besides, with anisotropic diffusion coefficients exist in the Reynolds Stress model, the equations for the transport of the Reynolds stresses are:

$$\frac{\partial \rho \overline{u_i u_j}}{\partial t} + \frac{\partial}{\partial x_k}\left(U_k \rho \overline{u_i u_j}\right) - \frac{\partial}{\partial x_k}\left[\left(\delta_{kl\mu} + \rho C_s \frac{k}{\varepsilon}\overline{u_l u_k}\right)\frac{\partial \overline{u_i u_j}}{\partial x_l}\right] = P_{ij} - \frac{2}{3}\delta_{ij}\rho\varepsilon + \Phi_{ij} + P_{ij,b} \tag{3-70}$$

the Boussinesq approximation modelling is depending on the production due to buoyancy. Therefore:

$$b_i = C_s \rho \beta \frac{k}{\varepsilon \sigma_\rho}\overline{u_l u_k}\frac{\partial T}{\partial x_k} \tag{3-71}$$

For the full buoyancy model, which is established on density differences, b_i is written as:

$$b_i = C_s \frac{k}{\varepsilon \sigma_\rho}\overline{u_l u_k}\frac{\partial \rho}{\partial x_k} \tag{3-72}$$

Finally, the equation of the ε is written:

$$\frac{\partial(\rho\varepsilon)}{\partial t} + \frac{\partial}{\partial x_k}\left(\rho\varepsilon U_k\right) = \frac{\varepsilon}{k}\left(C_{\varepsilon 1}P_k - C_{\varepsilon 2}\rho\varepsilon + C_{\varepsilon 1}\rho_{\varepsilon b}\right) + \frac{\partial}{\partial x_k}\left[\left(\mu\delta_{kl} + C_\varepsilon \rho \frac{k}{\varepsilon}\overline{u_l u_k}\right)\frac{\partial \varepsilon}{\partial x_l}\right] \tag{3-73}$$

Generally, the Standard Reynolds Stress Model have three sub-model versions based on the ε-equation and the pressure-strain correlation Φ_{ij} as shown in Table 3-4. The pressure strain is defined as the reason to lead the turbulence towards an isotropic state through reallocating the Reynolds stresses terms. Furthermore, the pressure strain equation can be written as:

$$\Phi_{ij} = \Phi_{ij,1} + \Phi_{ij,2} \tag{3-74}$$

Where, $\Phi_{ij,1}$ called the return-to-isotropy term or the slow term, and $\Phi_{ij,2}$ is called the rapid term.

Table 3-4: Classification Of Standard Reynolds Stress Turbulence Models

Standard Reynolds Stress Sub-Model	Reynolds Stress Model - LRR-IP
	QI Reynolds Stress Model - LRR-IQ
	SSG Reynolds Stress Model - SSG

Remarkably, the first two sub-models in Table 3-4 Reynolds Stress Model - LRR-IP, QI Reynolds Stress Model - LRR-IQ have been established by (Brian Edward Launder et al., 1975) and the pressure-strain relationship is linear in both models. Also, IP refers to Isotropizatio of Production while QI refers to Quasi-Isotropic. Alternatively, SSG Reynolds Stress Model has been developed by (Speziale et al., 1991) and it utilizes a quadratic relation for the pressure strain equation.

Overall, the pressure-strain correlations have a general form that compares among the three models. This form is based on:

- The anisotropy tensor a_{ij}
- Vorticity tensor Ω_{ij}
- Mean strain rate tensor S_{ij}

The general equation is:

$$\Phi_{ij,1} = -\rho\varepsilon\left[C_{s1}a_{ij} + C_{s2}\left(a_{ik}a_{kj} - \frac{1}{3}a_{mn}a_{mn}\delta_{ij}\right)\right] \tag{3-75}$$

$$\begin{aligned}\Phi_{ij,2} = {} & -C_{r1}Pa_{ij} + C_{r2}\rho kS_{ij} - C_{r3}\rho kS_{ij}\sqrt{a_{mn}a_{mn}} \\ & + C_{r4}\rho k\left(a_{ik}S_{jk} + a_{jk}S_{ik} - \frac{2}{3}a_{kl}S_{kl}\delta_{ij}\right) \\ & + C_{r5}\rho k\left(a_{ik}\Omega_{jk} + a_{jk}\Omega_{ik}\right)\end{aligned} \tag{3-76}$$

And:

$$a_{ij} = \frac{\overline{u_i u_j}}{k} - \frac{2}{3}\delta_{ij} \tag{3-77}$$

$$S_{ij} = \frac{1}{2}\left(\frac{\partial U_i}{\partial x_j} + \frac{\partial U_j}{\partial x_i}\right) \tag{3-78}$$

$$\Omega_{ij} = \frac{1}{2}\left(\frac{\partial U_i}{\partial x_j} + \frac{\partial U_j}{\partial x_i}\right) \tag{3-79}$$

This form can be used to model quadratic correlations and linear correlations by using suitable values of the constants. Each one of these models has different constants values implemented in Equations 3-71 to 3-79 as shown in Table 3-5 below (C. F. X. Ansys, 2010).

Table 3-5: Standard Reynolds Stress Sub-Models Constants

Model	Constants														
	$C_{\mu RS}$	$\sigma_{\varepsilon RS}$	C_S	C_ε	$C_{\varepsilon 1}$	$C_{\varepsilon 2}$	C_{s1}	C_{s2}	C_{r1}	C_{r2}	C_{r3}	C_{r4}	C_{r5}	σ_ρ	σ_ρ*
LRR-IP	0.1152	1.10	0.22	0.18	1.45	1.9	1.8	0.0	0.0	0.8	0.0	0.6	0.6	0.9	1.0
LRR-IQ	0.1152	1.10	0.22	0.18	1.45	1.9	1.8	0.0	0.0	0.8	0.0	0.873	0.665	0.9	1.0
SSG	0.1	1.36	0.22	0.18	1.45	1.83	1.7	-1.05	0.9	0.8	0.65	0.625	0.2	2/3	1.0

σ_ρ Refer to equation 3-71.

σ_ρ* Refer to equation 3-72.

II. Omega-Based Reynolds Stress Models

Omega-Reynolds Stress Model (SMC-ω) is based on ω equation which gives more accurate results, near-wall treatment, and it provides an automatic adjustment from a wall function to a low-Reynolds number formulation depending on the grid spacing. On the other hand, Omega Reynolds Stress and Baseline (BSL) Reynolds Stress models are the most known sub-models of Reynolds Stress SMC-ω Model provided in the CFX-ANSYS programme. Also, the modelled equations for the Reynolds stresses written as follows:

$$\frac{\partial \rho \overline{u_\imath u_j}}{\partial t} + \frac{\partial}{\partial x_k}\left(U_k \rho \overline{u_\imath u_j}\right) = P_{ij} - \frac{2}{3}\acute{\beta}\rho\omega k\delta_{ij} + \Phi_{ij} + P_{ij,b} - \frac{\partial}{\partial x_k}\left[\left(\mu + \frac{\mu_t}{\sigma_k}\right)\frac{\partial \overline{u_\imath u_j}}{\partial x_k}\right] \quad (3\text{-}80)$$

In addition, the buoyancy production σ_k can be modelled in the same way as in the previous Equations 3-71 and 3-72 with the same values for both equations based on density differences hypotheses (C. F. X. Ansys, 2010).

A. The Omega Reynolds Stress Model

The Omega Reynolds Stress Model based on the following equation for omega ω:

$$\frac{\partial\,(\rho\omega)}{\partial t} + \frac{\partial(U_k\rho\omega)}{\partial x_k} = \alpha\rho\frac{\omega}{k}P_k - \beta\rho\omega^2 + P_{\omega b} + \frac{\partial}{\partial x_k}\left[\left(\mu + \frac{\mu_t}{\sigma}\right)\frac{\partial\,\omega}{\partial x_k}\right] \quad (3\text{-}81)$$

The coefficients are: $\sigma = 2, \sigma^* = 2, \beta = 0.075$ and

$$\alpha = \frac{\beta}{\acute{\beta}} - \frac{k^2}{\sigma(\acute{\beta})^{0.5}} = \frac{5}{9} \quad (3\text{-}82)$$

B. The BSL Reynolds Stress Model

BSL Reynolds Stress Model is based on the following equation for omega ω:

$$\frac{\partial(\rho\omega)}{\partial t} + \partial(U_k\rho\omega) = \alpha_3\frac{\omega}{k}P_k + P_{\omega b} - \beta_3\rho\omega^2 + \frac{\partial}{\partial x_k}\left[\left(\mu + \frac{\mu_t}{\sigma_{\omega 3}}\right)\frac{\partial\,\omega}{\partial x_k}\right] + (1-F_1)2\rho\frac{1}{\sigma_2\omega}\frac{\partial k}{\partial x_k}\frac{\partial\omega}{\partial x_k} \quad (3\text{-}83)$$

The coefficients for set 1 (SMC- $\omega\ zone$) are: $\sigma_1 = 2, {\sigma_1}^* = 2, \beta = 0.075$ and

$$\alpha_1 = \frac{\beta}{\acute{\beta}} - \frac{k^2}{\sigma(\acute{\beta})^{0.5}} = 0.553 \quad (3\text{-}84)$$

Where: k known as the von Karamn constant with a value of 0.41. And β related to the $k-\omega$ model Equation 3-52.

The coefficients for set 2 (SMC- $\varepsilon\ zone$) are: $\sigma_2 = 0.856, {\sigma_1}^* = 1.0,\ \beta_2 = 0.0828$ and

$$\alpha_2 = \frac{\beta}{\acute{\beta}} - \frac{k^2}{\sigma(\acute{\beta})^{0.5}} = 0.44 \quad (3\text{-}85)$$

Contrariwise, a smooth linear interpolation has been used to blend the coefficients with the similar bulk function F , therfore Eq 3-83:

$$\varphi_3 = F.\varphi_3 + (1-F)\varphi_2 \quad (3\text{-}86)$$

Where:
$$F = \tanh(arg^4) \quad (3\text{-}87)$$

$$arg = min\left\{max\left(\frac{\sqrt{k}}{\acute{\beta}\omega y}, \frac{500\,\upsilon}{y^2\omega}\right), \frac{4\rho k}{CD_{k\omega}\sigma_{k-\varepsilon}y^2}\right\} \quad (3\text{-}88)$$

And:

$$CD_{k\omega} = max\left(2\rho\frac{1}{\sigma_{k-\varepsilon}\omega}\frac{\partial k}{\partial x_j}\frac{\partial\omega}{\partial x_j}, 10^{-10}\right) \quad (3\text{-}89)$$

3.9 Turbulence models limitations

This section includes the limitations of each turbulence model that will be used in this research. Generally, all the models have limitation depending on a variety of reasons such as the type of physical phenomena, swirling/ non-swirling flow, steady/ unsteady flow, turbulent/ laminar flow, sluggish regions in flows and the existence of curvatures in the flow streamline. However, each turblence model have different drawbacks form due to the method of solving any phenomena i.e. every model have a certain type of mathmetical approach. Therefore, the details of each model limitations are showing in Table 3-6 (I. Ansys, 2011; CFX, 2018; Wasserman, 2016):

Table 3-6: Turbulence Models Limitations

Turbulence Model	Limitations
Spalart–Allmaras	• One equation model i.e., one equation to predict the turbulence behaviour • Turbulence length and time scales are not clearly identified • Poor prediction of free shear flows, 3D flows, decaying turbulence • Inability to perform under predicting separation e.g., flows with great separation
Standard *k*-*ε*	• Poor predication of complicated flow e.g.: ❖ Sharp pressure gradient ❖ Separation flows ❖ Large streamline curvature ❖ Jet flows such as swirling jet flow • Low accuracy for no-slip walls conditions
RNG *k*-*ε*	• Poor predication of complicated flow e.g.: ❖ Sharp pressure gradient ❖ Jet flows such as swirling jet flow • Low accuracy for near wall conditions
Shear Stresses SST	• Difficult to convergence • Initial conditions have a great effect on the solving process • Poor predications of rotating flow e.g., swirling flows
RSM	• Initial conditions have a great effect on the solving process • High quality mesh is required i.e., very fine mesh • Long time of each simulation • High computational expenses i.e., large computing memory and CPU
Omega-RS	• Difficult to convergence • Initial conditions have a great effect on the solving process

3.10 Numerical errors and uncertainty

CFD applications are fastly growing and developing since the 1990s due to the advantages of CFD which have been recognised by many significant organizations and corporations that use it to design/develop environments across a large range of industries. Therefore, the results of the CFD modelling are very important as it may cause wrong decisions to occur, which costs losses in both money and time. Moreover, knowing the relation between the solutions, errors, and properties is highly studied by many researchers. For instance, (Schäfer, 2006) indicates these relations as shown in Figure 3-6 to reduce the error and increase the awareness of the model's designers.

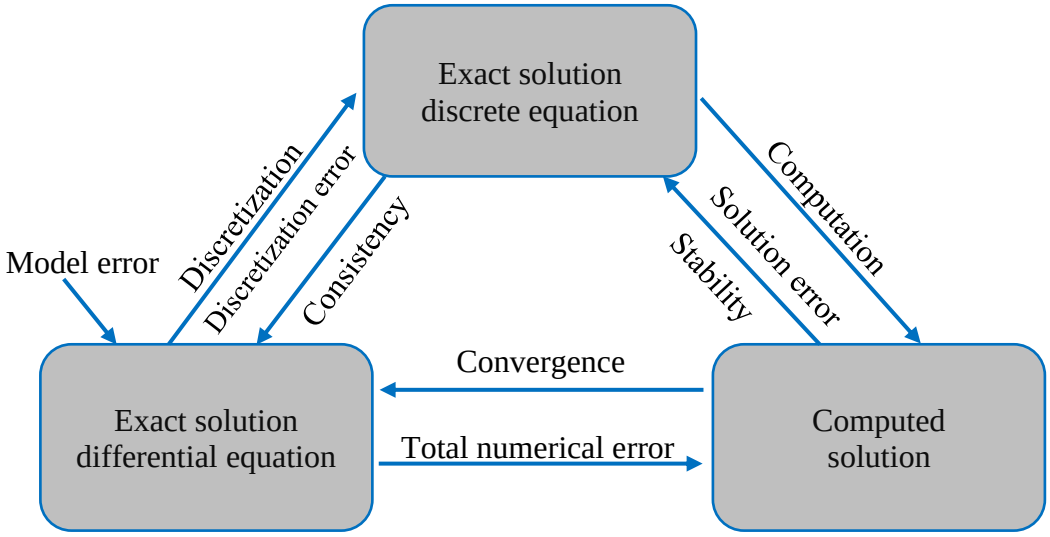

Figure 3-6: Relation Between Solutions, Errors, And Properties. Re-Produced From (Schäfer, 2006).

Furthermore, (Versteeg & Malalasekera, 2007) define much-accepted error and uncertainty which has been commonly used by many academic/industries companies, as follows:

- **Error:** a noticeable lack in a CFD model that is not associated with the absence of knowledge as follows:

  - ❖ Numerical errors: convergence iterative errors, discretisation errors, roundoff errors.
  - ❖ Coding errors: fault in the computer software.
  - ❖ User errors: human errors through the wrong use of the software program.

- **Uncertainty:** a possible lack in a CFD models that is produced by the absence of knowledge as follows:

- ❖ Input uncertainty: imprecision caused by limited information or estimated interpretation of geometry, boundary conditions or material properties.
- ❖ Physical model uncertainty: imprecision between actual flows and CFD caused by the inappropriate definition of physical or chemical processes e.g., turbulence or caused by the simplifying hypotheses in the modelling approach e.g., incompressible flow, steady flow.

Therefore, errors and uncertainty have a certain aspect of CFD modelling, it is essential to develop precise methods to improve the amount of confidence in its outcomes. In this context, the following methods are accomplished:

1. **Verification:** knowing as 'solving the equations right', the main use of this process is to compute the errors. It can be described as the process of clarifying that a model operation accurately defines the user's theoretical description of the model and the solution to the model.

2. **Validation:** knowing as 'solving the right equations', the main use of this process is to compute the uncertainty. It can be described as the process of evaluation of the precision of the model description of the real world from the viewpoint of the intended uses of the model.

These fundamentals will be the footing for the research started in subsequent chapters. Particularly, validation will be conducted by applying experimental data and numerical errors will be reduced by using suitable preferences.

Chapter 4 VALIDATION STUDY (PLANAR JET NUMERICAL MODELLING)

4.1 Planar jet first case study

The first case study has been theoretically explained in section 2.2.2 and numerically examined as in section 2.2.3. The experiment is based on the work done by (D. Dowling & Dimotakis, 1988; D. R. Dowling, 1988; D. R. Dowling & Dimotakis, 1990) to study and explore several fluid features in a planar jet flow. The experiment was based to investigate the mixing procedure features such as similarity of the turbulent concentration fields of a gas fluid flow in a momentum-driven round turbulent jet flow in a co-flow system. Alternatively, a numerical study has been published via using a direct numerical simulation DNS method to explore the passive scalar mixing in the above experiment and to approve the modelling ability of the mentioned method, more details can be seen in section 2.2.3 (Lubbers et al., 2001).

Therefore, next related sections will carry out the implantation process of converting the experiment lab system into RANS numerical modelling via using Workbench 2018, 2019 R1 ANSYS-CFX simulation programme.

4.1.1 Computational domain

The experiments domain as shown in Figure 4-1 which is showing the dimensions 2.3m x 1.2m and the gas phase jet mixing system. On the other hand, total volume of the enclosure system is about $3.4m^3$, the vertical gas phase is produced from a 0.02m jet nozzle along with a11 to 1 reduction ratio while the exit turbulence level is below 0.2%. The uniform co-flow gas velocity is 0.006 of the main jet velocities. The main gas flow is Ethylene C_2H_4 and have a velocity of 4.04m/s while the flow rate is having a single-stage mechanism and a metering valve. Moreover, the uniform cow-flow gas is Nitrogen N2 which has been injected from specific distribution manifold at velocity of 0.024m/s and the density ratio between the Ethylene and Nitrogen is 1.0015.

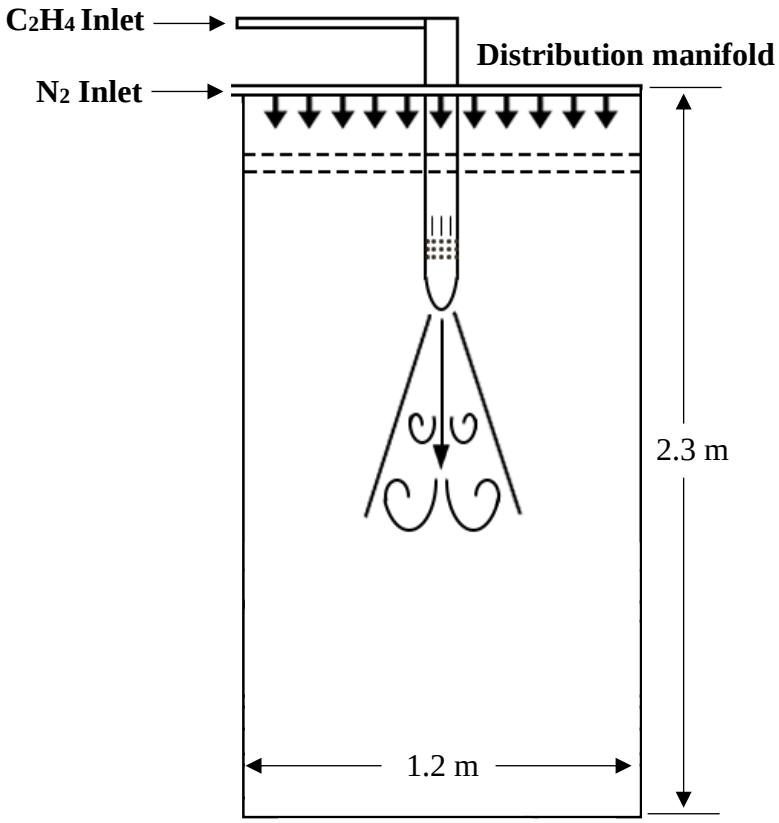

Figure 4-1: Experiment Domain. Re-Produced From (D. R. Dowling, 1988).

The maximum required length is at $80D_E$ where D_E is the Ethylene diameter, therefore there is no needs for large extra dimensions such as length and diameter as it will cost more computational time and more mesh elements number. Furthermore, the new domain should be calculated mathematically depending on the con angle θ and potential core length Z_o as shown in Figures 4-2 and 4-3. The potential core is the area where the inlet value of any quantity such as velocity, concentration and volume remain constant through it, and it is normally expanding up to $4D_E$ to $6D_E$. The computational results showed that the potential core length Z_o is equal to 0.09m, more details is explained in section 6.1.2. The con or core angle which shown in Figure 4-2 is calculated as follow:

$$tan\ \theta = \frac{r}{Z_o} = \frac{0.01}{0.09} \Longrightarrow \theta^o = 6.34\ ^o \qquad (4\text{-}1)$$

However, this value is for half angle, therefore, the core angle value is:

$$\theta^o = 6.34 \times 2 = 12.68^o$$

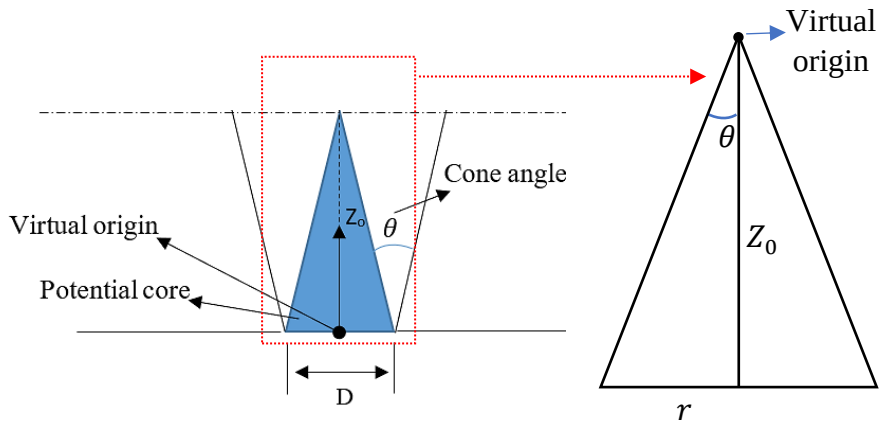

Figure 4-2: Core Angle Calculation.

Conversely, the measurements of axial concentrations fields in the experiment are from $20D_E$ to $80D_E$. Consequently, the simulation's domain length assumed to be up to $100D_E$, and the outer diameter is calculated as follow:

$$\frac{\mathrm{L}}{\mathrm{D_E}} = 100 \Longrightarrow \mathrm{L} = 200 \text{ cm} \tag{4-2}$$

$$r_{outer} = r_{inlet} + L \tan\theta \tag{4-3}$$

$$r_{outer} = 0.01 + (200 \times \tan 12.68) \simeq 23 \text{ cm}$$

Therefore, the outer diameter will be 50 cm. See Figure 4-3

On the other hand, Figure 4-4 shows the three-dimensional model geometry which has been created via using Workbench-Design Modeler program. The inlet dimensions of the main gas flow Ethylene C_2H_4 and Nitrogen N_2 are identical to the ones from experiment, however, the length of the domain re-scaled for optimising purposes as been explained before.

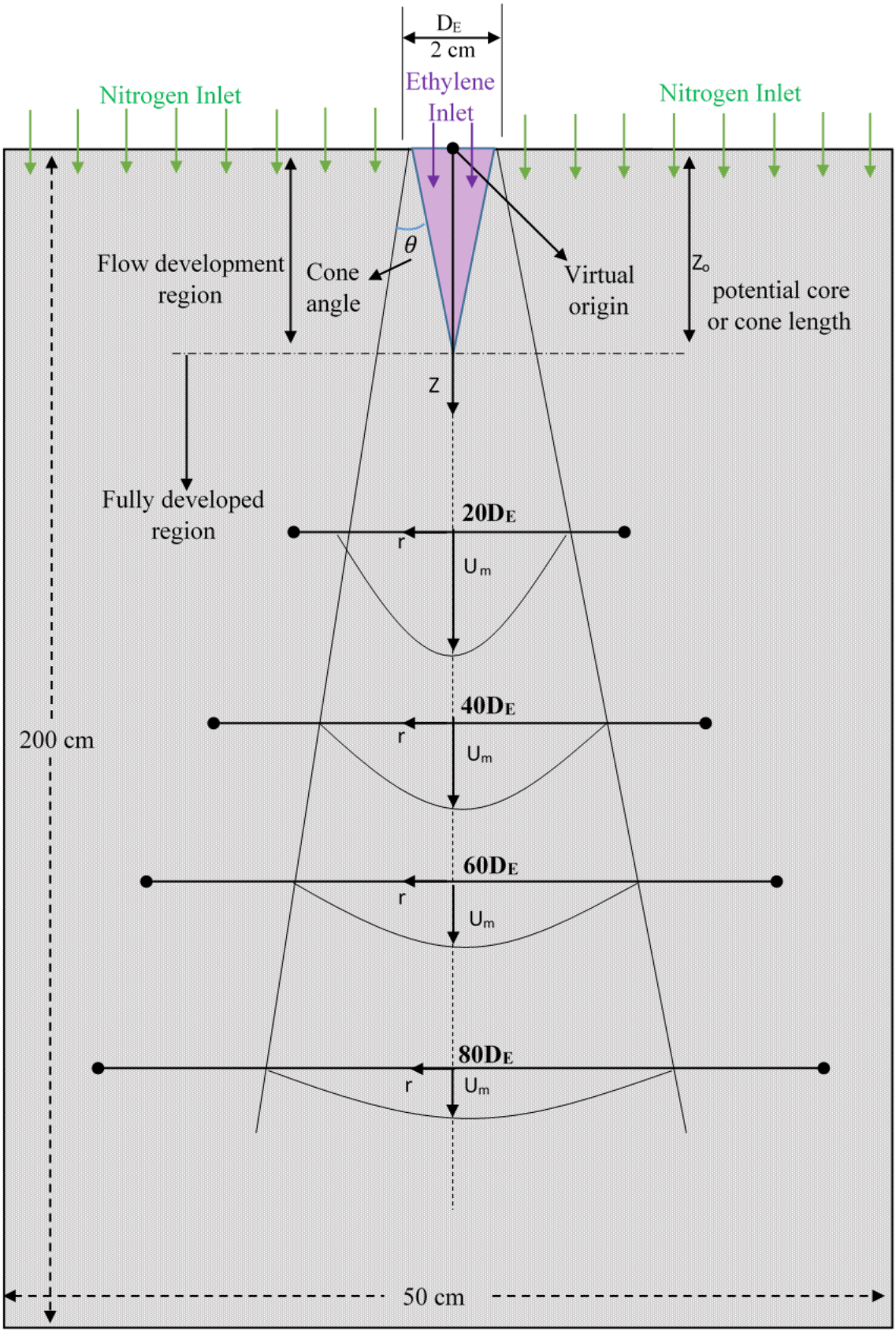

Figure 4-3: 2D Experiment Domain.

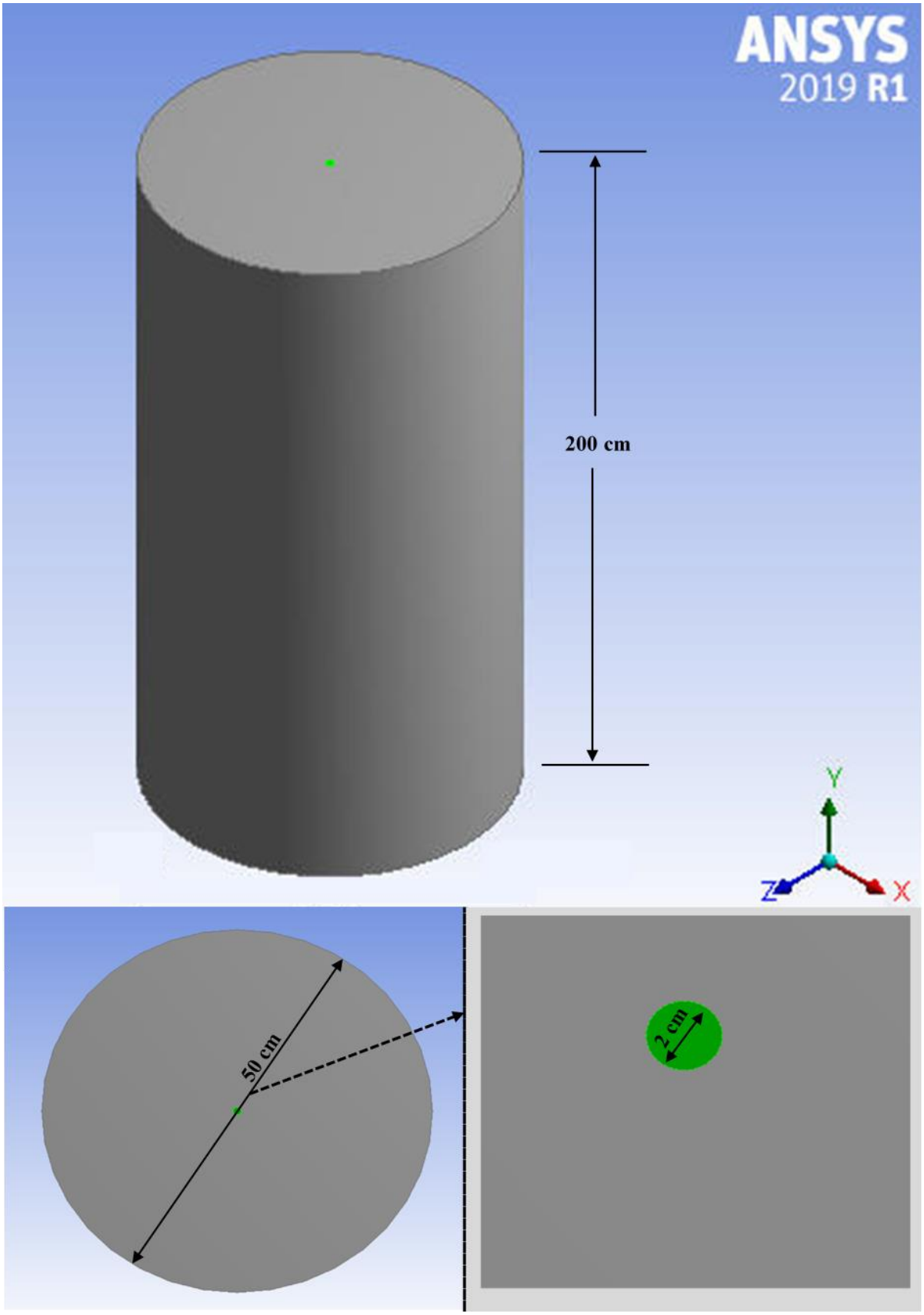

Figure 4-4: 3D Computational Domain.

4.1.2 Boundary Conditions B.C

The computational boundary conditions are shown in Table 4-1 and Figure 4-5. In the current study, steady state, three-dimensional and incompressible fluid of C_2H_4 and N_2 is simulated. Moreover, only the Standard k-ε has been used to model the flow. The boundary conditions for the present work are based on the experiment data mentioned in section 2.2.2 where the following conditions implemented inside the simulation:

The simulation's domain is a uniform co-flow mixture of Ethylene C2H4 and Nitrogen N2 gases. The inlets jet nozzles for both gases are at the top of the domain with value of 4.04 m/s for Ethylene and 0.025 m/s for Nitrogen as shown in Figure 4-5. Thus, Reynolds number is same as the experiment i.e., equal to 5000. Moreover, the equipment's volume in the experiment is turned into flow domain with a free slip wall condition. On the other hand, the pressure outlet condition is set to be 0 Pa atmospheric pressure.

Table 4-1: Computational B.C In ANSYS-CFX

Parameter	**Value**
Simulation type	3D, steady, incompressible
Domain	Ethylene C_2H_4 & Nitrogen N_2
Solver control	High resolution, First order
CFD algorithm	SIMPLE
Turbulence models	Standard *k-ε*
Turbulence intensity	0.02%
Residual Type	RMS 10^{-4}
Body (Nitrogen)	Free slip wall
Inlet one (Ethylene)	Velocity Inlet is 4.04 m/s
Inlet two (Nitrogen)	Velocity Inlet is 0.025 m/s
Outlet	Pressure outlet = 0 Pa

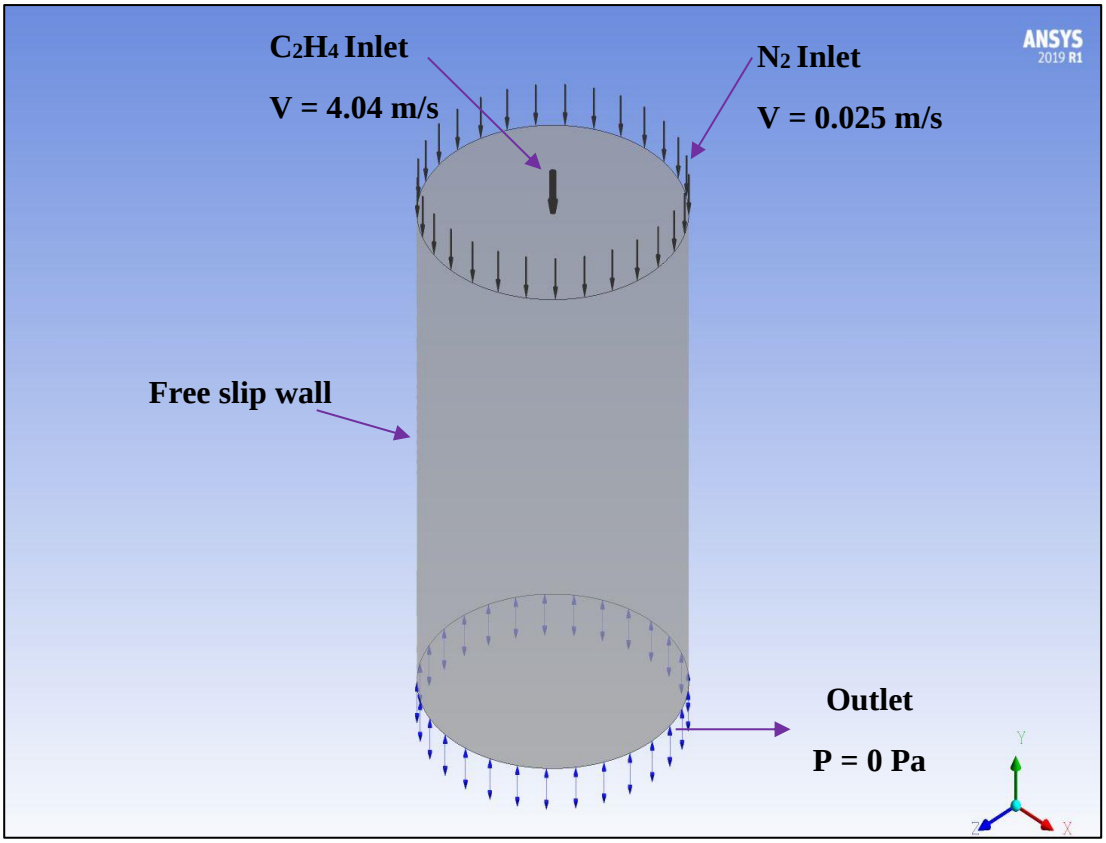

Figure 4-5: 3D Computational B.C.

4.1.3 Mesh sensitivity analysis

The main purpose of mesh independent study is to find the optimum mesh, depending on the most published investigations the independence mesh should have the following properties:

1) Most accurate result comparing with experimental data. But at the same time:

   a) Satisfy the convergence conditions which means that the solution has fulfilled the continuity equation such as steady state, mass flow rate in = mass flow rate out.

   b) Acceptable running time, optimum iteration time.

Furthermore, fulfilling the above conditions will approve that the chosen mesh is independent, and its results can be trusted. Therefore, one of the most important computational simulation steps is the mesh independence study. In addition, the present work uses various methods to satisfy these conditions as shown below:

1. Implementing different types of meshes as explained in section 6.1.1 to choose the right type of mesh.
2. Refinement the mesh

3. Duplicate the element size of the mesh
4. Choose a specific quantity such as volume fraction or velocity at a specific location to compare between each mesh.
5. Use Root Mean Sequard Error RMSE to compute the differences between mesh.
6. Choose the optimum mesh which have the accurate time with acceptable running time.

Therefore, the mesh study analyses of the current case study starting by creating different types of meshes such as Tetrahedral, Hexahedral and Polyhedral. Interestingly, the chosen mesh is one with the Tetrahedrons shape. The detailed explanation of the grid quality and its effects on the results is explained in section 6.1.1. Moreover, all the examined meshes have a fine grid quality and smooth transition. Next, Tables 4-2 and 4-3 show the meshes optimisation process starting from the first mesh M 1 with element size of 1,000,000 up to sixth mesh M 6 with element size of 32,000,000. Furthermore, Ethylene volume fraction ϑ_E has been chosen as a comparation quantity among the meshes at the same locations as the experiment data have been used $20D_E$, $40D_E$, $60D_E$ and $80D_E$. Then, evaluation methods among the meshes are based on:

First: Using average value of RMSE for all the volume fraction at each location via comparing it to the largest mesh M 6 as shown in Table 4-2 and Figures 4-6 and 4-7. In Figure 4-6, the volume faction is plotted against a non-dimensional parameter x/r where x refer to the location point in the computational domain and r is the Ethylene inlet radius.

Second: Using of mesh analysis based on volume fraction value at one point only of all the chosen locations, then take the difference value between each value and value of mesh 6 as shown in Table 4-3 and Figures 4-8 and 4-9.

Moreover, the above meshing independence steps indicate that the optimum mesh to be simulated for this experiment is mesh 5. This mesh has lowest average error percentage 0.73%, simultaneously the lowest different points value 1.91% among all the meshes as shown in the previous mentioned tables and figures. On the other hand, Figures 4-10 and 4-11 show the mesh refinement differences between the first mesh M 1 and the chosen mesh M 5. Critically, mesh refinement process concentrated on the Ethylene inlet to catch the near wall conditions. However, this experiment is focused on nearly all the domain from $20D_E$ to $80D_E$. Thus, mesh refinement process should be covering all the required domain to obtain the best trusted results.

Table 4-2: Mesh Analysis Based On RMSE For All Volume Fractions

Meshes	Element size	RMSE				Average
		$20D_E$	$40D_E$	$60D_E$	$80D_E$	
M 1	1,000,000	9.98%	11.11%	11.15%	11.72%	10.99%
M 2	2,000,000	8.63%	9.14%	9.46%	9.91%	9.29%
M 3	4,000,000	6.23%	6.33%	7.08%	7.52%	6.79%
M 4	8,000,000	1.47%	2.75%	3.92%	4.20%	3.08%
M 5	16,000,000	0.69%	0.71%	0.76%	0.77%	0.73%
M 6	32,000,000	0.00%	0.00%	0.00%	0.00%	0.00%

Table 4-3: Mesh Analysis Based On Volume Value At One Location

Meshes	Points Values for VF				Average
	$20D_E$	$40D_E$	$60D_E$	$80D_E$	
M 1	0.24679	0.20167	0.17562	0.16347	0.1968875
M 2	0.26663	0.23075	0.20388	0.19052	0.222945
M 3	0.31452	0.28054	0.24749	0.23021	0.26819
M 4	0.42466	0.35702	0.31089	0.29397	0.346635
M 5	0.44196	0.40239	0.38285	0.35138	0.394645
M 6	0.46319	0.41983	0.40083	0.37125	0.413775
M 6 - M 1	21.64%	21.82%	22.52%	20.78%	21.69%
M 6 - M 2	19.66%	18.91%	19.70%	18.07%	19.08%
M 6 - M 3	14.87%	13.93%	15.33%	14.10%	14.56%
M 6 - M 4	3.85%	6.28%	8.99%	7.73%	6.71%
M 6 - M 5	2.12%	1.74%	1.80%	1.99%	1.91%
M 6 - M 6	0.00%	0.00%	0.00%	0.00%	0.00%

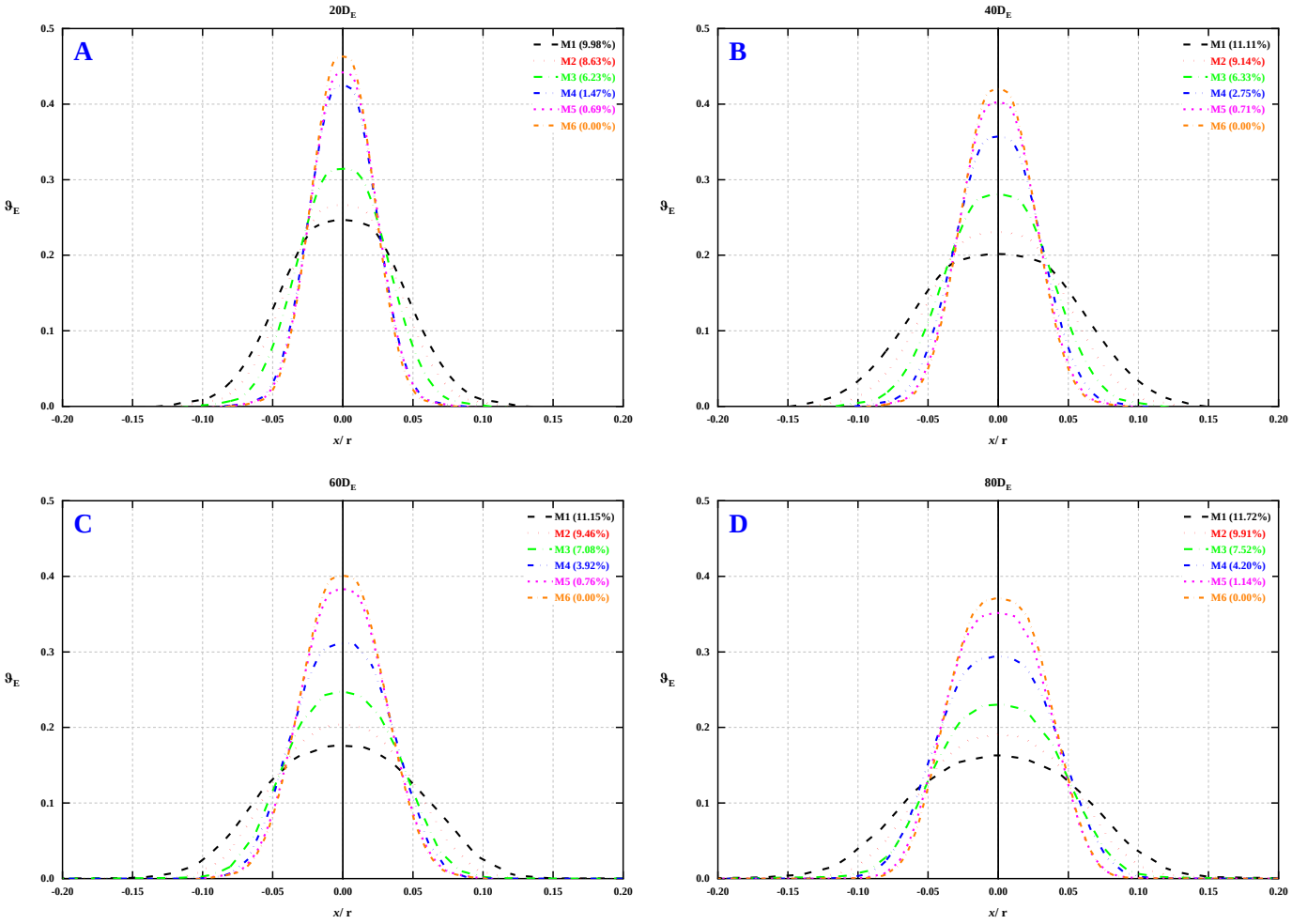

Figure 4-6: Ethylene Volume Fractions And RMSE Values For All Meshes At Different Locations: A. $20D_E$, B. $40D_E$, C. $60D_E$, And D. $80D_E$.

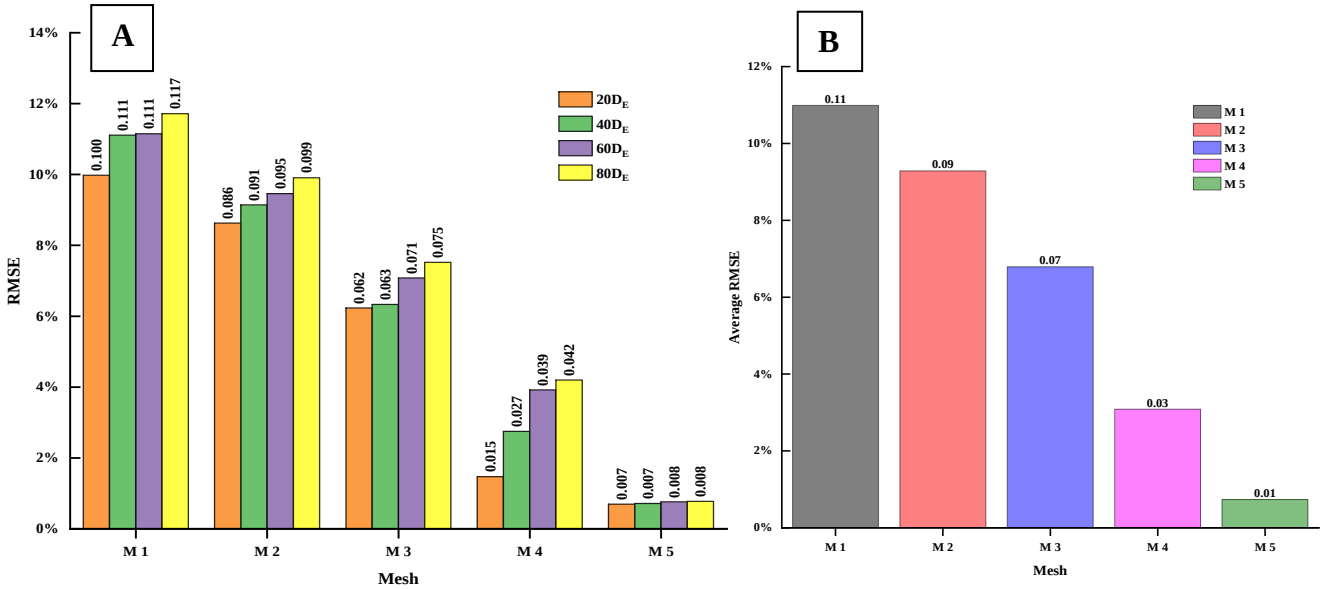

Figure 4-7: RMSE Comparison Among All The Meshes: A. All Values At All Locations, B. Average RMSE Value For Each Mesh.

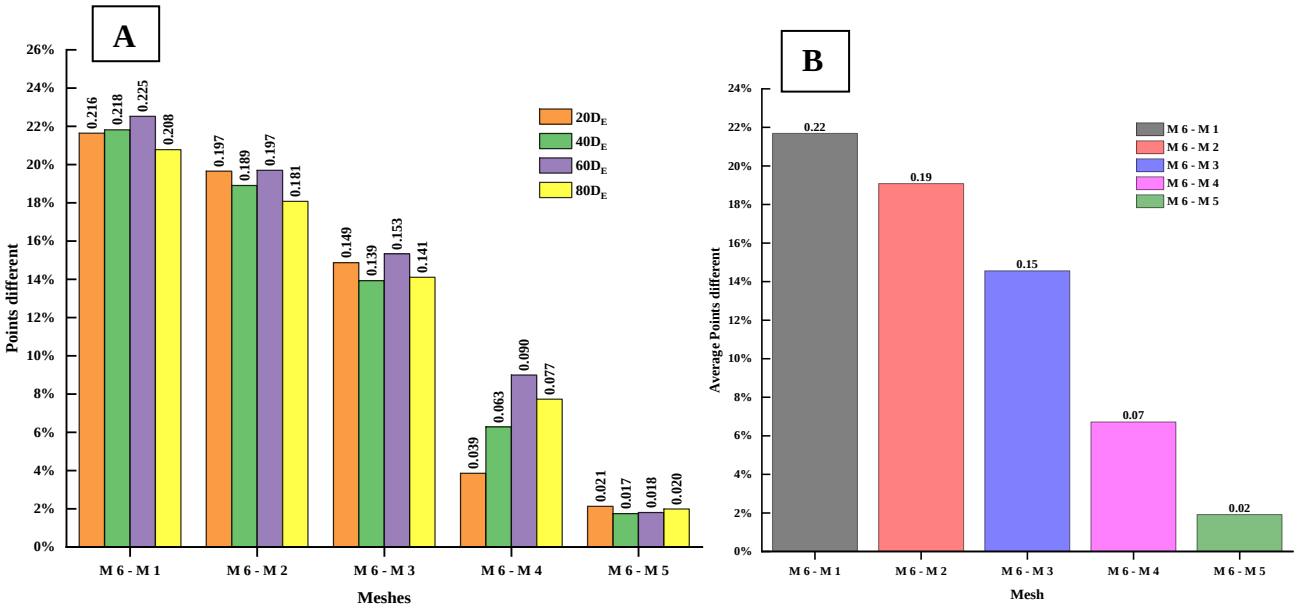

Figure 4-8: Point Based Comparison Among All The Meshes: A. All Points Values At All Locations, B. Average Points Value For Each Mesh.

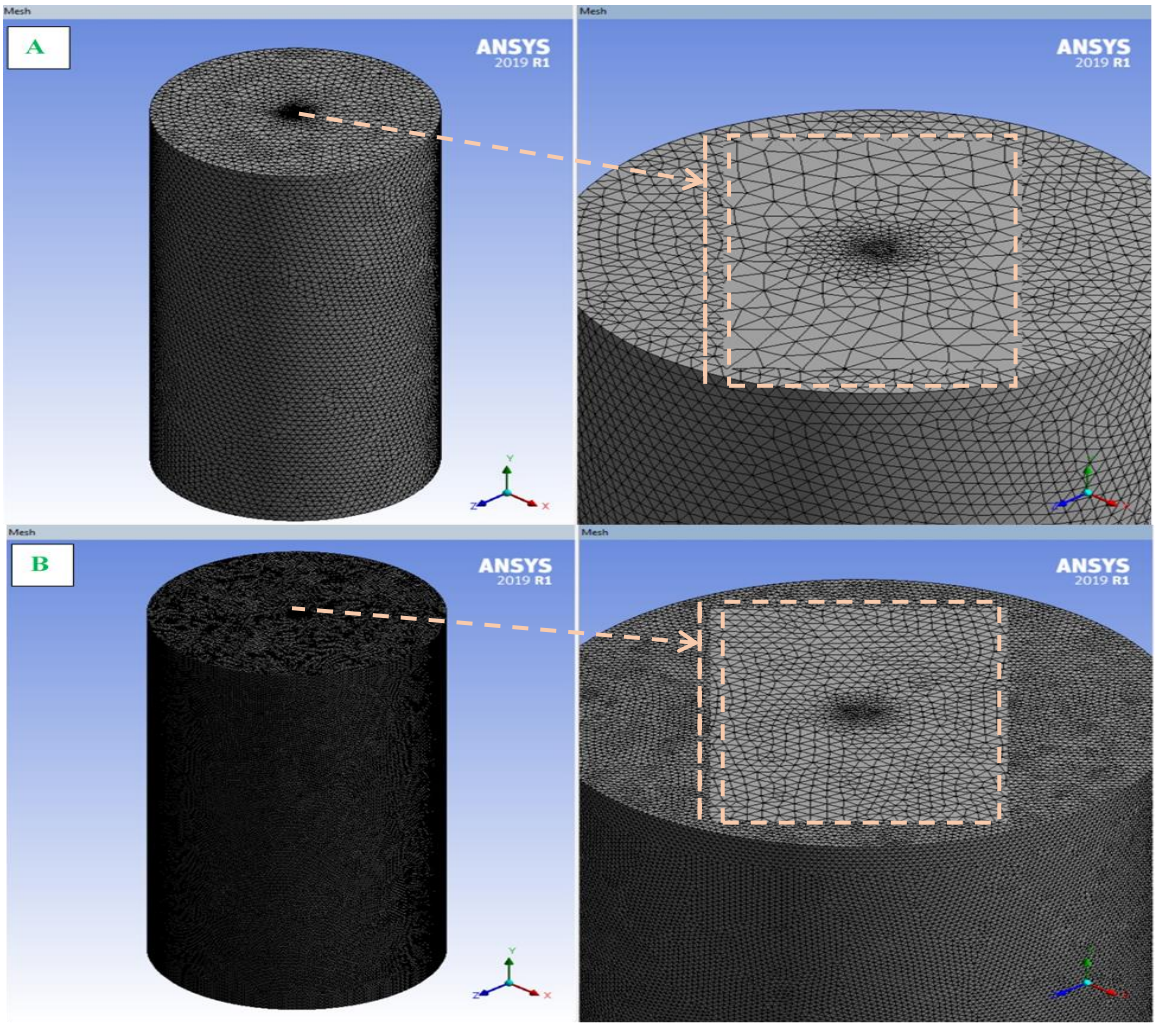

Figure 4-9: Mesh Refinement Differences. A. Mesh One, B. Mesh Five.

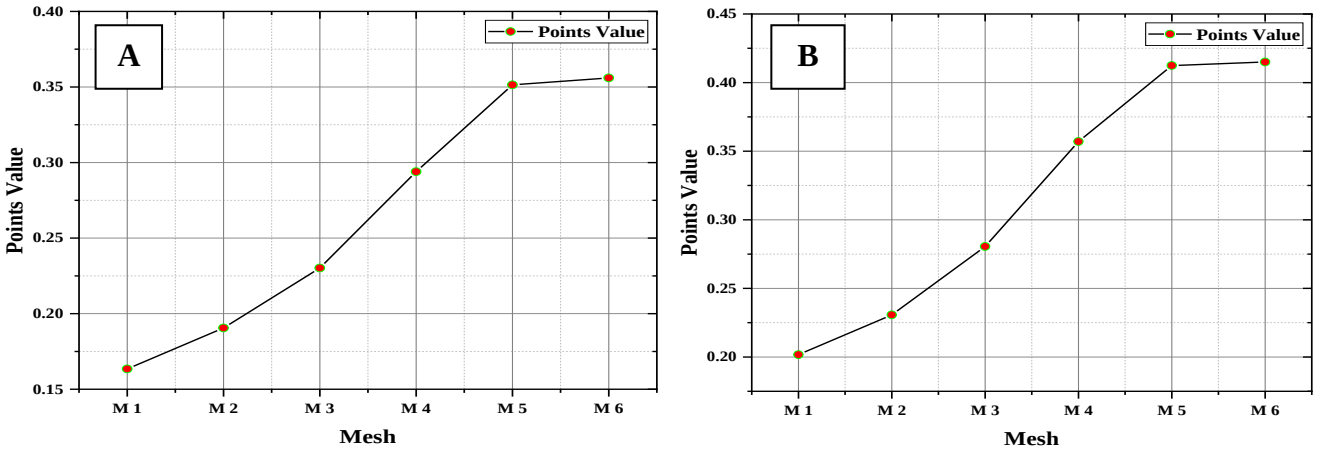

Figure 4-10: Point-Based Comparison Of Volume Fraction Value For Each Mesh. A. 40DE, B. 80DE.

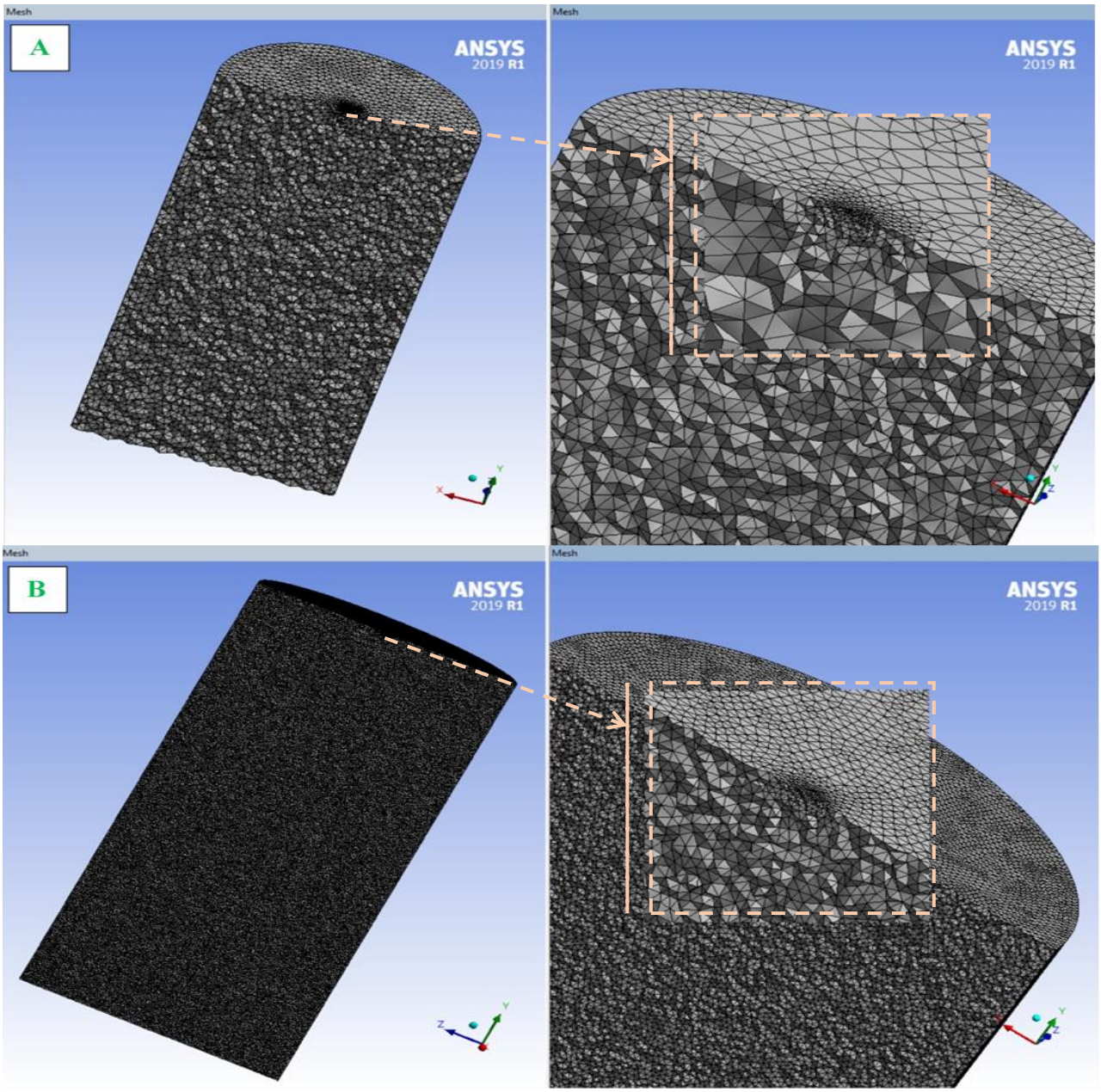

Figure 4-11: Mesh Refinement Differences (Cross-Section). A. Mesh One, B. Mesh Five.

4.2 Planar jet second case study

The second case of the planar jet flow is based on the experiment which has been used in this research as the main test to evaluate RANS turbulence models in ANSYS-CFX simulation program. The experiment has been explained in section 2.3.2 where a non-reacting fluid flow for a planar and swirl jet flow has been studied by applying Acetone vapour as the main gas flow. The experiment is established by (Stetsyuk, 2014) via using an atmospheric burner as shown in Figure 2-13 to create the swirling flow at different levels i.e., various swirling number. However, this burner is also able to create a planar flow by using the Acetone vapour only through the axial entrance without using any other gases such as air to create the swirl flow as shown in Figure 4-12. Therefore, the work done by (Stetsyuk, 2014) for a non-reacting planer jet flow used as a second case study to fulfil the research purposes.

4.2.1 Computational domain

Figures 2-13 and 4-13 show the main dimensions of the burner which has been used to implement the planar jet flow with inlet fuel diameter of 1.5 cm. To transfer the experiment system into a computational domain, a designer modeler program has been used along with Workbench ANSYS-CFX as shown in Figure 4-14. One the other hand, using the same steps as in section 4.1.1, it has been found that the core angle is 14.25^{o}. Furthermore, the results of the experiment located at $\mathrm{y/D_f} = 1, \mathrm{y/D_f} = 3, \mathrm{y/D_f} = 5$ and $\mathrm{y/D_f} = 7$ where y refer to the y-coordinator in 2D system and $\mathrm{D_f}$ is the fuel diameter equal to 1.5 cm. Therefore, the outer diameter can be calculated as follow:

$$\frac{\mathrm{y}}{\mathrm{D_f}} = 7 \Longrightarrow \mathrm{y} = 10.5 \text{ cm} \tag{4-4}$$

$$r_{outer} = r_{inlet} + \mathrm{y} \tan\theta \tag{4-5}$$

$$r_{outer} = 7.5 + (10.5 \times \tan 14.25) \simeq 10.5 \text{ cm}$$

Therefore, the computational hight suppose to be 10.5 cm and the outer diameter is 21 cm. However, this is very small area to compute which can cause some numerical issues during the run. Thus, it has been suggested by the author that the optimum domain dimensions will be 30.5 and 42 cm for hight and outer diameter respectively, as shown in Figure 4-13. Alternatively, there is no need to plot the burner cylinders in ANSYS-CFX because this simulation is only for a planar flow (it shorted to be Inlet) as shown Figure 4-14.

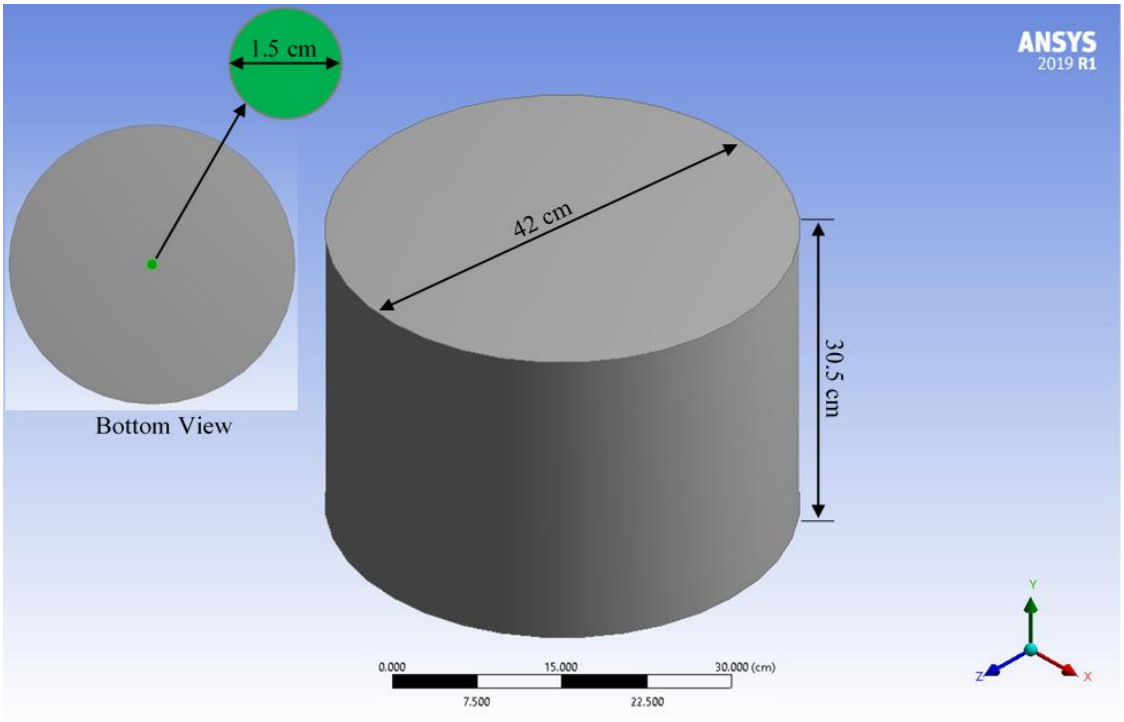

Figure 4-12: 3D Computational Domain.

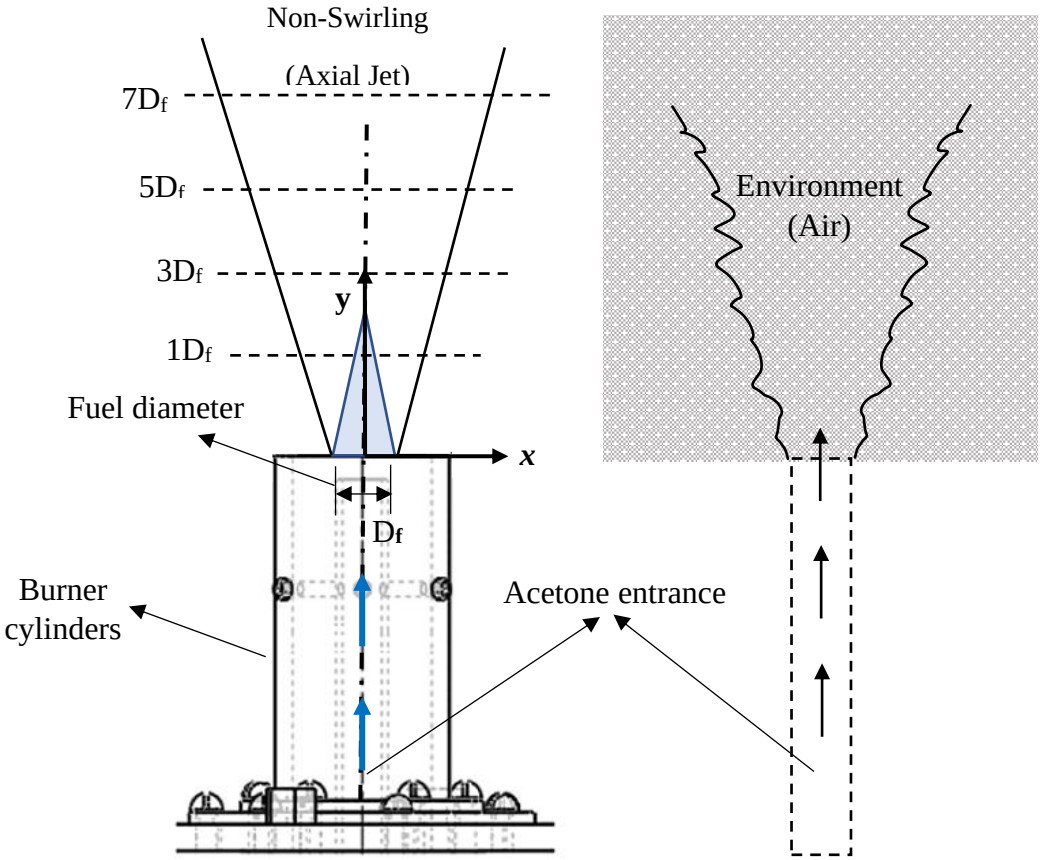

Figure 4-13: The Left-Hand Image Shows The Planar Burner Scheme. The Right-Hand Shows A Simple Diagram Of The Experiment Planar Jet Flow. Modified From (Stetsyuk, 2014).

4.2.2 Boundary Conditions B.C

The computational boundary conditions are generated according to the experiment data mentioned in section 2.3.2 and shown in Table 2-1 before. However, only Acetone vapour data will be used for the planar jet flow which is known as the passive scalar. Moreover, this research uses Methane CH_4 as the passive scalar in the runs because ANSYS-FX does not include Acetone data base, and the simulation's domain is a mixture of Methane and Air gases. Hence, the present work uses 3D, steady state and incompressible fluid CH_4 with a nozzle inlet velocity of 3.77m/s, alongside with Standard k-ε turbulence model to create the simulation. Thus, Reynolds number is same as the experiment i.e., equal to 3770. Conversely, the equipment's volume in the experiment is turned into flow domain with a free slip wall condition. In addition. the pressure outlet condition is set to be 0 Pa atmospheric pressure. Besides, Table 4-4 and Figure 4-14 show boundary conditions used in CFX solver.

Table 4-4: Computational B.C In ANSYS-CFX

Parameter	Value
Simulation type	3D, steady, incompressible, isothermal
Domain	Methane CH_4
Solver control	High resolution, First order
CFD algorithm	SIMPLE
Turbulence models	Standard k-ε
Turbulence intensity	0.02%
Residual Type	RMS 10^{-4}
Body (Air)	Free slip wall
Inlet (Methane)	Velocity Inlet 3.77 m/s
Outlet	Pressure outlet = 0 Pa

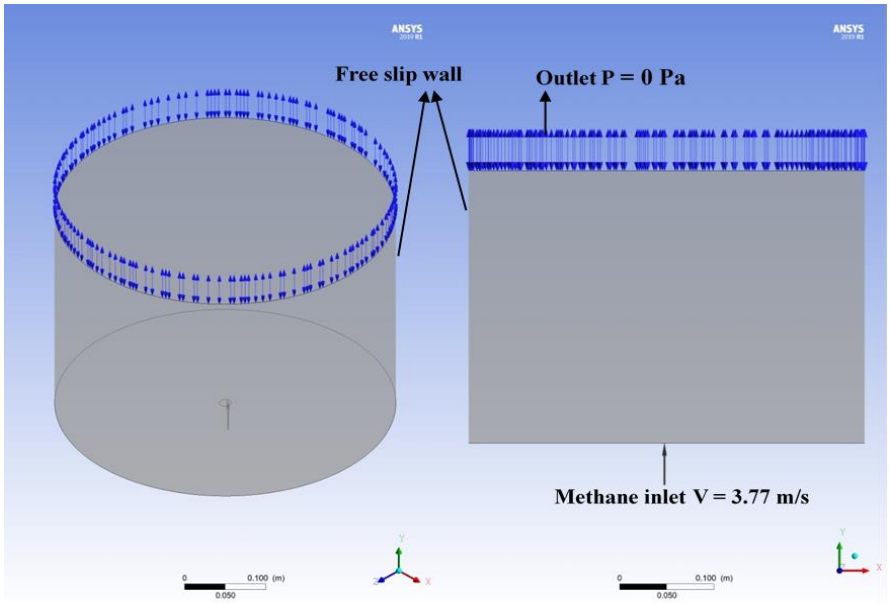

Figure 4-14: 3D Computational B.C.

4.2.3 Mesh sensitivity analysis

Mesh independence study is based on the previous fundamentals process explained in section 4.1.3 and a Tetrahedrons mesh has been used to achieve the present study's goals. The main reasons of choosing this type of mesh are the ability of indicating the correct values of various quantities such as volume fraction and velocity profile for Methane. Moreover, the mentioned mesh has a huge compatibility between ANSYS-CFX solving method and this type of flow, more details are in section 6.9. Like the previous case study, Tables 4-5 and 4-6 present the optimisation process to choose the proper mesh where the element size of the first mesh M 1 starting from 500,000 then 1,000,000 up to sixth mesh M 6 with element size of 16,000,000. Moreover, the starting mesh size is half than the earlier case study due to the small domain of this case. Besides, Methane CH_4 volume fraction ϑ uses to compare among the meshes at the same locations as the experiment data uses $1D_f$, $3D_f$, $5D_f$ and $7D_f$, where D_f is the fuel CH_4 diameter. Excitingly, using the same comparing steps as in previous case study via employing RMSE and point value-based analysis reveal that the optimum mesh to use is mesh five M 5 with a total element size of 8,000,000. As illustrated in Table 4-5 and Figures 4-15 and 4-16, the average RMSE value of volume fraction for the meshes start decreasing from 8.94% of mesh one M 1 to 0.73% of mesh five M 5 comparing with mesh six M 6. In Figure 4-15, the volume faction is mapped versus a non-dimensional parameter x/R where x refer to the location point in the computational domain and R is the Methane inlet radius. In addition, it appears from Table 4-6 that the point-based value of volume fraction in mesh five is very close to mesh six's value with an average value of 2.15% as plotted in Figure 4-17. From the Figure 4-18, the mesh differences between M 5 and M 6 are very small which is almost same value at $3D_F$ and $7D_F$ (randomly chosen) which assure that the chosen mesh is appropriate to use as the independence mesh for this simulation. On the other hand, Figures 4-19 and 4-20 provide a recognizable vision of the mesh refinement differences between the first mesh M 1 and the chosen mesh M 5. Remarkably, mesh refinement process concentrated on the Methane inlet to capture the near wall conditions and covering all the required domain to obtain the best trusted results.

Table 4-5: Mesh Analysis Based On RMSE For All Volume Fractions. Second Case Study

Meshes	Element size	RMSE				Average
		y/ D_f = 1	y/ D_f = 3	y/ D_f = 5	y/ D_f = 7	
M 1	500,000	1.32%	8.43%	12.07%	13.94%	8.94%
M 2	1,000,000	0.71%	6.32%	8.80%	10.82%	6.66%
M 3	2,000,000	1.20%	4.58%	5.98%	7.13%	4.72%
M 4	4,000,000	0.81%	2.82%	3.30%	4.49%	2.85%
M 5	8,000,000	0.37%	0.36%	1.01%	1.17%	0.73%
M 6	16,000,000	0.00%	0.00%	0.00%	0.00%	0.00%

Table 4-6: Mesh Analysis Based On Volume Value At One Location. Second Case Study

Meshes	Points Values for VF				Average
	y/ D_f = 1	y/ D_f = 3	y/ D_f = 5	y/ D_f = 7	
M 1	0.95975	0.57965	0.47134	0.41045	0.605298
M 2	0.97483	0.65448	0.54228	0.47914	0.662683
M 3	0.96269	0.71457	0.63047	0.57284	0.720143
M 4	0.97243	0.787	0.72129	0.65182	0.783135
M 5	0.98726	0.89489	0.81293	0.76815	0.865808
M 6	0.99261	0.90895	0.83472	0.81295	0.887308
M 6 - M 1	3.29%	32.93%	36.34%	40.25%	28.20%
M 6 - M 2	1.78%	25.45%	29.24%	33.38%	22.46%
M 6 - M 3	2.99%	19.44%	20.43%	24.01%	16.72%
M 6 - M 4	2.02%	12.20%	11.34%	16.11%	10.42%
M 6 - M 5	0.53%	1.41%	2.18%	4.48%	2.15%
M 6 - M 6	0.00%	0.00%	0.00%	0.00%	0.00%

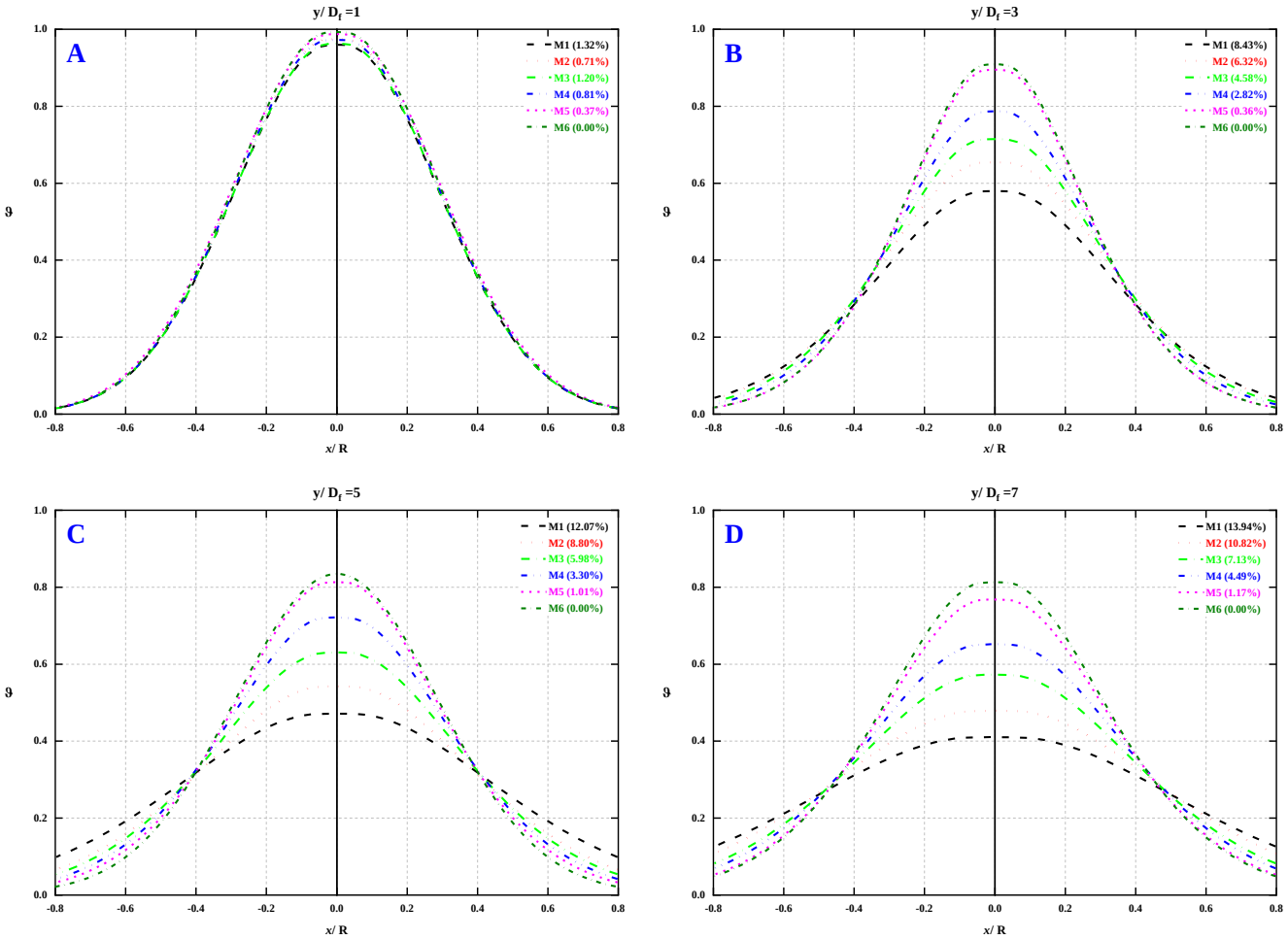

Figure 4-15: Methane Volume Fractions And RMSE Values For All Meshes At Different Locations: A. 1D$_f$, B. 3D$_f$, C. 5D$_f$, And D. 7D$_f$. Second Case Study.

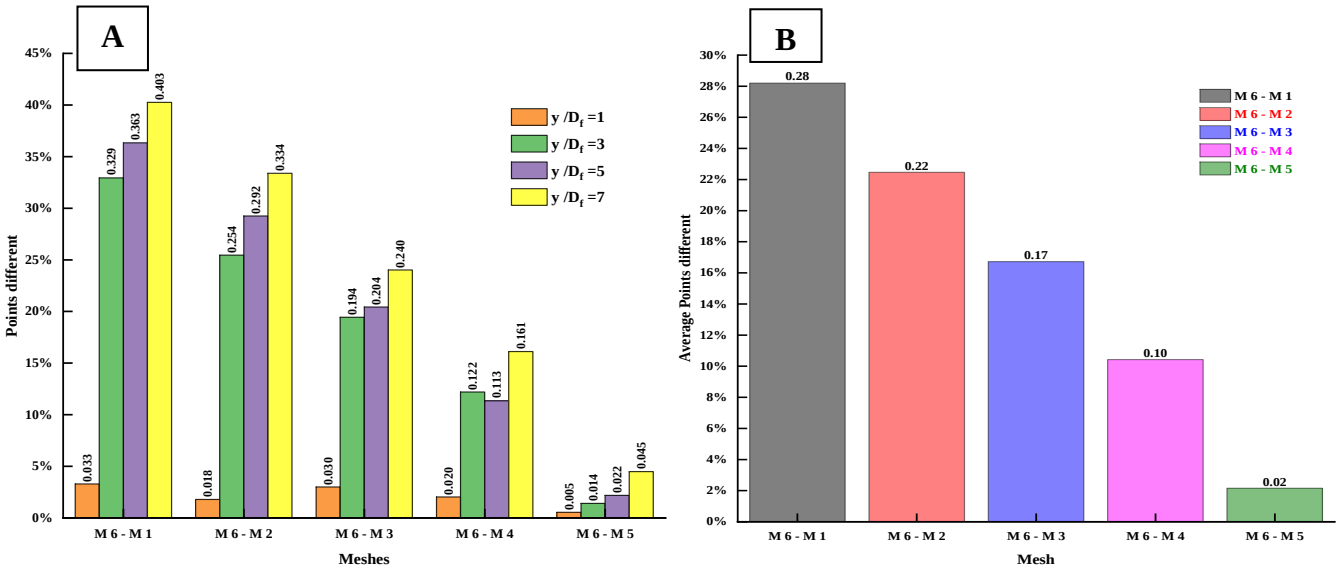

Figure 4-16: Point Based Comparison Among All The Meshes: A. All Points Values At All Locations, B. Average Points Value For Each Mesh. Second Case Study.

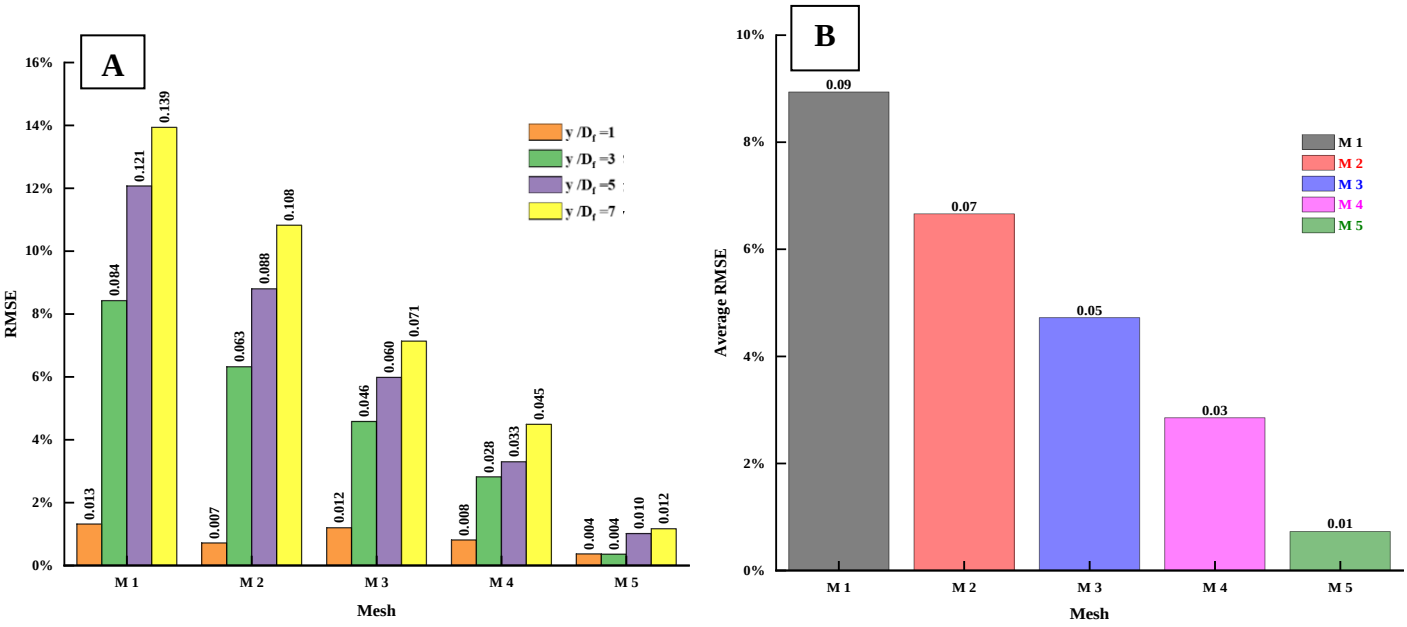

Figure 4-17: RMSE Comparison Among All The Meshes: A. All Values At All Locations, B. Average RMSE Value For Each Mesh. Second Case Study.

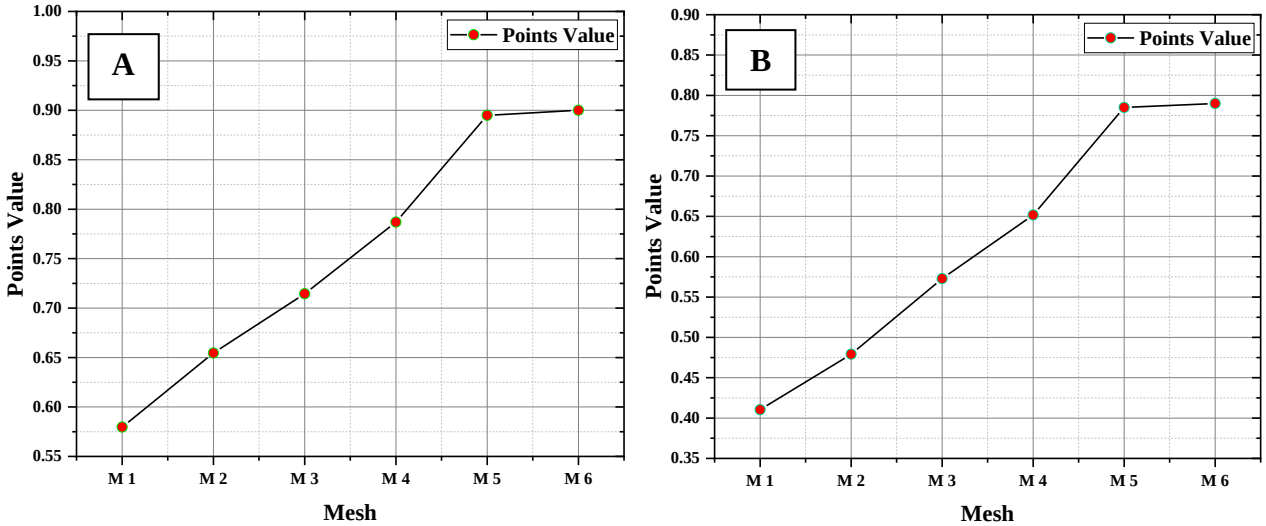

Figure 4-18: Point-Based Comparison Of Volume Fraction Value For Each Mesh. A. $3D_f$, B. $7D_f$. Second Case Study.

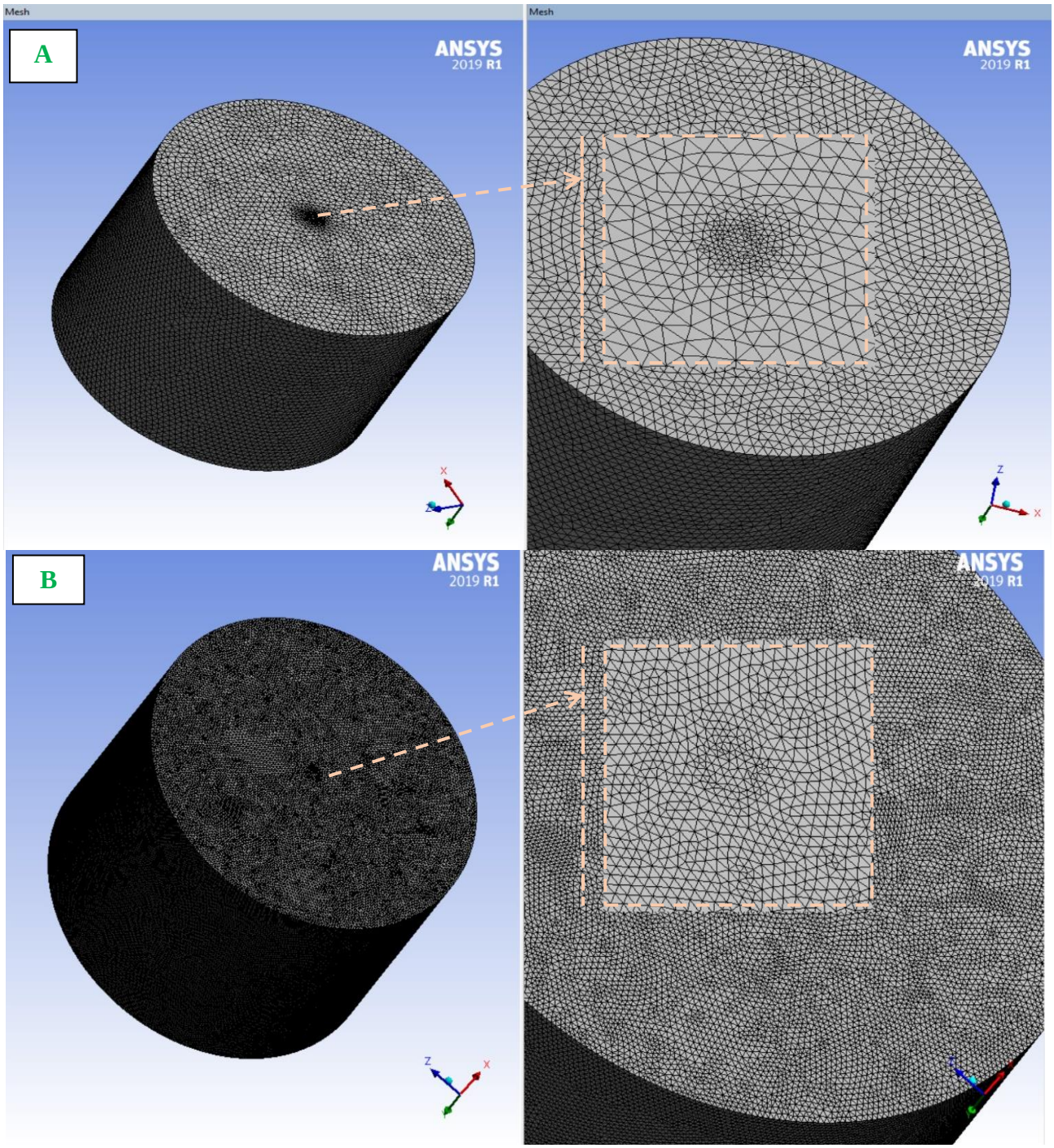

Figure 4-19: Mesh Refinement Differences. A. Mesh One, B. Mesh Five. Second Case Study.

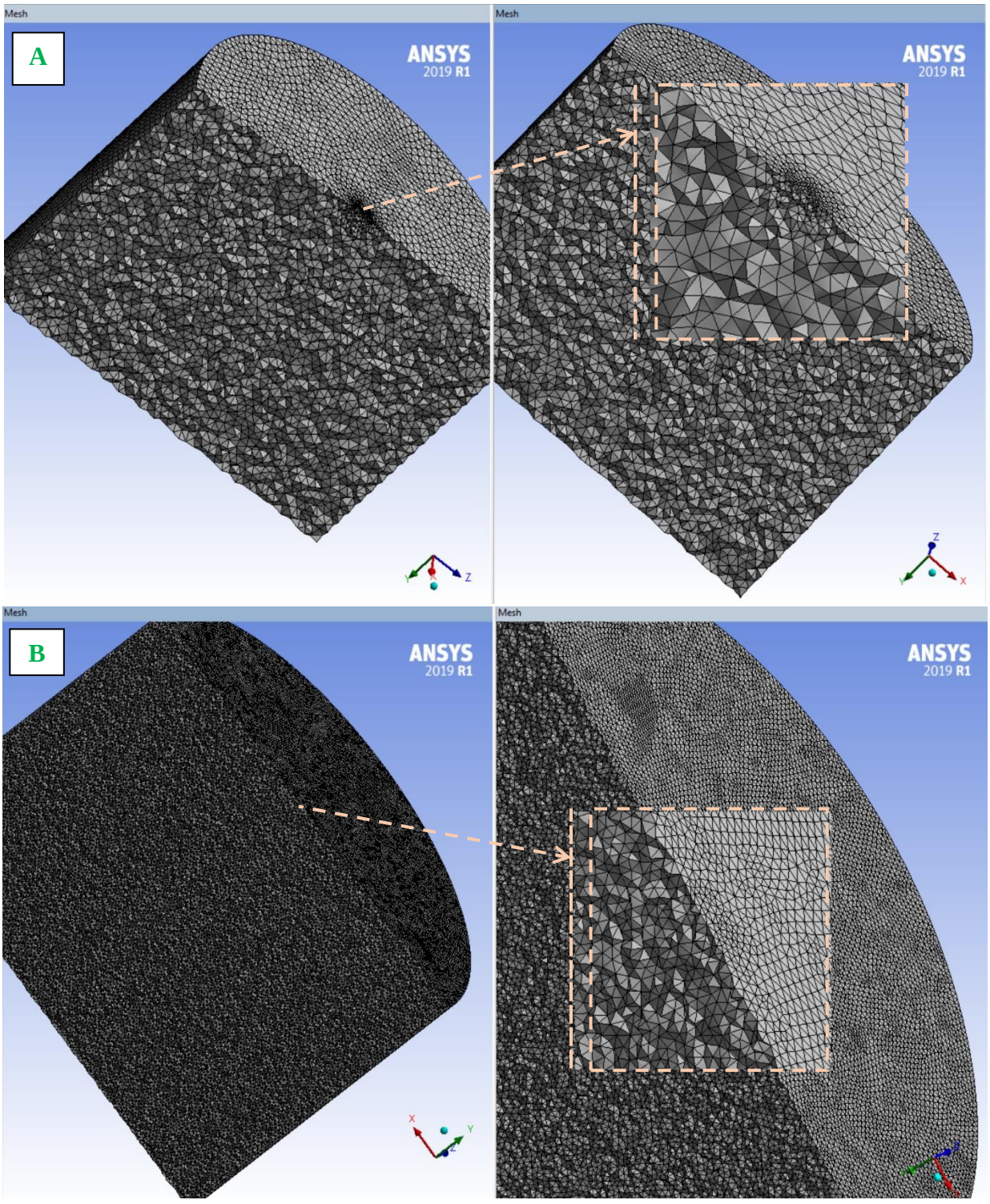

Figure 4-20: Mesh Refinement Differences (Cross-Section). A. Mesh One, B. Mesh Five. Second Case Study.

4.3 Summery

In summary, the current chapter underline the main steps to setup the computational process of two planar jet flow cases which can be highlighted as follow:

1. Convert the experimental system into a computational domain via using DesignModeler programme which consider as a sub-programme of Workbench R18.

2. The dimensions of the main gas flow which is the Inlet are same as the experiments. However, the simulation domain is depending on the required data locations.

3. Implementations of different types of meshes to proof the ability of catching the correct feature. Meshing sub-programme is used for this purpose.

4. Mesh independence study to use the optimum mesh with a trusted result by flowing the logic steps explained before.

5. Applying the accurate boundary conditions to the domain when using CFX-Pre-sub-programme, then run the simulation as the next program.

The programme approved the ability of performing this kind of flow as explained in chapter six sections 6.1, 6.2. Therefore, next chapter will use the above steps to create the numerical modelling of swirl jet flow with a using of different programme to create the geometry.

Chapter 5 SWIRL JET NUMERICAL MODELLING

5.1 Computational domain

The experiment lab conditions, and setup is previously explained in sections 2.3.2 and plotted in Figures 2-13, 2-14 and 2-15. The experiment is based on using an atmospheric burner to generate reacting such as combustion environment and non-reacting flow at different swirl number. Although the experiment is carried out both kinds of flow, the author work will be only on the non-reacting as isothermal swirl jet flow.

Therefore, the right side of Figure 5-1 has been taken from (Stetsyuk, 2014) experiment and it is illustrating the main burner dimensions that need to be modelled. Moreover, it can be seen in the mentioned figure that the there are three inlets' locations i.e., two for Air and one for the passive scalar which is Acetone vapour. On the other hand, the left side of Figure 5-1 is drawn by the author to illustrate the computational domain dimensions along with flow expectation inside the domain. The figure is showing the locations of volume fraction computing i.e., $1D_f$, $3D_f$, $5D_f$ and $7D_f$. Therefore, the main purpose of this figure is to show and illustrate the actual atmospheric burner and the computational domain of the same burner. Moreover, the first inlet for air is called Axial through the outer cylinder with axial diameter D_a = 50.8 mm while the second Air inlets is through six tangential slots 52 mm length, 2.5 mm wide to generate the swirl. Nevertheless, Acetone vapour enters the domain throughout a hollow cylinder with a length of 414 mm and fuel diameter D_f = 15 mm.

Consequently, the jet mixing between the swirling Air and the planar Acetone vapour starts by the end of the burner cylinders. On the other hand, the data collection is taken via using a laser-induced fluorescence technique at four locations $1D_f$, $3D_f$, $5D_f$ and $7D_f$. Thus, to simplify the experiment system, the author proposes that there is no need to generate all the burner details showed in Figure 2-13. Instead, only the burner cylinders in addition to the environment domain will be created to carry out the numerical modelling as shown in Figure 5-1. Since the geometry of the burner is greatly important and complicated, the numerical model geometry is created by using SolidWorks computer programme due to the flexibility of the program.

Then, the previous computational domain steps as shown in sections 4.1.1 and 4.2.1 are used to obtain the appropriate domain for the swirl environment. However, three more domains have been tested to besetment the swirl effect, computational running time and for meshing study reasons as shown in Figure 5-2. Lastly, Figures 5-3 and 5-4 show the optimum computational domain to be use in this study, the outer diameter of the mixing domain is the

same as the previous planar study 420 mm see section 4.2.1. However, the length is a little bit bigger due to swirl effect 400 mm.

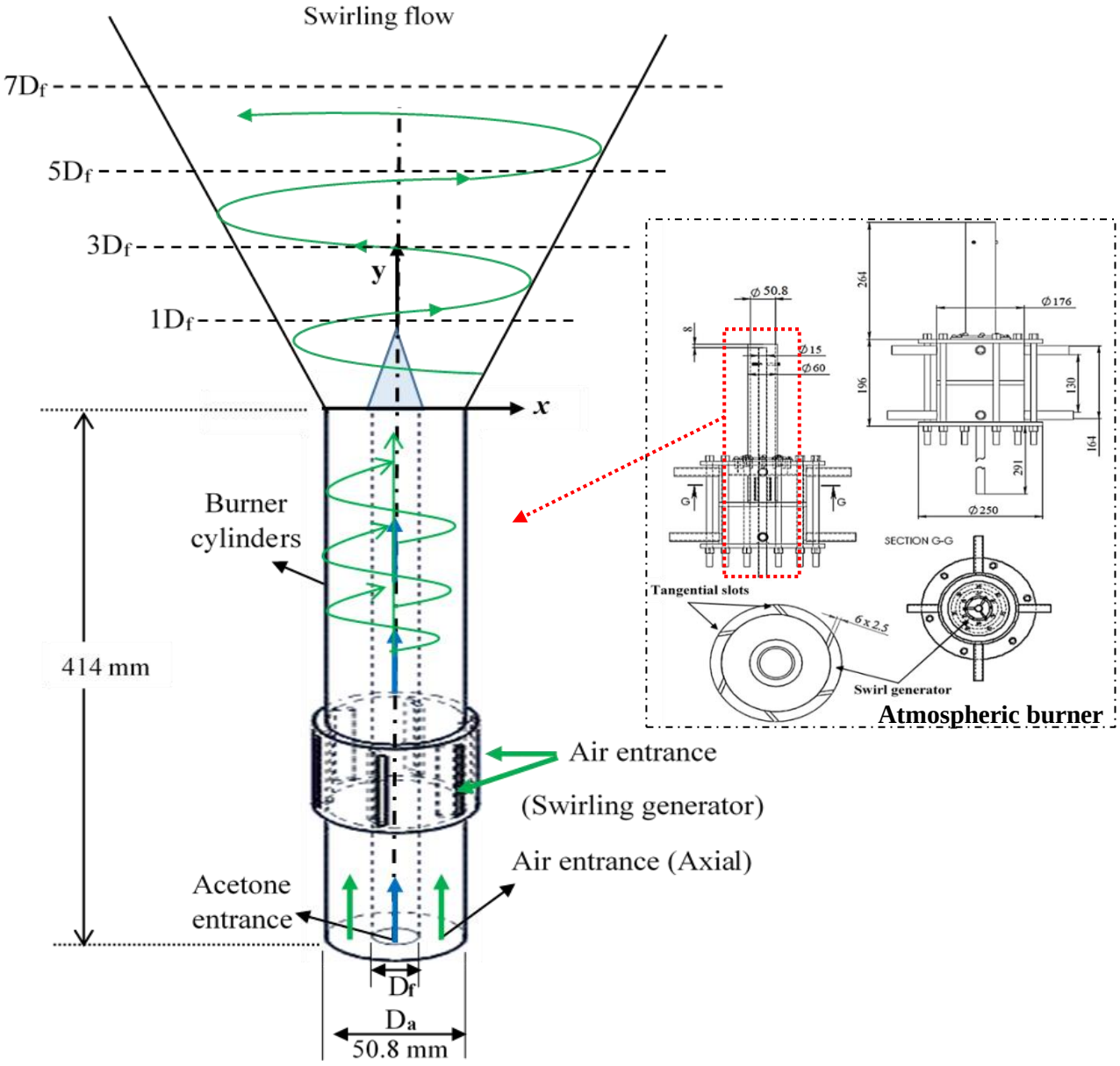

Figure 5-1: Computational Domain Scheme (Left). Atmospheric Burner (Right). Modified From (Stetsyuk, 2014).

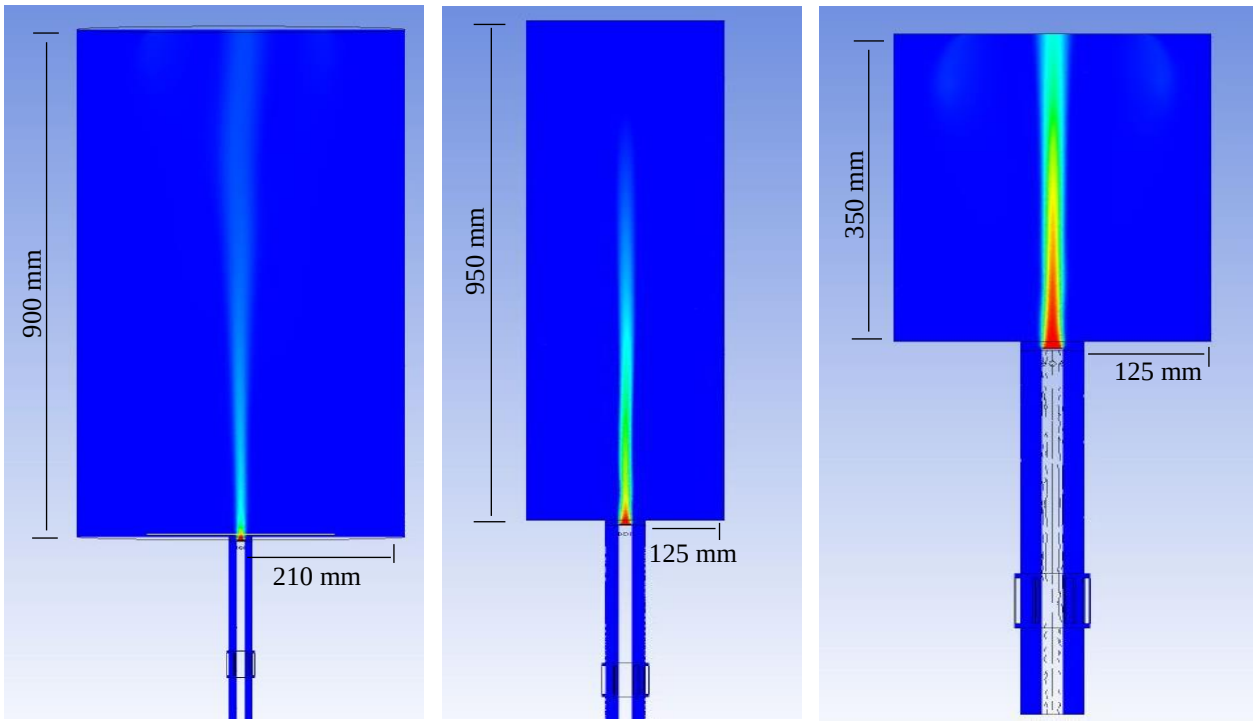

Figure 5-3: Computational Domain Samples.

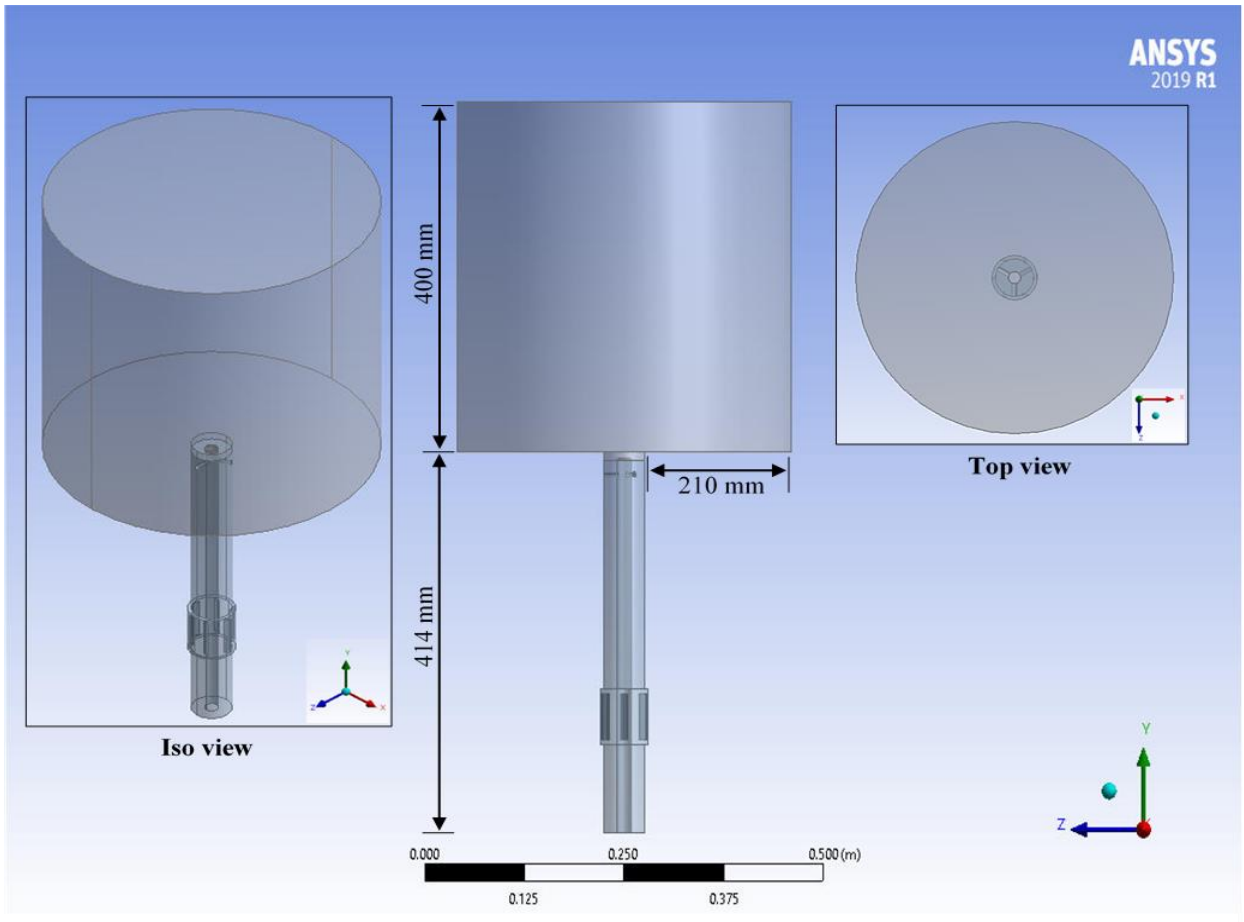

Figure 5-2: 3d Computational Numerical Domain Scheme. Swirling Simulation.

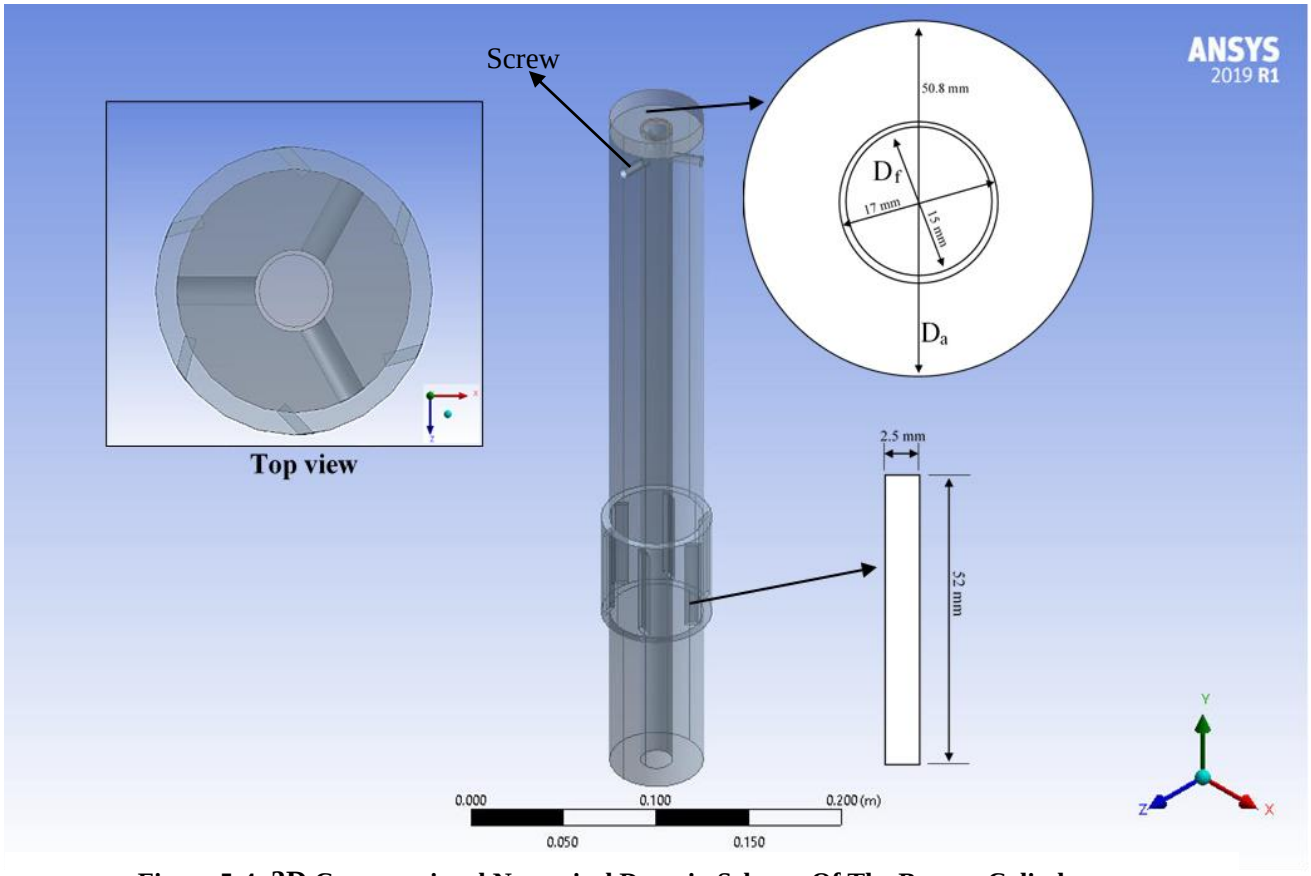

Figure 5-4: 3D Computational Numerical Domain Scheme Of The Burner Cylinders.

5.2 Boundary conditions

The experiment boundary condition is illustrated before in Table 2-1 which include the volumetric flow rate values for the axial, swirl generator and the scalar, these values are depending on the swirl number. For instance, to increase the swirl strength the volumetric flow rate of the axial decreases simultaneously with increasing of its value at the slots inlets and vice versa. However, the sum up of both axial and swirl inlets values should be constant 900 l/min where the total Reynolds number is always equal to 28662. Moreover. The scalar inlet value is constant at all swirl number circumstances 40 l/min with a Reynolds number of 3770.

Furthermore, ANSYS-CFX setup program does not implement a volumetric rate value of the boundary conditions to any subject. Therefore, the inlets values in Table 2-1 converts into a suitable form as shown in Table 5-1 where $\dot{m}$ refer to mass flow rate at the axial and swirl while the velocity v has been used for the scalar. As been mentioned before, Methane has been applied instead of Acetone vapour in this work to indicate the effect of the diffusivity and turbulence (more details in results discussion). The setup state of the run is shown in Table 2-

2, the turbulence model in the previous table refer to various models (see section 5.4) employed in this study. With a view to obtain best running time in addition to smooth run, an initial condition is applied to simulation as shown in Table 2-3 for Air and Methane. The initial condition for Methane is applied for the vertical velocity u only as the scalar inlet direction is also vertical. While the initial volume fraction for Air is one which means there is only air in the environment domain at time zero. Lastly, Figures 5-5 and 5-6 demonstrate the main boundary conditions inside CFX setup which have applied to produce the simulation.

Table 5-1: Simulation Boundary Conditions. Swirling Simulation

S	Axial		Swirl		Axial & Swirl	Scalar		
	V l/min	$\dot{m}$ Kg/s	V l/min	$\dot{m}$ Kg/s	Re	V l/min	v m/s	Re
0.3	500	0.0098	400	0.0079	28662	40	3.77	3770
0.58	350	0.007	550	0.0109				
1.07	150	0.003	750	0.015				

Table 5-2: Computational B.C In ANSYS-CFX. Swirling Simulation

Parameter	Value
Simulation type	3D, steady, incompressible, isothermal (25 C)
Domain	Methane (CH_4) & Air
Solver control	High resolution, First order
CFD algorithm	SIMPLE
Turbulence models	Depending on the author choice
Turbulence intensity	0.02%
Residual Type	RMS 10^{-4}
Body (Air)	Free slip wall
Pipe	No slip wall
Inlet one (scalar) Methane	v (3.77 m/s)
Inlet two (axial) Air	$\dot{m}$ Kg/s (depending on the used swirl number)
Inlet three (slits) Air	$\dot{m}$ Kg/s (depending on the used swirl number)
Outlet	Opening pressure @ fluids value of (Air =1, Methane =0)

Table 5-3: Initial B.C In ANSYS-CFX. Swirling Simulation

Methane	u m/s	3.77
	v m/s, w m/s	0
	Volume fraction	Auto, start from (0)
Air	u m/s, v m/s, w m/s	Auto, start from (0)
	Volume fraction	1

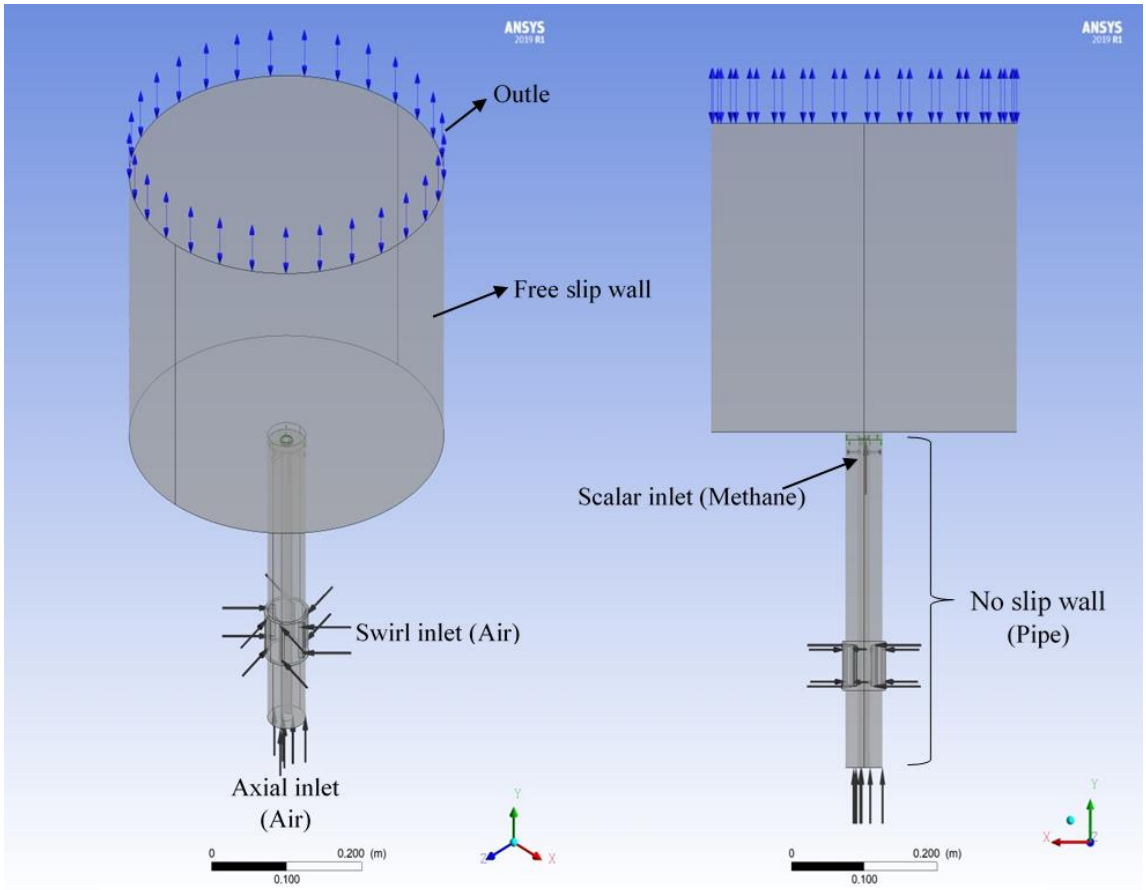

Figure 5-6: 3D Computational B.C. Swirling Simulation.

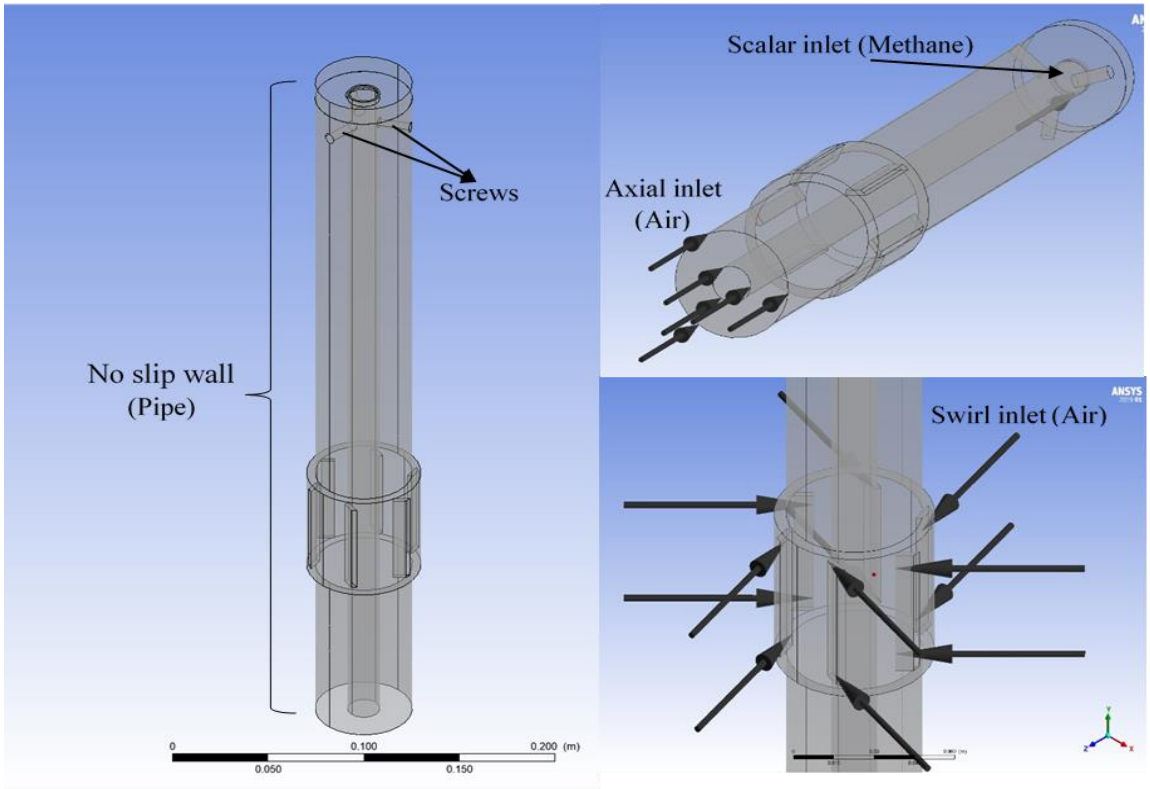

Figure 5-5: 3D Computational B.C. At The Burner Cylinders.

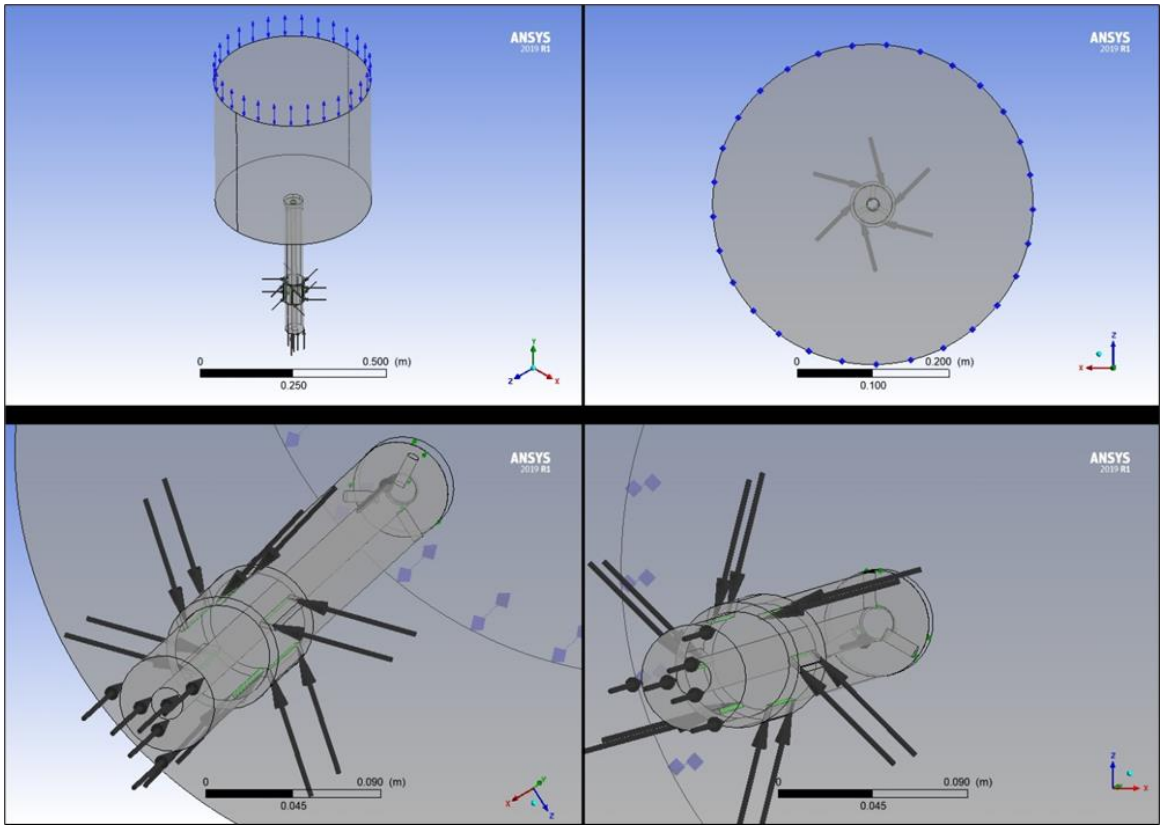

Figure 5-7: 3D Computational B.C. At Different Views.

5.3 Mesh sensitivity analysis

Mesh independence study is established on the earlier basic process described in sections 4.1.3 and 4.2.2 where a Tetrahedrons mesh is employed to accomplish the present study's objectives. Like the previous two cases, Tables 5-4 and 5-5 represent the optimisation procedure to select the suitable mesh where the element size of the first mesh M 1 starting from 1,000,000 then 2,000,000 up to sixth mesh M 6 with element size of 32,000,000. Although the computational domain is relatively small in this study, the starting mesh is big to cover all the domain significantly. Likewise, Methane CH_4 volume fraction ϑ uses to compare among the meshes at $1D_f$, $3D_f$, $5D_f$ and $7D_f$. Remarkably, using the same evaluating steps as in previous cases via hiring RMSE and point value-based analysis show that the optimum mesh is mesh five M 5 with a total element size of 16,000,000.

The average RMSE value of volume fraction for all meshes start reducing from 15.19% at mesh one M 1 to 1.56% at mesh five M 5 competing with mesh six M 6 as clarified in Figures 5-8 and 5-9 and Table 5-4.

Likeness, the differences in point-based value of volume fraction for all meshes starting from a large average value at M 6 - M 1 with a value of 33.43%, then starts decreasing to the lowest value at M 6 – M 5 with a value of 2.22% as appears in Table 5-5 and mapped in Figure 5-10.

Likeness, the differences in point-based value of volume fraction for all meshes starting from a large average value at M 6 - M 1 with a value of 33.43%, then starts decreasing to the lowest value at M 6 – M 5 with a value of 2.22% as appears in Table 5-5 and mapped in Figure 5-10. To expand the mesh independence study, two random locations for M 5 and M 6 employed to indicate the differences in volume fraction value between them. Therefore, the points values are taking at $1D_F$ and $7D_F$. The results indicate that the difference value between both meshes is very small which led to more confidence by selecting M 5 as the proper one to use for this simulation as presenting in Figure 5-11.

Significantly, meshing creating process starting by dividing all the domain into tow bodies; the first one refers to free slip wall known as environmental domain, the second body refer to no slip wall refers to the pipe. Therefore, the mesh refinement process for the computational domain starts by increase the element number near the inlets and at the environment domain where the data collection taking from $1D_f$, $3D_f$, $5D_f$ and $7D_f$ to obtain the finest trusted results. Thus, the increasing of mesh size is mainly occurring at the environment domain first body which known as free slip wall in Figure 5-5. However, the pipe as shown in Figure 5-6 element size remains constant during meshing process. Figures 5-12 and 5-13 illustrate a clear vision of the mesh refinement variances between M 1 and the chosen mesh M 5.

Table 5-4: Mesh Analysis Based On RMSE For All Volume Fractions. Swirling Simulation

Meshes	Element size	RMSE				Average
		y/ D_f = 1	y/ D_f = 3	y/ D_f = 5	y/ D_f = 7	
M 1	1,000,000	9.98%	17.85%	17.24%	15.69%	15.19%
M 2	2,000,000	8.62%	15.05%	14.28%	13.03%	12.75%
M 3	4,000,000	7.88%	13.29%	12.21%	10.64%	11.00%
M 4	8,000,000	5.26%	8.03%	7.82%	6.82%	6.98%
M 5	16,000,000	0.95%	1.85%	1.72%	1.70%	1.56%
M 6	32,000,000	0.00%	0.00%	0.00%	0.00%	0.00%

Table 5-5: Mesh Analysis Based On Volume Value At One Location. Swirling Simulation

Meshes	Points Values for VF				Average
	y/ D_f = 1	y/ D_f = 3	y/ D_f = 5	y/ D_f = 7	
M 1	0.56957	0.1639	0.1054	0.08591	0.231195
M 2	0.6006	0.22968	0.16629	0.13697	0.283385
M 3	0.63239	0.26874	0.2111	0.18445	0.32417
M 4	0.68538	0.4238	0.31528	0.27192	0.424095
M 5	0.81096	0.5381	0.44566	0.37875	0.543368
M 6	0.83869	0.55818	0.46797	0.39728	0.56553
M 6 - M 1	26.91%	39.43%	36.26%	31.14%	33.43%
M 6 - M 2	23.81%	32.85%	30.17%	26.03%	28.21%
M 6 - M 3	20.63%	28.94%	25.69%	21.28%	24.14%
M 6 - M 4	15.33%	13.44%	15.27%	12.54%	14.14%
M 6 - M 5	2.77%	2.01%	2.23%	1.85%	2.22%
M 6 - M 6	0.00%	0.00%	0.00%	0.00%	0.00%

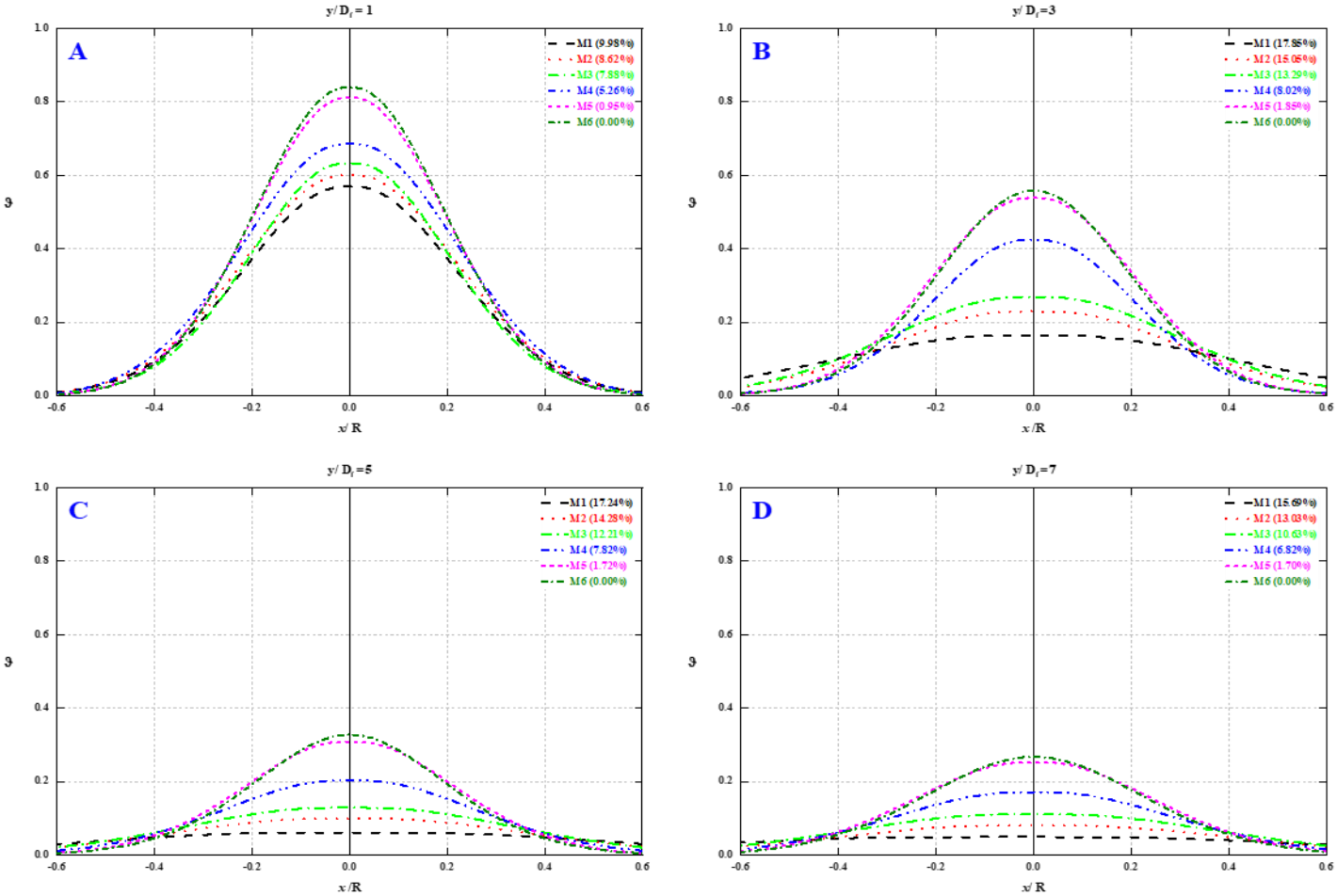

Figure 5-8: Methane Volume Fractions And RMSE Values For All Meshes At Different Locations: A. 1D_f, B. 3D_f, C. 5D_f, And D. 7D_f. Swirling Simulation.

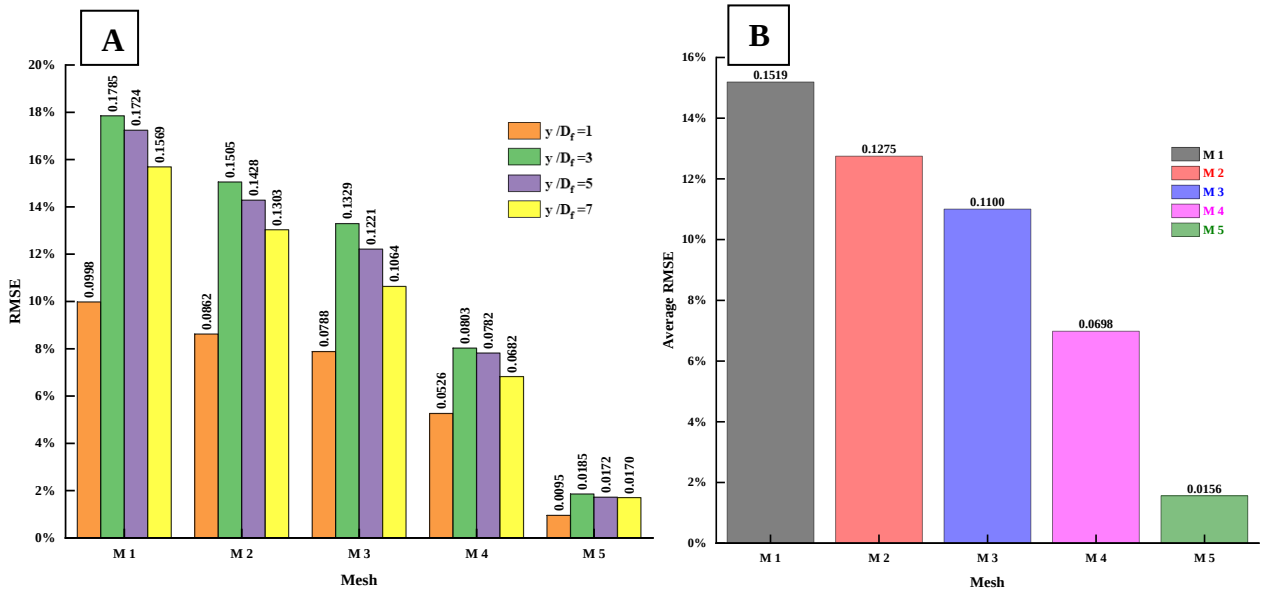

Figure 5-9: RMSE Comparison Among All The Meshes: A. All Values At All Locations, B. Average RMSE Value For Each Mesh. Swirling Simulation.

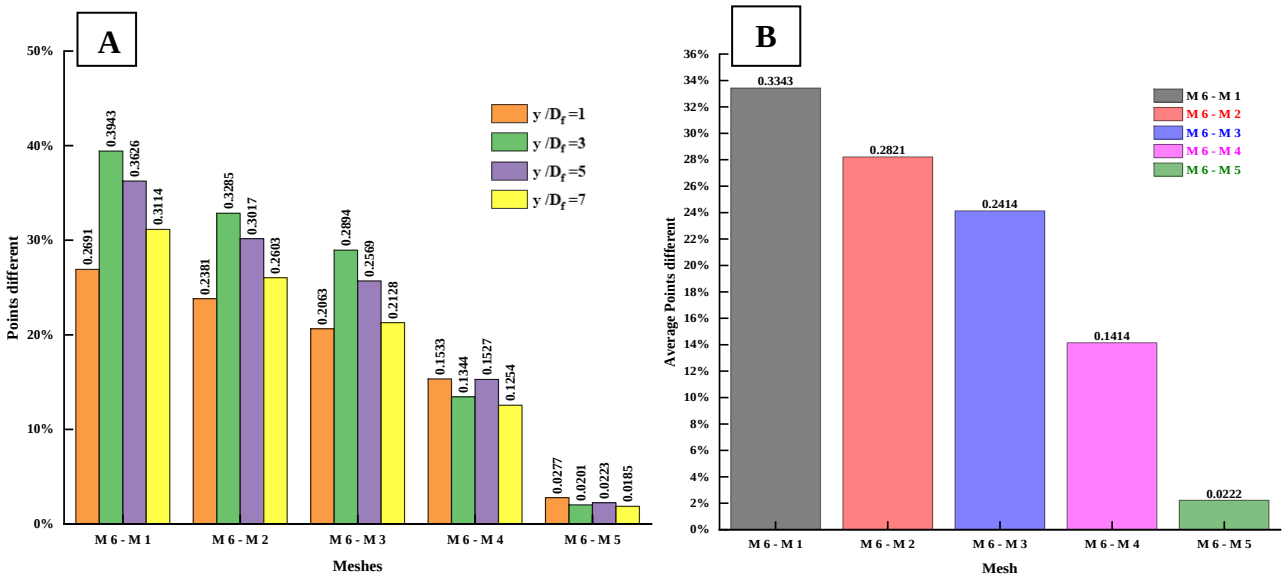

Figure 5-10: Point-Based Comparison Among All The Meshes: A. All Points Values At All Locations, B. Average Points Value For Each Mesh. Swirling Simulation.

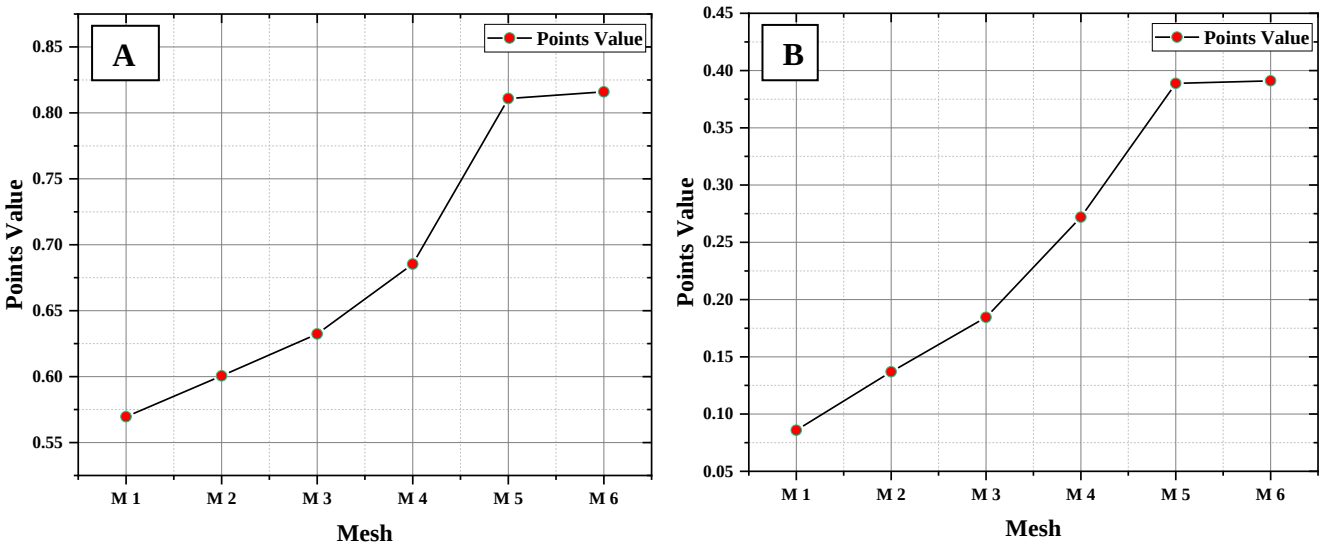

Figure 5-11: Point-Based Comparison Of Volume Fraction Value For Each Mesh. A. 1D_f, B. 7D_f. Swirling Simulation.

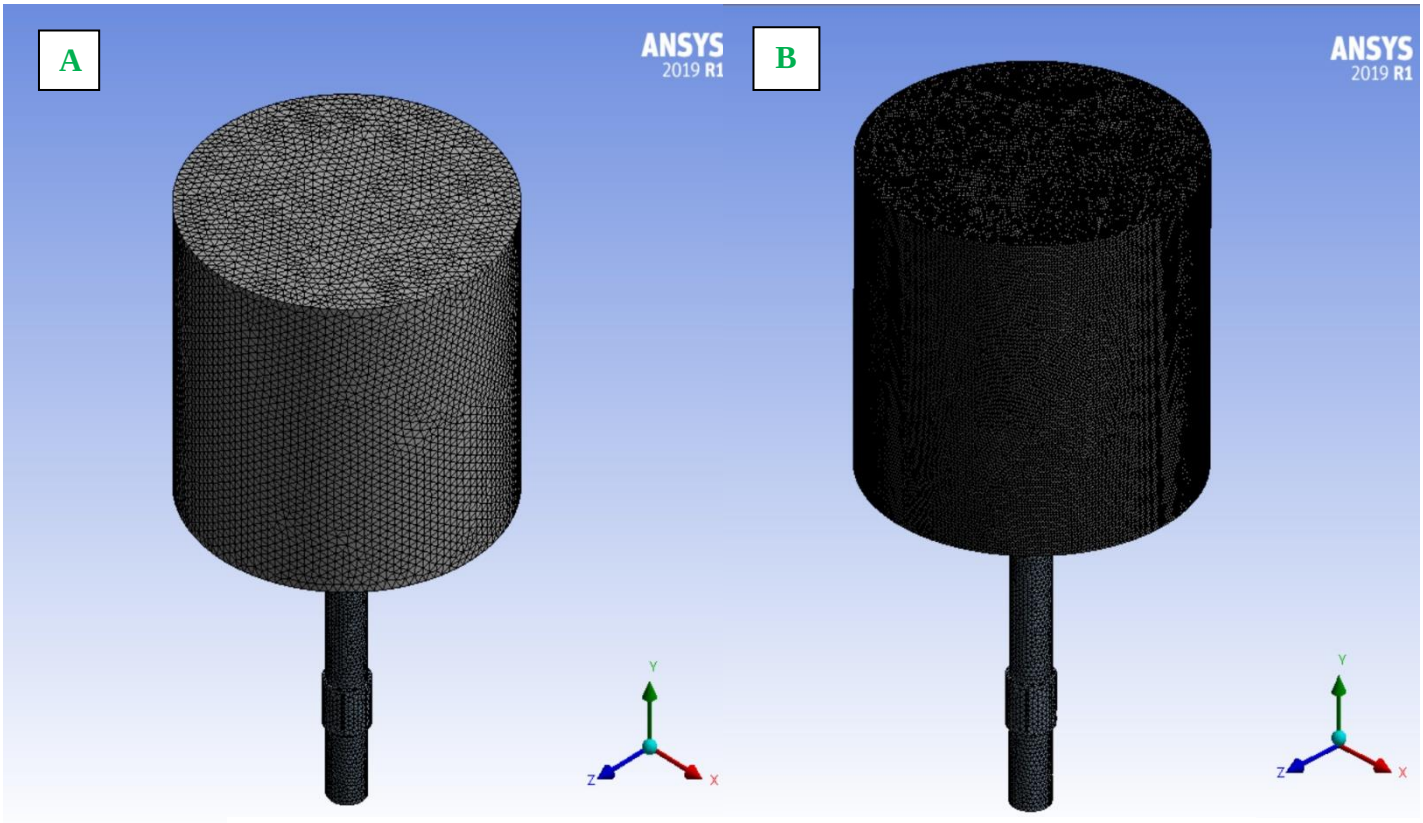

Figure 5-12: Mesh Refinement Differences. A. Mesh One, B. Mesh Five. Swirling Simulation.

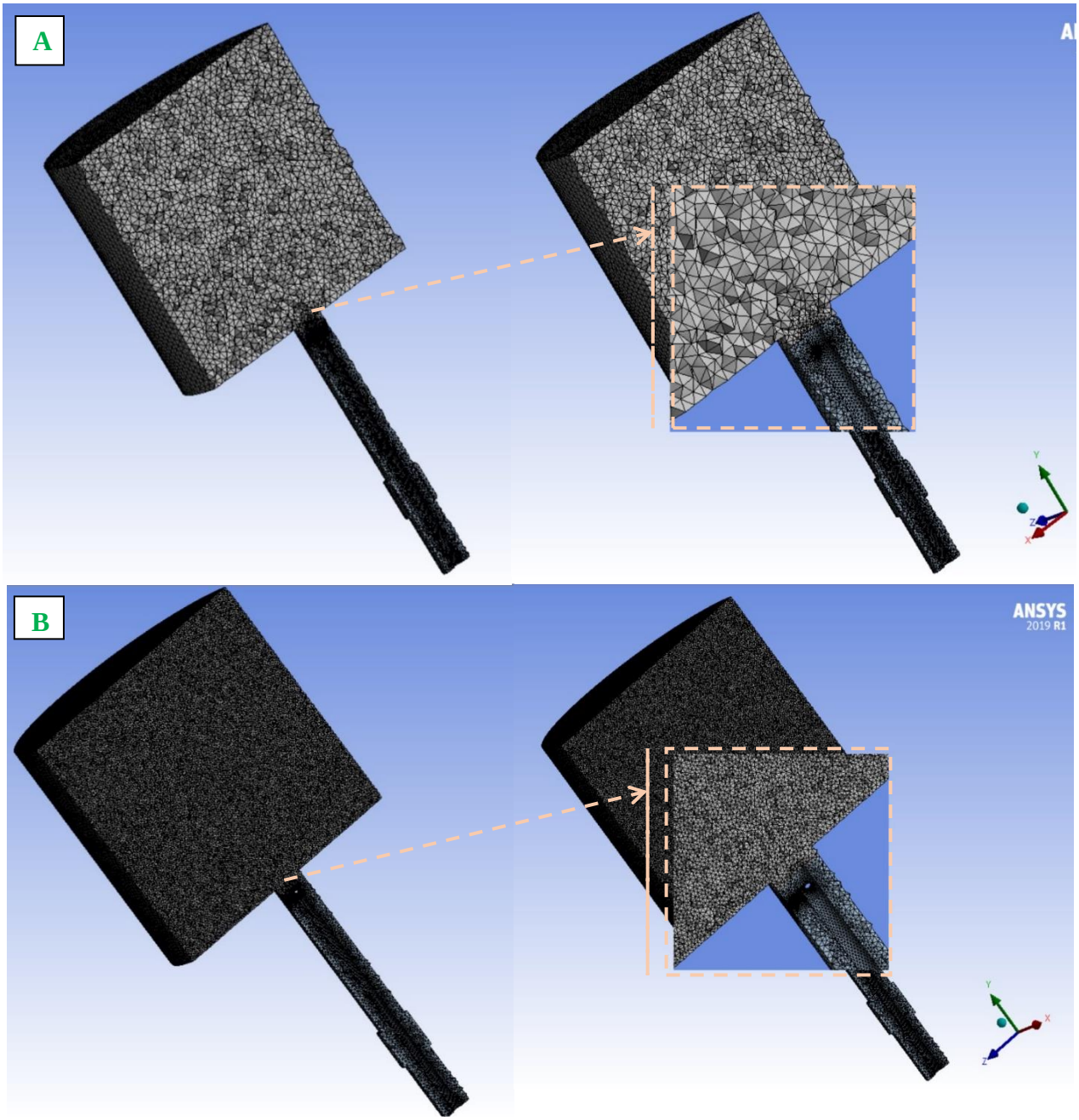

Figure 5-13: Mesh Refinement Differences (Cross-Section). A. Mesh One, B. Mesh Five. Swirling Simulation.

5.4 Turbulence models

The related numerical studies have been reviewed in section 2.3.3 specify that the most models used in the previous studies are as follow:

1. General Reynolds stress model RSM

2. k-ε turbulence model

3. RNG k-ε turbulence model

4. Shear Stresses SST

Furthermore, some published research applied more than the mentioned models, but the swirl strength is very low and there is more need to include more turbulence models at different swirl strength. Therefore, the RANS turbulence models use in this study are as follow:

1. Standard k-ε turbulence model
2. RNG k-ε turbulence model
3. Shear Stresses SST
4. The Standard Reynolds Stress Model RSM, as follow:

a) Launder, Reece and Rodi turbulence model (Isotropizatio of Production) (LRR-IP-RS)

b) Speziale, Sarkar and Gatski turbulence model (SSG-RS)

5. Omega-Based Reynolds Stress Model (Omega-RS)

The above models represent most of the RANS models implemented in ANSYS-CFX simulation program. The differs among each turbulence models are explained in section 3.9 which show each model's limitations. On the other hand, the first three turbulence models examined in this study due to their common use in various published work for different types of flow. For instance, standard k-ε turbulence model is good for fully turbulent flows, while RNG k-ε turbulence model has large ability of modelling strained flows and low Reynolds number flows. Interestingly, Shear Stresses SST is good for transitional, free shear and compressible flows due to the ability of modelling near-wall conditions. In addition, it is a common knowledge that RSM turbulence models are good for swirling flow. Hence, most of them employed in this study to indicate the drawbacks and limitation for all of them. Therefore, indicate the ability of these models to perform the swirling flow at different strength is highly recommended to identify the advantage/disadvantage attached to them (I. Ansys, 2011; CFX, 2018; Wasserman, 2016).

Chapter 6 RESULT & DISCUSSION

6.1 Planar jet case study one

The next sections demonstrate the results of the first case study for the planar jet flow by comparing them with RANS turbulence model e.g., standard k-ε turbulence model only that uses by the author in this work. However, the first section 6.1.1 indicates the effects of mesh quality on the results by applying different types of meshes along with different quality. Then, section 6.1.2 involves a detailed study of the self-similar area which been computed by the RANS model to compare it later with the published data. Lastly, the RANS turbulence model will be evaluated with the experimental and numerical case study data via using RMSE method as shown in section 6.1.3 below.

6.1.1 Effects of mesh quality

Generally, the quality of the mesh has a huge effect on the results, so it is very important to obtain the correct mesh types alongside with the best quality. Therefore, many meshes examined to determine the correct mesh which able to compute an accurate analysis. The first chosen mesh is uniform mesh as shown in Figures 6-1, 6-2 and 6-3 where different kinds of implementing technique has been used such as cut-cell and body dividing methods. Curiously, the results of this kind of mesh are not correct due to incompatibility between them and ANSYS-CFX solving method, see section 6.9. Alternatively, the Tetrahedrons mesh shows a massive potential to capture the volume fraction value as it is the main computed quantity. Moreover, the initial mesh offers a weak data collection due to the low number of nodes inside the mesh as shown in Figure 6-4A and the mesh results are not symmetrical, as expected. Therefore, by using a mesh refinement process and increasing the element number, the mesh begins indicating the correct and logical values with a symmetrical result as shown in Figure 6-4B. As a result, it is very important to choose the correct mesh along with the proper mesh size.

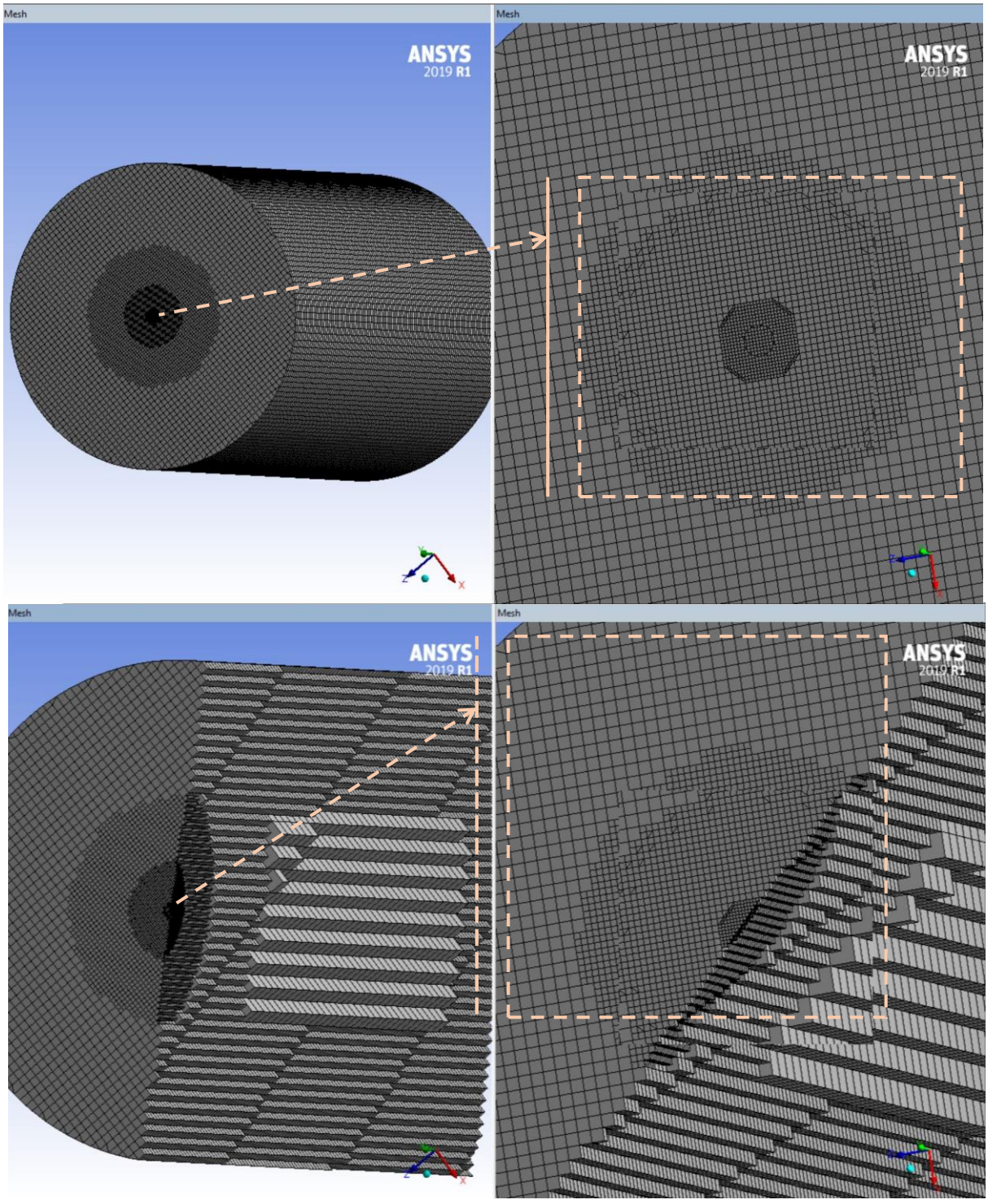

Figure 6-1: Cut-Cell Meshing Technique At Different Views.

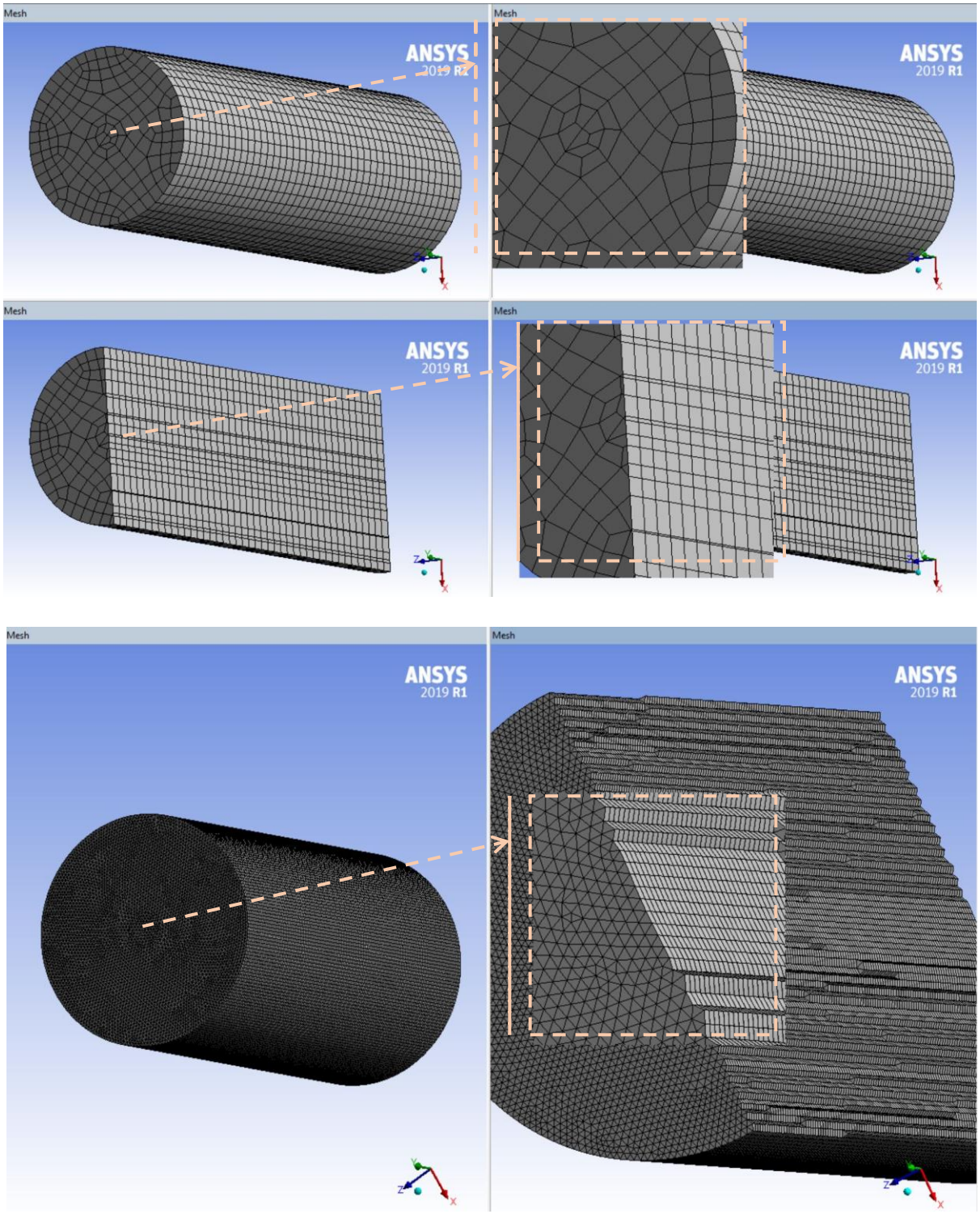

Figure 6-2: Uniform Meshing Technique At Different Views.

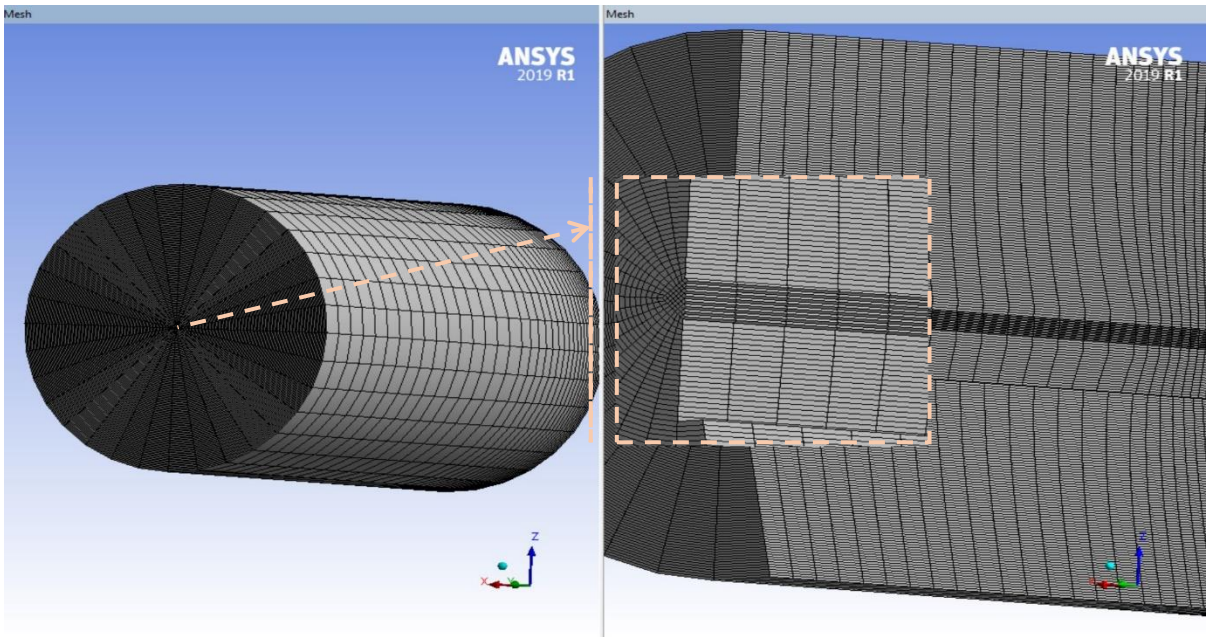

Figure 6-3: Multi-Body Uniform Meshing Technique At Different Views.

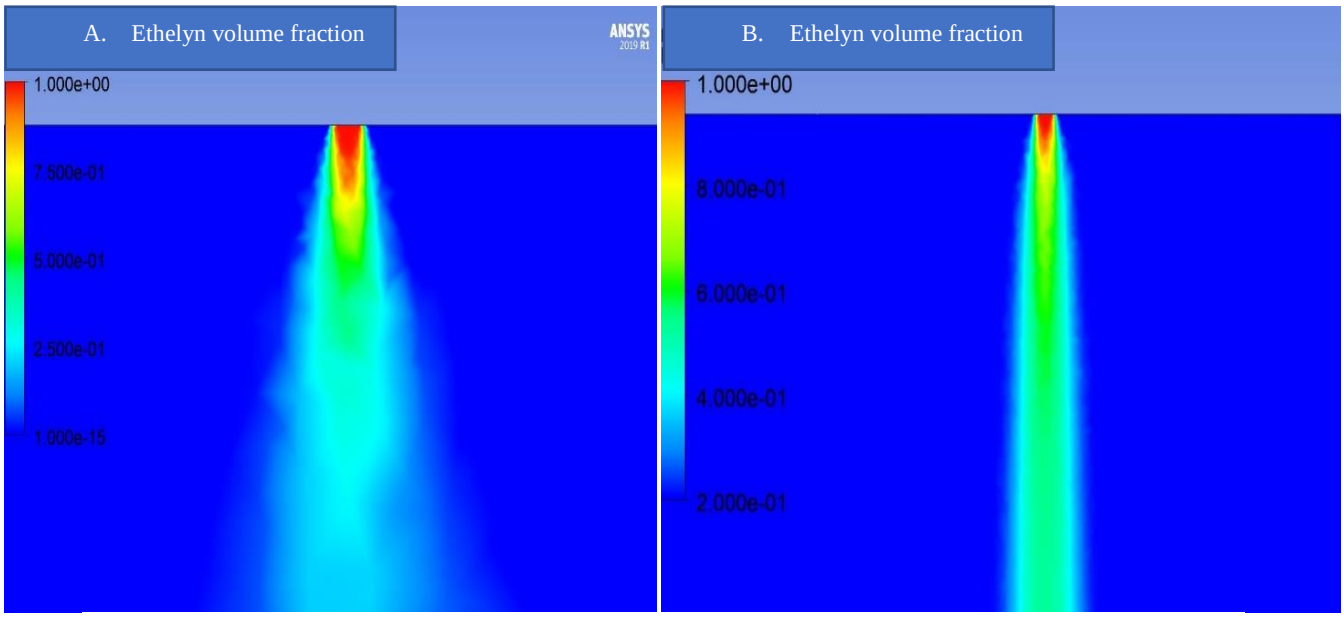

Figure 6-4: Mesh Quality Effects On The Results: A. Low Mesh Size. B. High Mesh Size.

6.1.2 Self-similar area

The published numerical study done by (Lubbers et al., 2001), which based on the same experiment that performed by (D. Dowling & Dimotakis, 1988; D. R. Dowling, 1988; D. R. Dowling & Dimotakis, 1990), is to investigate the self-similar area in a certain location has been explained in sections 2.2.2, 2.2.3, and 4.1. The self-similar area is the zone where any quantity profiles such as velocity profiles is similar at various values of x known as self-similar. In another meaning, it happens when the profiles of velocity can be brought to harmony through scale factors which rely on one transformed coordinate where the flow has reached a sort of equilibrium. The result of this phenomena is represented by reducing the governing equations to an ordinary differential equation form. Plus, all terms at an identical relative location have an identical relative value for the dynamic's equations and boundary conditions. Hence, Self-similar area is an asymptotic state (Carazzo et al., 2006) where a specific flow reaches as soon as its internal adjustments are finalized. In addition, different types of this phenomena can be reached such as a complete self-similar flow occurs at the turbulence moments and at all levels of motion. Or a partial self-similar flow appears at a specific intensity of the mean momentum equations only c.

The numerical simulation is conducted via using the standard k-ε turbulence model contained by ANSYS-CFX 2019 simulation programme. The discussion of the results begins with establishing the right outcome data from the chosen mesh. In other words, the Volume Fraction (VF) at specific location is computed to ensure the validation of the mesh. The findings indicates that the volume fraction of Ethylene start decreases along the jet axial starting from 0.442 at 20 D_E till 0.351 at 80D_E, as shown in Figure 6-5. Furthermore, the volume fraction is calculated against a dimensionless factor x/r where x refer to the location point in the computational domain and r is the Ethylene inlet radius. The symmetrical results along the logic results provide more confidence to the run for incoming outcomes. Initially, the potential core length Z_o referred in section 4.1.1 is computed via using the volume fraction alongside the jet axial length x as shown in Figure 6-6. The mentioned figure indicates that all meshes are sharing nearly the same value of the potential core equal to 0.09m, which uses to calculate the core angle before. On the other hand, the self-similar area is computed by using the concentration mean profile as a function of the similarity coordinate η which is a non-dimensional parameter, known as the ratio between the radial distance to the jet centreline to the differences between the potential core and the axial distance i.e., distance to the jet orifice, as follow:

$$\eta = \frac{r}{x - Z_o} \tag{6-1}$$

Or sometimes uses as:

$$\eta = \frac{r}{r^{0.5}} \tag{6-2}$$

Where $r^{0.5}$ is the radial distance where the local mean axial concentration is equal to half the value of the mean centreline concentration. Moreover, the mean concentration value is calculated by dividing the local concentration value C_i to the maximum concentration value C_o.

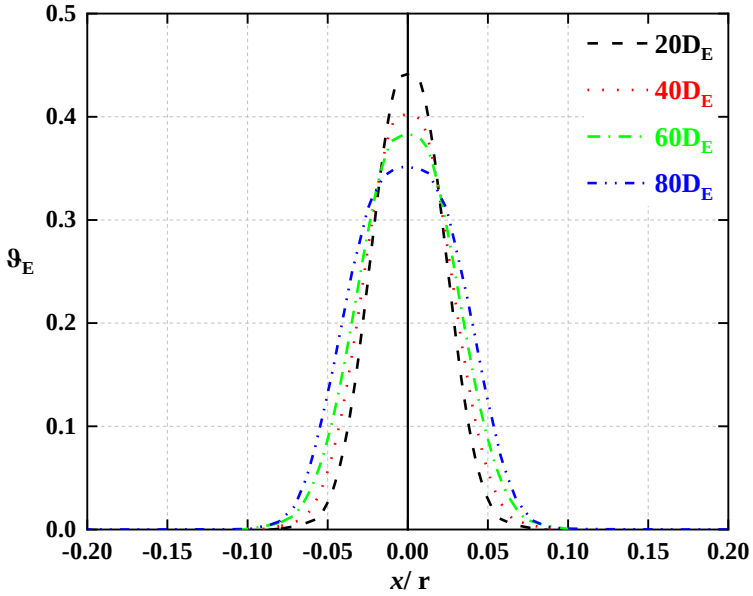

Figure 6-5: VF Of Ethylene At Different Locations In The Chosen Mesh

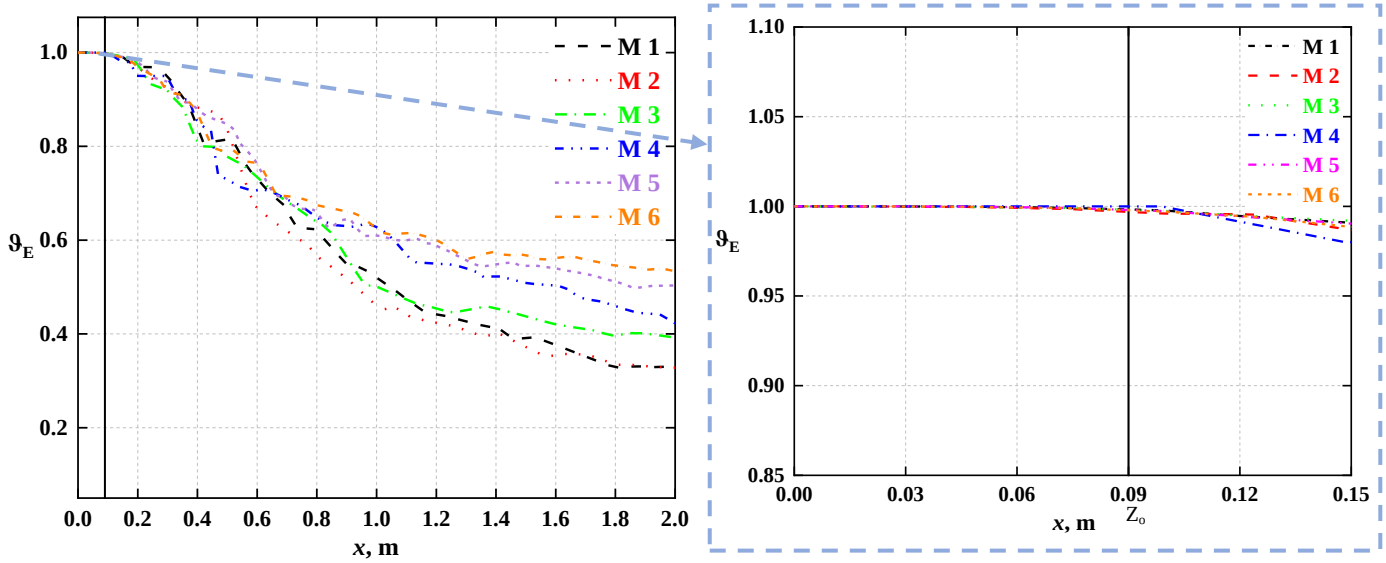

Figure 6-6: VF Of Ethylene Along The Jet Axial And The Potential Core Length Estimation.

Consequently, the mean concentration values obtained form the simulation are captured for the hall computational domain starting from $6D_E$ until $80D_E$ to indicate the starting point of self-similar area as shown in Figure 6-7. In addition. RMSE method is used to explain the deviation among all the computed locations by comparing each value to the last location 80 D_E. In this figure, the first few locations show a random behaviour because of transition region effects where the fluids flow not fully developed yet. Then, by eliminating these profiles, the results became clearer as shown in Figure 6-8. Although the previous figure reveal that mean concentration profile at $16D_E$ has a potential probability of being the self-similar area, the RMSE value is fairly high to be trustee. Therefore, it has been assumed that the self-similar area starting point is at the first location have an RMSE value of less than 10%. Thus, Figures 6-8 and 6-9 demonstrate the starting location of self-similar area is at $24D_E$ which have a value of RMSE equal to 9.90%. The results of the present study also suggest that the self-similar area is in the region $24D_E < x \leq 80D_E$ as shown in Figure 6-10. The last figure illustrates the self-similar area at the same locations as the experiment uses except the first location $24D_E$ because the starting point of the self-similar area in the experiment is at $20D_E$.

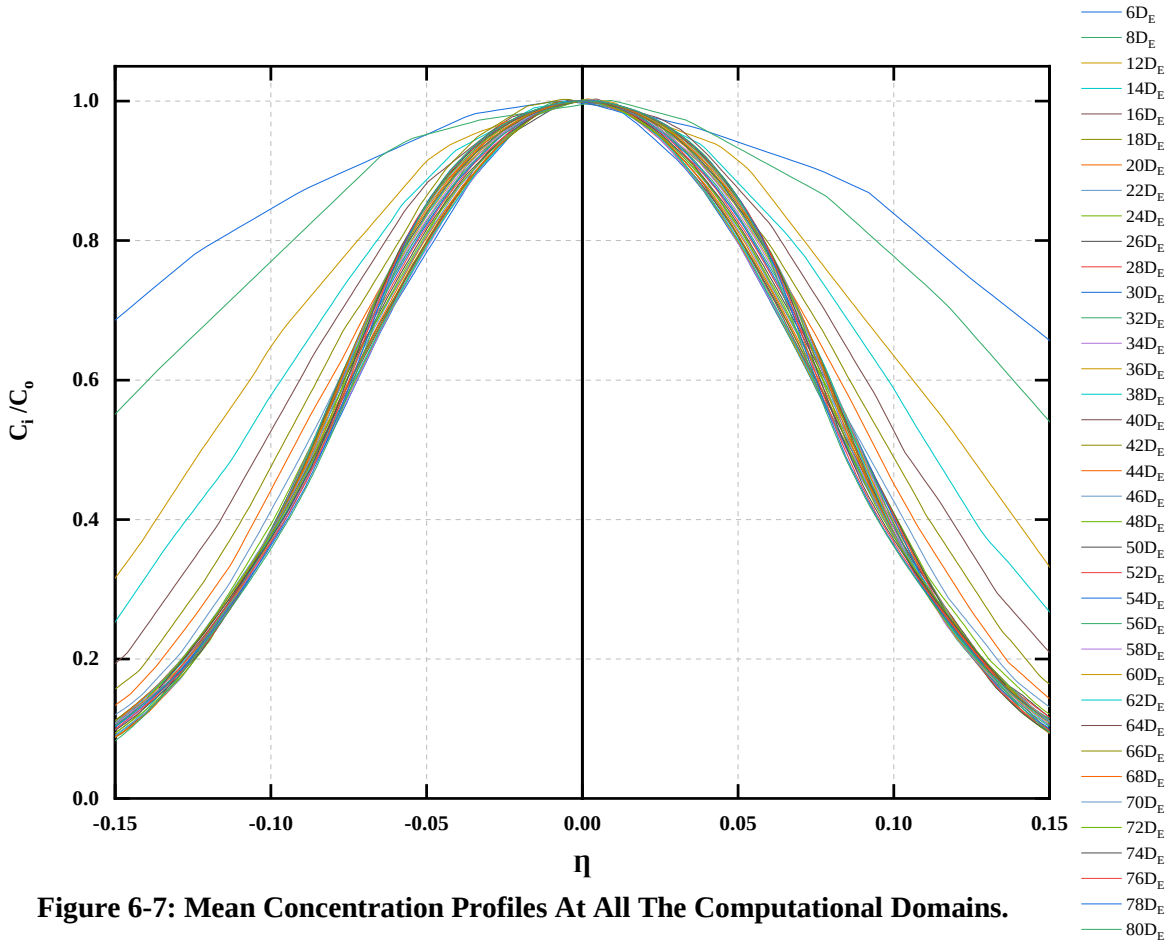

Figure 6-7: Mean Concentration Profiles At All The Computational Domains.

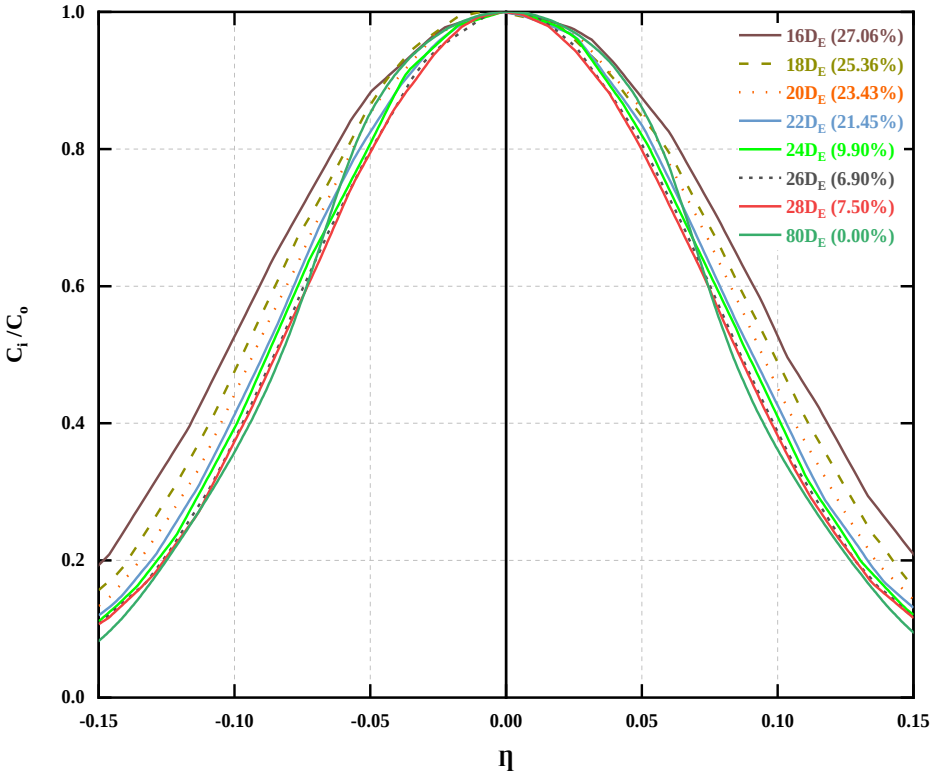

Figure 6-8: Mean Concentration Profiles Elimination Process. RMSE Percentage Included.

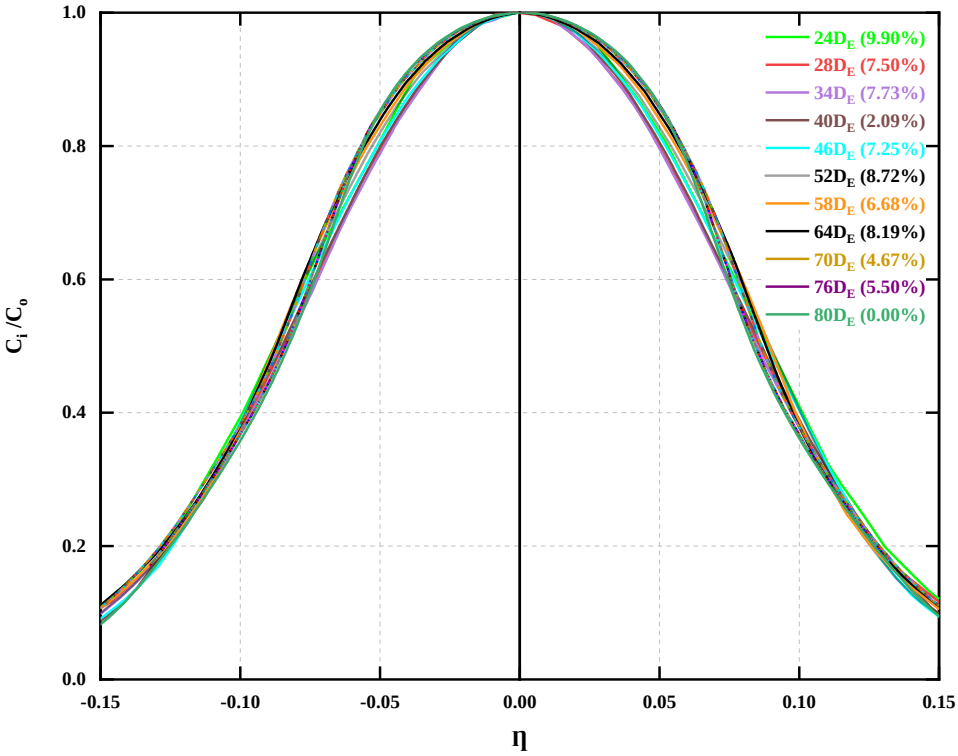

Figure 6-9: Self-Similar Area Starting Location. RMSE Percentage Included.

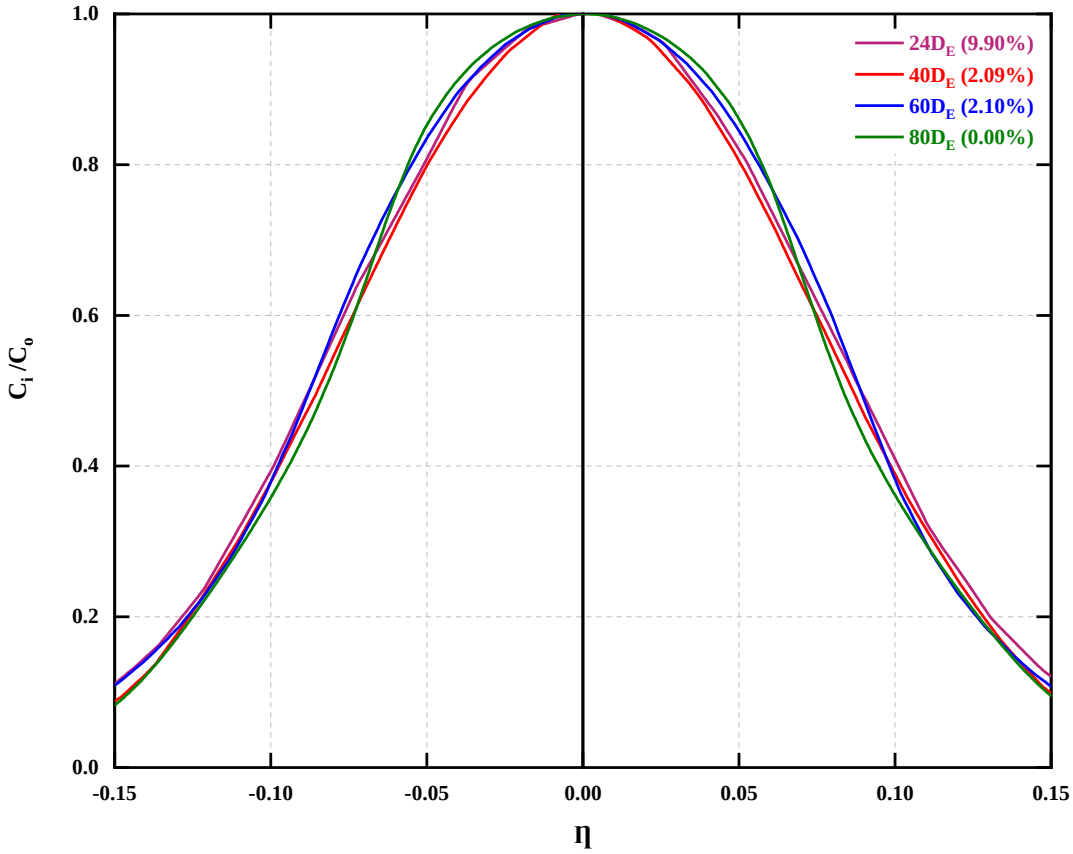

Figure 6-10: Self-Similar Area At Different Locations. RMSE Percentage Included.

6.1.3 Turbulence model outcome

The simulation finding provides evidence that the mean concentration profiles in the self-similar area are having a Gaussian profile. These new findings are concluded through using the curve fitting tool inside MATLAB R2020b for a random mean concentration profile as shown in Figures 6-11 with an R-square value of 0.9963. On the other hand, half-width known as the distance between the transverse plane and the centreline jet flow where the mean quantity such as concentration and velocity become half of the corresponding centreline quantity. Furthermore, the jet spread rate is computed as the slop of the axial half-width line (usually half-width have a linear increasing) which have a general value of 0.11 at a high Reynolds number (Yue, 1999). Therefore, by applying the Gaussian fitting profile along with half-width value will indicate the concentration spreading rate K_c as follow:

First, the author simulation results show that the estimation value of the half-width $\eta^{1/2}$, i.e., the value of $r/x - Z_o$ at $C_i/C_o = 0.5$ is computed by taking the average value of the mean

concentration profiles at $24D_E$, $40D_E$, $60D_E$ and 80 D_E, which approximately equal to 0.109 as illustrated in Figure 6-12. Then, due to Gaussian effect, which means:

$$\frac{C_i}{C_o} = exp(-K_c \eta^2) \tag{6-3}$$

Thus, by solving the above equation with the given values of mean concentration and half-width, will obtain $K_c = 58.34$. Moreover, the related numerical investigation indicates that the spread rate and half-width values of the experiment are $K_c = 59.1$ and 0.108 respectively. Which means, the present finding also support the published study which concluded that the mean concentration is self-similar and not depending on the Reynolds number. Alternatively, the RMSE method is applied between the author simulation and the experiment data to indicate the deviation among them. The outcome findings reveal a very good agreement between the RANS turbulence model and the experiment where the maximum error percentage is 6.73% at $60D_E$ and the lowest is 4.95% at $40D_E$ as shown in Figure 6-13. Furthermore, Table 6-1 show the total average RMSE percent for at the above locations which indicate that the expect error percent is less that 10% for the computational domain. Lastly, the above simulation findings seem reliable and are in decent agreement with the published data. As a conclusion, the standard k-ε turbulence model is success in this type of investigations for a planar jet flow.

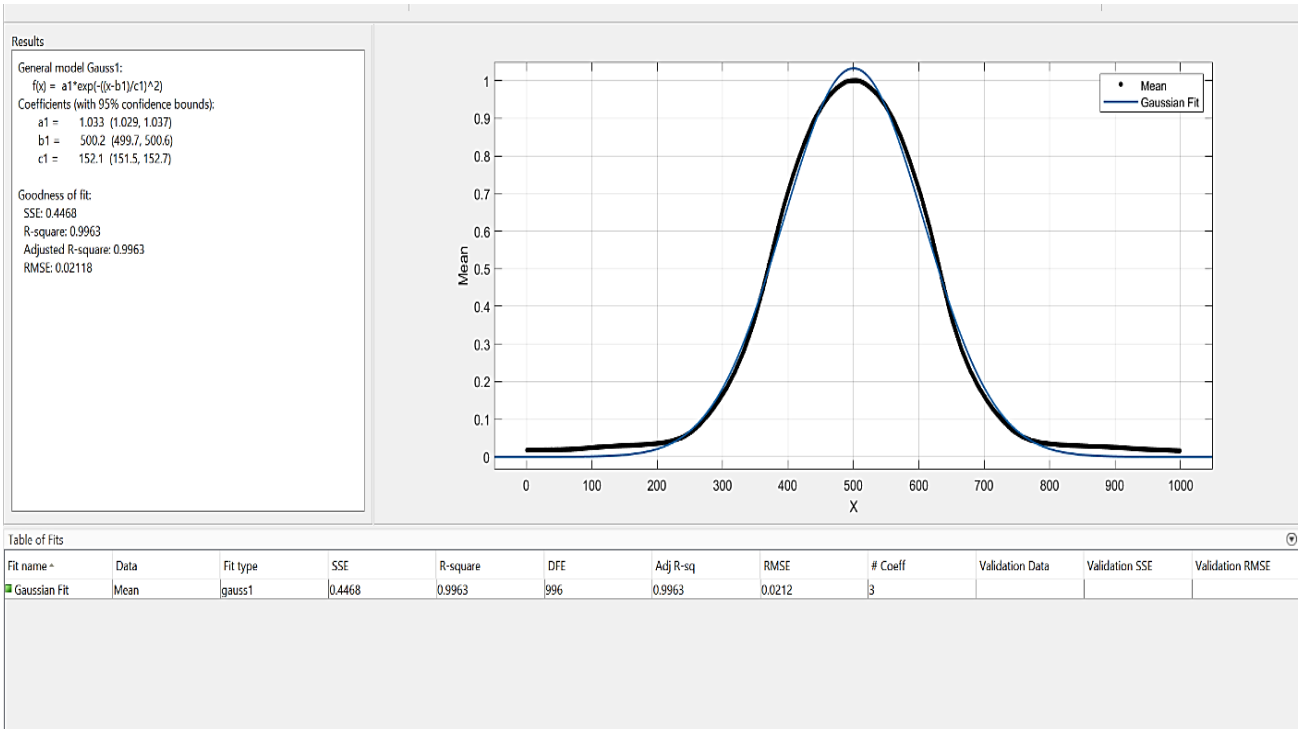

Figure 6-11: Curve Fitting Tool For The Mean Concentration Profile

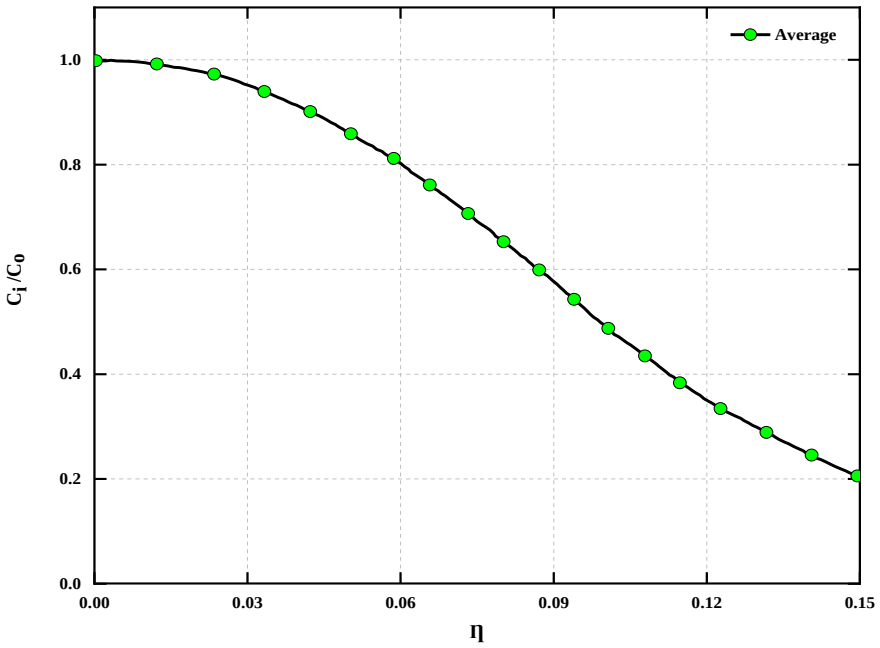

Figure 6-12: Half-Width Indication For An Average Mean Concentration Profile.

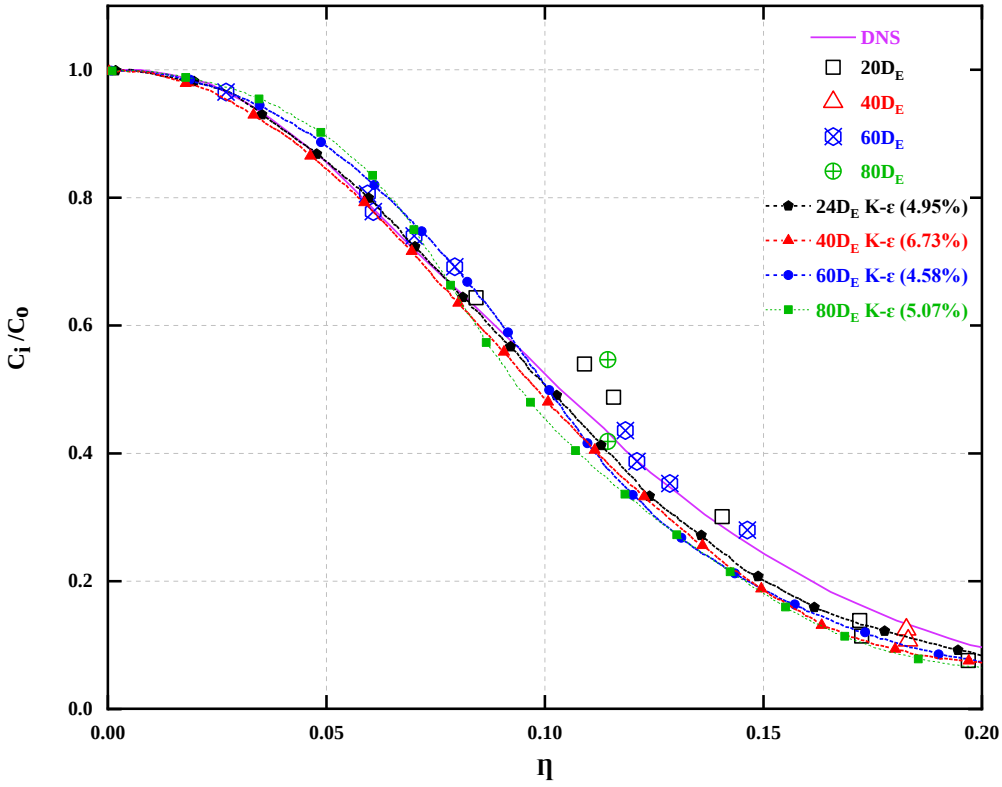

Figure 6-13: The Simulation Outcome; Standard k-ε Results At Different Locations For The Mean Concentration Profiles, Along With The Published DNS Numerical Method And The Experiment Data. RMSE Percentage Included.

Table 6-1: RMSE Percent Value At A Specific Location. First Planar Case Study

Location	RMSE Percent %
24 D_E	4.95
40 D_E	6.73
60 D_E	4.58
80 D_E	5.07
Average	5.33

6.2 Planar jet case study two

The features of second planar jet flow are explained in sections 2.3.2 and 4.2 where the volume fraction is used to assess the RANS turbulence model i.e., Standard k-ε turbulence model only, by comparing them with the experimental study data via using RMSE method. Therefore, the next first section is demonstrating the effects of mesh quality on the results when different kinds of meshes applied down. The sections after 6.2.2 and 6.2.3 are showing the turbulence model results and the effect of the diffusivity in the simulation. Finally, the 2D and 3D contours is established to show the effects of turbulence model in a planar jet flow.

6.2.1 Effects of mesh quality

It has been designated before that the mesh type structure has a huge effect on the simulation outcomes, the same process is used as the previous case study to choose the correct mesh. Moreover, to reach the desirable mesh, few types of mesh form is applied. For instance, Figures 6-14 to 6-16 illuminate a different view of a uniform mesh structure where different methods are applied to generate the mesh. Unfortunately, all these types were not able to predict the right flow phenomena due to incompatibility between them and ANSYS-CFX solving method, see section 6.9. Instead, a Tetrahedrons mesh reveals a good possibility to describe the volume fraction value as been explained in section 4.2.3.

Moreover, the original mesh presents a low data collection for the volume fraction because of the low number of nodes inside the mesh as shown in Figure 6-17A where the mesh results are not symmetrical, as expected. Therefore, the mesh refinement process is used along with increasing the element number, the mesh starts implying the correct and logical values with a symmetrical result as shown in Figure 6-17B.

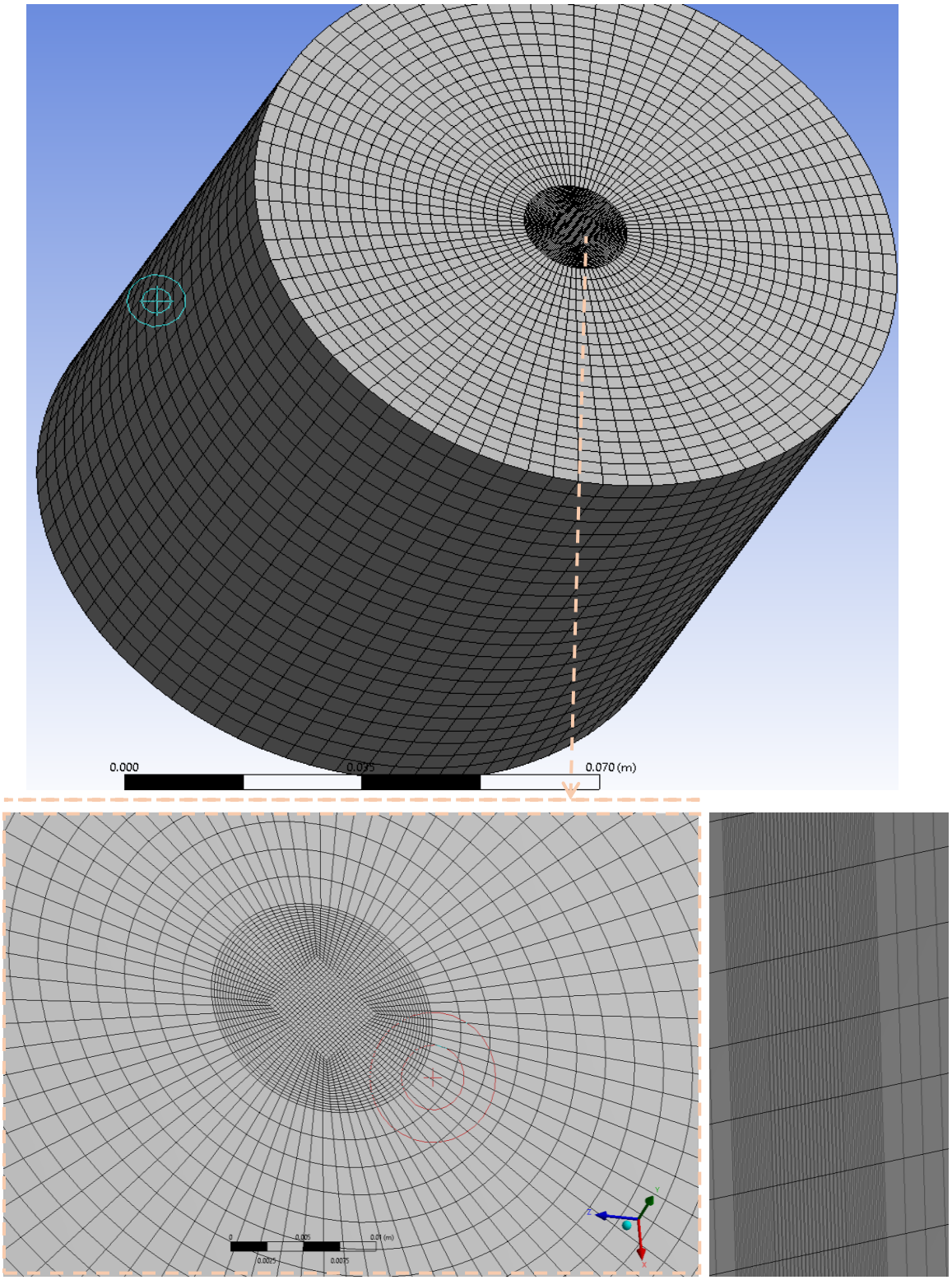

Figure 6-14: Uniform Mesh With A Structure Inlet At Different Views.

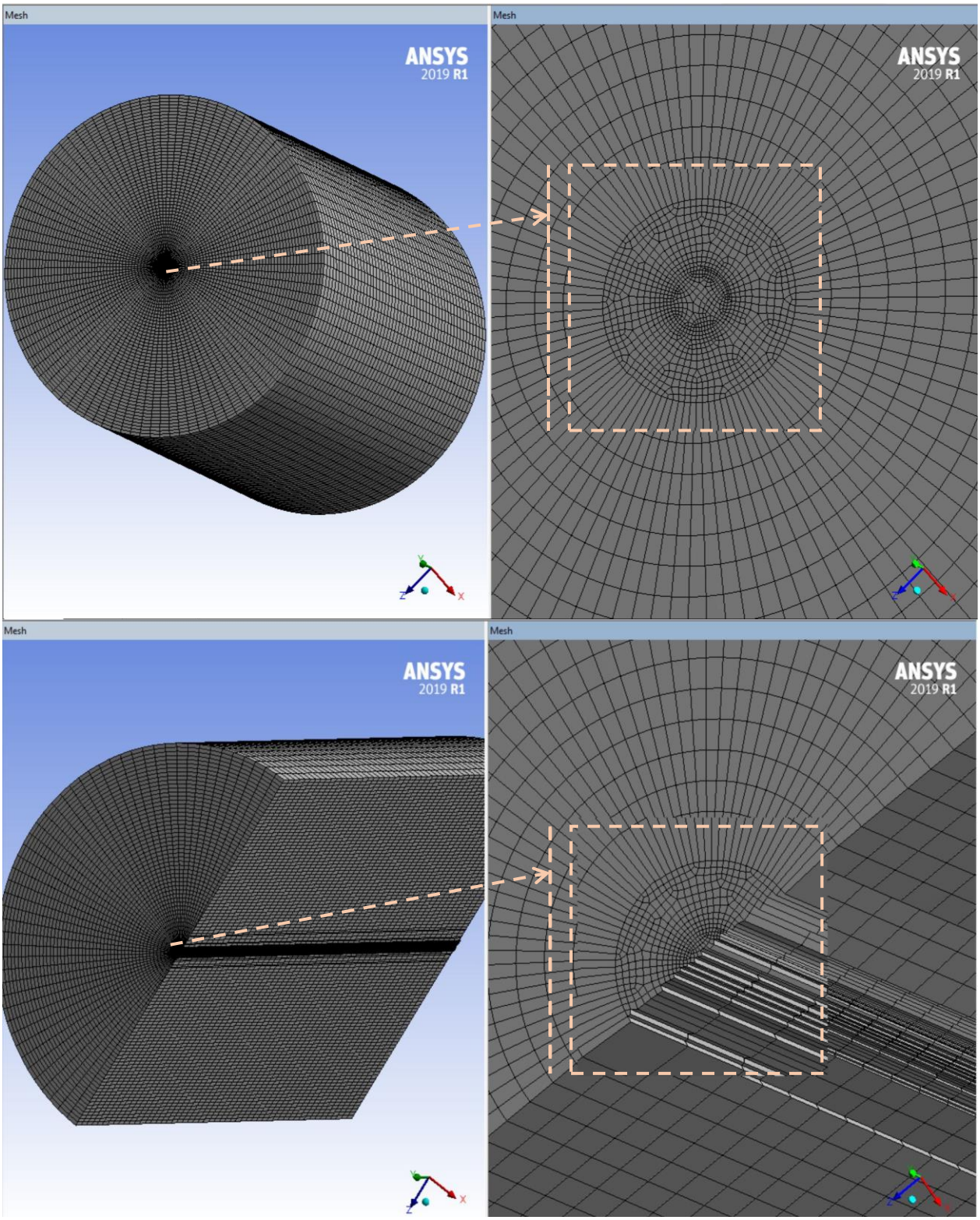

Figure 6-15: Uniform Mesh With A Tetrahedrons Inlet At Different Views.

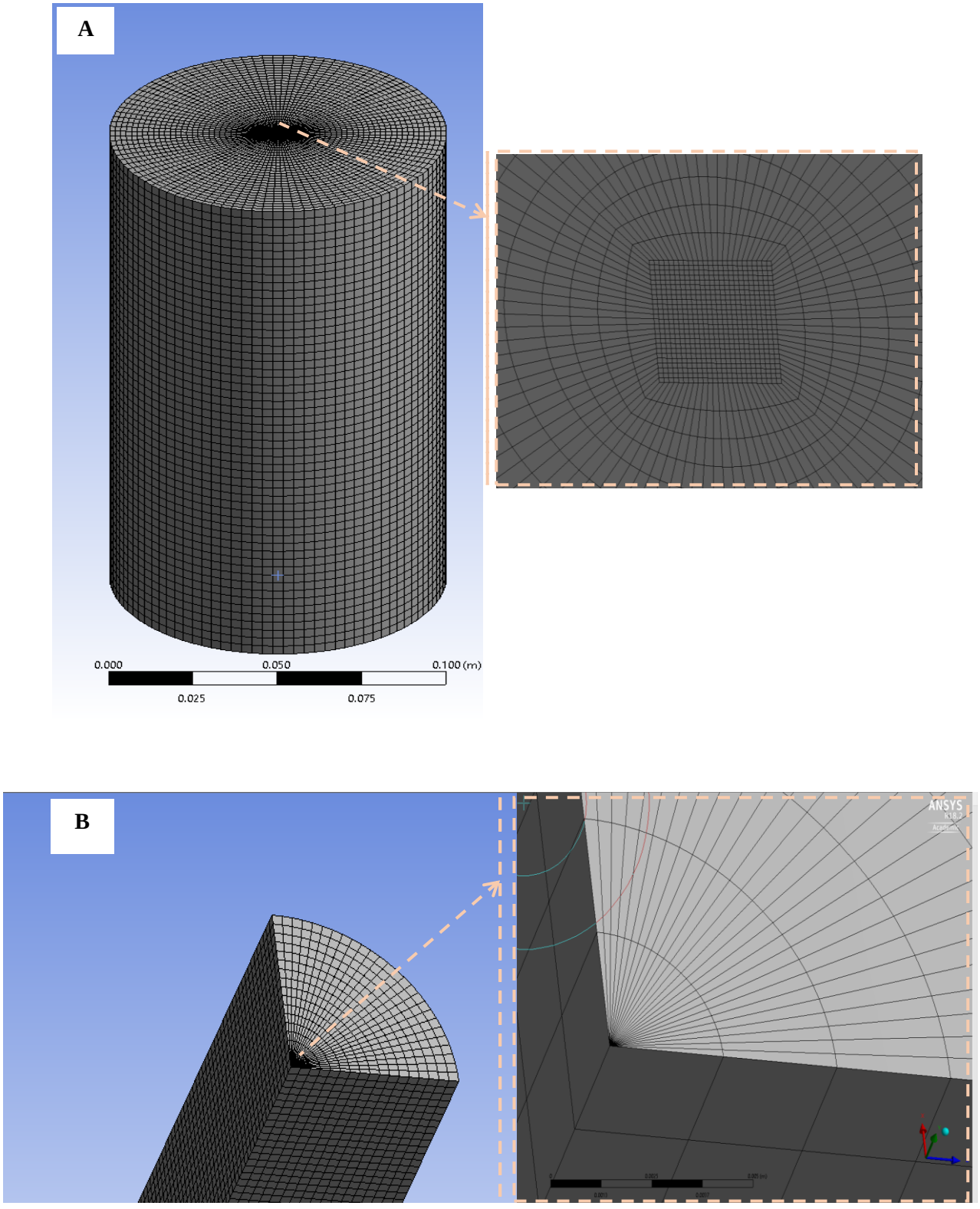

Figure 6-16: A. Uniform Mesh With A Structure Cylinder Centre At Different Views.

B. Quarter-Cylinder Uniform Mesh.

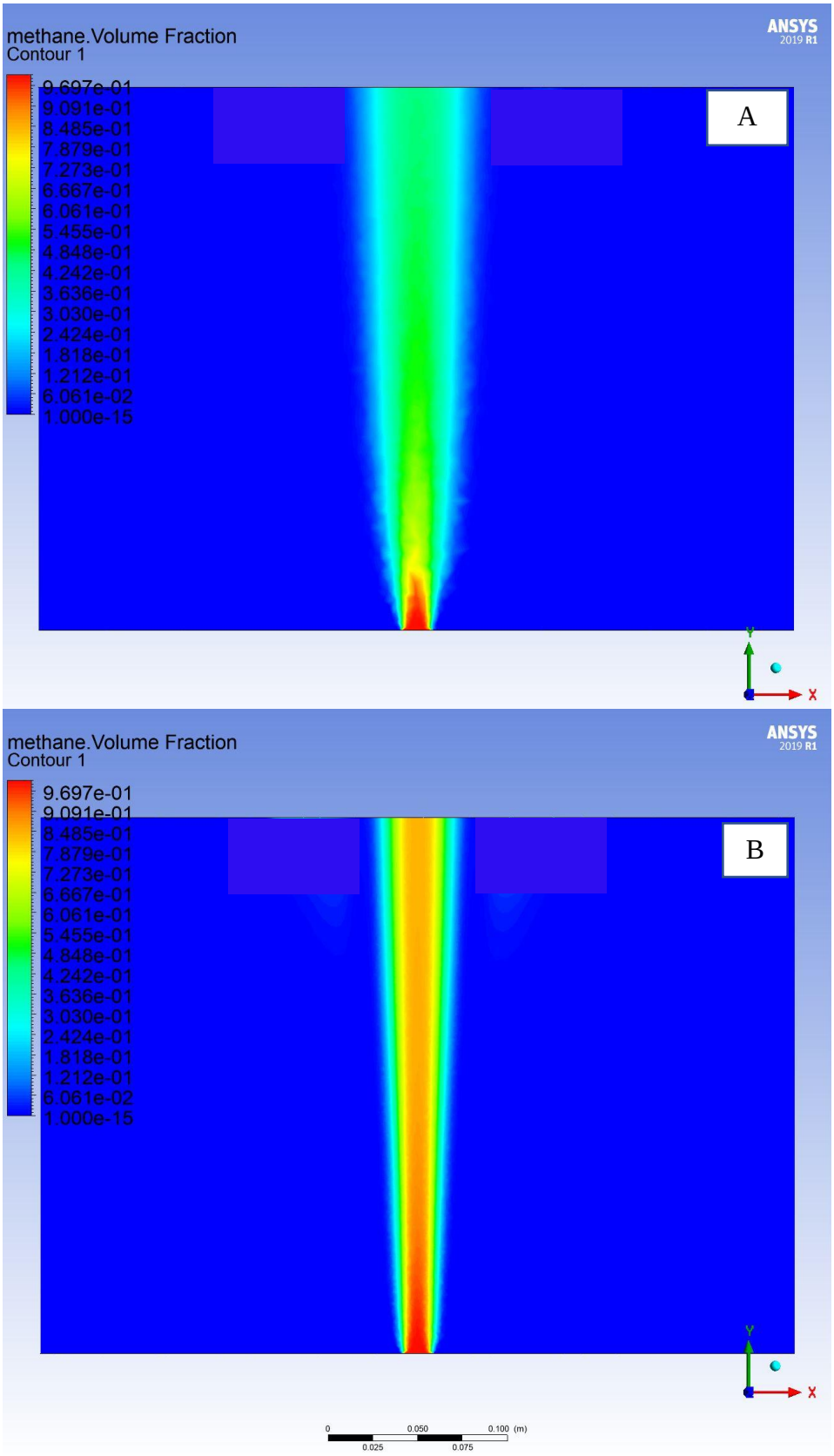

Figure 6-17: Mesh Quality Effects On The Volume Fraction:

A. Low Mesh Size. B. High Mesh Size.

6.2.2 Turbulence model outcome

The standard k-ε turbulence model is applied to study the planar jet flow via computing the volume fraction of Methane at the same locations as the experiment applied $1D_f$, $3D_f$, $5D_f$ and $7D_f$. However, the chosen mesh needs to be checked by taking out the volume fraction at the above places. The findings specified the validity of the mesh by showing the decreasing of the Methane volume fraction along the axial jet flow as shown in Figure 6-18. The earlier figure stated that the highest volume fraction is at $1D_f$ due to the close distance to the Methane inlet, while it reached the lowest value at the farthest distance from the orifice $7D_f$. Furthermore, the volume fraction is computed against a dimensionless factor x/R where x is the radial location in the computational domain and R is the Methane inlet radius.

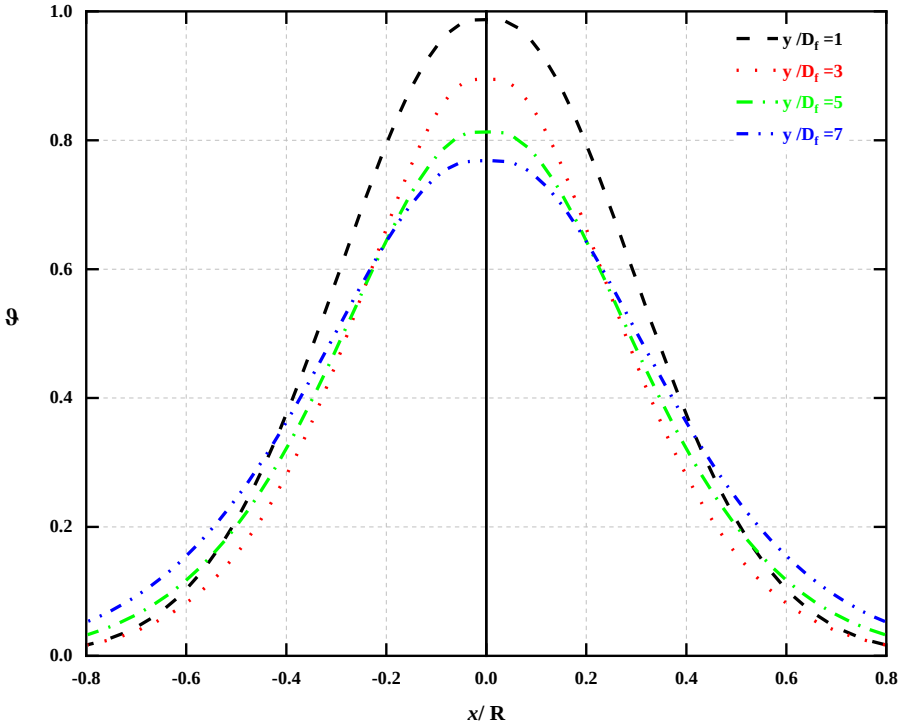

Figure 6-18: VF Of Methane At Different Locations In The Chosen Mesh.

Interestingly, Methane volume fraction at $1D_f$, $3D_f$ and $5D_f$ plotted in Figures 6-19 to 6-21 clearly show the great rapprochement between the experiment data and the author simulation. The RMSE percent attached to the previous figures show the small differences between the model and the experiment data, which is equal to 7.8%, 5.59% and 6.71% at the above location receptively. In another words, the model shows a brilliant prediction at the first three location, while the next section will explain the model outcome for the last location $7D_f$.

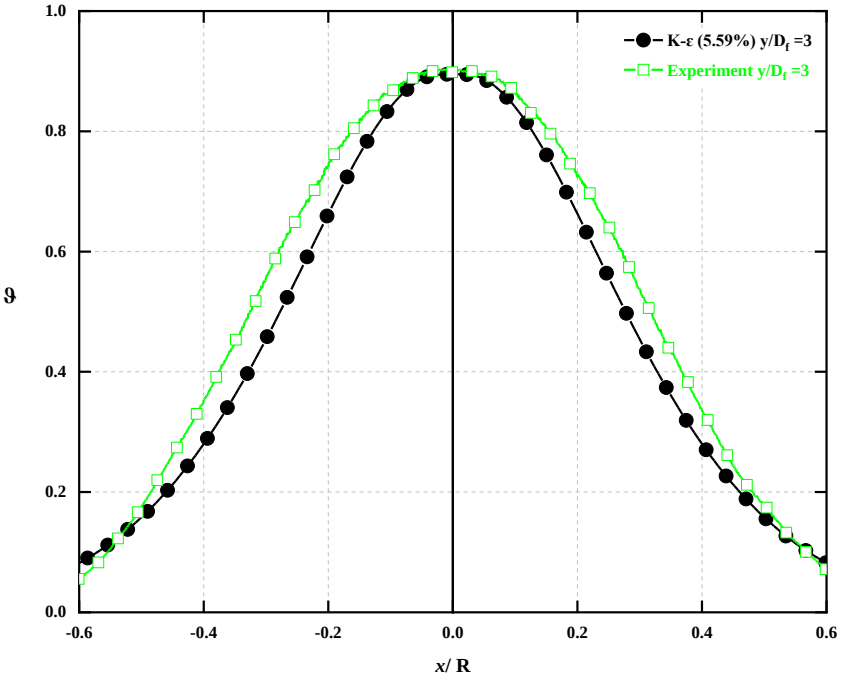

Figure 6-19: Vf Of Methane And Stetsyuk's Experiment At 1d$_f$. *k-ε*. Second Case Planar Jet Flow.

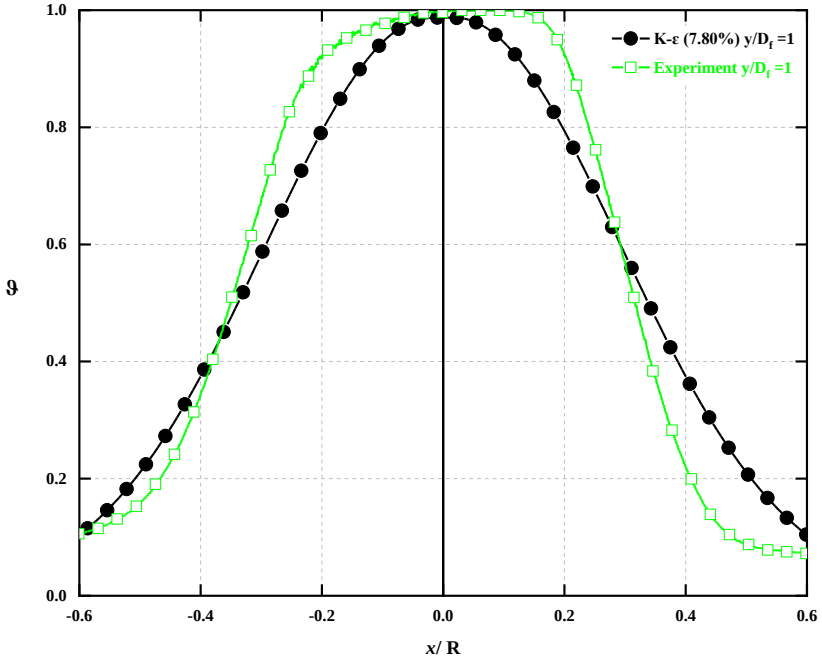

Figure 6-20: VF Of Methane And Stetsyuk's Experiment At 3D$_f$. *k-ε*. Second Case Planar Jet Flow.

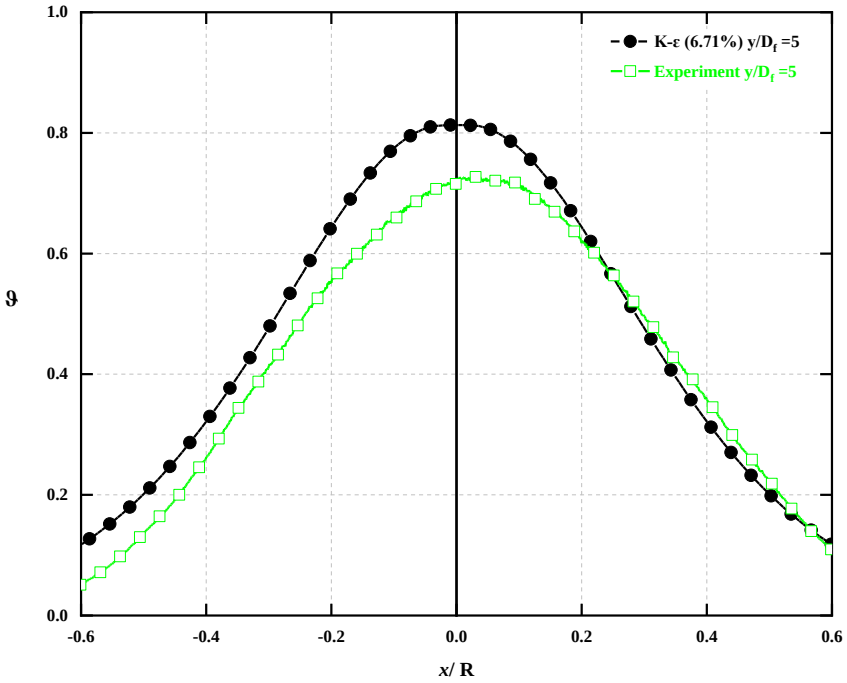

Figure 6-21: VF Of Methane And Stetsyuk's Experiment At 5D$_f$. *k-ε*. Second Case Planar

6.2.3 Effects of diffusivity

This section is focused on the effects of diffusivity on the results. Primarily, the diffusion effect reveals on the simulation due to the difference between the experiment scalar and the author simulation scalar. Whereas the experiment used the Acetone vapour as the passive scalar or tracer, the author simulation used the Methane to be the main scalar in this study. The reasons behind that are mainly to indicate the turbulence/diffusivity effect and the limited data base for ANSYS-CFX. Although the Reynolds number in this simulation is low 3770, the diffusivity effect did not occur at the first three locations because of the domination of the turbulence effect on the flow. Consequently, the module error percent was at an acceptable level.

Figure 6-22, however, shows that the RMSE percent between the author result and the experiment is alternatively high 23.89% at 7D$_f$, which reveal the effect of diffusivity on the flow where the diffusivity of Methane is 0.2182m^2/s while it is 0.124m^2/s for Acetone. This effect take place in the diffusivity term of the passive scalar Equation 3-25, see section 3.6. Alternatively, there is around 10% computing error in the experiment data due to laser diagnosed technique. The above reasons led to divergency between the simulation and the experiment numbers. Furthermore, Figures 6-23 and 6-24 explain all locations results between this study and the experiments outcome, while Table 6-2 display the total average RMSE percent for at the above locations.

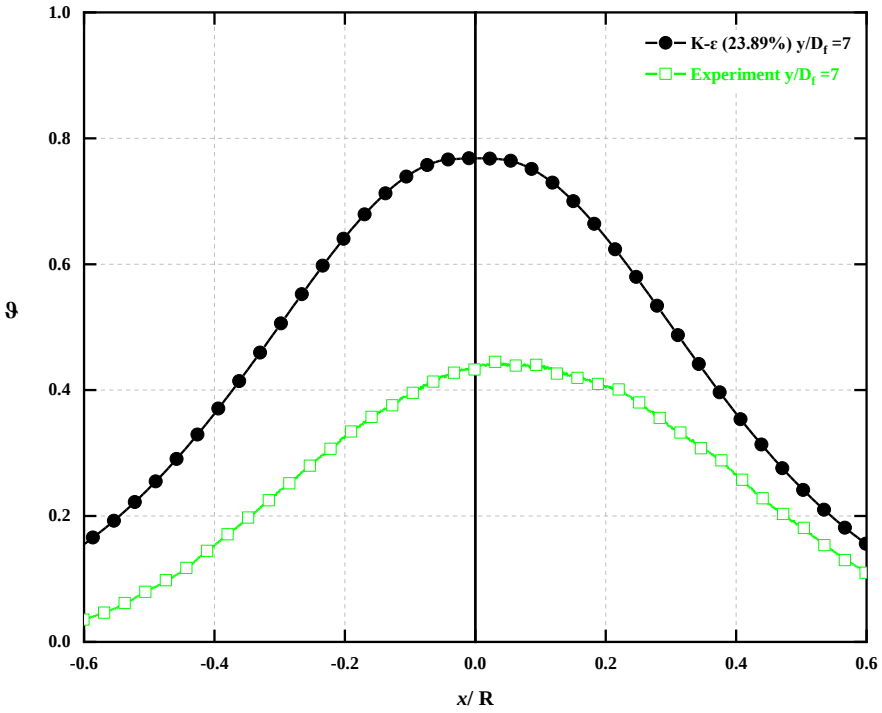

Figure 6-22: VF Of Methane And Stetsyuk's Experiment At 7D$_f$. *k-ε*. Second Case Planar Jet Flow.

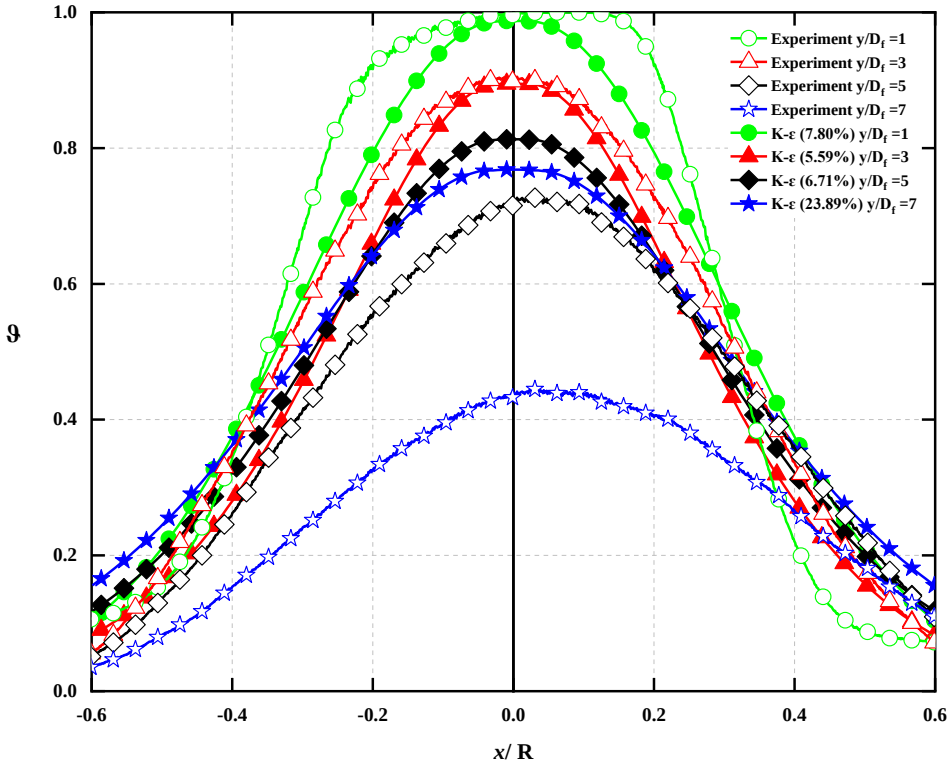

Figure 6-23: VF Of Methane And Stetsyuk's Experiment At All Locations. *k-ε*. Second Case Planar Jet

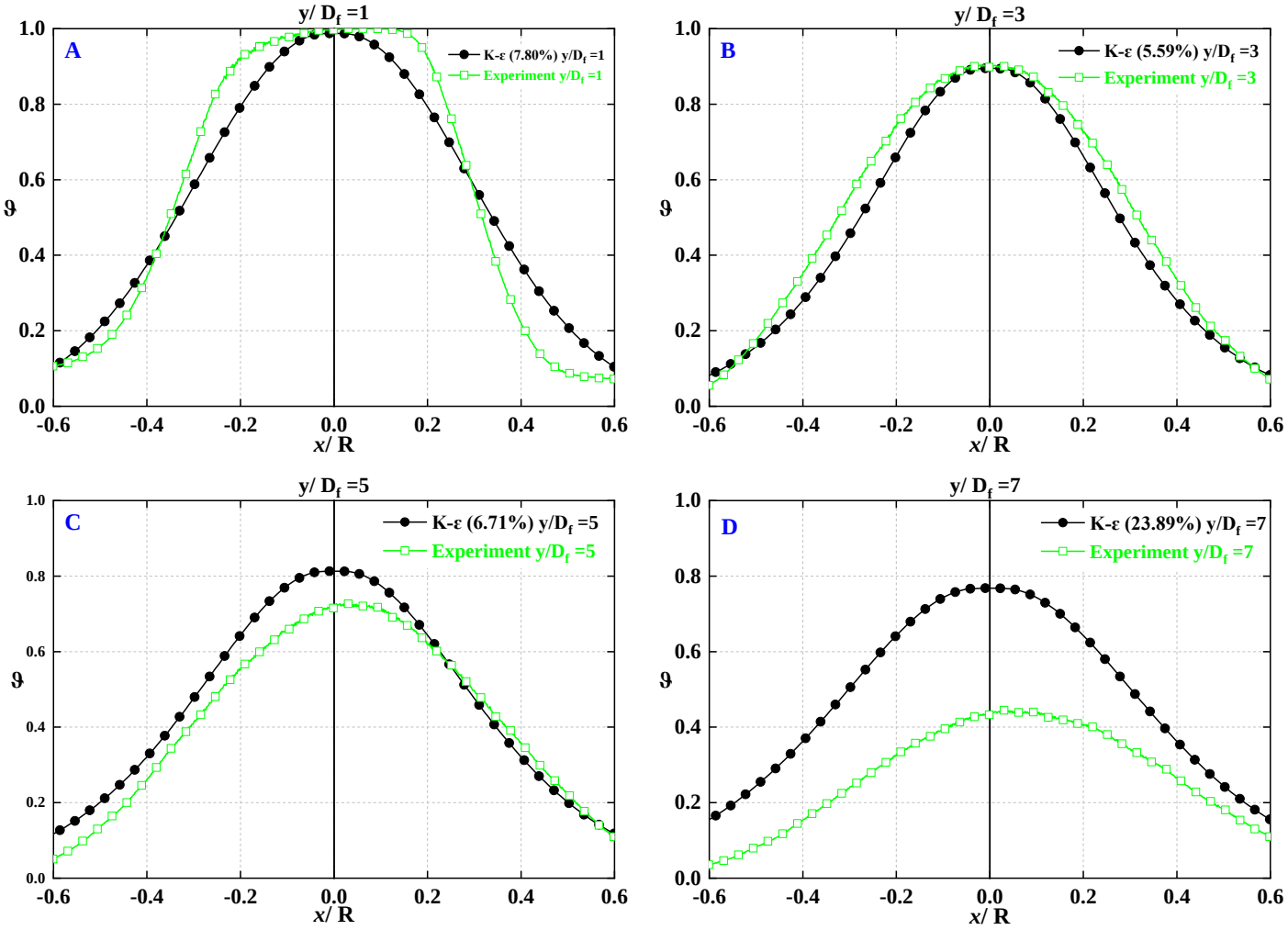

Figure 6-24: VF Of Methane Stetsyuk's Experiment. A. 1D$_f$, B. 3D$_f$, C.5D$_f$, D. 7D$_f$. *k-ε*. Second Case Planar Jet Flow.

Table 6-2: RMSE Percent Value At A Specific Location. Second Planar Case Study

Y/D$_f$	RMSE Percent %
1	7.80%
3	5.59%
5	6.71%
7	23.89%

6.2.4 Symmetric analyses

The symmetric profile has a significant impact on the simulation's outcome because it's showing the effect of swirl degrees on the flow profile which help to understand the swirl phenomena around the nozzle. Furthermore, the symmetric profiles are depending on many factors such as swirl degree, shape of nozzle and presence of flow defection e.g., screws.

Therefore, a 2D and 3D contours are employed in this study to illustrate the volume fraction of Methane at different sides as shown in Figure 6-25. In addition, the contours are based on using a non-dimensional scale for all the coordinates at different location i.e., at $1D_f$, $3D_f$, $5D_f$ and $7D_f$ above the inlet's orifice. Generally, the results at all locations show that the highest amount of Methane volume fraction is located at the centre of the inlet nozzle which proof the ability of turbulence model to predict this type of flow.

On the other hand, the contour at first location has largest amount of Methane's volume fraction among all the locations and it is gradually decrease at the second, third and fourth location. Moreover, the mentioned contours are shown that the volume fraction of Methane is gradually and equally decreases towards the end of nozzle's dimensions at each location i.e., the planar flow has no effect on the symmetric profile at the mentioned locations. Therefore, the turbulence model can predict the symmetric profile for the planar jet flow.

Conversely, the next sections related to this topic will show different results than the current results due to presences of swirl flow and a geometry effect i.e., screws inside the burner geometry.

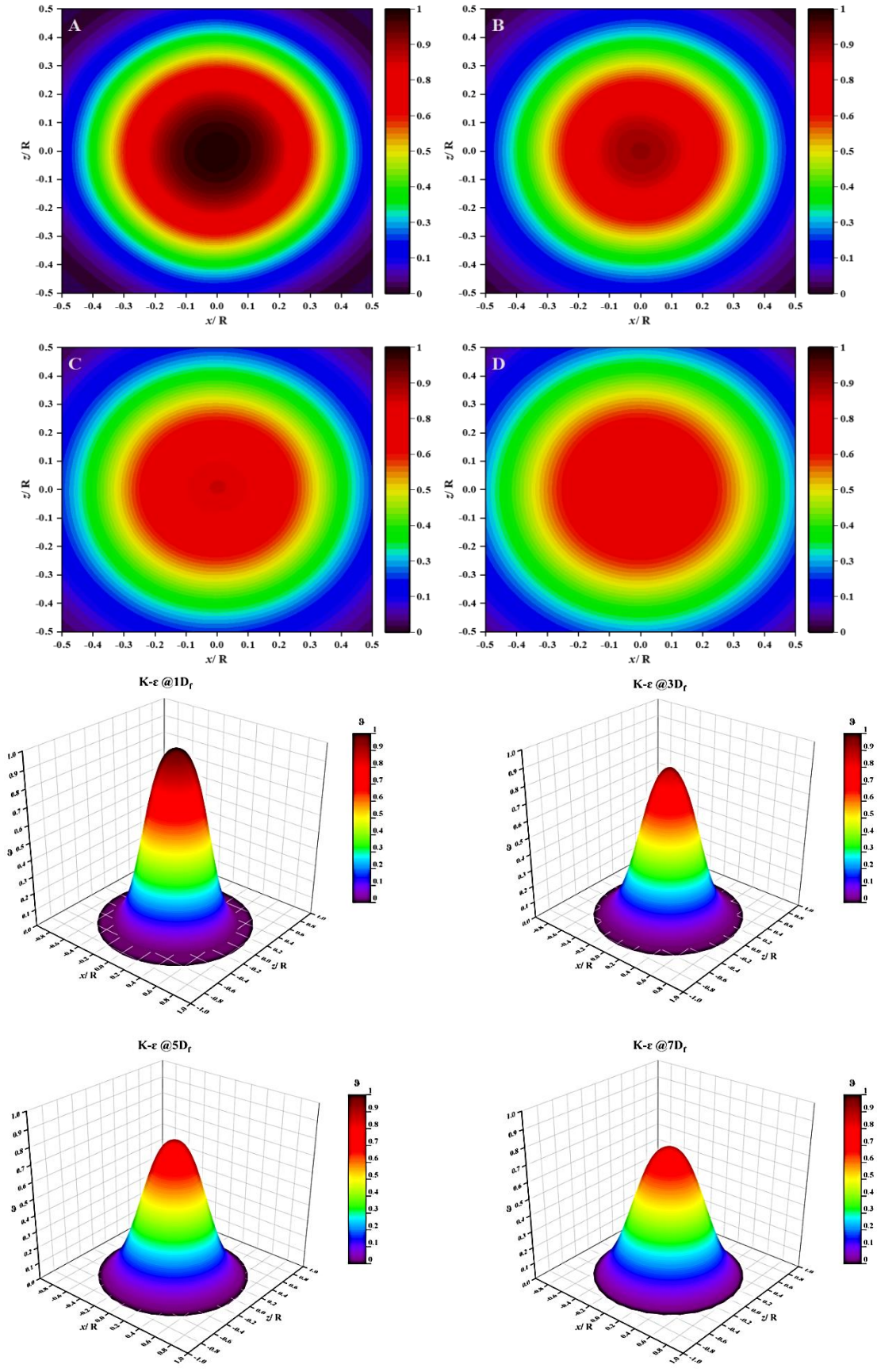

Figure 6-25: 2D (Top View) And 3D VF Contours Of Methane. A. $1D_f$, B. $3D_f$, C.$5D_f$, D. $7D_f$. *k-ε*. Second Case Planar Jet Flow.

Furthermore, the velocity of Methane contour, vectors and streamline is computed and plotted in Figures 6-26 and 6-27 to discover more flow features for this type of flow. The velocity findings seem to have a logic form along with the vector direction and the three-dimensional streamline. Finally, the above simulation discoveries appear dependable and are in good agreement with the published experiments data. Therefore, the standard k-ε turbulence model can achieve the investigation aims for the planar jet flow.

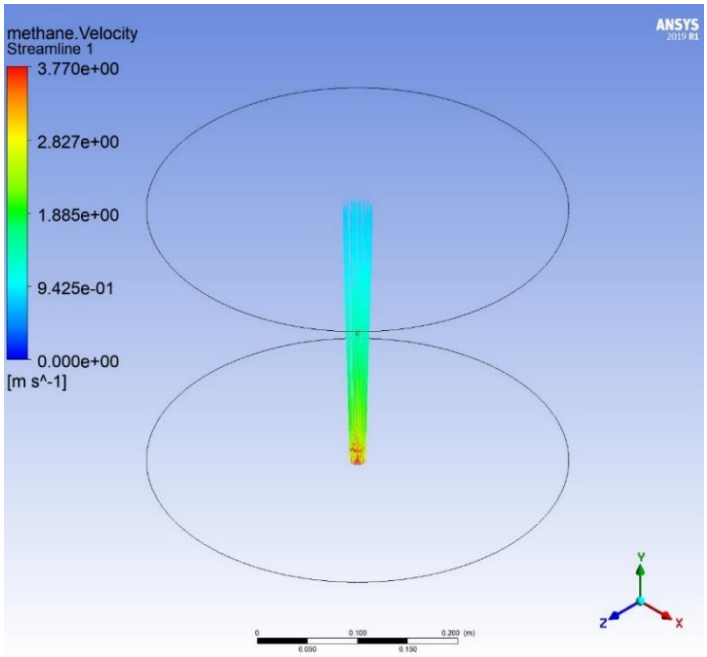

Figure 6-26: k-ε Methane Velocity 3D Streamline. Second Case Planar Jet Flow.

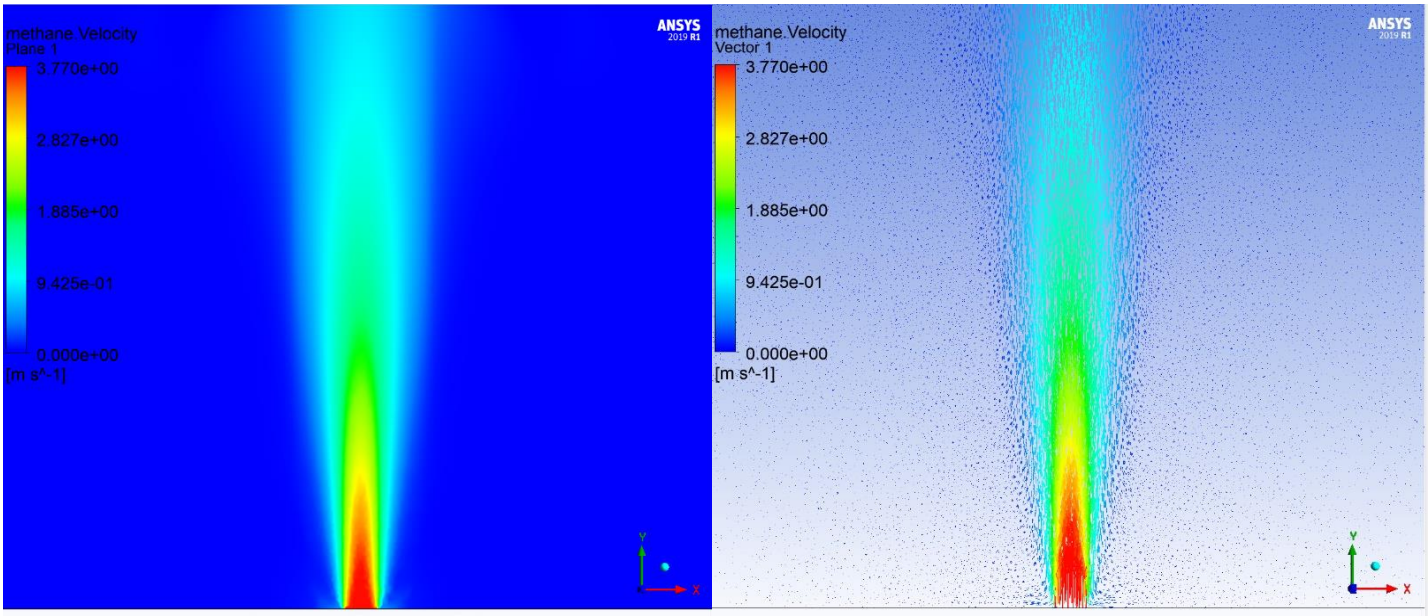

Figure 6-27: k-ε Methane Velocity Profile And Vectors. Second Case Planar Jet Flow.

6.3 Swirl jet flow

The swirl jet flow study is the key part of this work where multi-swirl strength e.g., depending on the swirl number value, is numerically computed via applying ANSYS-CFX simulation programme. Therefore, three swirl strengths are used to indicate the aims of this study: at S=0.3, S=0.58 and S=1.07. As been mentioned before, the swirl study is based on the experiment data which have been don by (Stetsyuk, 2014). Furthermore, many RANS turbulence models are applied at each swirling number where RMSE method is also used to compare between the model and the experiment data.

6.4 First swirl number (S=0.3)

The flow boundary conditions are explained in section 5.2 and noted in Table 5.1. Importantly, the volume fraction is used to illustrate the simulation findings in the previous case studies of planar jet flow. However, Methane mass fraction or mixture fraction ω_M is applied to fulfil the purposes of this study in all swirl cases. Therefore, Methane volume fraction ϑ at each location is converted to a mass fraction as shown below:

$$\omega_M = \frac{W_M}{Total\ mass} \tag{6-4}$$

Where:

$$Total\ mass = W_M + W_{Air} = \vartheta \left(\frac{M_{wM}}{22.414}\right) + ((1-\vartheta)\left(\frac{M_{wAir}}{22.414}\right) \tag{6-5}$$

Where W_M, M_{wM} and W_{Air}, M_{wAir} is the mass and molecular weight of Methane and Air, respectively. And 22.414 is referring to the volume gas constant at Standard Conditions for Temperature and Pressure (STP) which assumed in for Methane in this study.

Consequently, the following section is providing the effects of mesh quality on the results. Besides, the next sections 6.4.2 and 6.4.3 are showing the turbulence models results and the effect of the diffusivity. In the End, a 2D and 3D contours are created to show the effects of turbulence models on the symmetrical shape generation in a swirl jet flow.

6.4.1 Effects of mesh quality

The discoveries form the previous case studies make the chosen of the correct type of mesh simple and accurate. In another word, there is no need to examine various types of meshes, instead, a Tetrahedrons mesh is utilized to perform the simulation. However, the quality of mesh has a big impact on the results. For instance, Methane volume fraction in the first mesh is not demonstrated correctly, while it is accurate in the chosen mesh as shown in Figure 6-28 when standard k-ε is used.

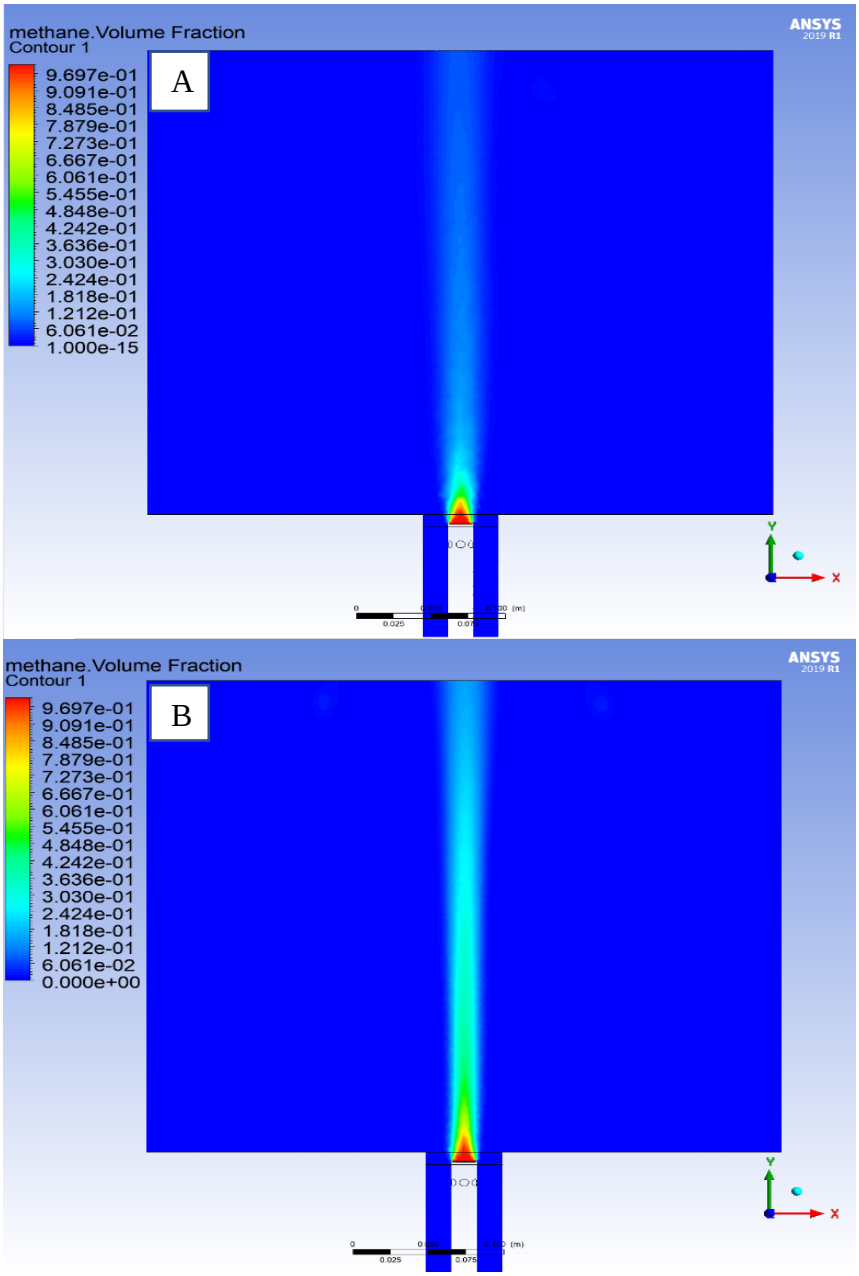

Figure 6-28: Mesh Quality Effects On The Volume Fraction:

A. Low Mesh Size. B. High Mesh Size. Swirling Flow

6.4.2 Effects of turbulence modelling

The author has applied various RANS turbulence models to study the swirl flow, see section 5.4. Thus, Methane mass fraction at the same locations as the experiment is applied $1D_f$, $3D_f$, $5D_f$ and $7D_f$. Nevertheless, the selected mesh needs to be checked first by extract the mass fraction at the above locations. The results specified the authenticity of the mesh by demonstrating the decreasing of the Methane mass fraction along the axial jet flow as shown in Figure 6-29. Furthermore, the mass fraction is calculated against a dimensionless factor x/R where x is the radial location in the computational domain and R is the Methane inlet radius.

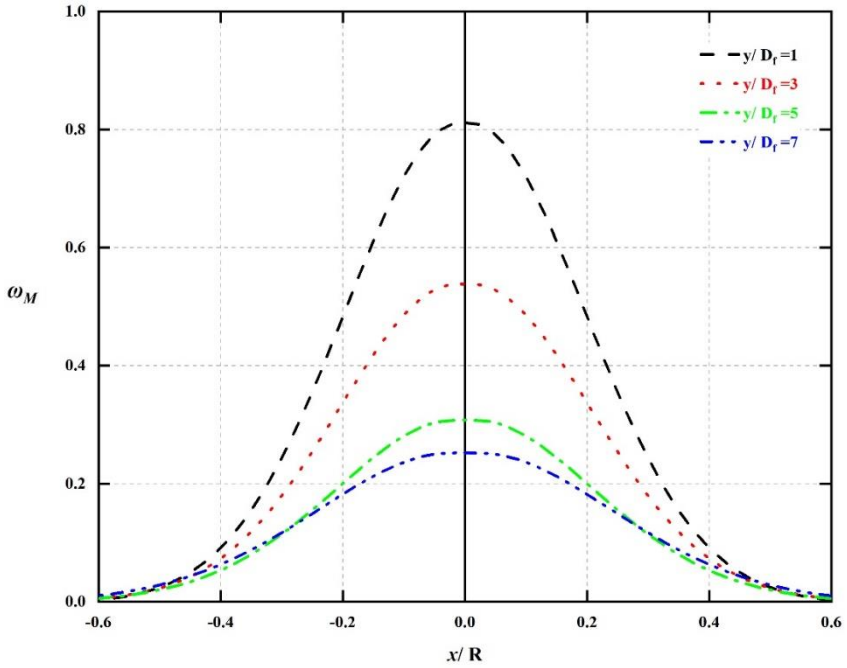

Figure 6-29: Methane Mass Fraction At Different Locations In The Chosen Mesh.

Two-Equations based turbulence models:

Furthermore, a comprehensive study for each selected model is established to indicate the turbulence model effects on the results. First, a standard k-ε turbulence model is applied through the simulation. Interestingly, Methane mixture fraction at $1D_f$, $3D_f$,$5D_f$ and $7D_f$ schemed in Figures 6-30 and 6-31 visibly show the effect of the swirl on the flow where the maximum value at the first location is less than the identical one in the previous planar jet case. Moreover, The RMSE percent attached to the earlier figures reveal a large difference between the model and the experiment data at the first two location, which is equivalent to 24.76%, 24.95%. While the model shows a great prediction at the last two locations 7.35%, 4.45%. The reason behind that is the weakness of the model to predict the flow at high mixing area $1D_f$,

$3D_f$ which is very close to the fuel inlet orifice. Though, the model succeeds for the last two locations as the turbulence effect slightly decreased.

RNG k-ε and Shear Stresses turbulence SST models show more familiar results as the standard k-ε turbulence model. However, the RMSE values at the first tow locations are slightly higher, equal to 26.87%, 26.39% for the RNG k-ε and 26.28%, 25.86% for the SST turbulence model. However, all the models have almost the same RMSE value for the last tow locations, equal to 7.49%, 4.43% for the RNG k-ε and 7.39%, 4.14% for the SST turbulence model as shown in Figures 6-32, 6-33, 6-34 and 6-35.

Reynolds stress turbulence models

Launder, Reece and Rodi turbulence model Isotropizatio of Production (LRR-IP-RS) is used at the same simulation environment. This model is based on the standard Reynolds Stress Model RSM, the model findings indicate that the Methane mass fraction have a similar behaviour as the ones from the previous turbulence models. However, error percent is faintly different. To be specific, the RMSE percent reveal a significant difference between the model and the experiment data at the first two location, equal to 28.04%, 26.64%. Though, the model presents a good prediction at the last two locations 7.48%, 4.31%. Therefore, this model has almost the same error percent as the previous model for this type of flow conditions. However, the model good prediction profiles at the last two locations as shown in Figures 6-36 and 6-37.

Next, Speziale, Sarkar and Gatski turbulence model (SSG-RS) is employed to this study. Which is also based on the standard Reynolds Stress Model RSM, the model results signify that the Methane mass fraction have a parallel performance as in the previous models. As an illustration, the RMSE percent disclose a large difference between the model and the experiment data at the first two location, equal to 28.04%, 26.96%. However, the model offers a good prediction at the last two locations 8.02%, 3.65% as shown in Figures 6-38 and 6-39. Hence, this model has almost the same error percent as the LRR-IP-RS model for this type of flow conditions, due to equations similarity between them.

Finally, Omega-Based Reynolds Stress Model (Omega-RS) is engaged into this study to examine types of RSM models. Likewise, this model shows similar findings as the previous models where the RMSE as the first two locations high 26.95%, 26.50% comparing with the last two locations 7.71%, 3.88% as shown in Figures 6-40 and 6-41.

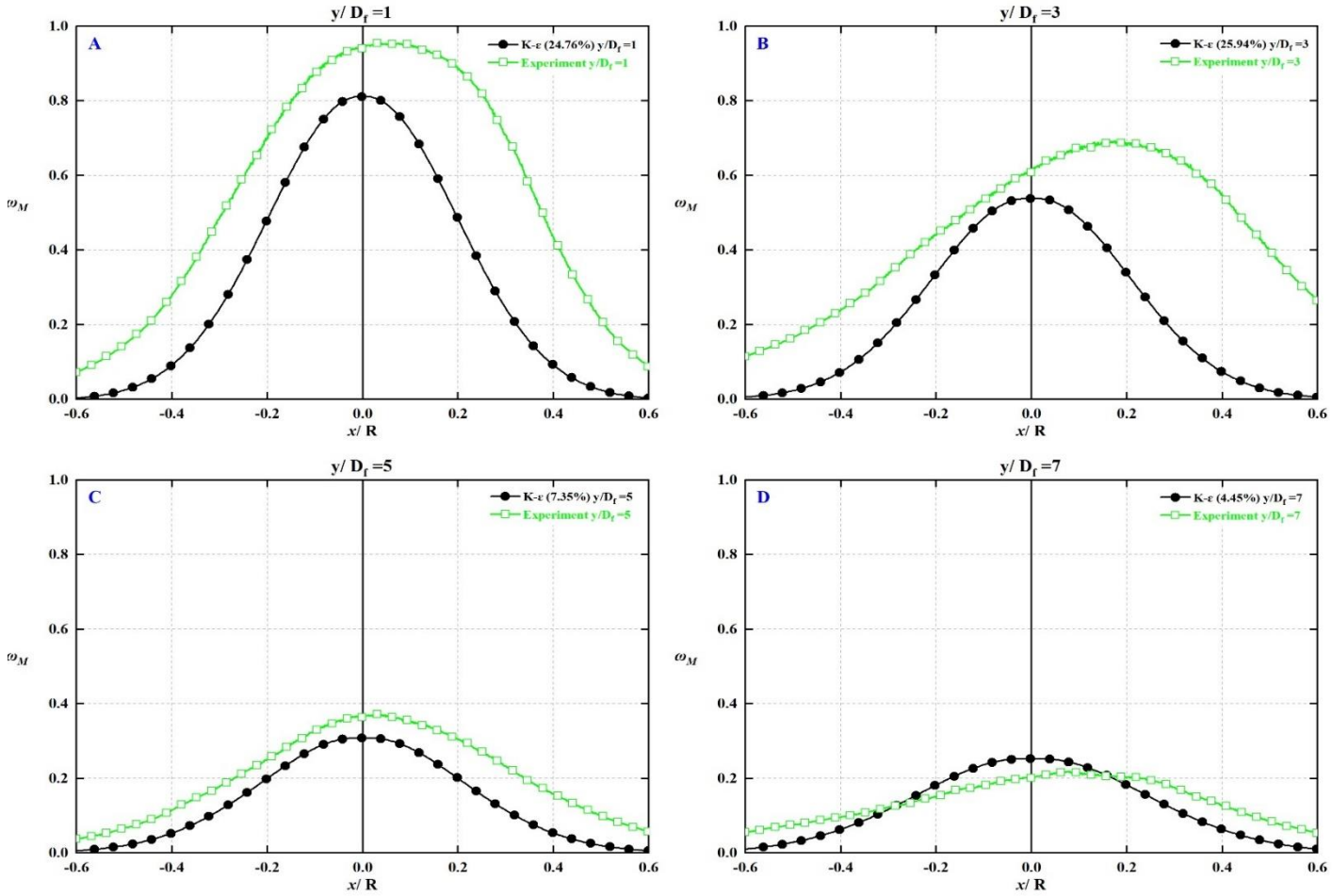

Figure 6-30: Mixture Fraction Of Methane And Stetsyuk's Experiment. A. 1D_f, B. 3D_f, C.5D_f, D. 7D_f. S=0.3, *k*-*ε*.

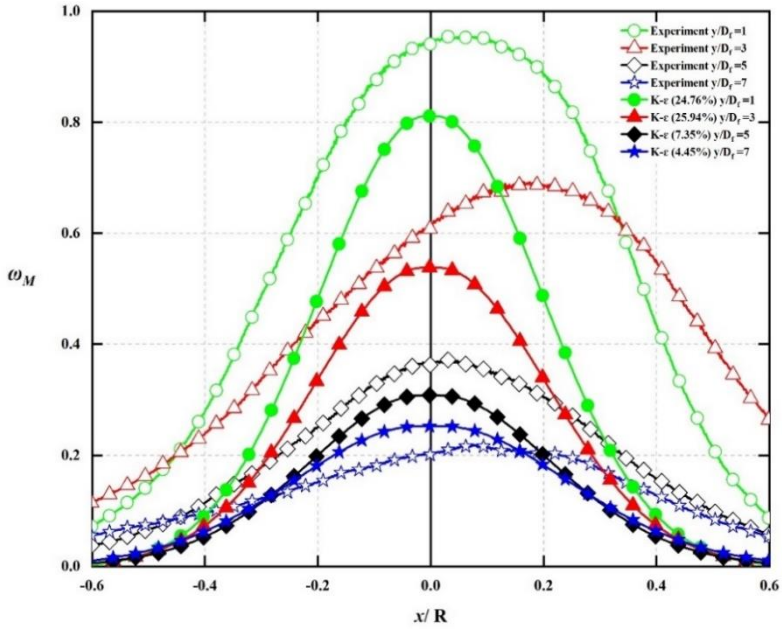

Figure 6-31: Mixture Fraction At All Locations For Methane And Stetsyuk's Experiment. S=0.3, *k*-*ε*.

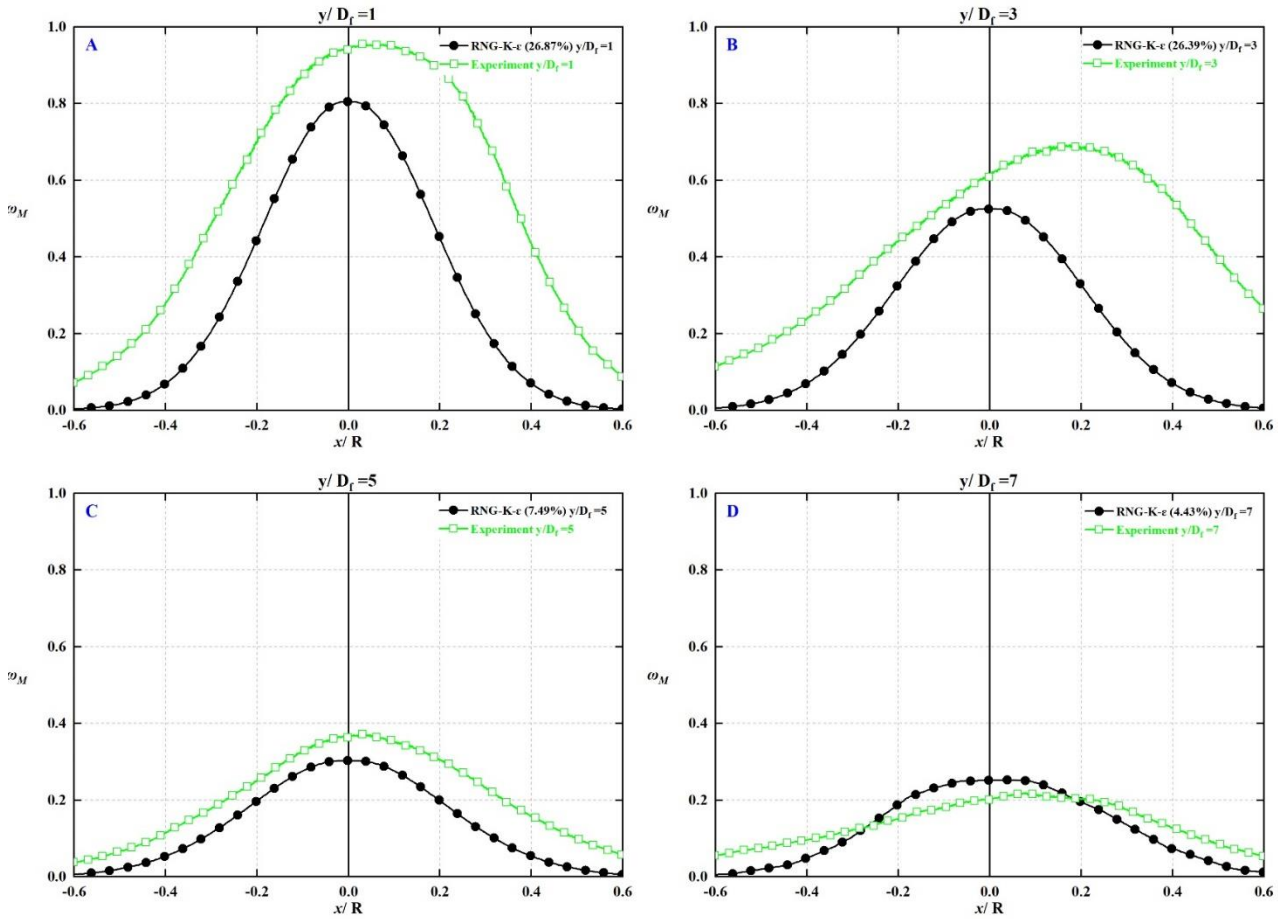

Figure 6-32: Mixture Fraction Of Methane And Stetsyuk's Experiment. A. 1D_f, B. 3D_f, C.5D_f, D. 7D_f. S=0.3, RNG *k-ε*.

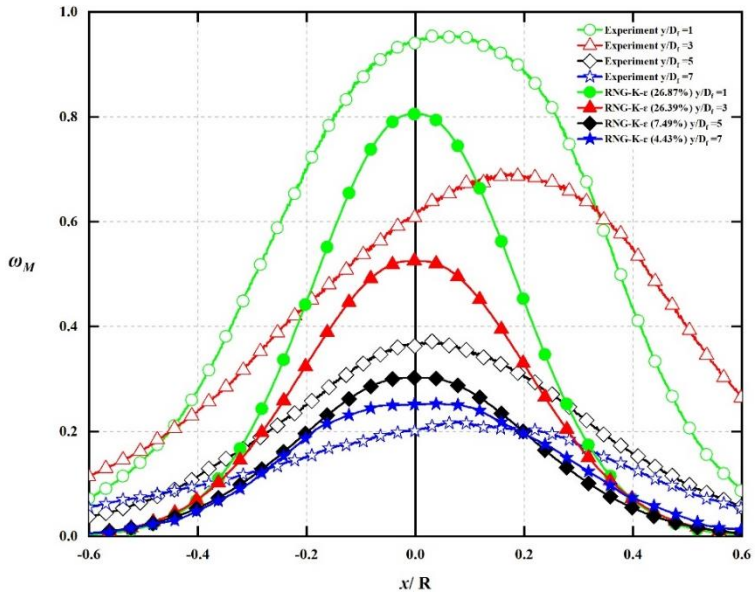

Figure 6-33: Mixture Fraction At All Locations For Methane And Stetsyuk's Experiment. S=0.3, RNG *k-ε*.

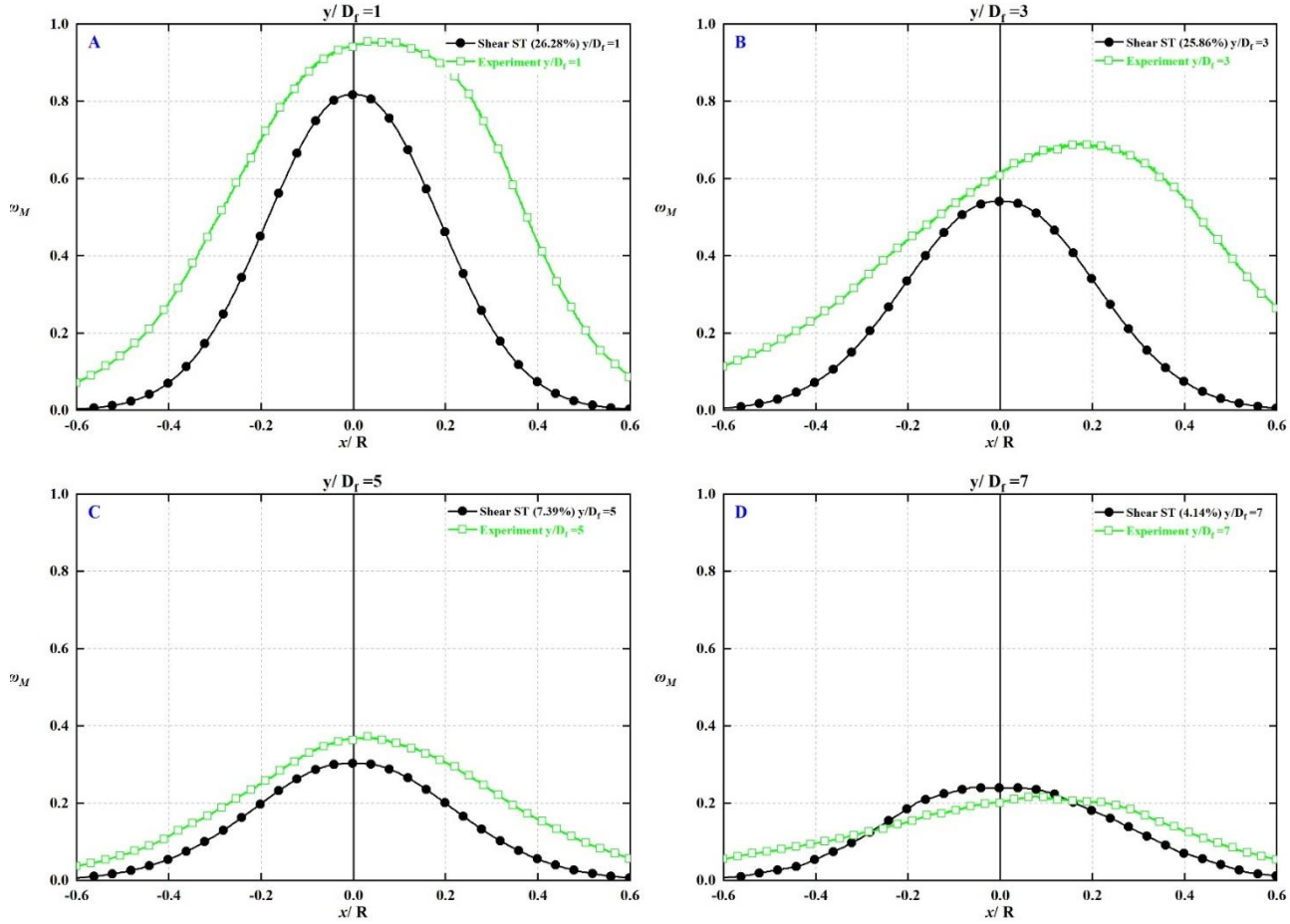

Figure 6-34: Mixture Fraction Of Methane And Stetsyuk's Experiment. A. 1D_f, B. 3D_f, C.5D_f, D. 7D_f. S=0.3, SST.

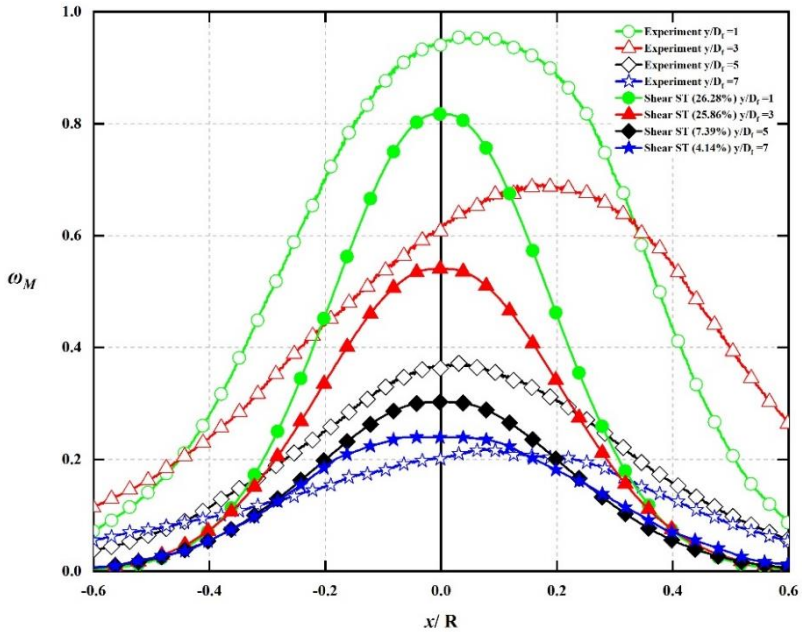

Figure 6-35: Mixture Fraction At All Locations For Methane And Stetsyuk's Experiment. S=0.3, SST.

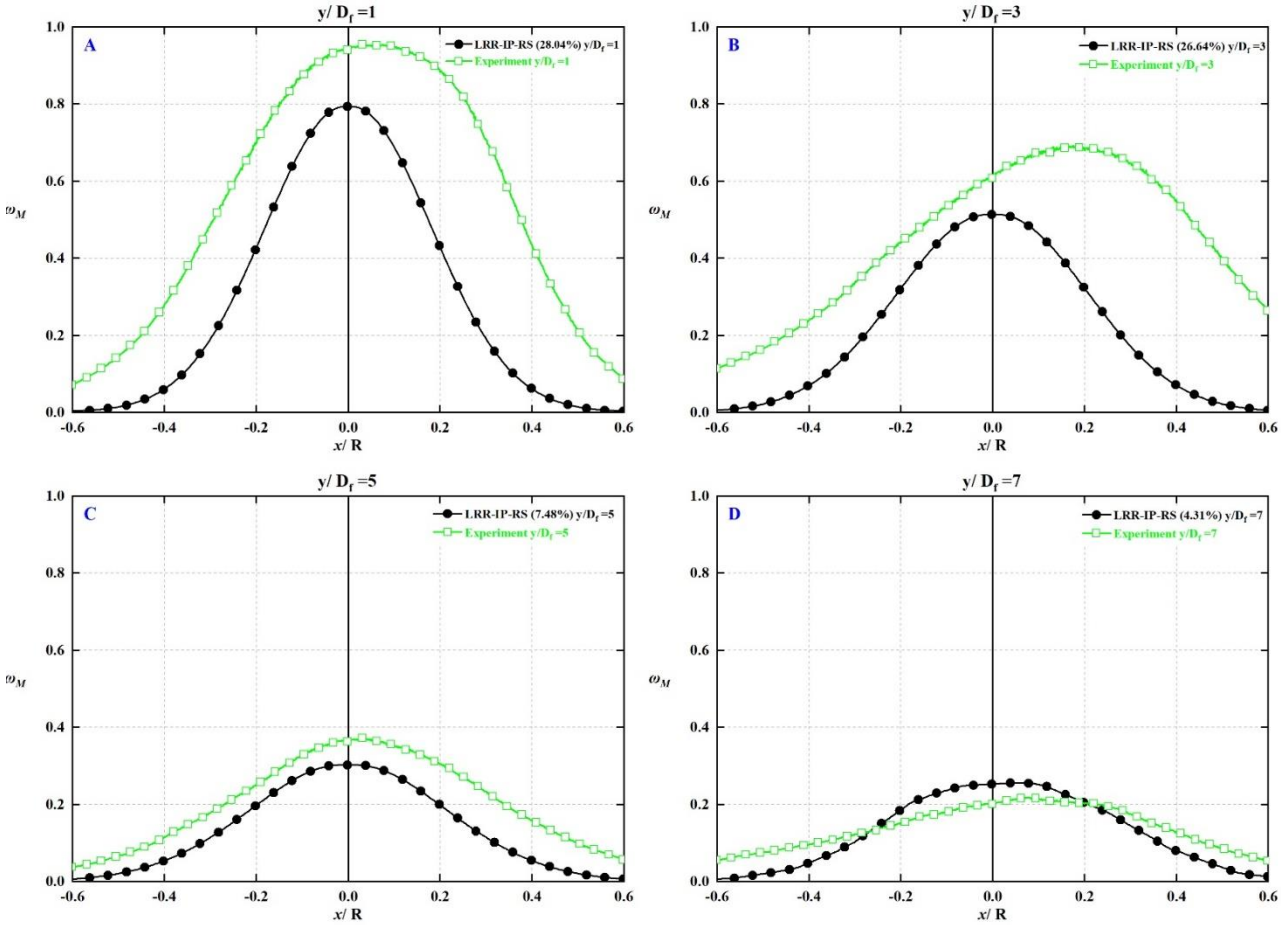

Figure 6-36: Mixture Fraction Of Methane And Stetsyuk's Experiment. A. 1D_f, B. 3D_f, C.5D_f, D. 7D_f. S=0.3, LRR-IP-RS.

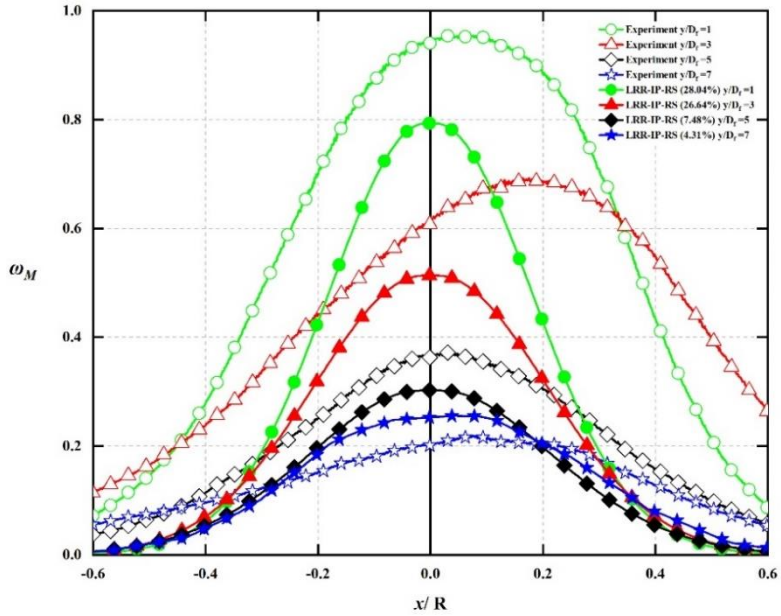

Figure 6-37: Mixture Fraction At All Locations For Methane And Stetsyuk's Experiment. S=0.3, LRR-IP-RS.

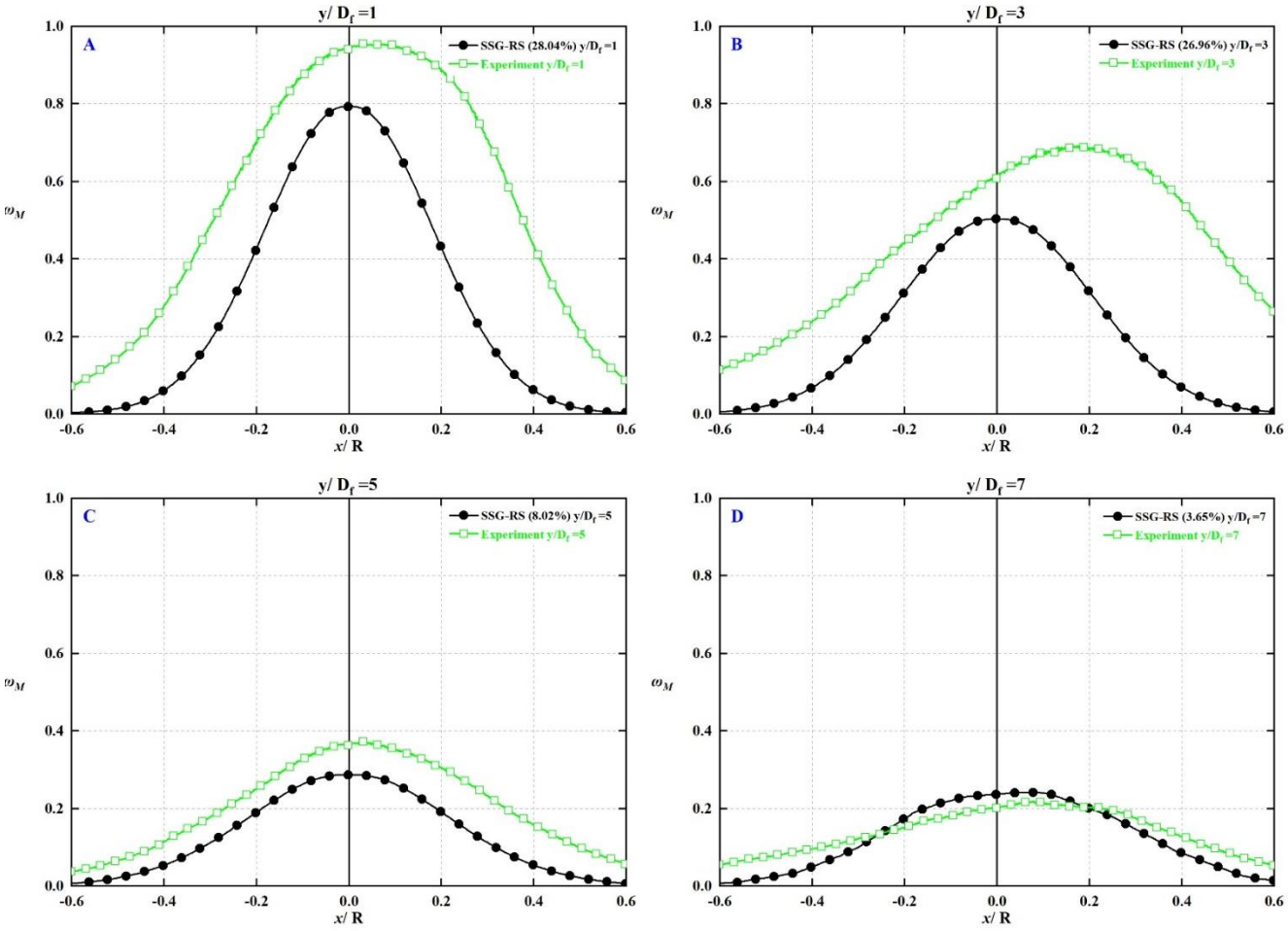

Figure 6-38: Mixture Fraction Of Methane And Stetsyuk's Experiment. A. 1D_f, B. 3D_f, C.5D_f, D. 7D_f. S=0.3, SSG-RS.

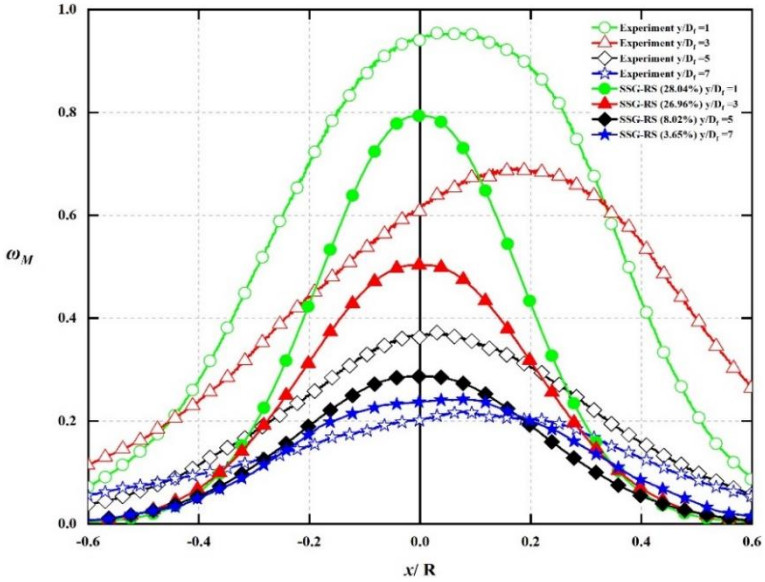

Figure 6-39: Mixture Fraction At All Locations For Methane And Stetsyuk's Experiment. S=0.3, SSG-RS.

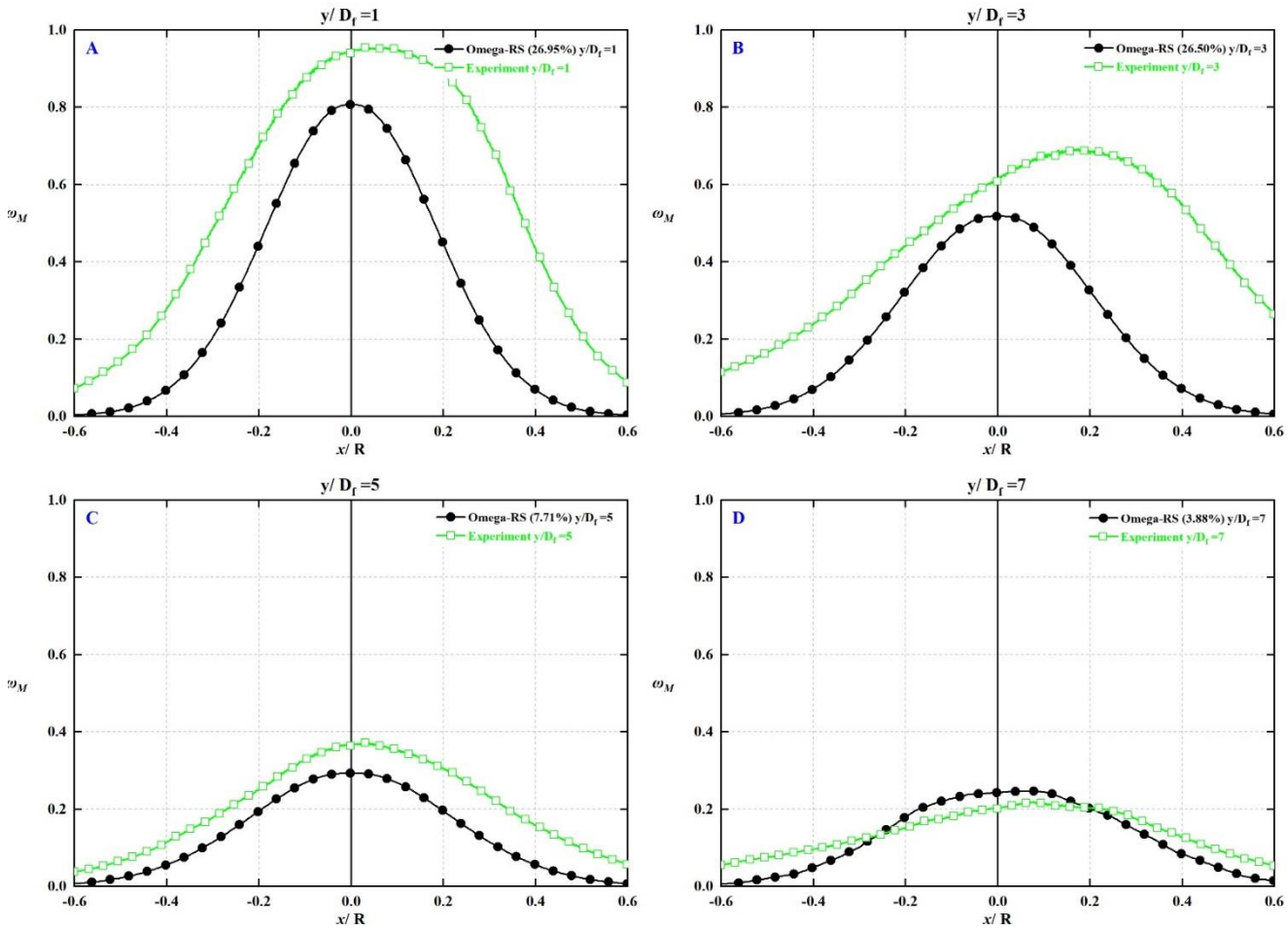

Figure 6-40: Mixture Fraction Of Methane And Stetsyuk's Experiment. A. 1D_f, B. 3D_f, C.5D_f, D. 7D_f. S=0.3, Omega-RS.

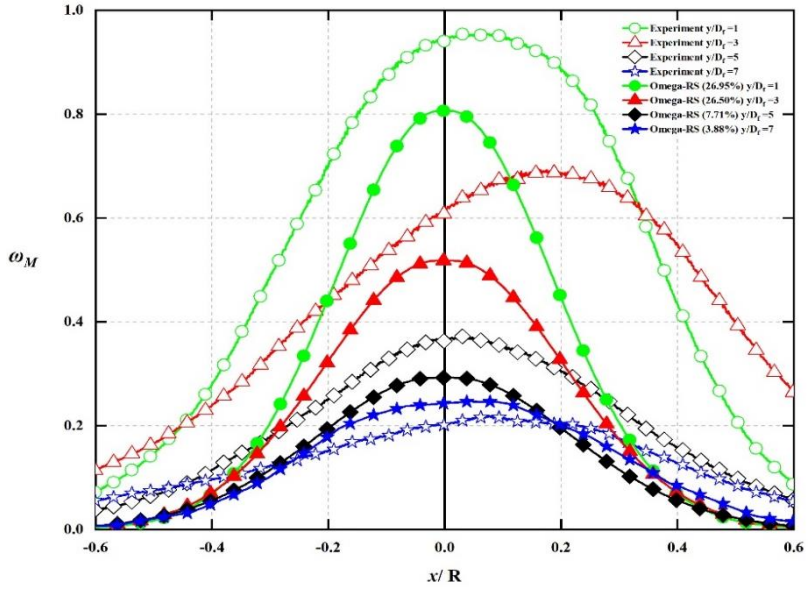

Figure 6-41: Mixture Fraction At All Locations For Methane And Stetsyuk's Experiment. S=0.3, Omega-RS.

6.4.3 Effects of 'zero diffusivity'

This section designates the effect of diffusivity in two scenarios. First, the diffusivity effect between the author simulation and the experiment data when existing of swirling flow. Second, the impact on the results in case of making the diffusivity value inside the CFX programme equal to 0.

Earlier, the results from the second case planar jet flow which is the same current experiment but with planar flow only indicate a remarkable effect between the author simulation and the related experiment especially at $7D_f$ as in Figure 6-19, where the RMSE percent is 23.89%. However, the findings in Figure 6-42 reveal a significance decreases of RMSE percent down to 4.45% when a same turbulence model applied at $7D_f$. This results state that there is no effect of the diffusivity when the turbulence inside the flow increases, and the flow is relatively random. Moreover, the 'zero diffusivity' term refer to apply a zero Methane diffusivity into the simulation system to insure the previous state. Fascinatingly, the results of all models show no differences in mass/mixture fraction values at all locations. Therefore, it can be declaring that the diffusivity effect is decaying when the swirl flow occurs and the turbulence effect dominating the flow.

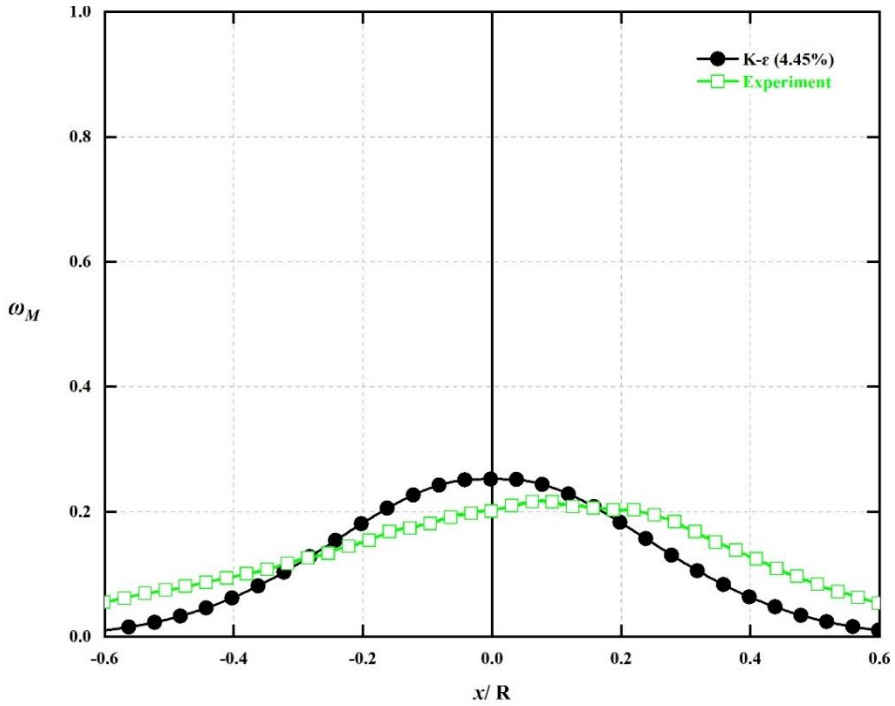

Figure 6-42: Mass Fraction Of Methane And Stetsyuk's Experiment At $7D_f$. k-ε, S=0.3.

6.4.4 Symmetric analyses

The symmetric form is examined in this study via using a 2D and 3D contours for the mass fraction at the selected locations before. The contours results denote a slightly non-symmetric effect due to existence of the swirl and the existence of the screws in the geometry, see section 6.7. As can be seen in Figures 6-43 To 6-48, the turbulence models were able to predict the change in the symmetric shape at each location at different level of prediction. Therefore, the simulations findings indicate that the swirl flow influences the symmetric shape at swirl strength of S=0.3.

To sum up, Table 6-3 demonstrate the final RMSE results of the selected models. In general, all models show a good agreement with the experimental data considering the numerical and experiments errors and uncertainty. However, the standard K-ε along with the shear stress turbulence models (highlighted) have slightly the lowest average error percent because of their ability to indicate the pressure gradients better than the other models. Furthermore, all models show the highest error percentage at the first two locations due to swirl influences on:

1. Increasing of turbulence level
2. Creation of recirculation zone at very low level

Table 6-3: RMSE Percent For All The Models At A Specific Location. S=0.3

Model	RMSE				Average error percent
	Y/ D_f				
	1	3	5	7	
K-ε	24.76%	25.94%	7.35%	4.45%	15.62%
RNG-K-ε	26.87%	26.39%	7.49%	4.43%	16.29%
Shear ST	26.28%	25.86%	7.39%	4.14%	15.92%
LRR-IP-RS	28.04%	26.64%	7.48%	4.31%	16.62%
SSG-RS	28.04%	26.96%	8.02%	3.65%	16.67%
Omega-RS	26.95%	26.50%	7.71%	3.88%	16.26%

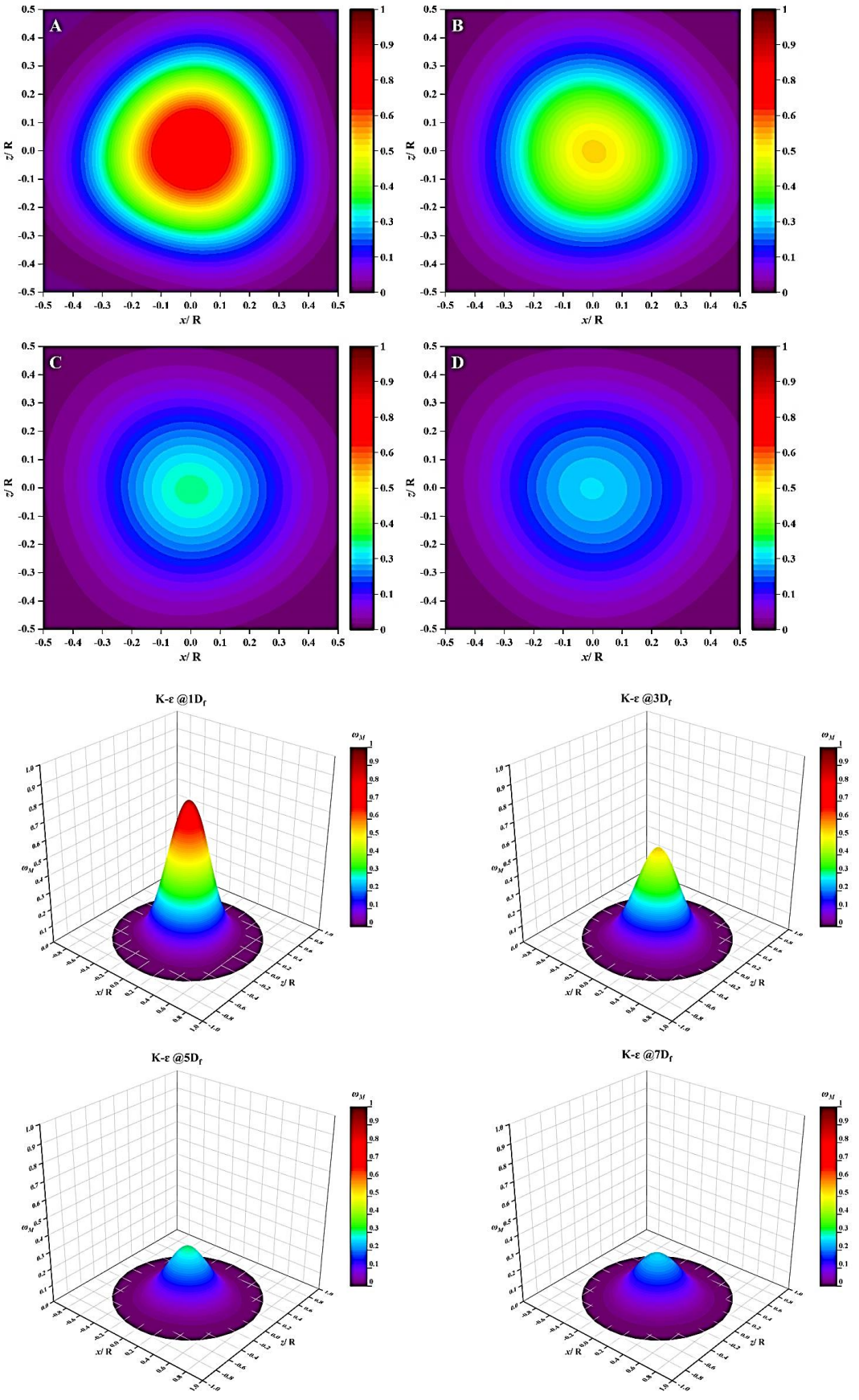

Figure 6-43: 2D (Top View) And 3D ω_M Contours Of Methane. A. 1D$_f$, B. 3D$_f$, C.5D$_f$, D. 7D$_f$. k-ε .S=0.3.

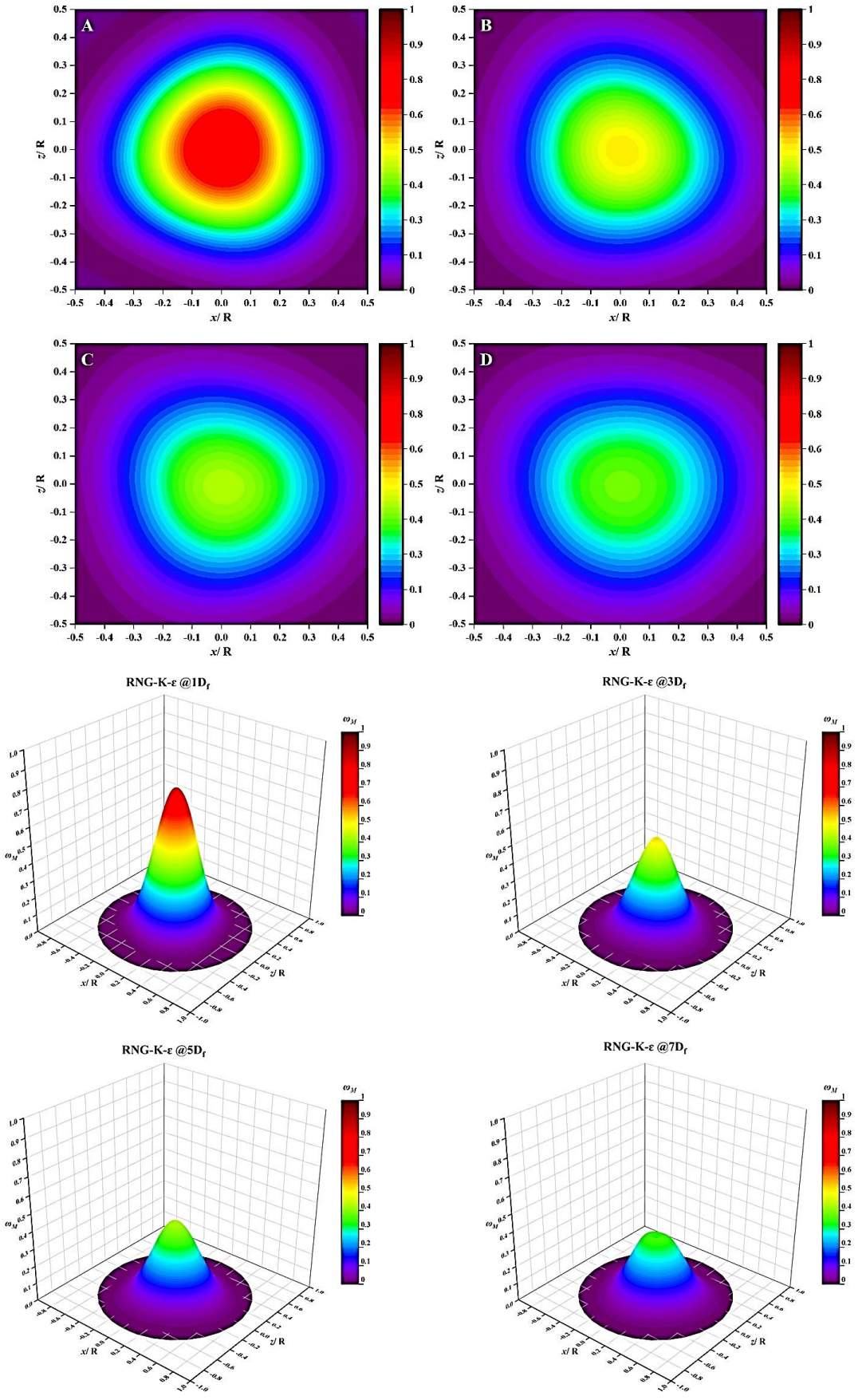

Figure 6-44: 2D (Top View) and 3D ω_M contours of Methane. A. 1D$_f$, B. 3D$_f$, C.5D$_f$, D. 7D$_f$. RNG k-ε .S=0.3.

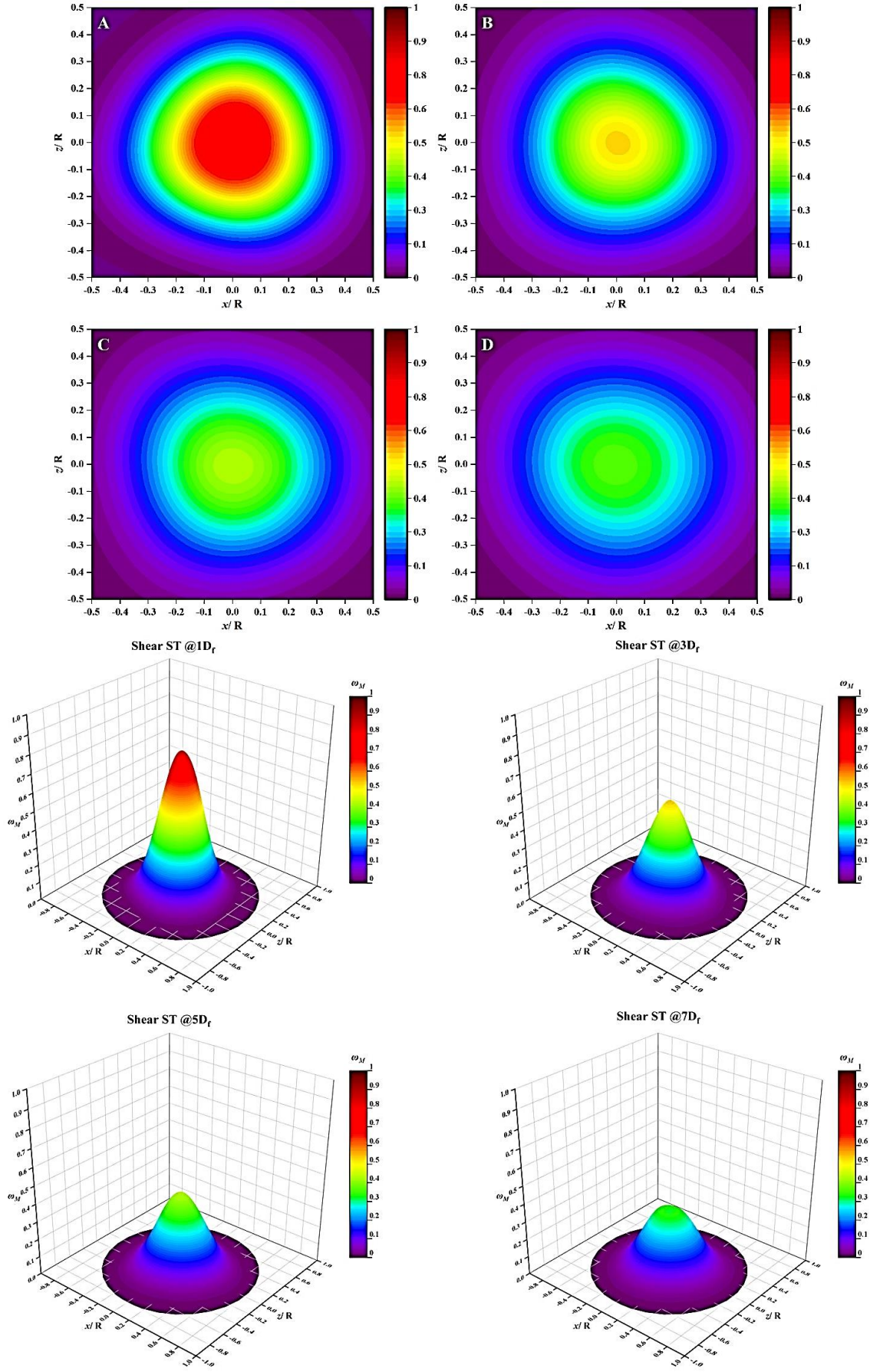

Figure 6-45: 2D (Top View) And 3D ω_M Contours Of Methane. A. 1D$_f$, B. 3D$_f$, C.5D$_f$, D. 7D$_f$. SST. S=0.3.

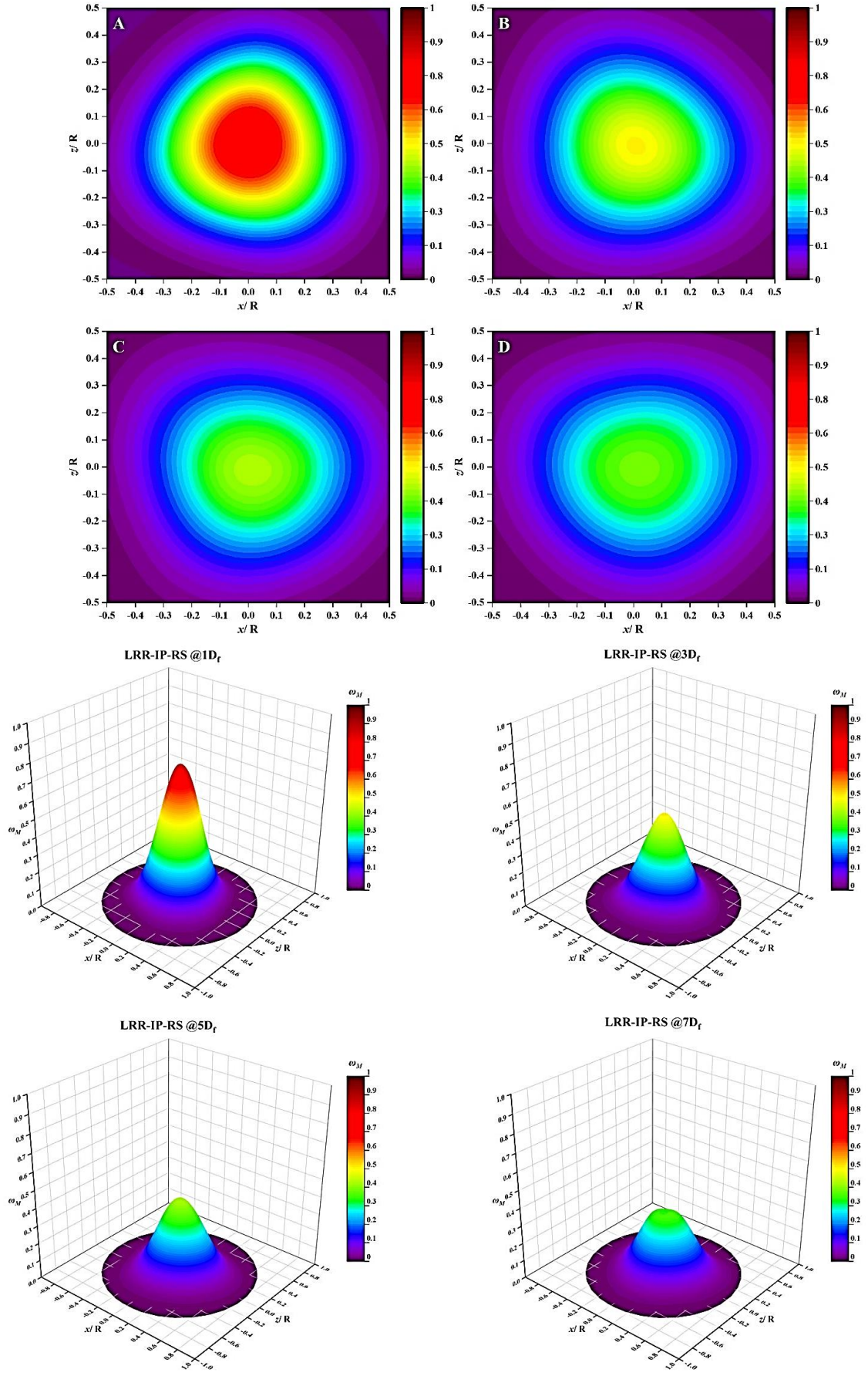

Figure 6-46: 2D (Top View) And 3D ω_M Contours Of Methane. A. 1D$_f$, B. 3D$_f$, C.5D$_f$, D. 7D$_f$. LRR-IP-RS. S=0.3.

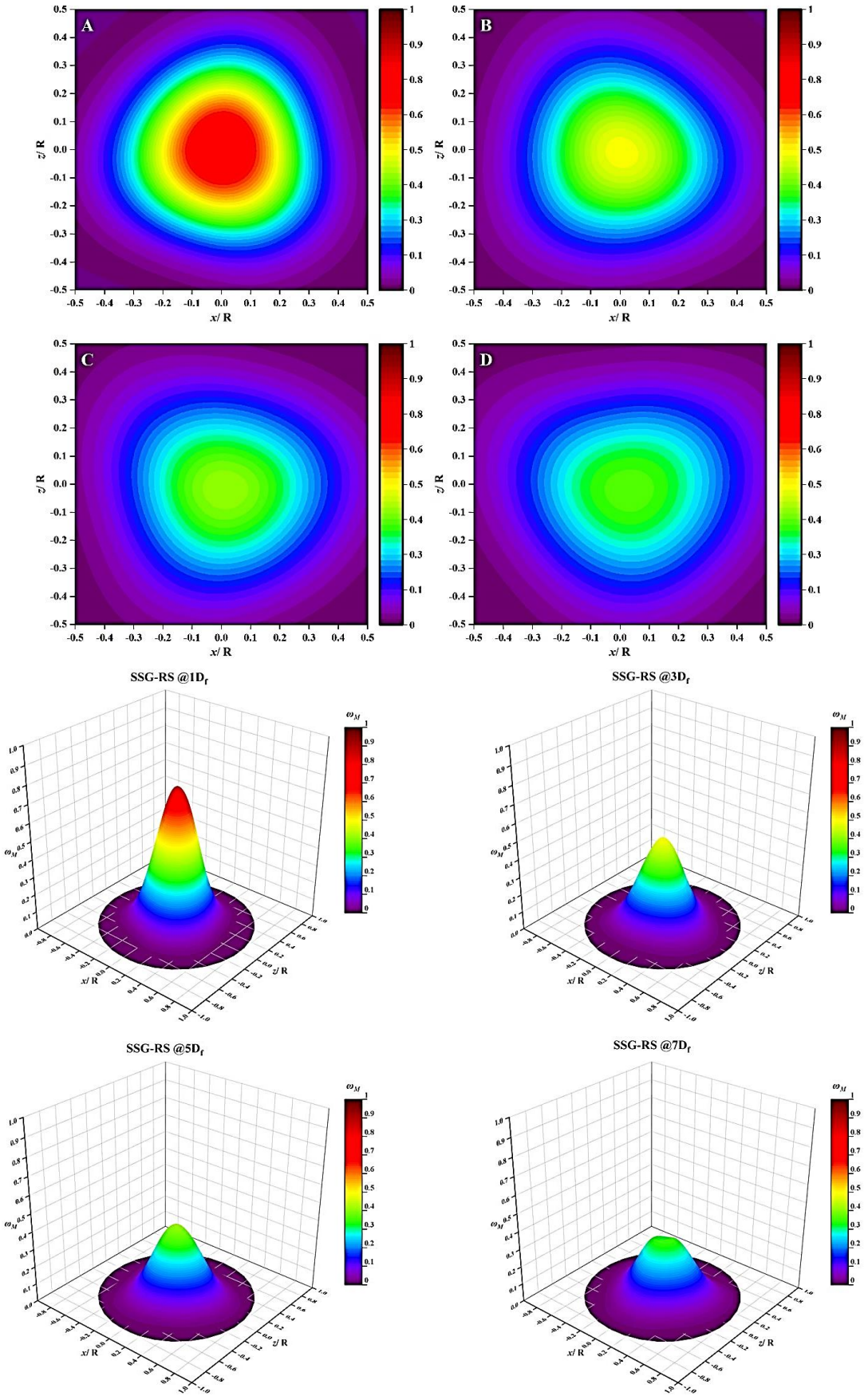

Figure 6-47: 2D (Top View) And 3D ω_M Contours Of Methane. A. $1D_f$, B. $3D_f$, C.$5D_f$, D. $7D_f$. SSG-RS. S=0.3.

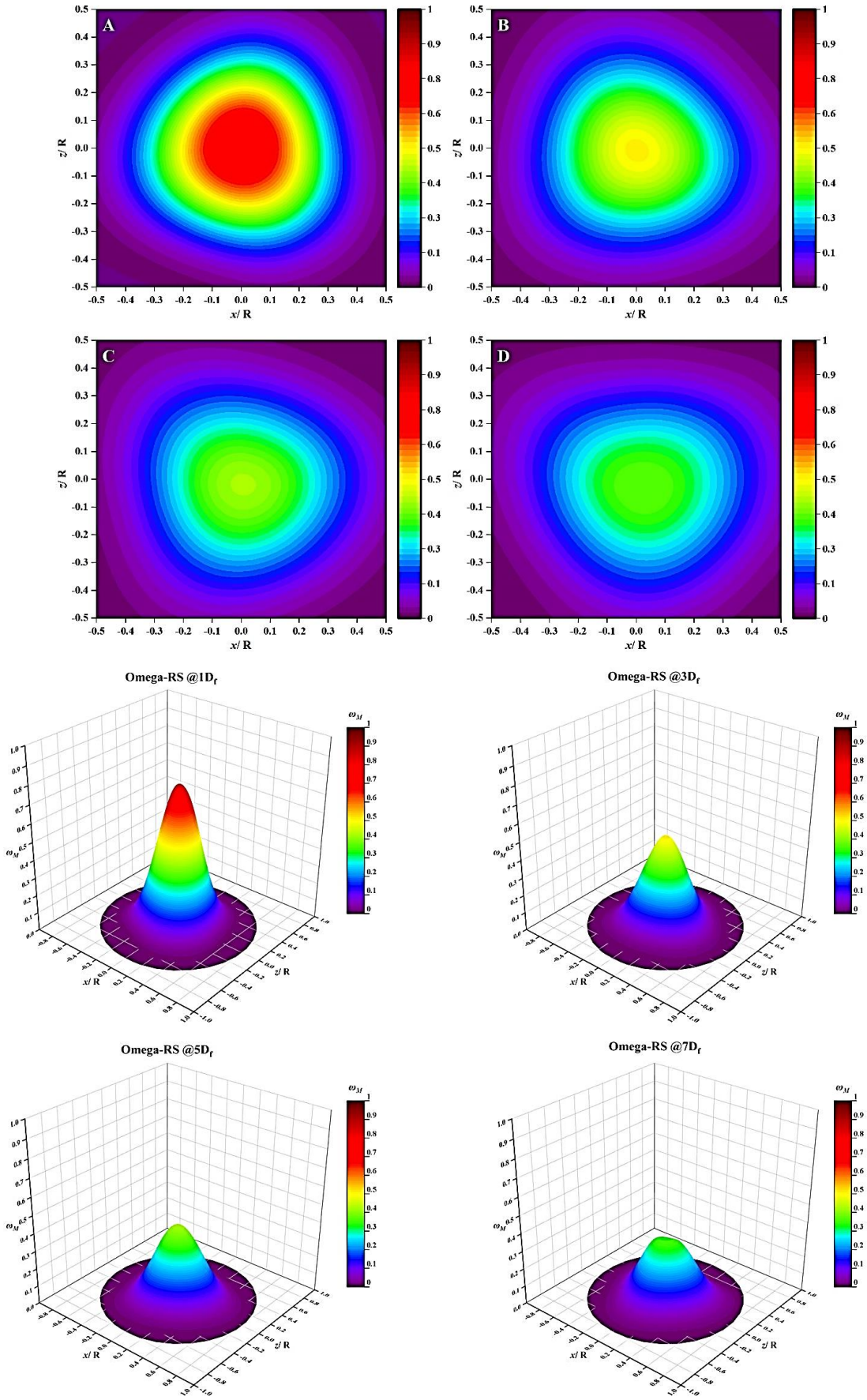

Figure 6-48: 2D (Top View) And 3D ω_M Contours Of Methane. A. $1D_f$, B. $3D_f$, C.$5D_f$, D. $7D_f$. Omega-RS. S=0.3.

6.5 Second swirl number (*S*=0.58)

The only difference between the first and second swirl number simulation is the boundary condition as shown in Table 5.1. Therefore, same process as the first swirl number is used to analyse the outcome of this study.

6.5.1 Effects of turbulence modelling

The effects of using different turbulence models are also recognised in this study at swirl flow of 0.58 via applying Methane mixture fraction at $1D_f$, $3D_f$,$5D_f$ and $7D_f$.

Two-Equations based turbulence models:

First, the RMSE percent for the standard k-ε turbulence model shows an expected behaviour among the computed locations. For instance, the RMSE values at the first three locations $1D_f$, $5D_f$, $5D_f$ reveal a large difference between the model and the experiment data which is equivalent to 17.92%, 10.01, 16.46% respectively. Though, the model shows a good prediction at $7D_f$ where the RMSE percent is 6.29%. Therefore, the weakness of the model to predict the flow at high mixing areas is highly rising under these conditions where the swirling increases randomly, see Figures 6-49 and 6-50.

Furthermore, the RNG k-ε findings as illustrated in Figures 6-51 and 6-52 indicate more weakness than the previous model where the RMSE values are 17.79%, 9.83%, 10.08%, 11.41% at $1D_f$, $3D_f$,$5D_f$,$7D_f$ respectively.

Likewise, SST model show nearly the same error percent's value as shown in Figures 6-53 and 6-54, where the RMSE values are 17.27%, 10.23%, 10.21% and 10.16% at $1D_f$, $3D_f$,$5D_f$ and $7D_f$ respectively.

Reynolds stress turbulence models

As in Figures 6-55 and 6-56. LRR-IP-RS turbulence model findings indicate that the Methane mass fraction have a similar behaviour as the ones from the previous turbulence models. Nevertheless, error percent is very different from them. For instance, the RMSE percent reveal a minor difference between the model and the experiment data at the last two locations $5D_f$ and $7D_f$ with a value of 9.28% and 8.81% respectively. However, RMSE percentages is similar as the two equations-based turbulence models k-ε, RNG k-ε and SST which is equal to 18.34% and 10.02% at $1D_f$ and $5D_f$, respectively. These results emphasize

the fact the turbulence hardly occurs very close to inlet due to the increasing of swirling strength.

Following, SSG-RS turbulence model results signify that the Methane mass fraction have a similar performance as in the LRR-IP-RS turbulence model as available in Figures 6-57and 6-58. The RMSE percent disclose a minor difference between the model and the experiment data at $3D_f$ and $5D_f$, equal to 9.59% and 9.02%. However, the RMSE value at the last location is relatively high 11.85% due to the weakness of the models at areas far from the walls.

Lastly, Omega-RS turbulence model is showing better results than all the previous models where the RMSE values are equal to 16.94%, 8.79%, 8.89% and 8.71% at $1D_f$, $3D_f$,$5D_f$ and $7D_f$, respectively as shown in Figures 6-59 and 6-60.

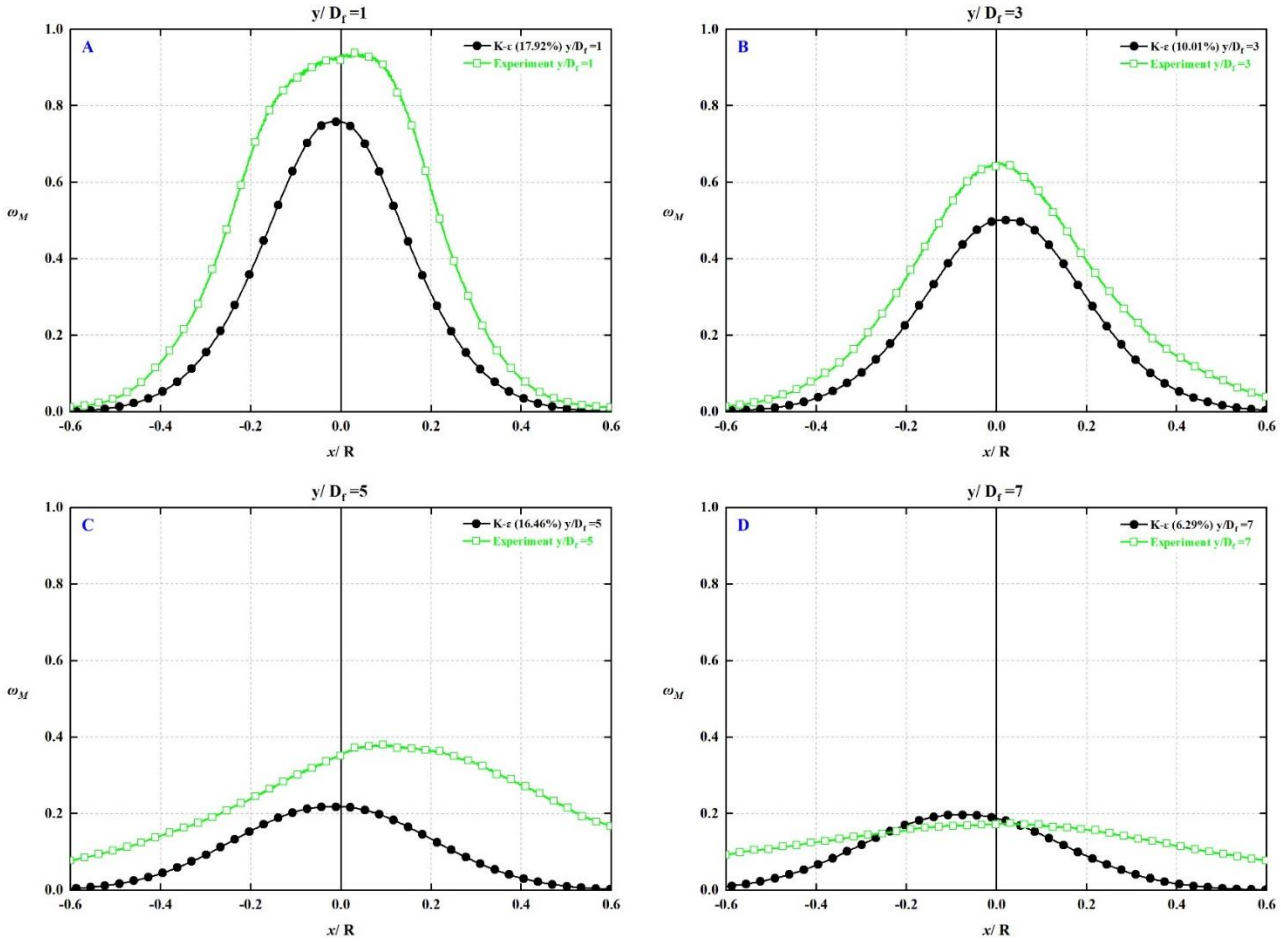

Figure 6-49: Mixture Fraction Of Methane And Stetsyuk's Experiment. A. 1D_f, B. 3D_f, C.5D_f, D. 7D_f. S=0.58, *k-ε*.

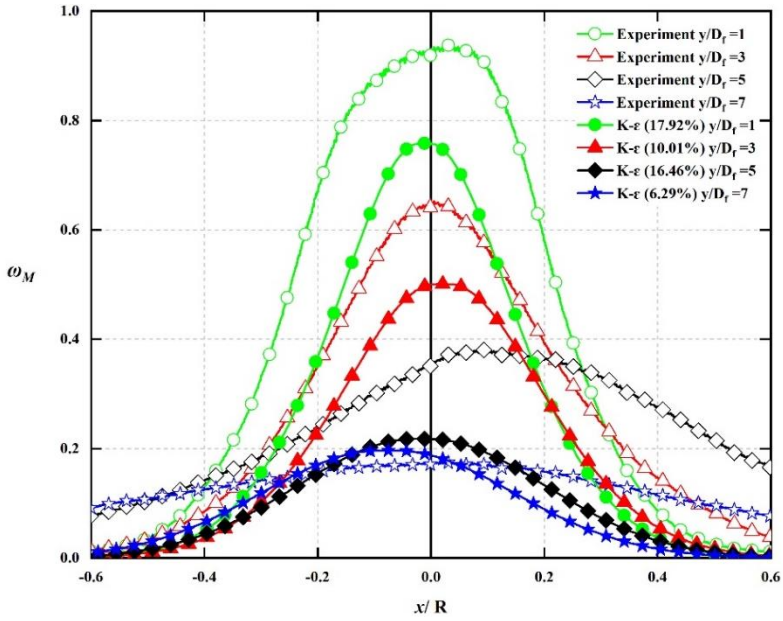

Figure 6-50: Mixture Fraction At All Locations For Methane And Stetsyuk's Experiment. S=0.58, *k-ε*.

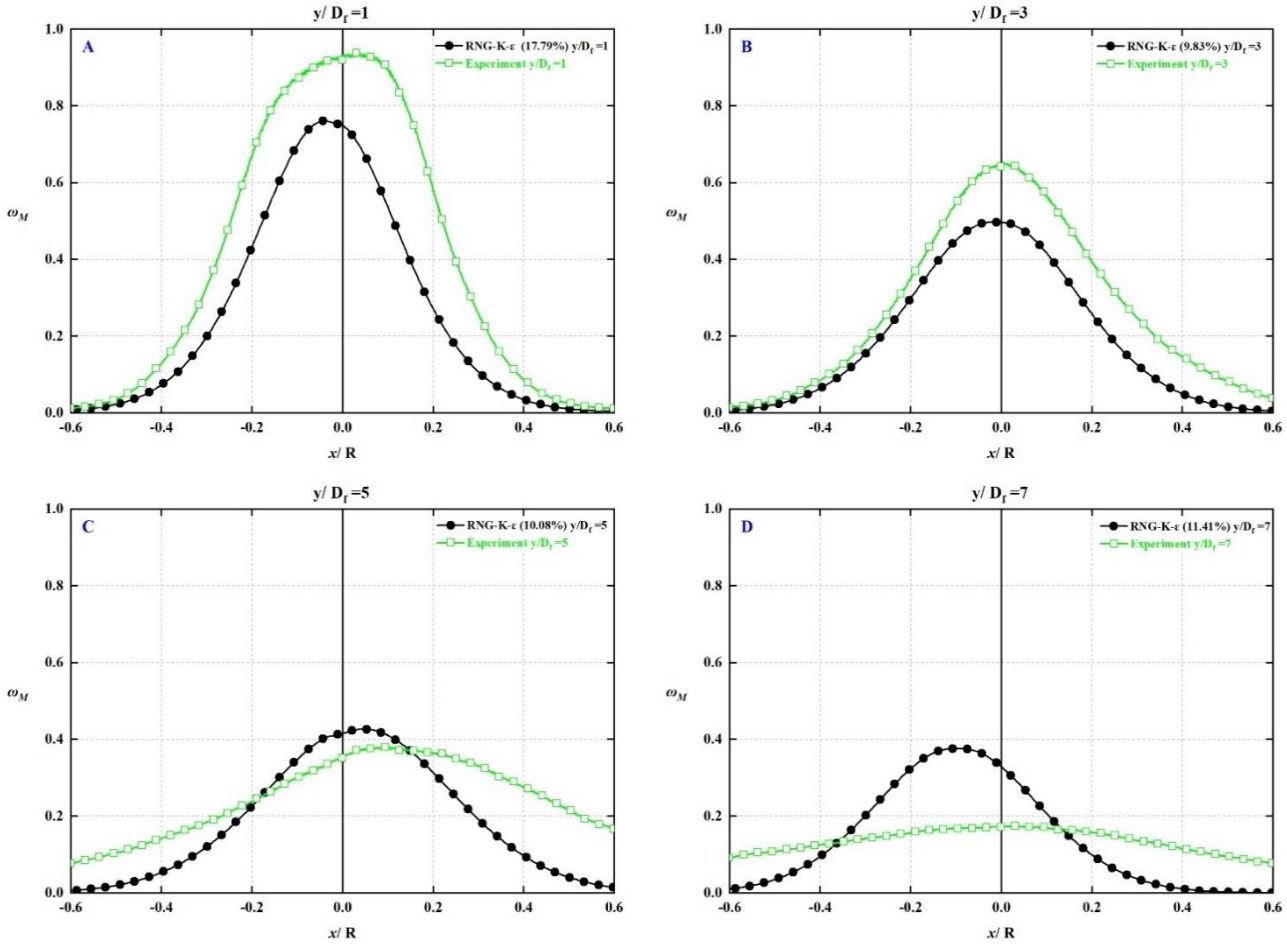

Figure 6-51: Mixture Fraction Of Methane And Stetsyuk's Experiment. A. 1D_f, B. 3D_f, C.5D_f, D. 7D_f. S=0.58, RNG *k-ε*.

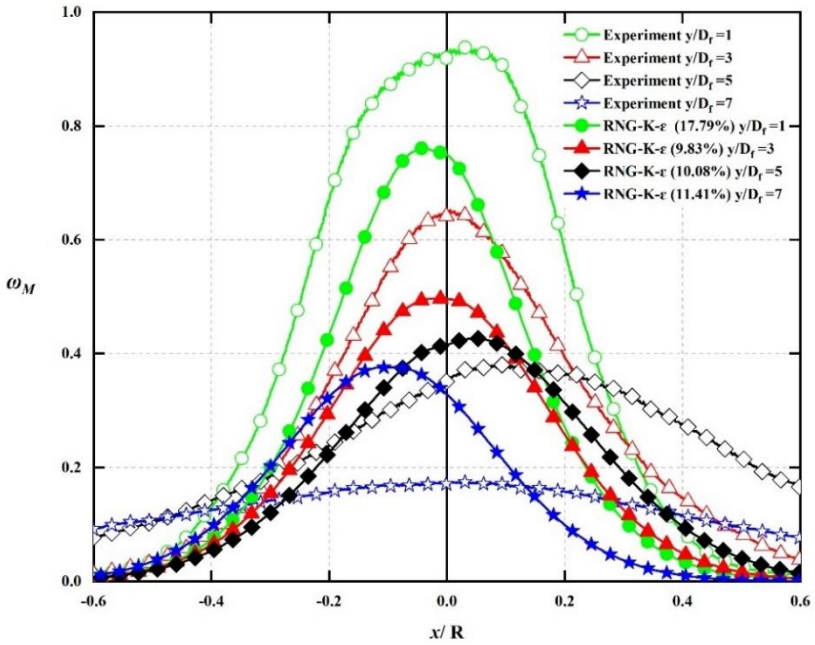

Figure 6-52: Mixture Fraction At All Locations For Methane And Stetsyuk's Experiment. S=0.58, RNG *k-ε*.

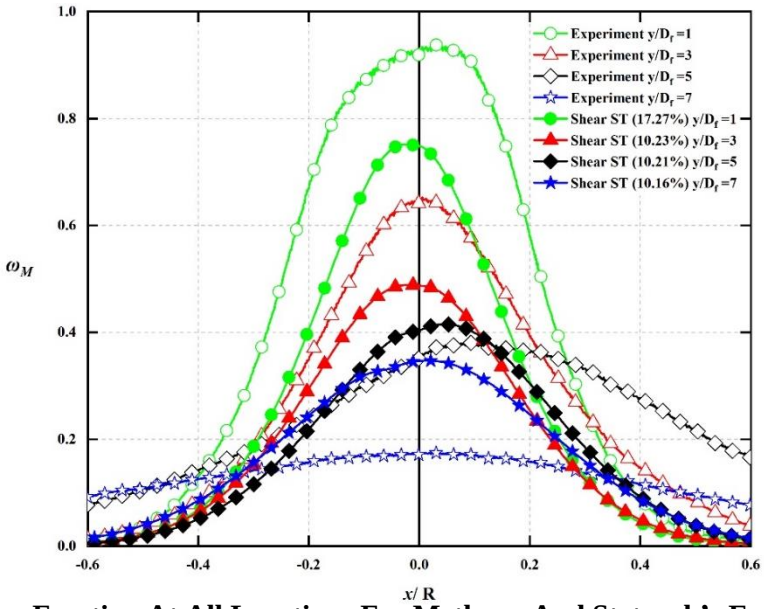

Figure 6-53: Mixture Fraction At All Locations For Methane And Stetsyuk's Experiment. S=0.58, SST.

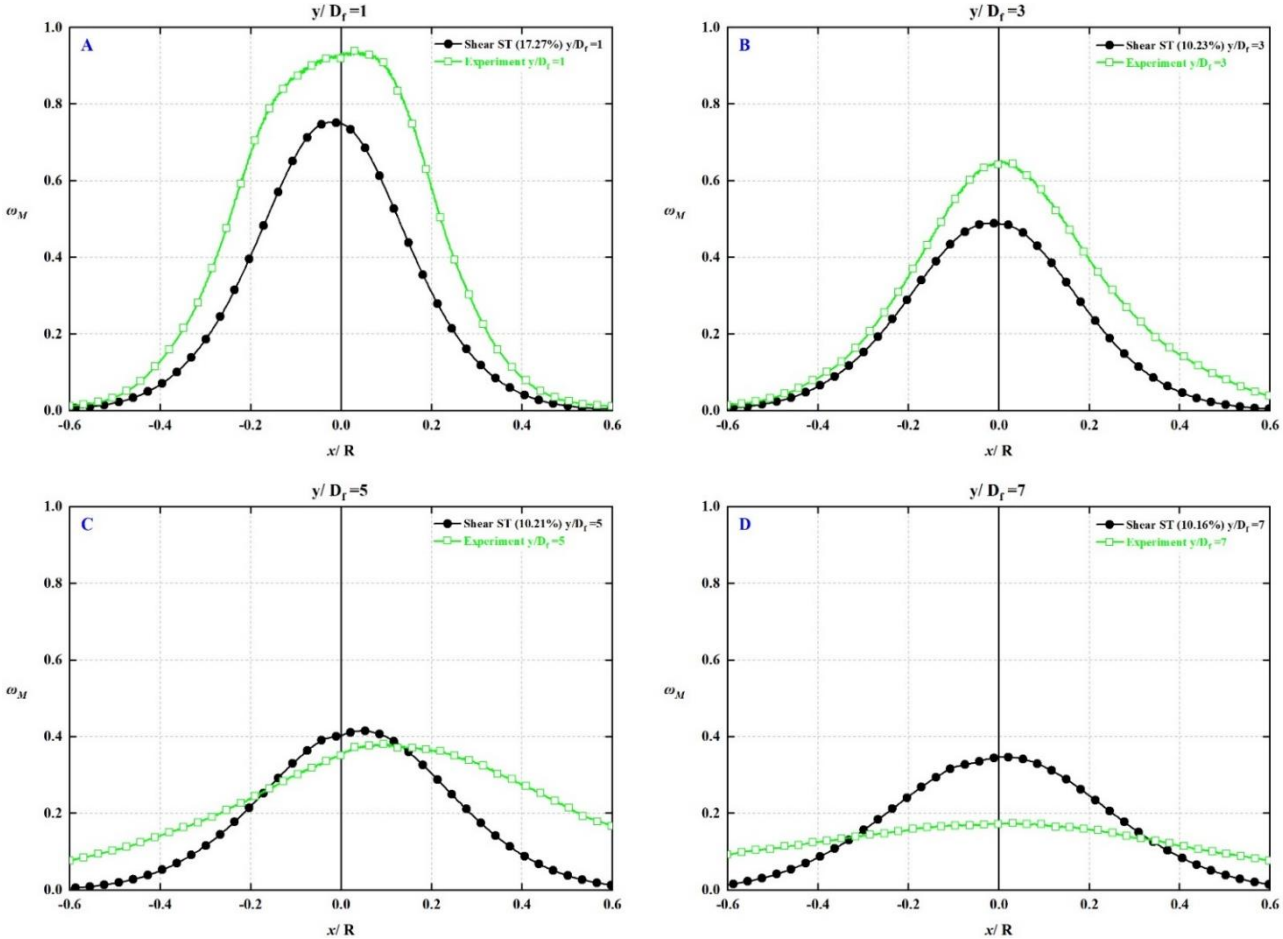

Figure 6-54: Mixture Fraction Of Methane And Stetsyuk's Experiment. A. $1D_f$, B. $3D_f$, C.$5D_f$, D. $7D_f$. S=0.58, SST.

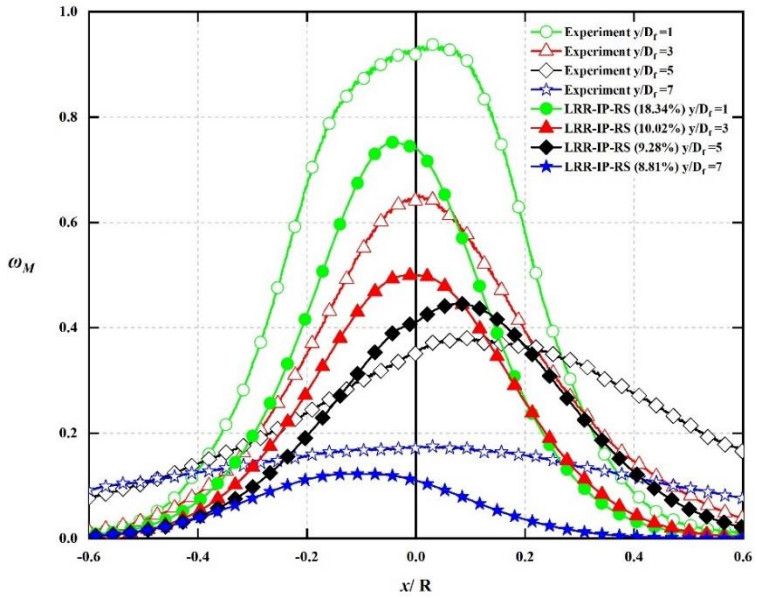

Figure 6-55: Mixture Fraction At All Locations For Methane And Stetsyuk's Experiment. S=0.58, LRR-IP-RS.

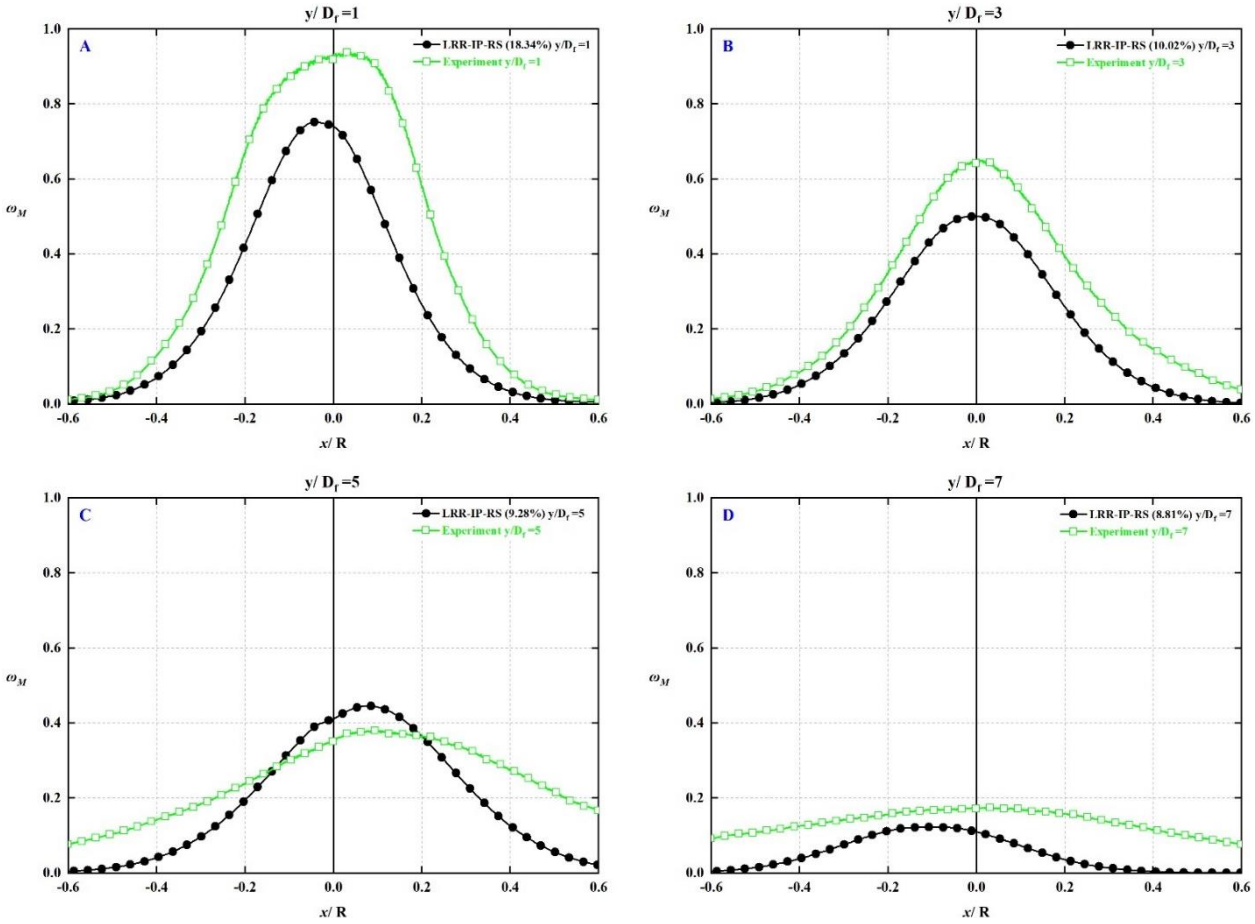

Figure 6-56: Mixture Fraction Of Methane And Stetsyuk's Experiment. A. 1D$_f$, B. 3D$_f$, C.5D$_f$, D. 7D$_f$. S=0.58, LRR-IP-RS.

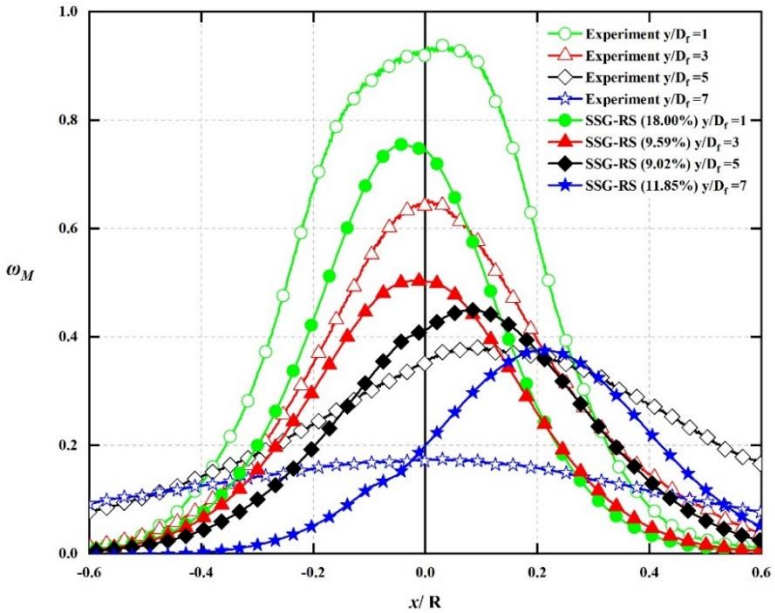

Figure 6-57: Mixture Fraction At All Locations For Methane And Stetsyuk's Experiment. S=0.58, SSG-RS.

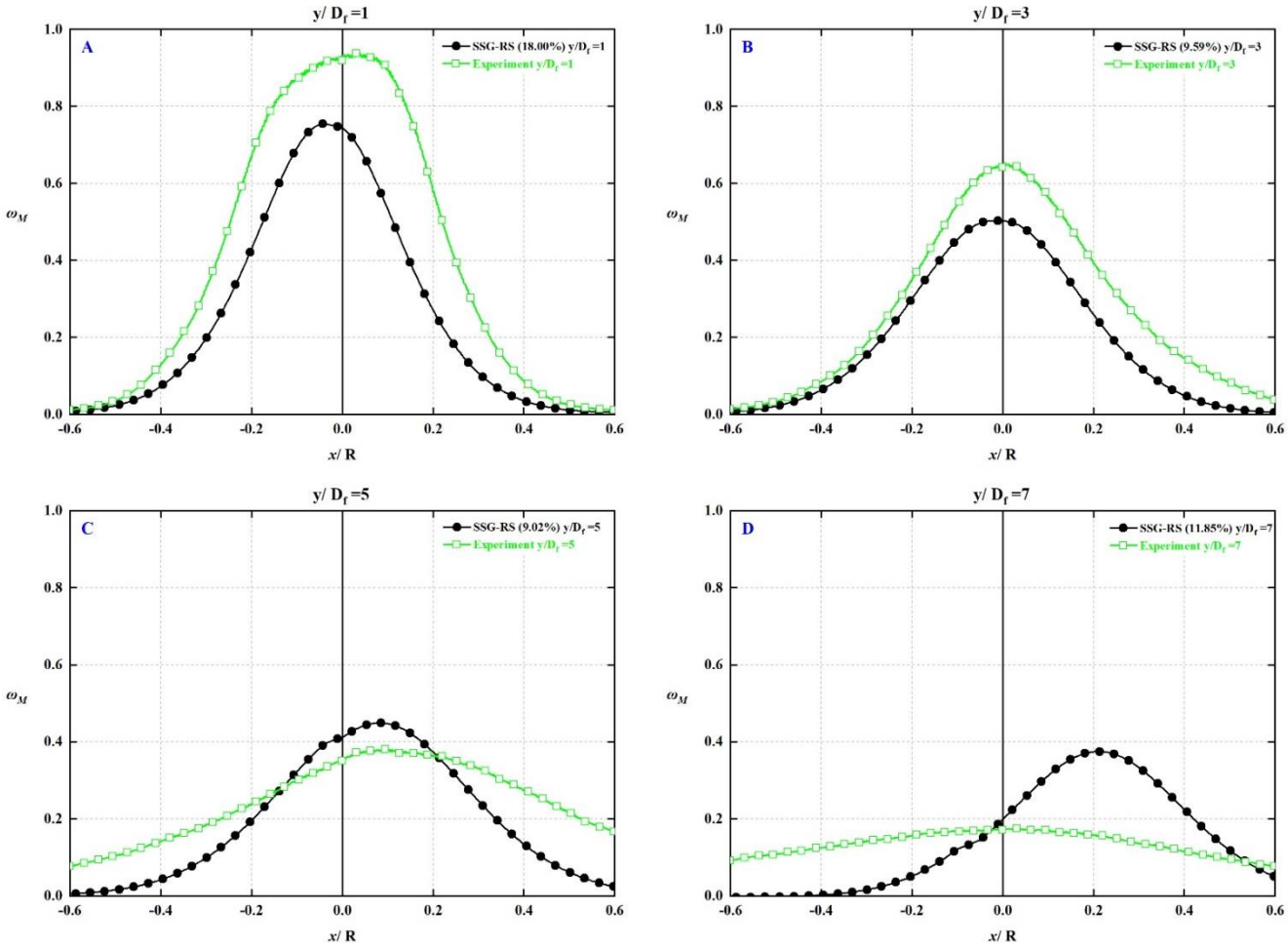

Figure 6-58: Mixture Fraction Of Methane And Stetsyuk's Experiment. A. 1D$_f$, B. 3D$_f$, C.5D$_f$, D. 7D$_f$. S=0.58, SSG-RS.

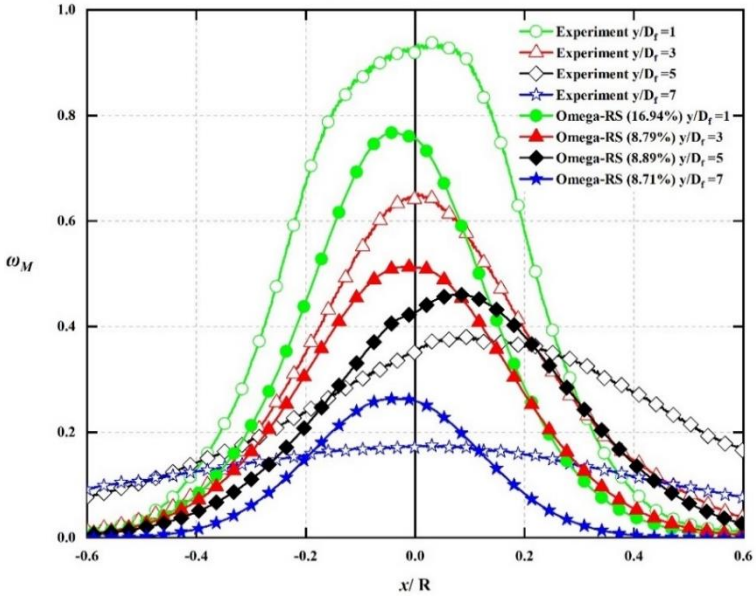

Figure 6-59: Mixture Fraction At All Locations For Methane And Stetsyuk's Experiment. S=0.58, Omega-RS.

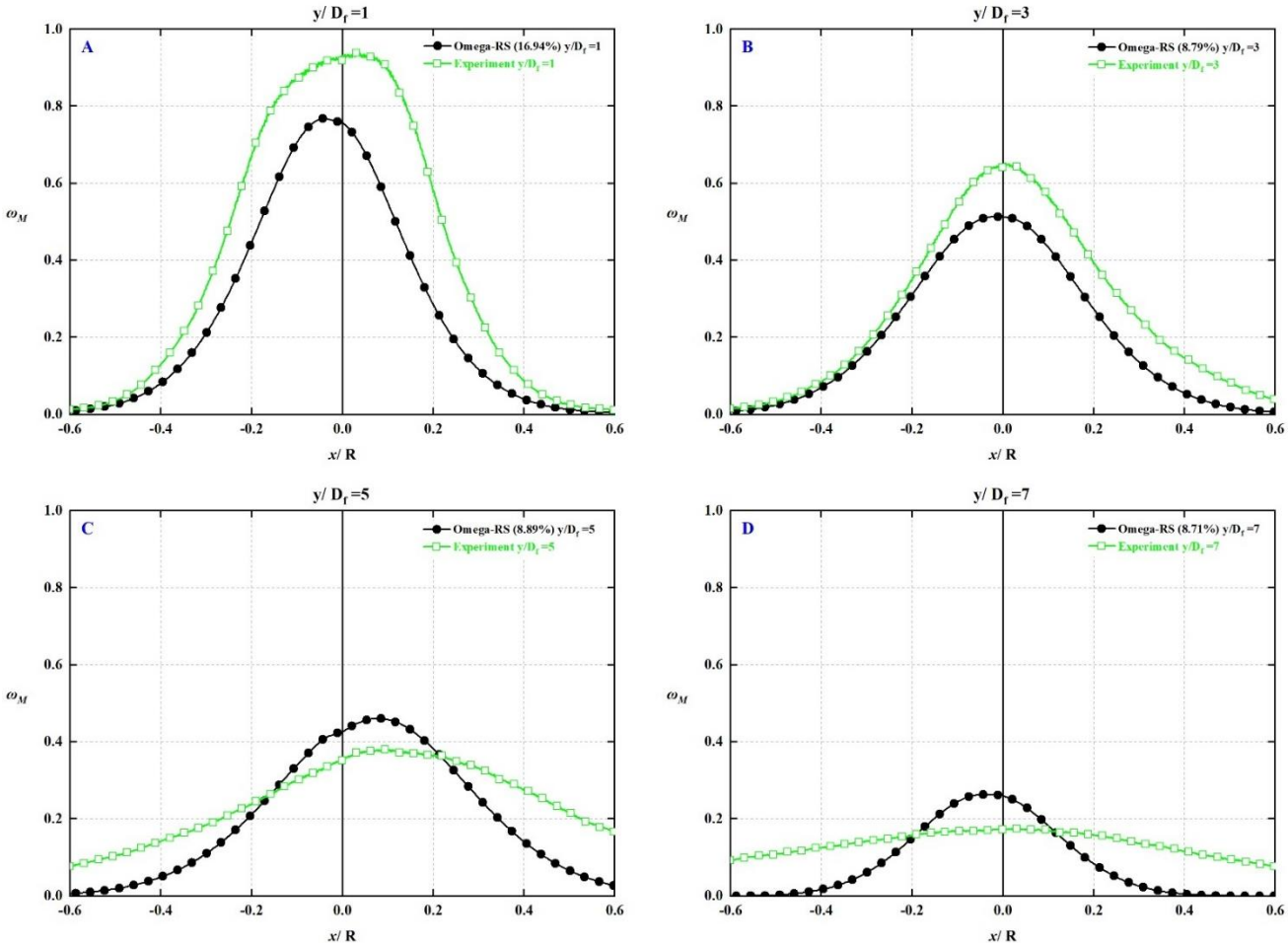

Figure 6-60: Mixture Fraction Of Methane And Stetsyuk's Experiment. A. 1D_f, B. 3D_f, C.5D_f, D. 7D_f. S=0.58, Omega-RS.

6.5.2 Symmetric analyses

The results of all the turbulence models for symmetric analyses are showing in Figures 6-61 To 6-66 via using a 2D and 3D contours. The mentioned contours signify that the non-symmetric form is higher than the first swirling number because of the increasing in the swirl strength and the existence of the screws in the geometry, more details in see section 6.7. However, the models show different level of computing this feature. For instance, two-equations based turbulence models predict a small non-symmetric shape at the last two locations. Though, the RMS turbulence models predict a large effect of non-symmetric structure. To put it another way, the RMS turbulence models are more able to predict the swirl and the screws effect more than the two-equations based turbulence models. Therefore, the simulations findings suggest that the swirl flow influences the symmetric contour at very high level when the swirl strength is 0.58.

Summarising, Table 6-4 determine the final RMSE results of the selected models. Although, the two-equations based turbulence models sharing almost same average error percent as the RSM models, these models are not able to predict the swirl flow recirculation zone. Overall, the RMS turbulence models show a good agreement with the experimental data considering the numerical and experiments errors and uncertainty. To specify, the highlighted Omega-RS turbulence model have the lowest error percent among them as it provides an automatic adjustment from a wall function to a low-Reynolds number formulation depending on the grid spacing. After all, all models show a large error percent near the inlet orifice due to the creatin of recirculation zone at high turbulence flow.

Table 6-4: RMSE Percent For All The Models At A Specific Location. S=0.58

Model	RMSE				Average error percent
	Y/ D_f				
	1	3	5	7	
K-ε	17.92%	10.01%	16.46%	6.29%	12.67%
RNG-K-ε	17.79%	9.83%	10.08%	11.41%	12.28%
Shear ST	17.27%	10.23%	10.21%	10.16%	11.97%
LRR-IP-RS	18.34%	10.02%	9.28%	8.81%	11.61%
SSG-RS	18.00%	9.59%	9.02%	11.85%	12.11%
Omega-RS	16.94%	8.79%	8.89%	8.71%	10.83%

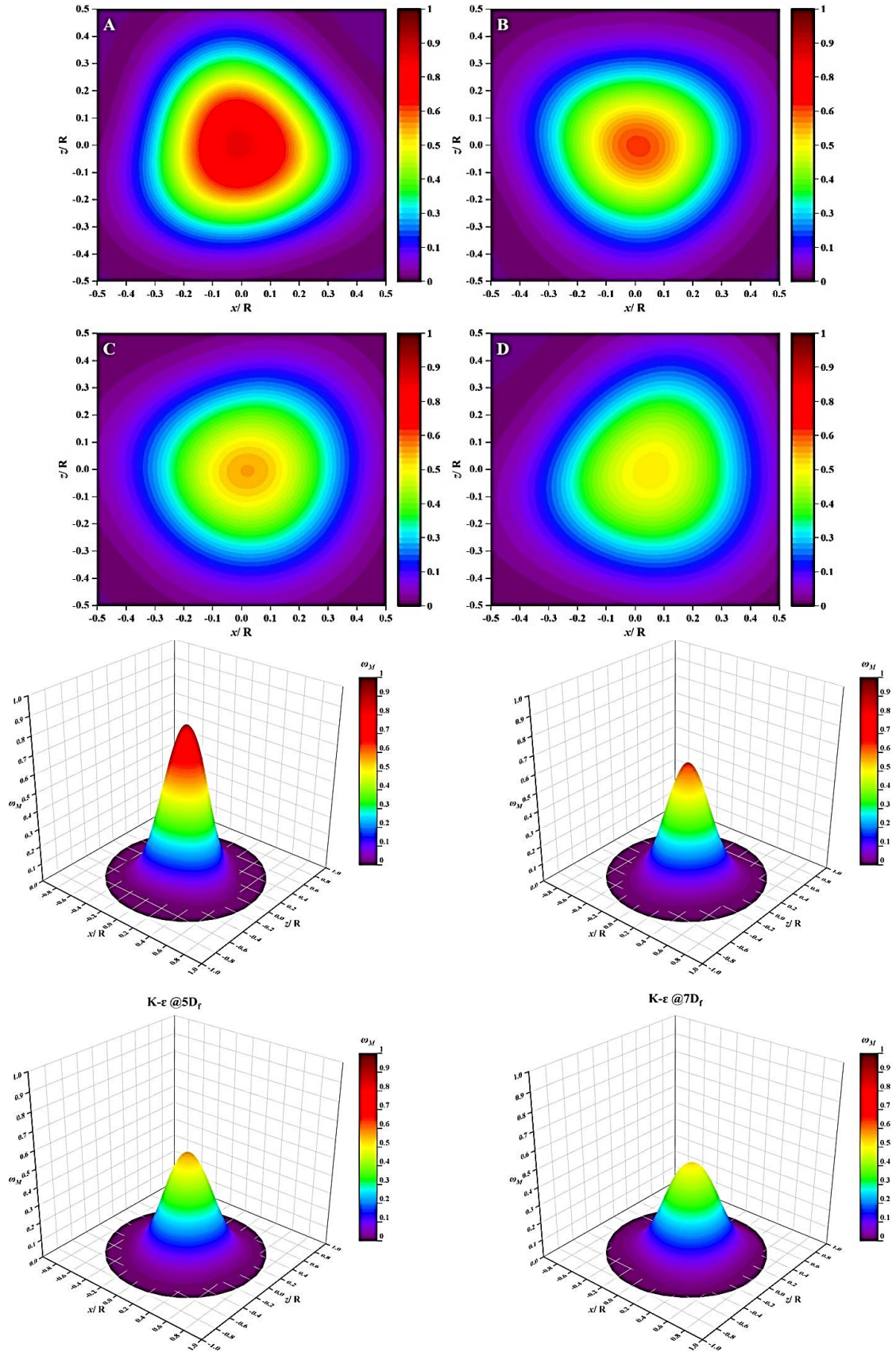

Figure 6-61: 2D (Top View) And 3D ω_M Contours Of Methane. A. 1D$_f$, B. 3D$_f$, C.5D$_f$, D. 7D$_f$. k-ε .S=0.58.

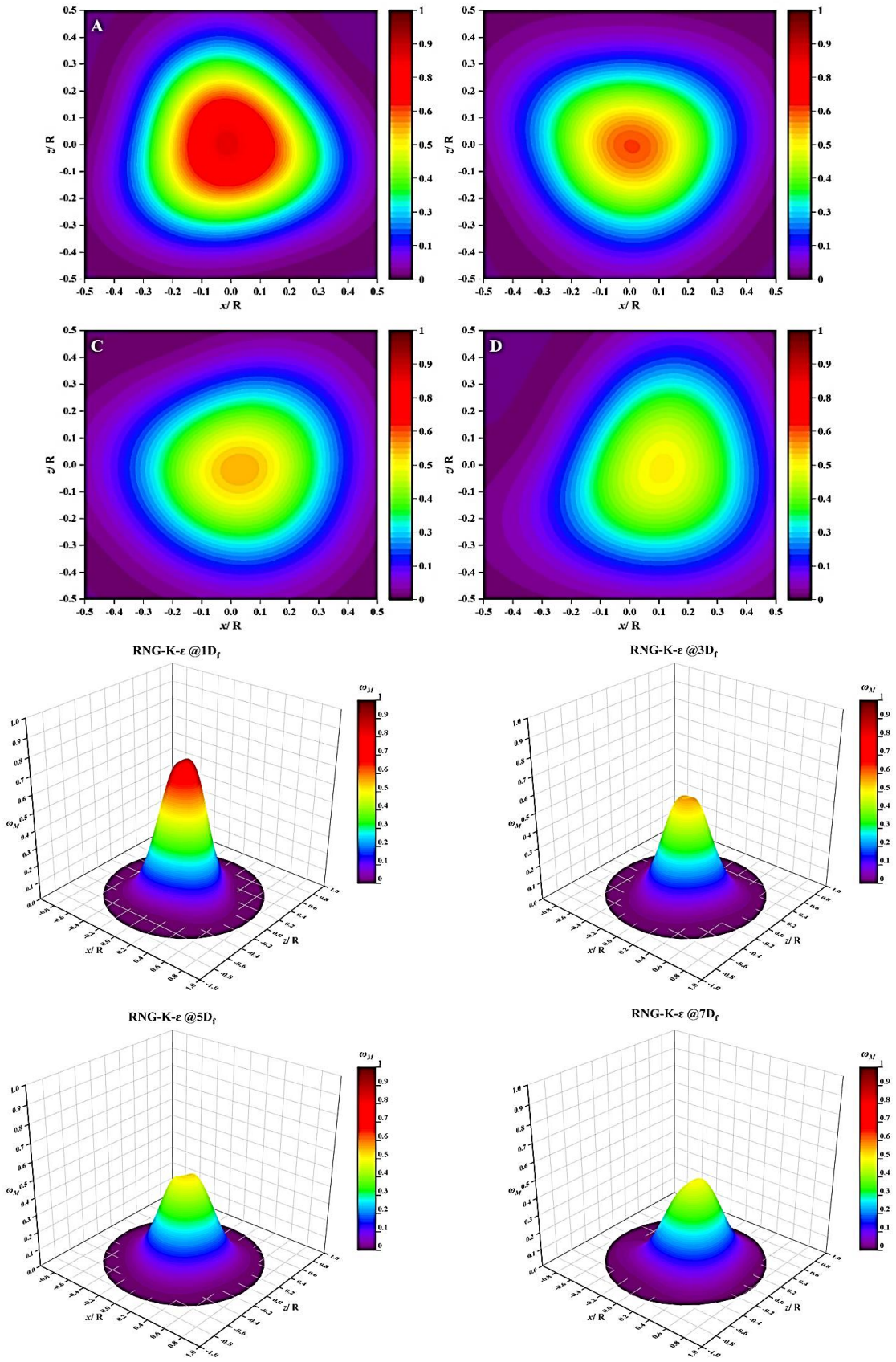

Figure 6-62: 2D (Top View) And 3D ω_M Contours Of Methane. A. 1D$_f$, B. 3D$_f$, C.5D$_f$, D. 7D$_f$. RNG k-ε .S=0.58.

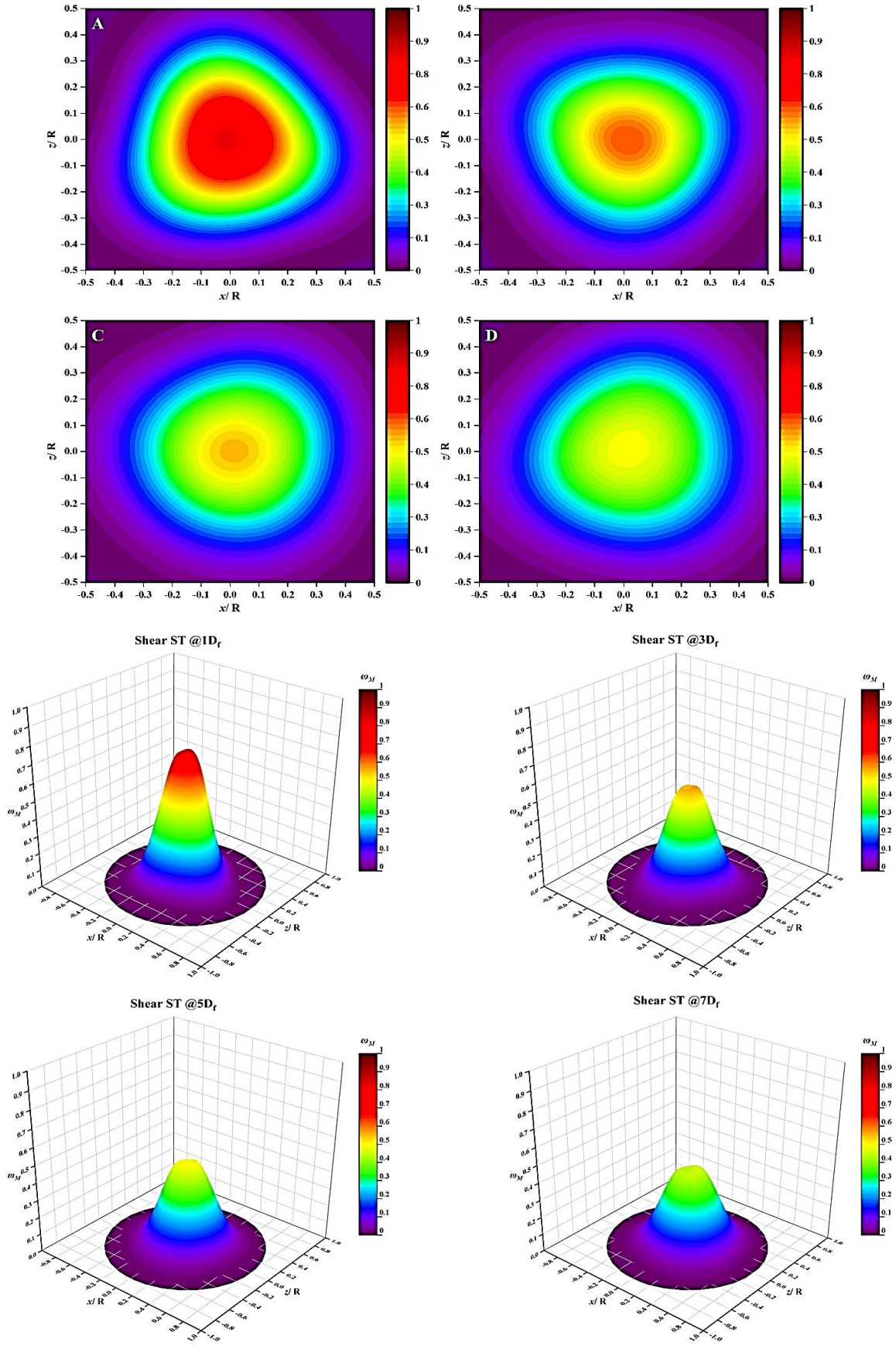

Figure 6-63: 2D (Top View) And 3D ω_M Contours Of Methane. A. 1D_f, B. 3D_f, C.5D_f, D. 7D_f. SST. S=0.58.

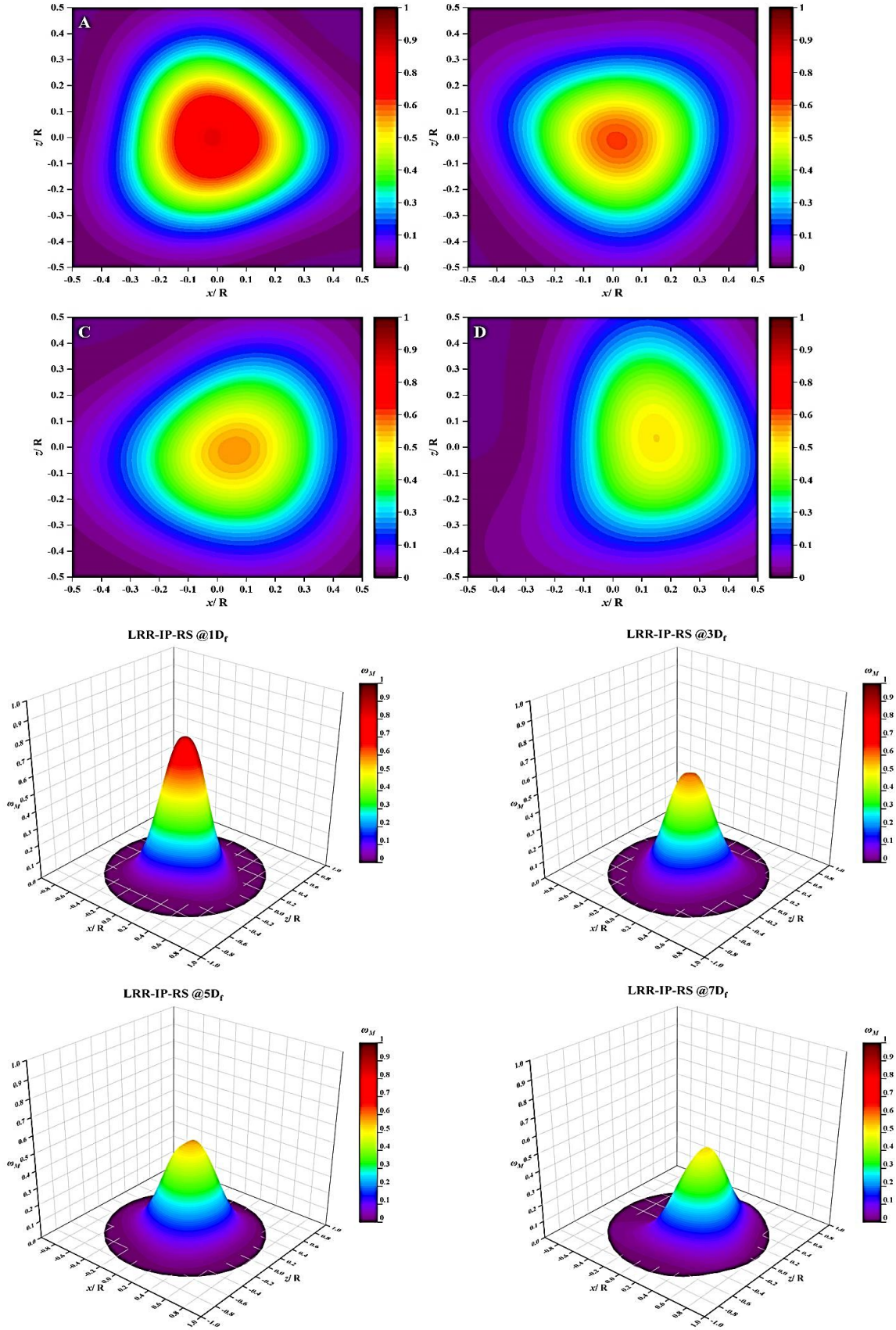

Figure 6-64: 2D (Top View) And 3D ω_M Contours Of Methane. A. 1D$_f$, B. 3D$_f$, C.5D$_f$, D. 7D$_f$. LRR-IP-RS. S=0.58.

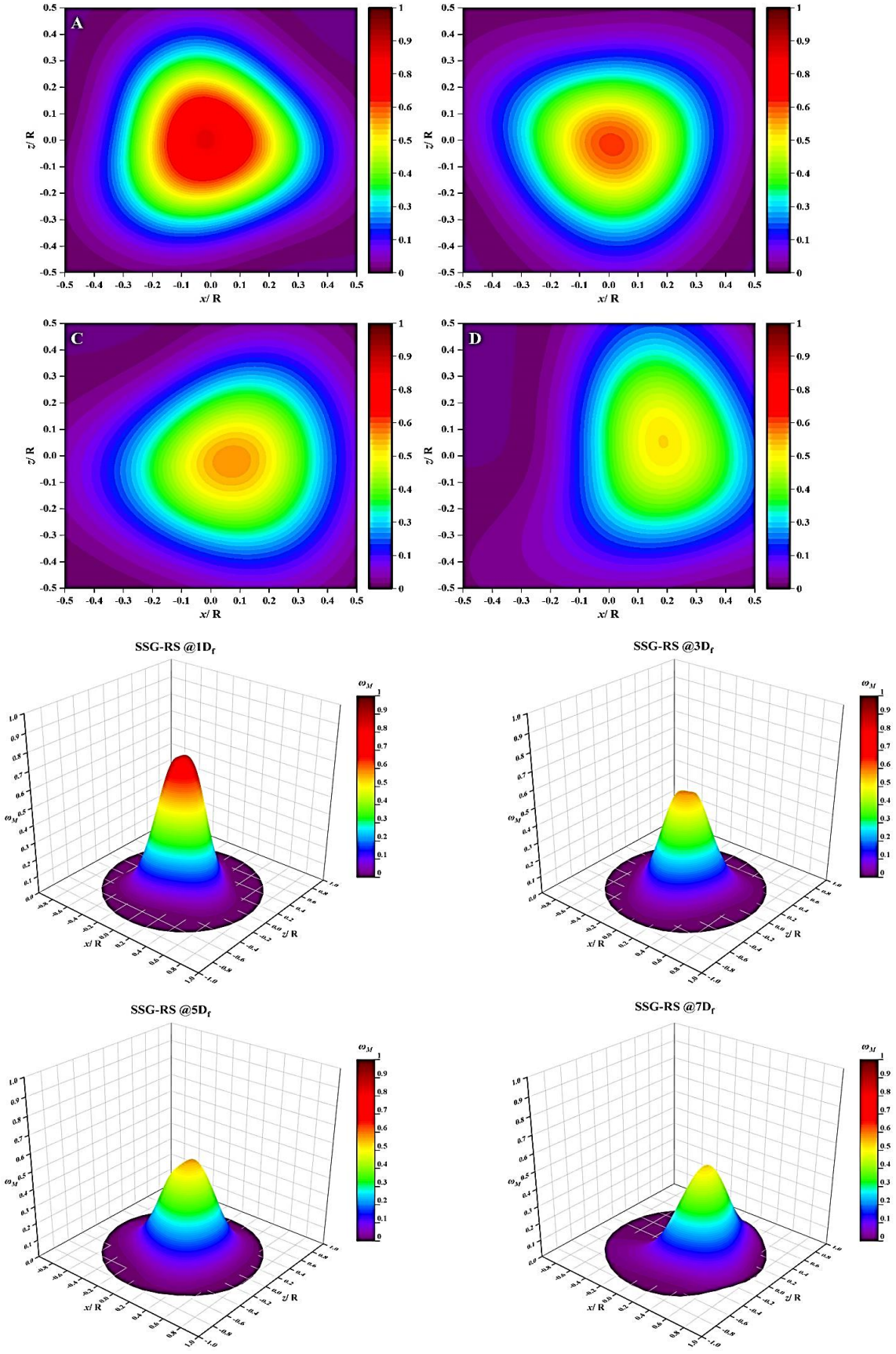

Figure 6-65: 2D (Top View) And 3D ω_M Contours Of Methane. A. 1D$_f$, B. 3D$_f$, C.5D$_f$, D. 7D$_f$. SSG-RS. S=0.58.

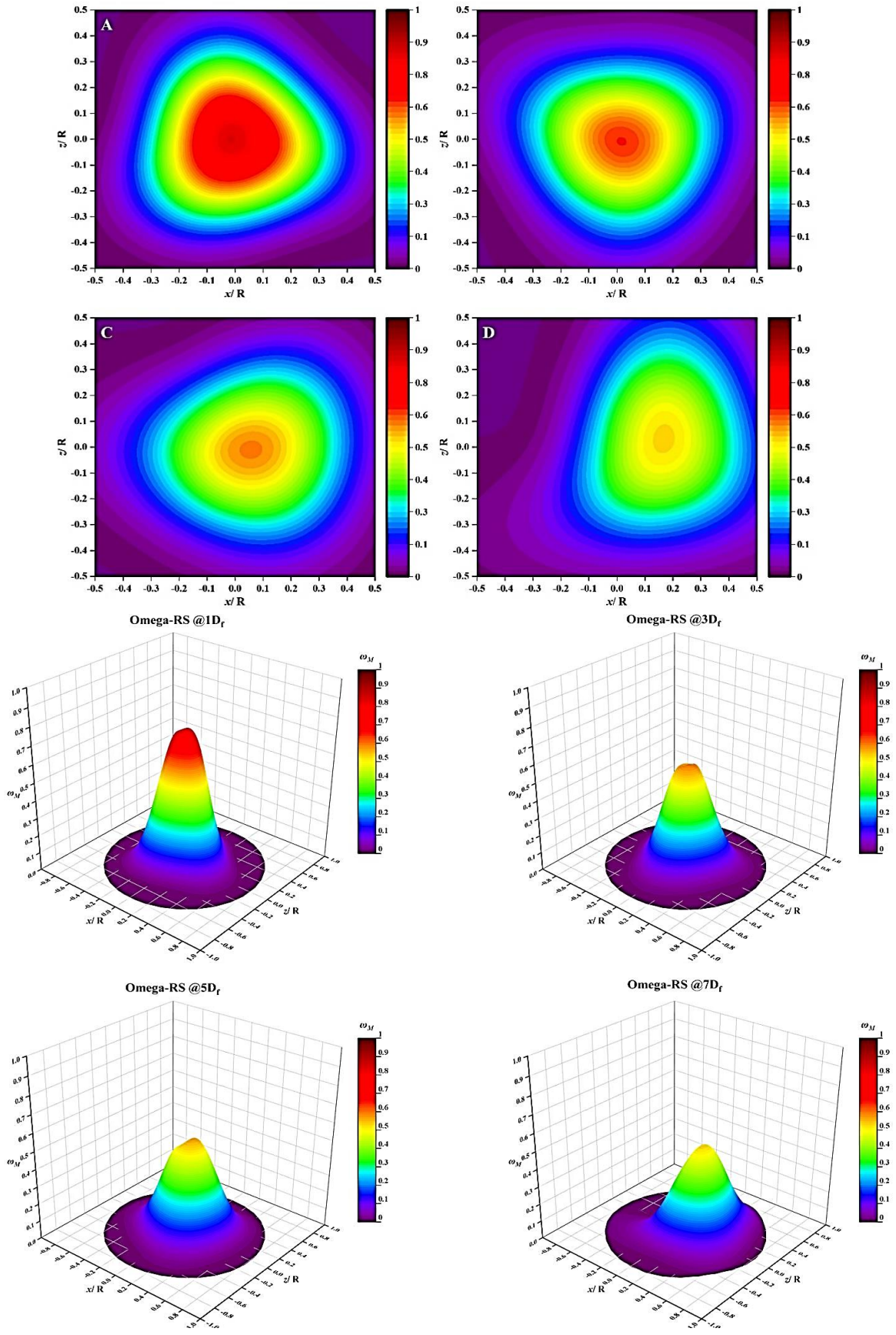

Figure 6-66: 2D (Top View) And 3D ω_M Contours Of Methane. A. 1D$_f$, B. 3D$_f$, C.5D$_f$, D. 7D$_f$. Omega-RS. S=0.58.

6.6 Third swirl number (S=1.07)

The difference between the first, second and third swirl number simulation is the boundary condition, which can be seen in Table 5.1. Hence, same process as the first and second swirl number is utilized to analyse the results of this study.

6.6.1 Effects of turbulence modelling

The effects of using different turbulence models are also examined in this research at swirl flow of 1.07 by employing Methane mixture fraction at $1D_f$, $3D_f$,$5D_f$ and $7D_f$. The simulation findings are in below:

Two-Equations based turbulence models:

Interestingly, all the RANS two-equations based turbulence models have failed modelling the swirl flow at high swirl number. Note that the models did not reach the convergence during the simulation.

For instance, the standard k-ε turbulence model shows very high RMSE percent at all locations equal to 24.79%, 51.61%, 53.65% and 60.05% as illustrated in Figures 6-67 and 6-68. Therefore, the weakness of the model to predict the flow at high mixing areas is appearing under these conditions where the swirling at the highest level. Although the RNG k-ε findings show better RMSE results 12.93%, 24.01%, 21.19% and 9.17% at $1D_f$, $3D_f$,$5D_f$ and $7D_f$, the model considered the flow like a planar jet flow and couldn't indicate the swirl existence correctly as the first model as shown in Figure 6-69 and 6-70. Similarly, SST model show approximately the same error percent's range as shown in Figures 6-71 and 6-72, where the RMSE values are 22.91%, 53.94%, 53.36% and 45.44% at $1D_f$, $3D_f$,$5D_f$ and $7D_f$, respectively.

Reynolds stress turbulence models

Remarkably, both the SSG-RS Omega-RS turbulence models have failed modelling the swirl flow. However, the LRR-IP-RS turbulence model show an acceptable result at high swirl number flow.

Therefore, LRR-IP-RS turbulence model findings as shown in Figures 6-73 and 6-74 denote that the RMSE percent have a minor difference between the model and the experiment data at the last three locations $3D_f$, $5D_f$ and $7D_f$ with a value of 10.73%, 4.28% and 3.02% respectively. However, the RMSE percent is quietly high at $1D_f$ with a value of 40.87% due to

high turbulence flow at this zone. Which mean that the model able to predict the high swirling zone.

On the other hand, Figures 6-75 and 6-76 show the huge divergence between the SSG-RS turbulence model and the experiment data where the RMSE is 11.26%, 59.40%, 52.81% and 38.50% at the selected locations. Knowing that the first value of RMSE is wrong due to incorrect simulation outcome.

Lastly, Omega-RS turbulence model is showing similar RMSE values as the previous model, equal to 32.15%, 8.18%, 56.82% and 20.39% at $1D_f$, $3D_f$,$5D_f$ and $7D_f$, respectively as shown in Figures 6-77 and 6-78. Knowing that the second value of RMSE is not right due to incorrect simulation outcome.

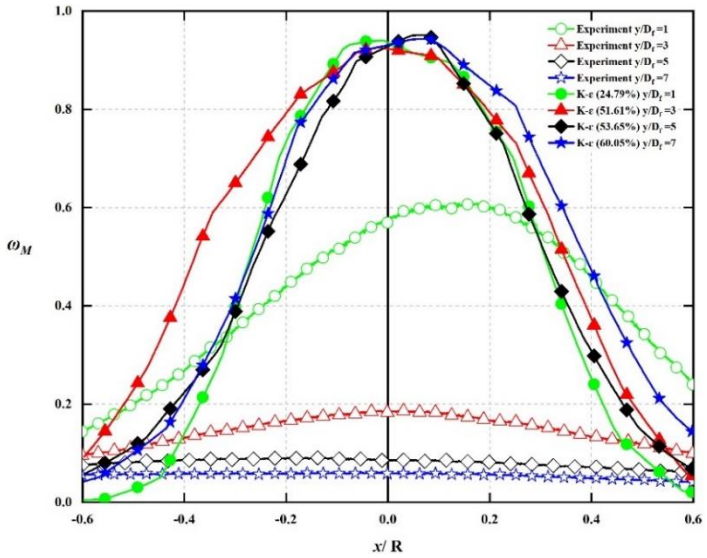

Figure 6-67: Mixture Fraction At All Locations For Methane And Stetsyuk's Experiment. S=1.07, *k-ε*.

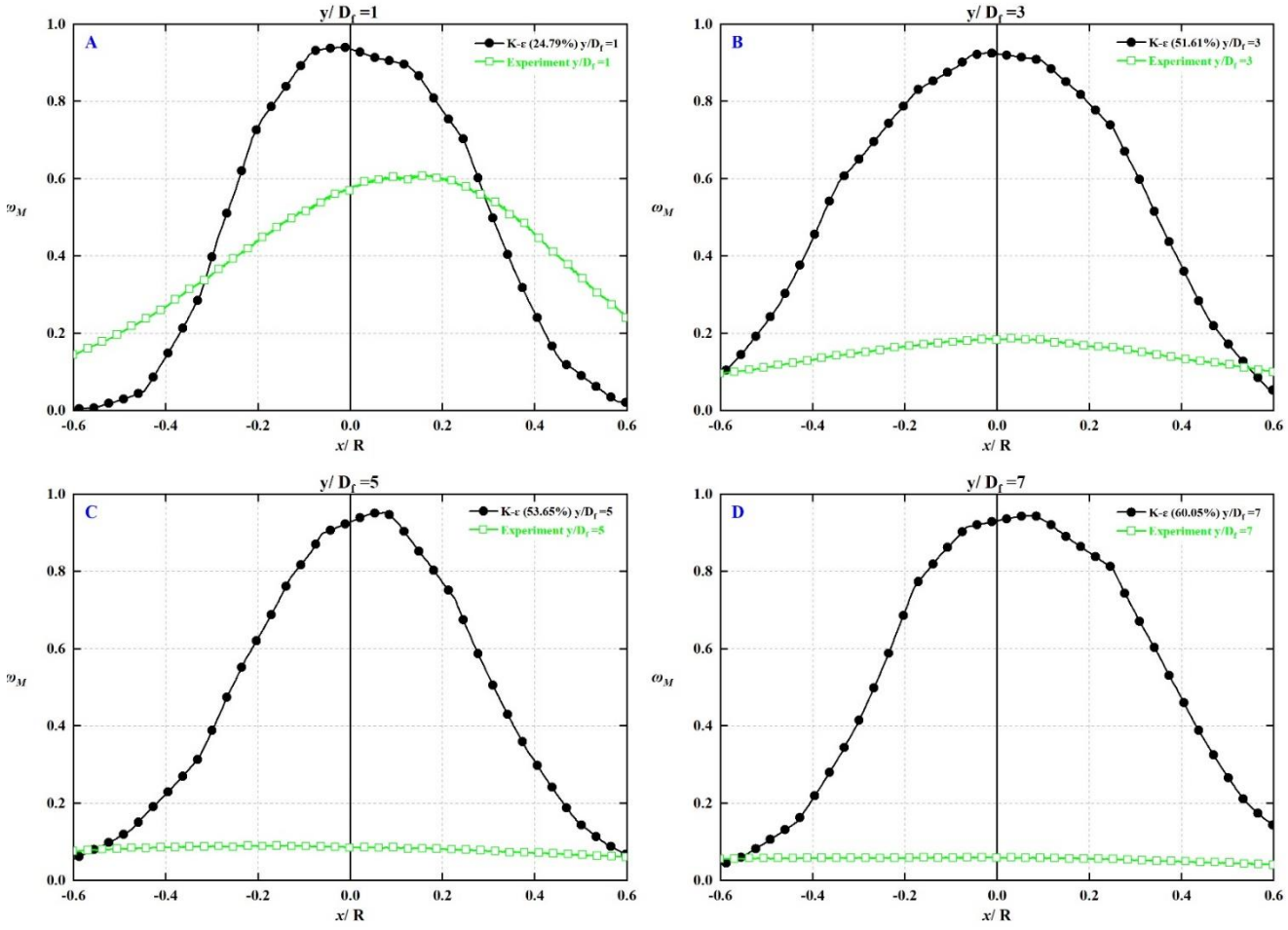

Figure 6-68: Mixture Fraction Of Methane And Stetsyuk's Experiment. A. 1D_f, B. 3D_f, C.5D_f, D. 7D_f. S=1.07, *k-ε*.

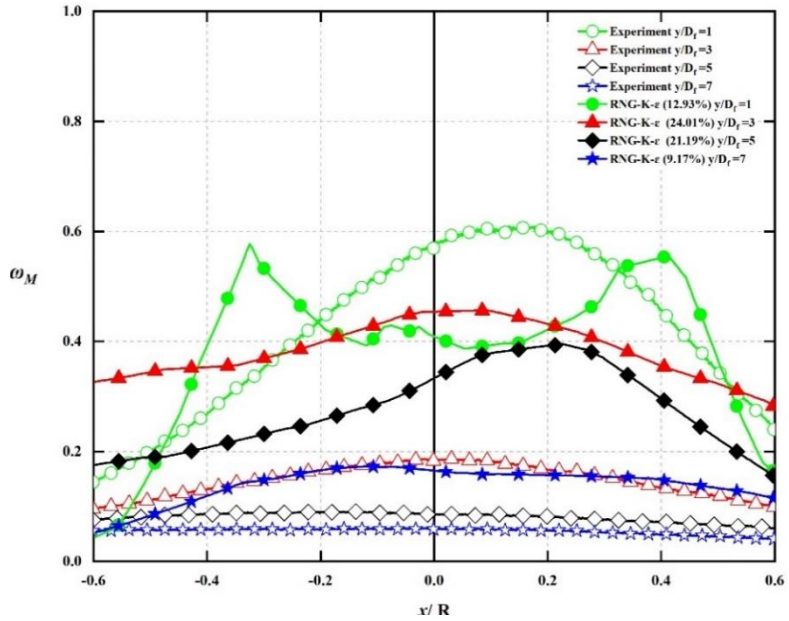

Figure 6-69: Mixture Fraction At All Locations For Methane And Stetsyuk's Experiment. S=1.07, RNG *k-ε*.

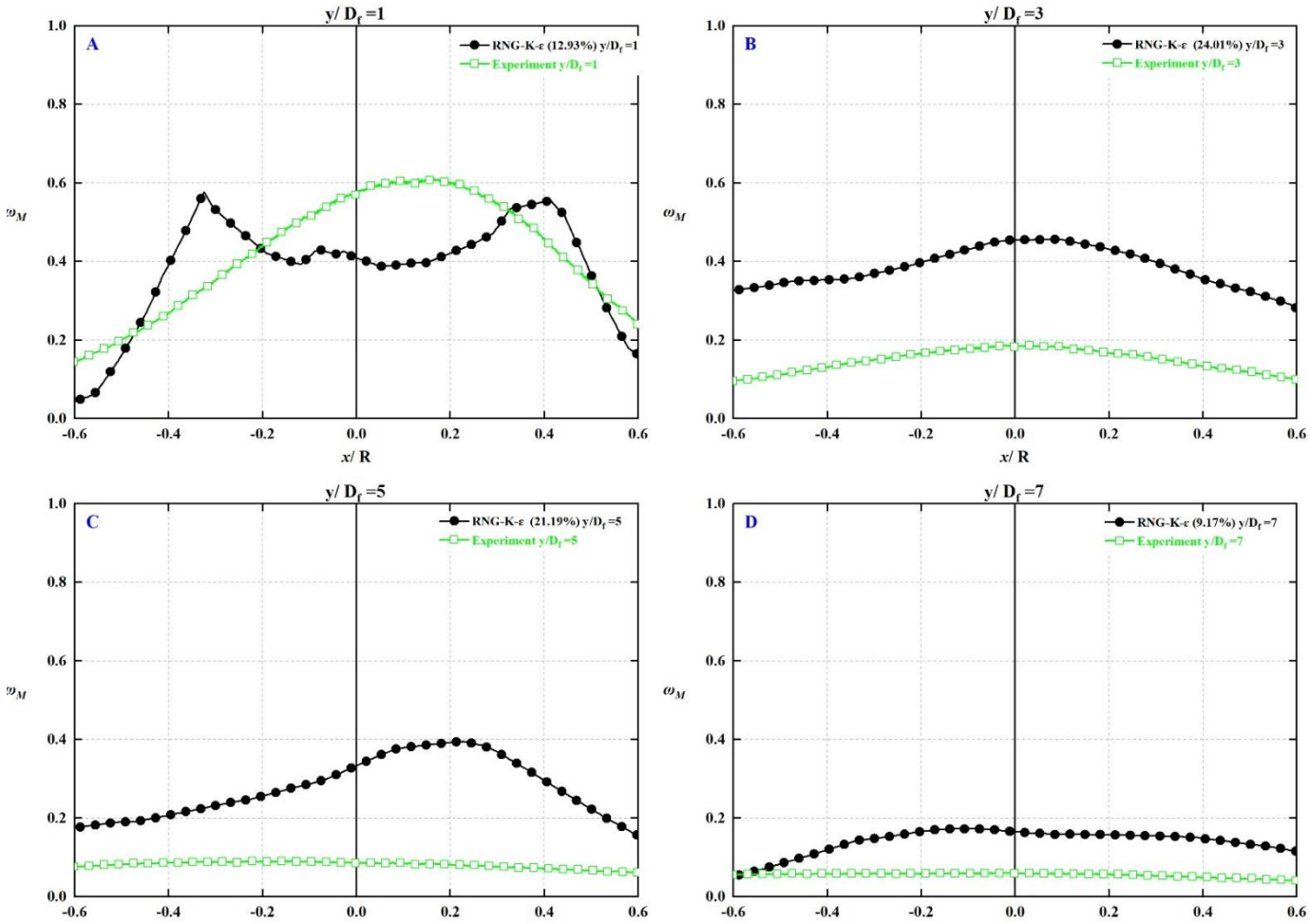

Figure 6-70: Mixture Fraction Of Methane And Stetsyuk's Experiment. A. $1D_f$, B. $3D_f$, C.$5D_f$, D. $7D_f$. S=1.07, RNG *k-ε*.

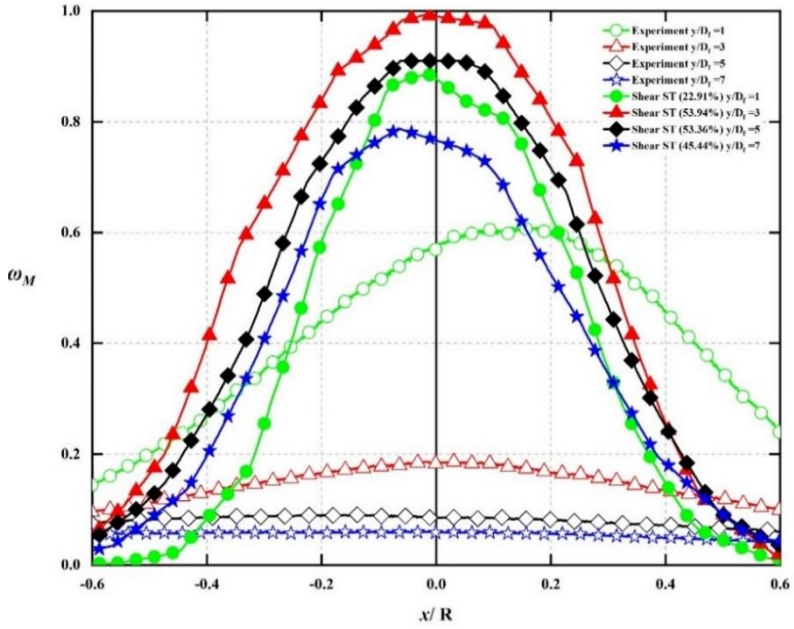

Figure 6-71: Mixture Fraction At All Locations For Methane And Stetsyuk's Experiment. S=1.07, SST.

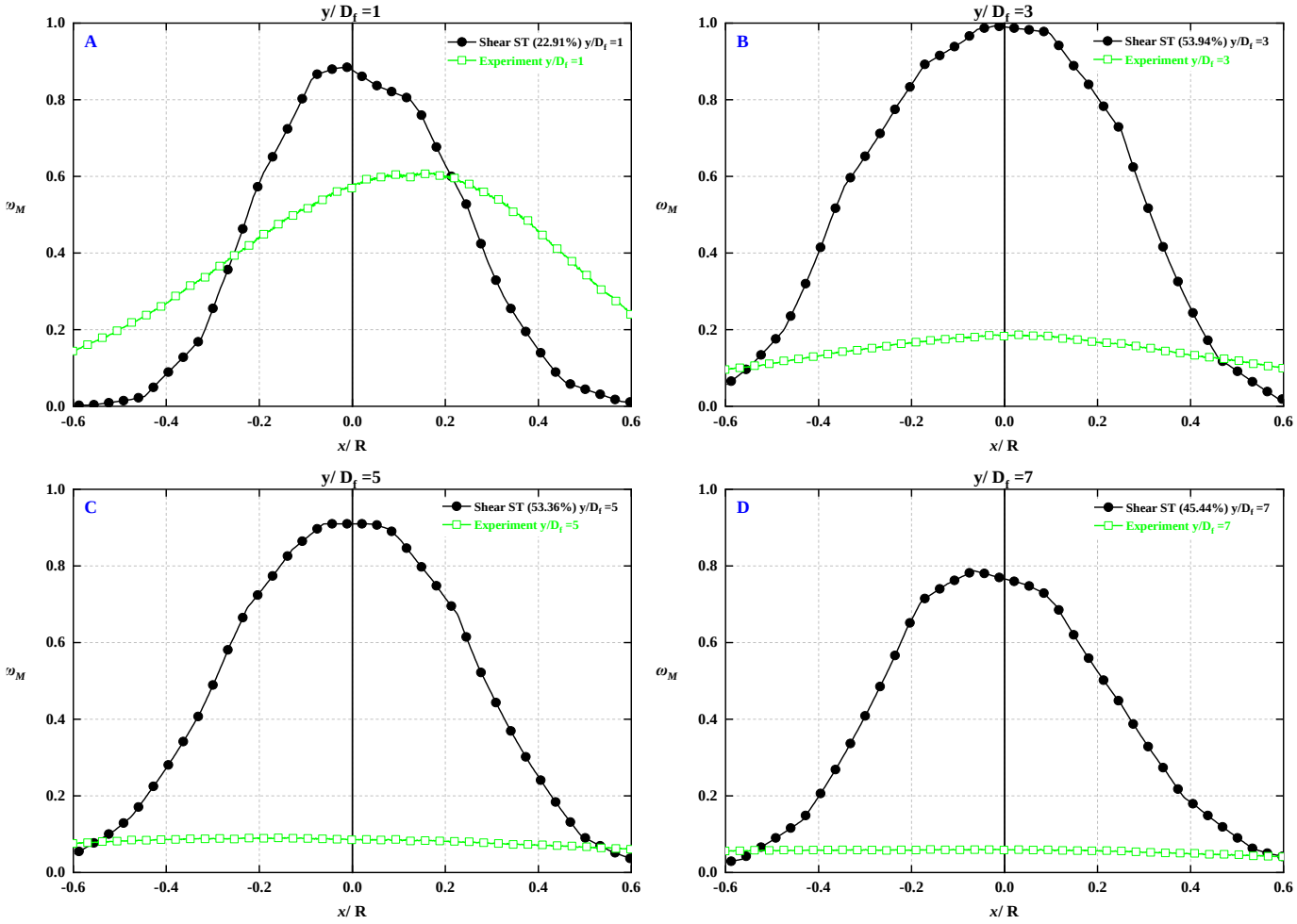

Figure 6-72: Mixture Fraction Of Methane And Stetsyuk's Experiment. A. $1D_f$, B. $3D_f$, C.$5D_f$, D. $7D_f$. S=1.07, SST.

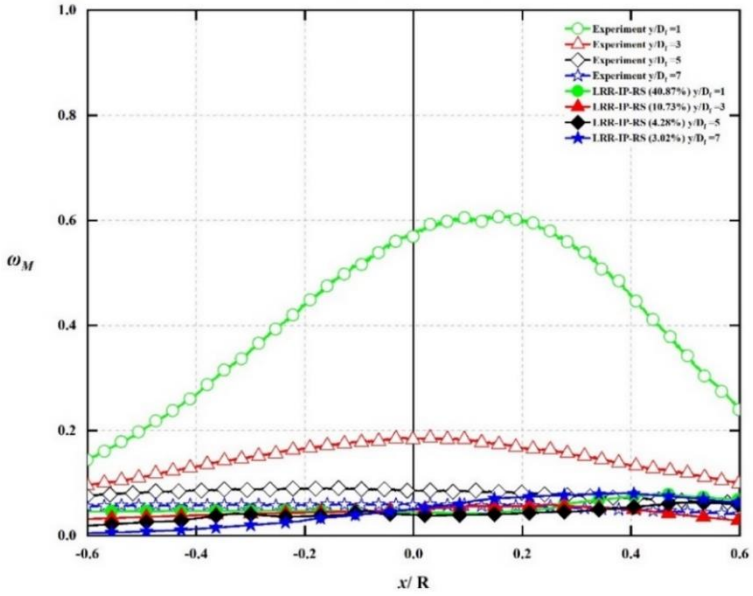

Figure 6-73: Mixture Fraction At All Locations For Methane And Stetsyuk's Experiment. S=1.07, LRR-IP-RS.

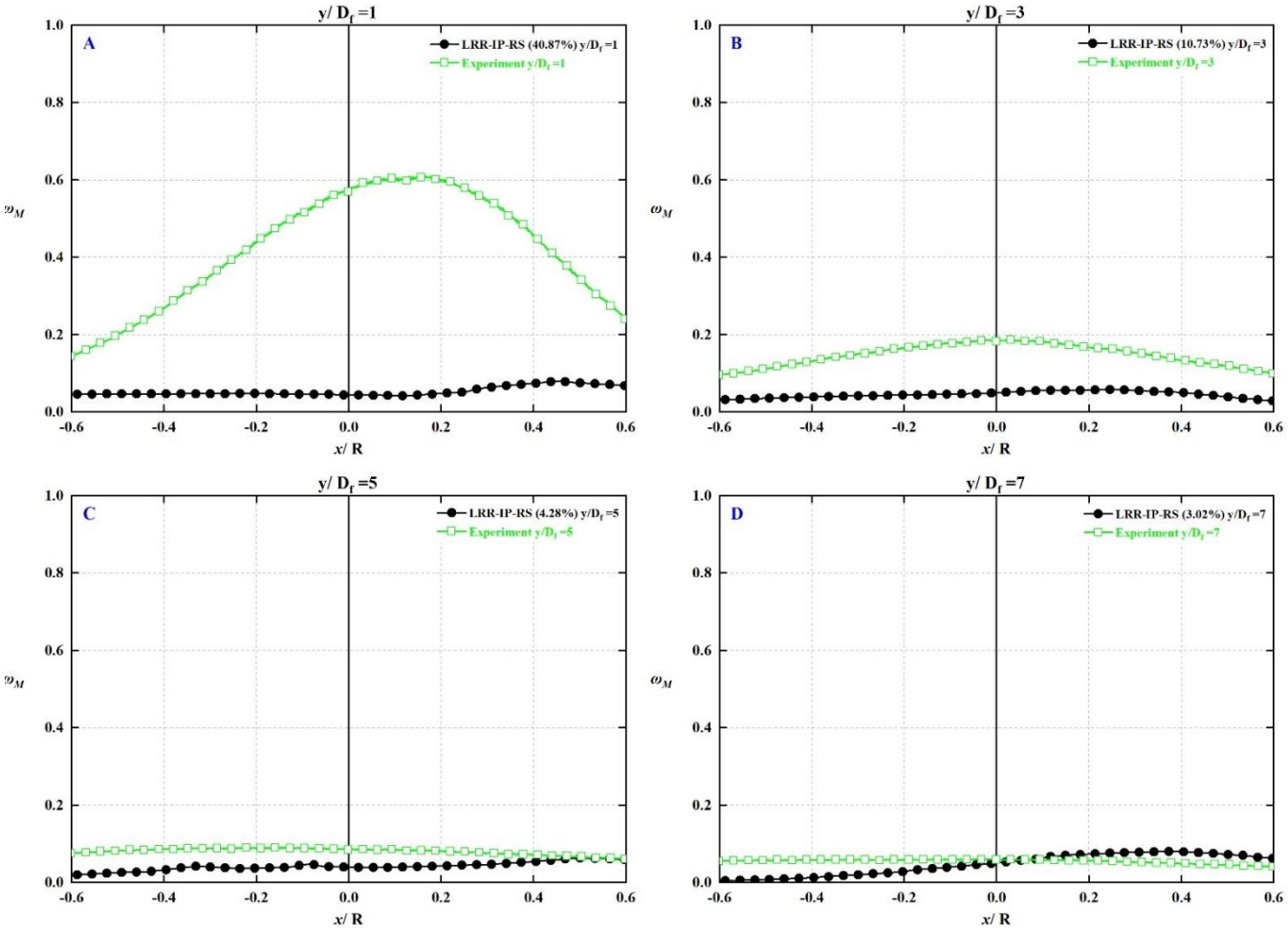

Figure 6-74: Mixture Fraction Of Methane And Stetsyuk's Experiment. A. $1D_f$, B. $3D_f$, C.$5D_f$, D.$7D_f$. S=1.07, LRR-IP-RS.

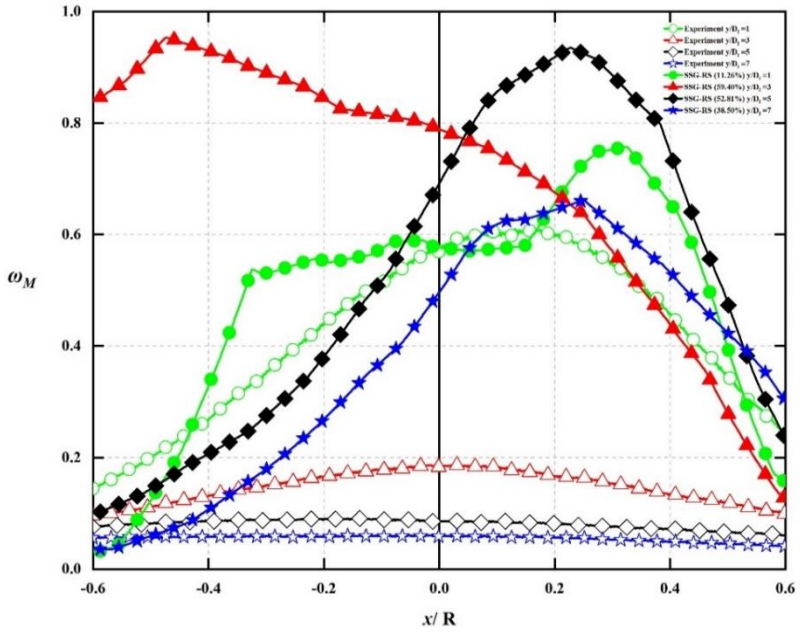

Figure 6-75: Mixture Fraction At All Locations For Methane And Stetsyuk's Experiment. S=1.07, SSG-RS.

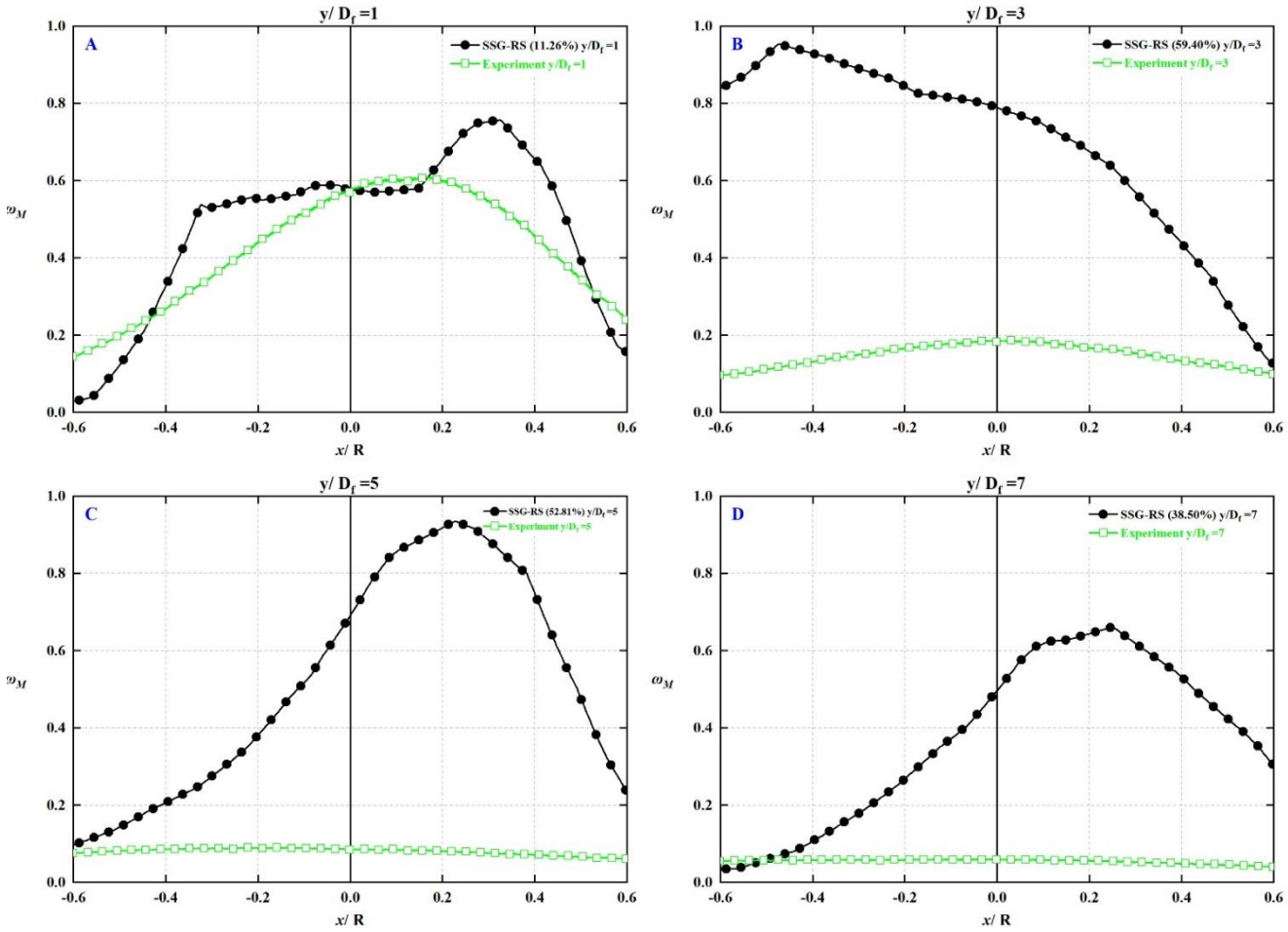

Figure 6-76: Mixture Fraction Of Methane And Stetsyuk's Experiment. A. 1D$_f$, B. 3D$_f$, C.5D$_f$, D. 7D$_f$. S=1.07, SSG-RS.

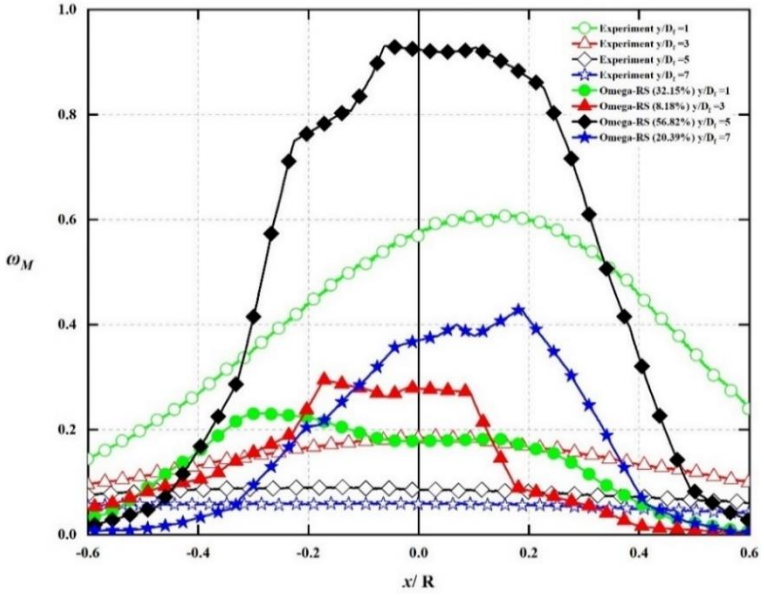

Figure 6-77: Mixture Fraction At All Locations For Methane And Stetsyuk's Experiment. S=1.07, Omega-RS.

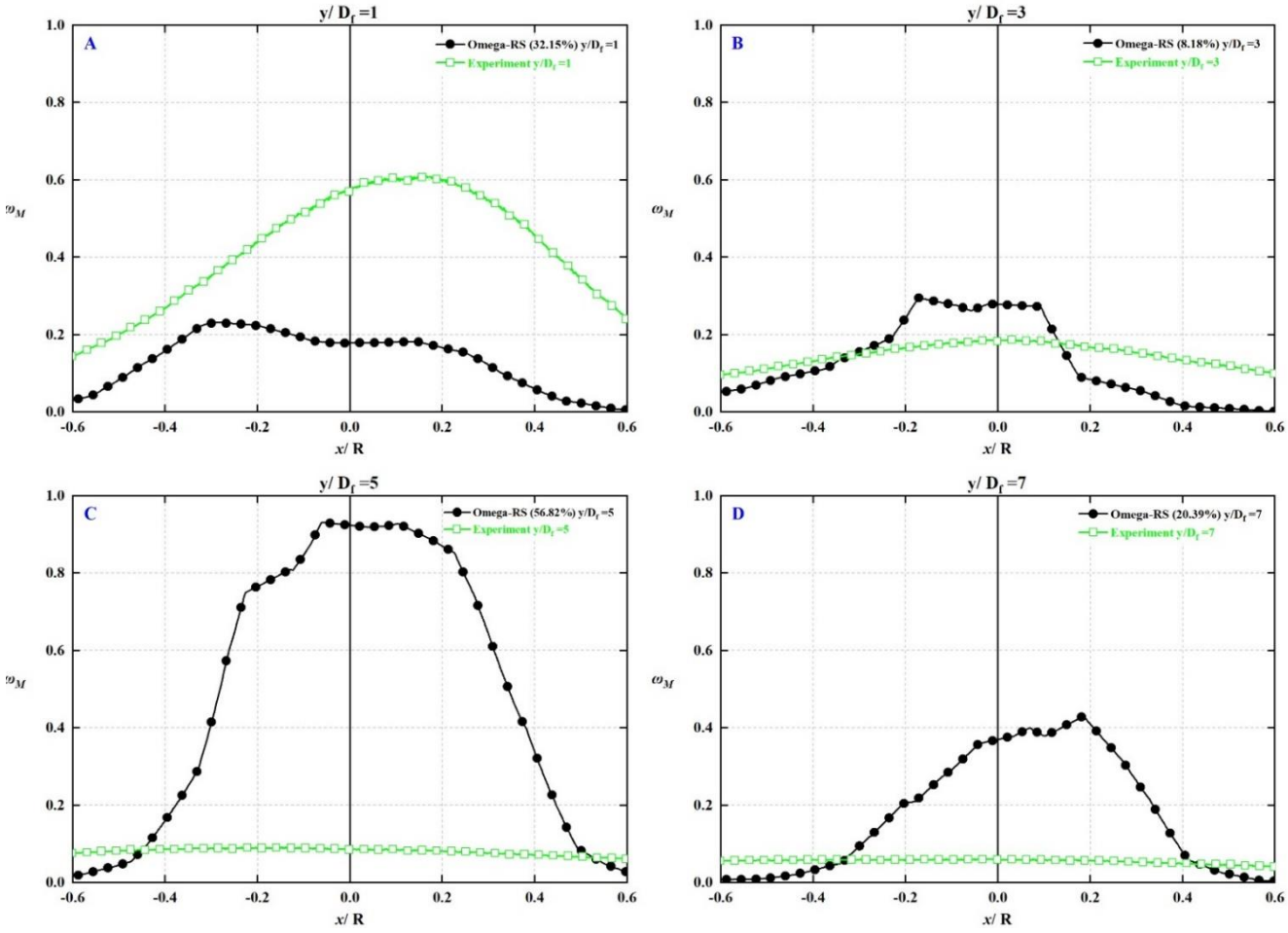

Figure 6-78: Mixture Fraction Of Methane And Stetsyuk's Experiment. A. 1D$_f$, B. 3D$_f$, C.5D$_f$, D. 7D$_f$. S=1.07, Omega-RS.

6.6.2 Symmetric analyses

Figures 6-79 To 6-84 illustrate the 2D and 3D contours of Methane mixture fraction for all turbulence models to examine the symmetric effect. As it been mentioned before, most of the models have failed modelling the swirling flow. Therefore, the non-symmetric structures are appeared at different level for each model. For instance, two-equations based turbulence models predict a small non-symmetric shape through the computational domain because these models represent the flow like a planar flow at high velocity. Thus, the related Figures 6-79, 6-80 and 6-81 show the contours with high mixture fraction in all locations. Generally, all the RMS turbulence models predict a huge effect of non-symmetric structure due to the swirl force. However, Methane mass fraction is not correct specially in SSG-RS and Omega-RS turbulence model. Therefore, the RMS turbulence models can predict the high swirl effect on the symmetric structure more than the two-equations based turbulence models. In addition, the non-symmetric form can be related to existence of screws inside the domain as detailed in section 6.7. Therefore, the simulations results recommend that the swirl flow influences the symmetric contour largely when the swirl strength is 1.07.

In brief, Table 6-5 determine the last RMSE results of the selected models. Though, the RNG k-ε show a low average RMSE value, the model is failed modelling as been explained before. Therefore, the two-equations based turbulence models are not able to predict the swirl flow because of recirculation zone. Overall, the highlighted LRR-IP-RS turbulence model with an average RMSE value of 14.72% show a good agreement with the experimental data considering the numerical and experiments errors and uncertainty. Additionally, all models show a huge error percent in all computational domain due to the creatin of recirculation zone at high turbulence flow.

Finally, by taking all the previous RMSE average values at all swirling number, the LRR-IP-RS turbulence model show the lowest error percent among them. Thus, this model has the best prediction outcome with an RMSE value of 14.72% as highlighted in Table 6-6. Moreover, section 6.8 demonstrates more results of this model such as velocity streamline and vectors at multi swirl number.

Table 6-5: RMSE Percent Value For All The Models At A Specific Location. S=1.07

Model	RMSE Y/ D_f				Average error percent
	1	3	5	7	
K-ε	24.79%	51.61%	53.65%	60.05%	47.52%
RNG-K-ε	12.93%	24.01%	21.19%	9.17%	16.82%
Shear ST	22.91%	53.94%	53.36%	45.44%	43.92%
LRR-IP-RS	40.87%	10.73%	4.28%	3.02%	14.72%
SSG-RS	11.26%	59.40%	52.81%	38.50%	40.49%
Omega-RS	32.15%	8.18%	56.82%	20.39%	29.39%

Table 6-6: Average RMSE Percent For All The Models At All Swirling Number

Model	Ave. Error Percent			Total Ave. Error Percent
	S=0.3	S=0.58	S=1.07	
K-ε	15.63%	12.67%	47.52%	25.27%
RNG-K-ε	16.30%	12.28%	16.82%	15.13%
Shear ST	15.92%	11.97%	43.92%	23.93%
LRR-IP-RS	16.62%	11.61%	14.72%	14.32%
SSG-RS	16.67%	12.12%	40.49%	23.09%
Omega-RS	16.26%	10.83%	29.39%	18.83%

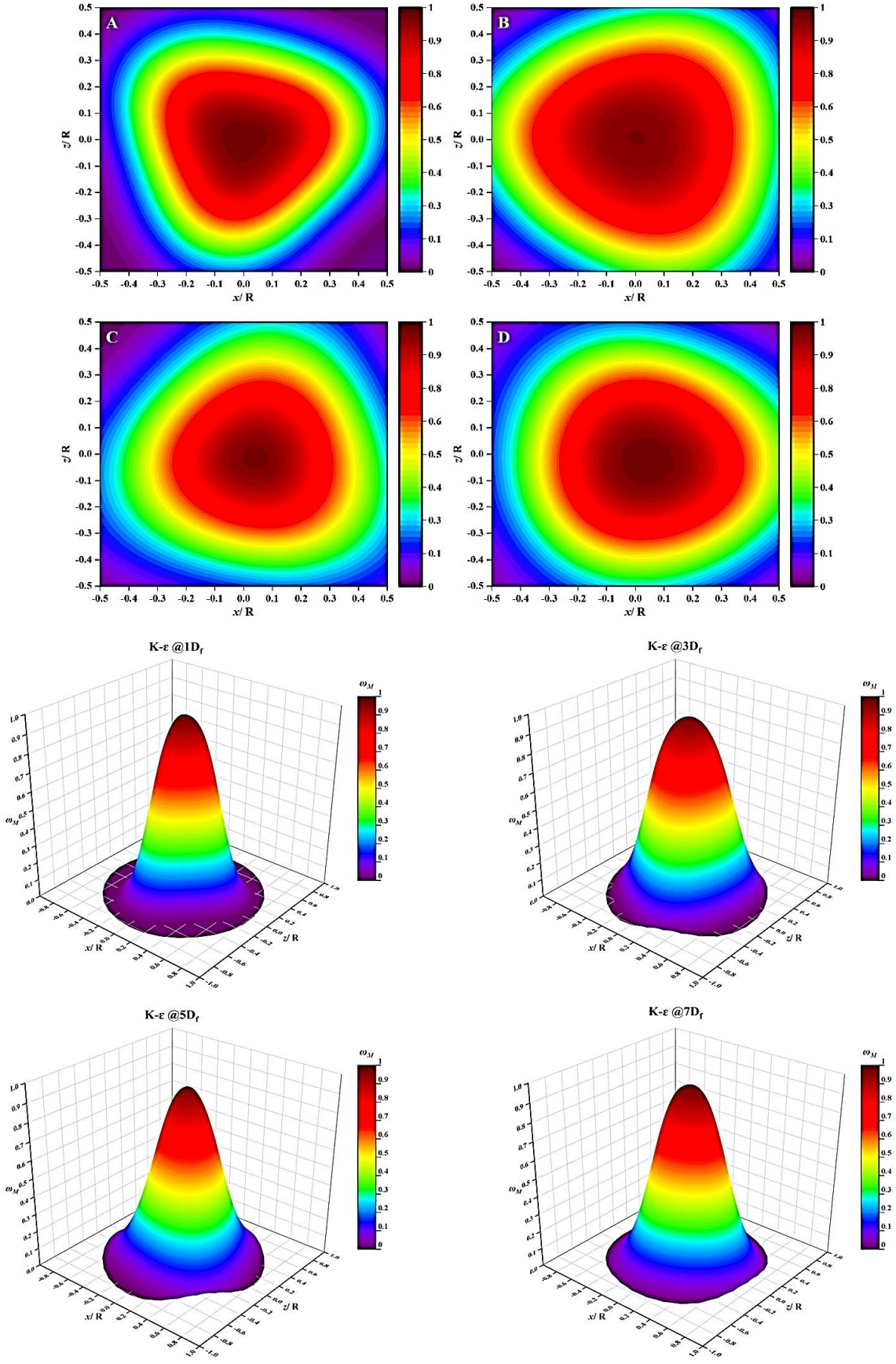

Figure 6-79: 2D (Top View) And 3D ω_M Contours Of Methane. A. 1D$_f$, B. 3D$_f$, C.5D$_f$, D. 7D$_f$. k-ε .S=1.07.

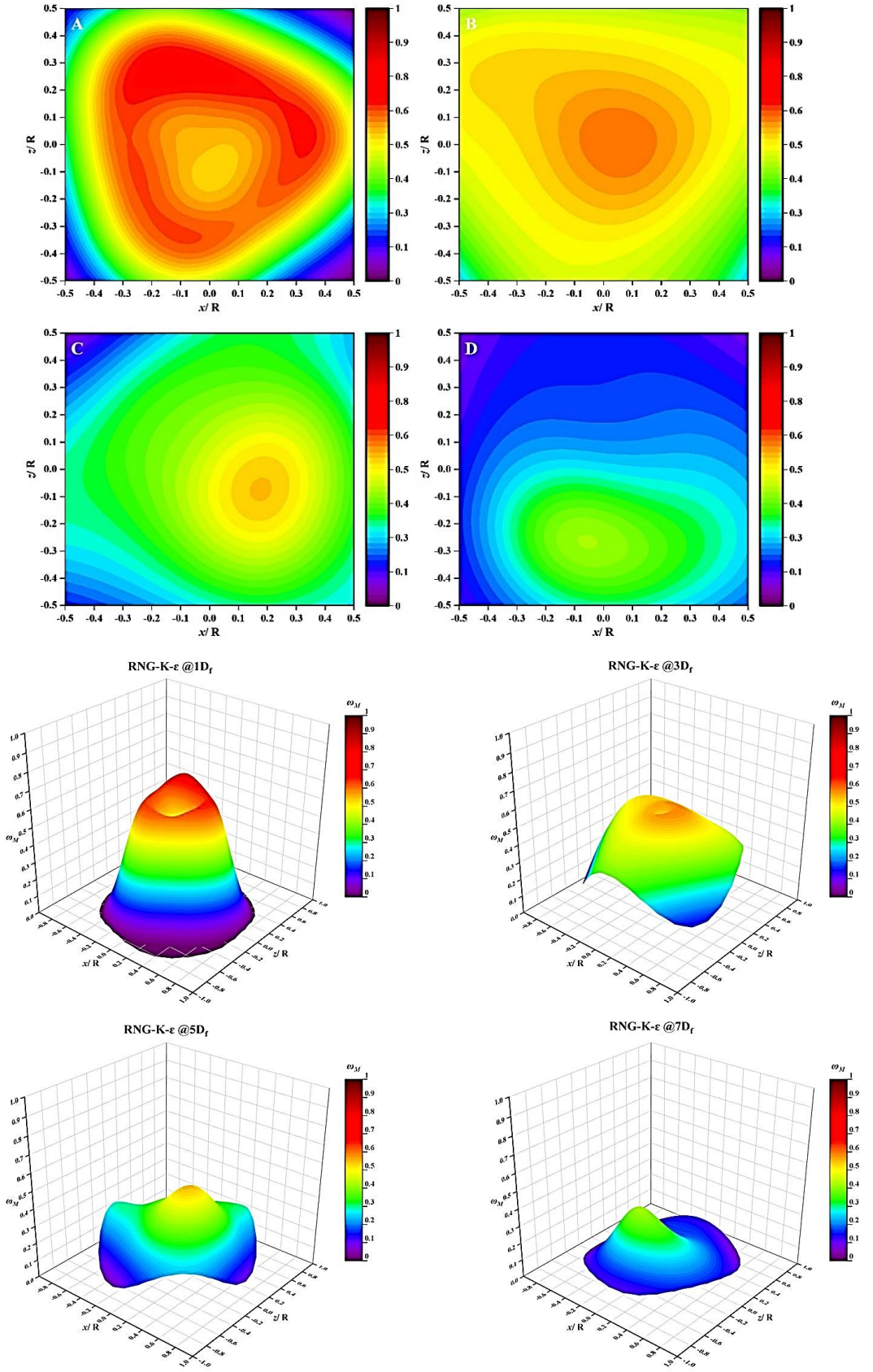

Figure 6-80: 2D (Top View) And 3D ω_M Contours Of Methane. A. 1D$_f$, B. 3D$_f$, C.5D$_f$, D. 7D$_f$. RNG k-ε .S=1.07.

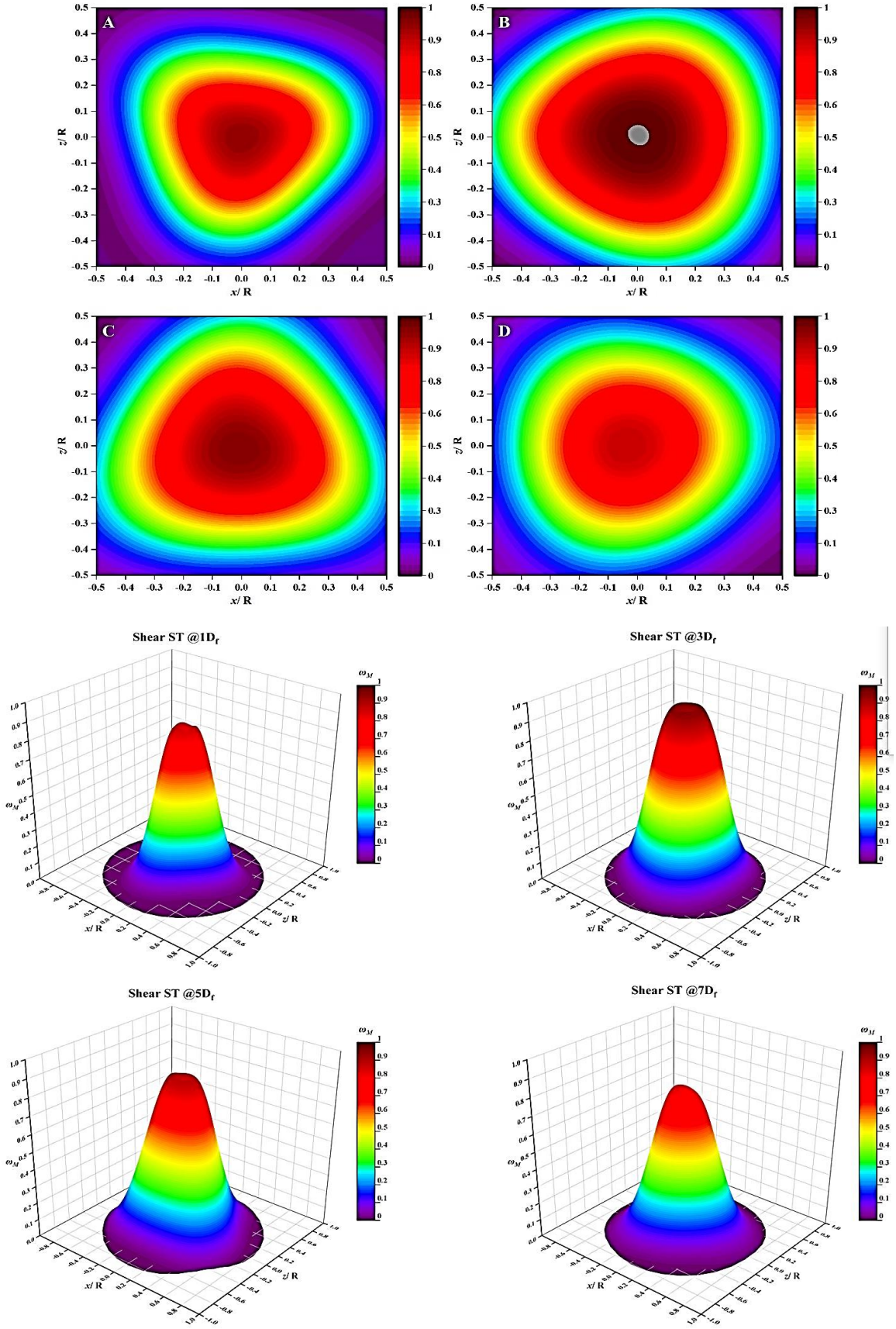

Figure 6-81: 2D (Top View) And 3D ω_M Contours Of Methane. A. 1D_f, B. 3D_f, C.5D_f, D. 7D_f. SST. S=1.07.

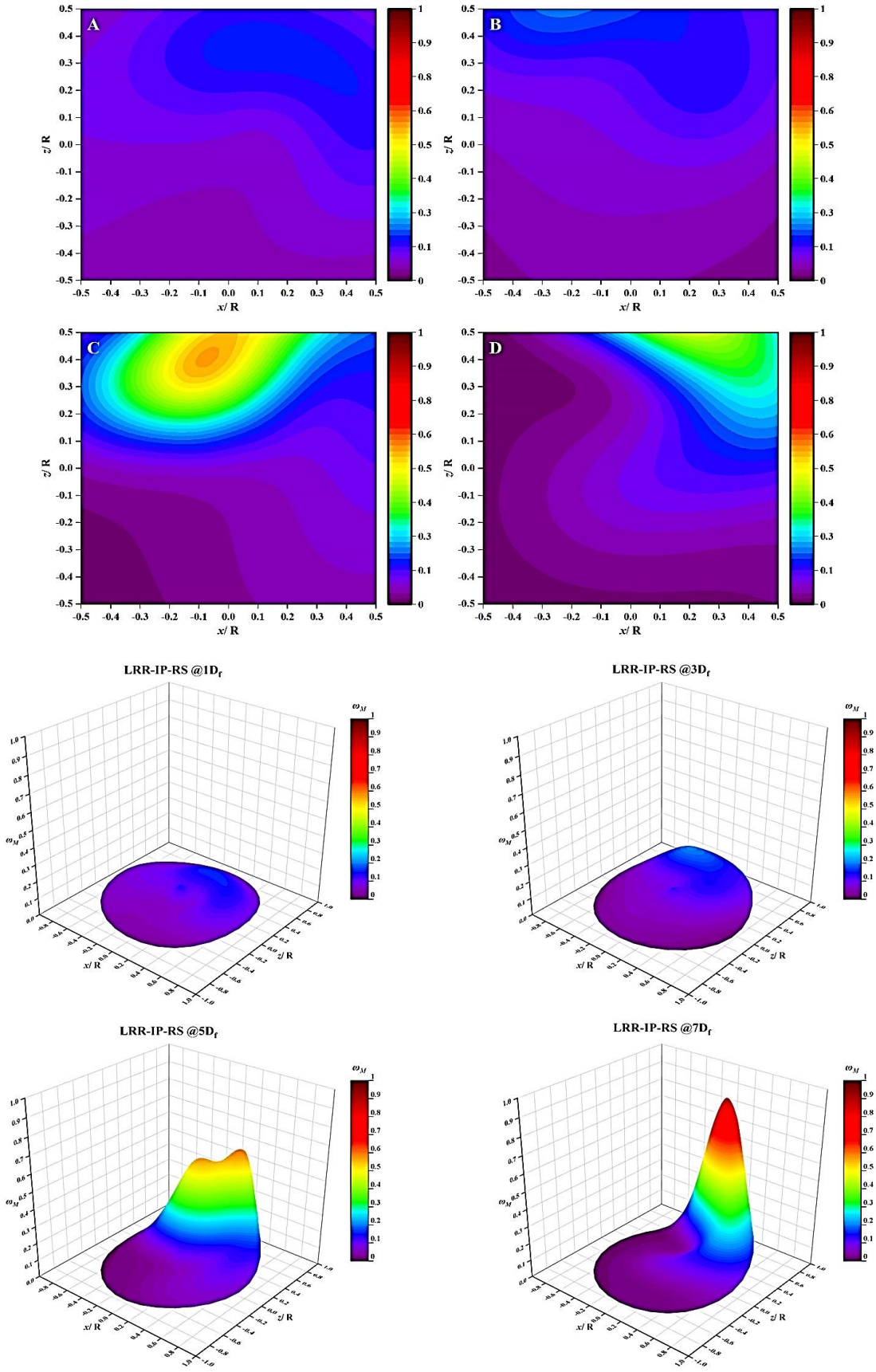

Figure 6-82: 2D (Top View) And 3D ω_M Contours Of Methane. A. 1D$_f$, B. 3D$_f$, C.5D$_f$, D. 7D$_f$. LRR-IP-RS. S=1.07.

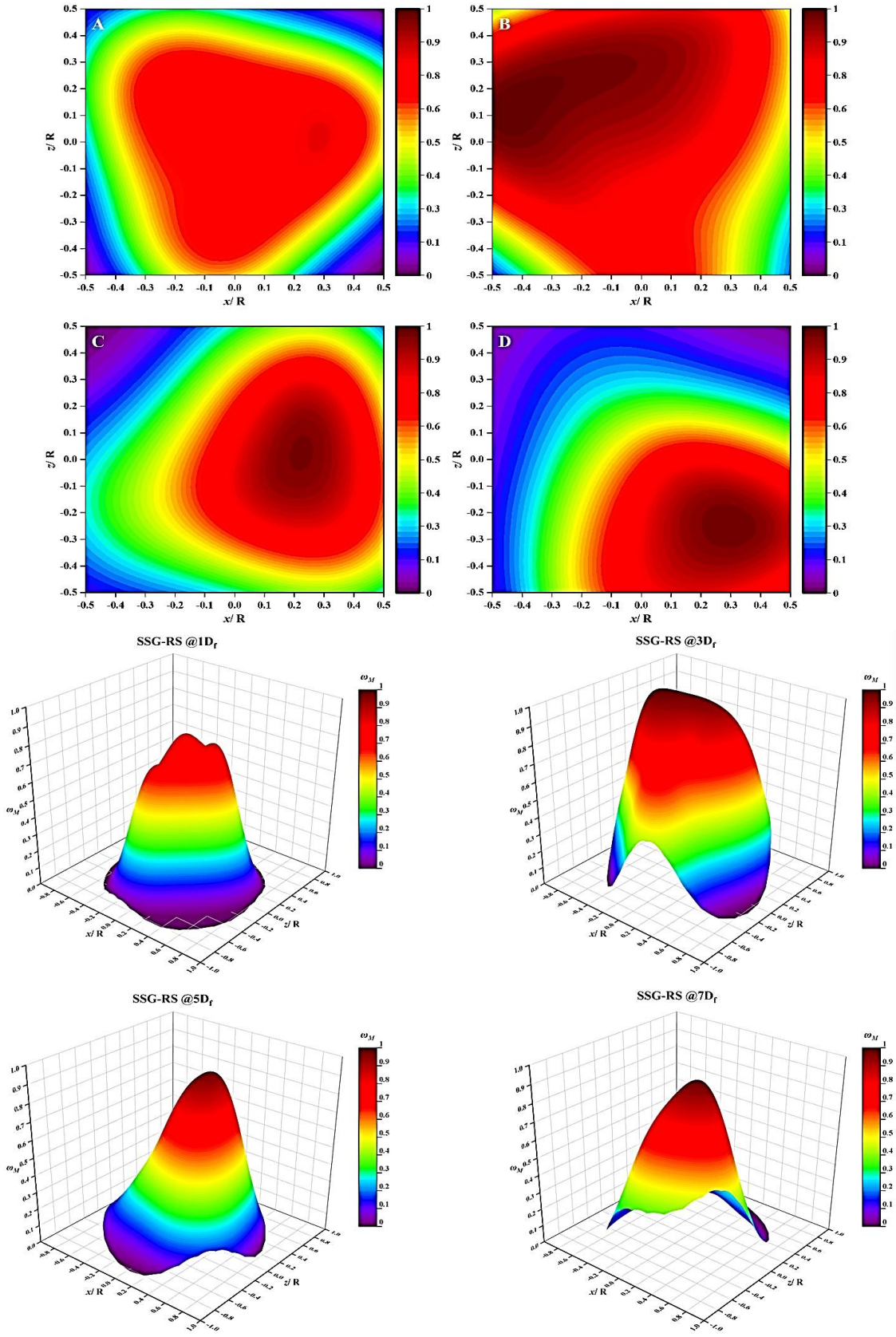

Figure 6-83: 2D (Top View) And 3D ω_M Contours Of Methane. A. 1D$_f$, B. 3D$_f$, C.5D$_f$, D. 7D$_f$. SSG-RS. S=1.07.

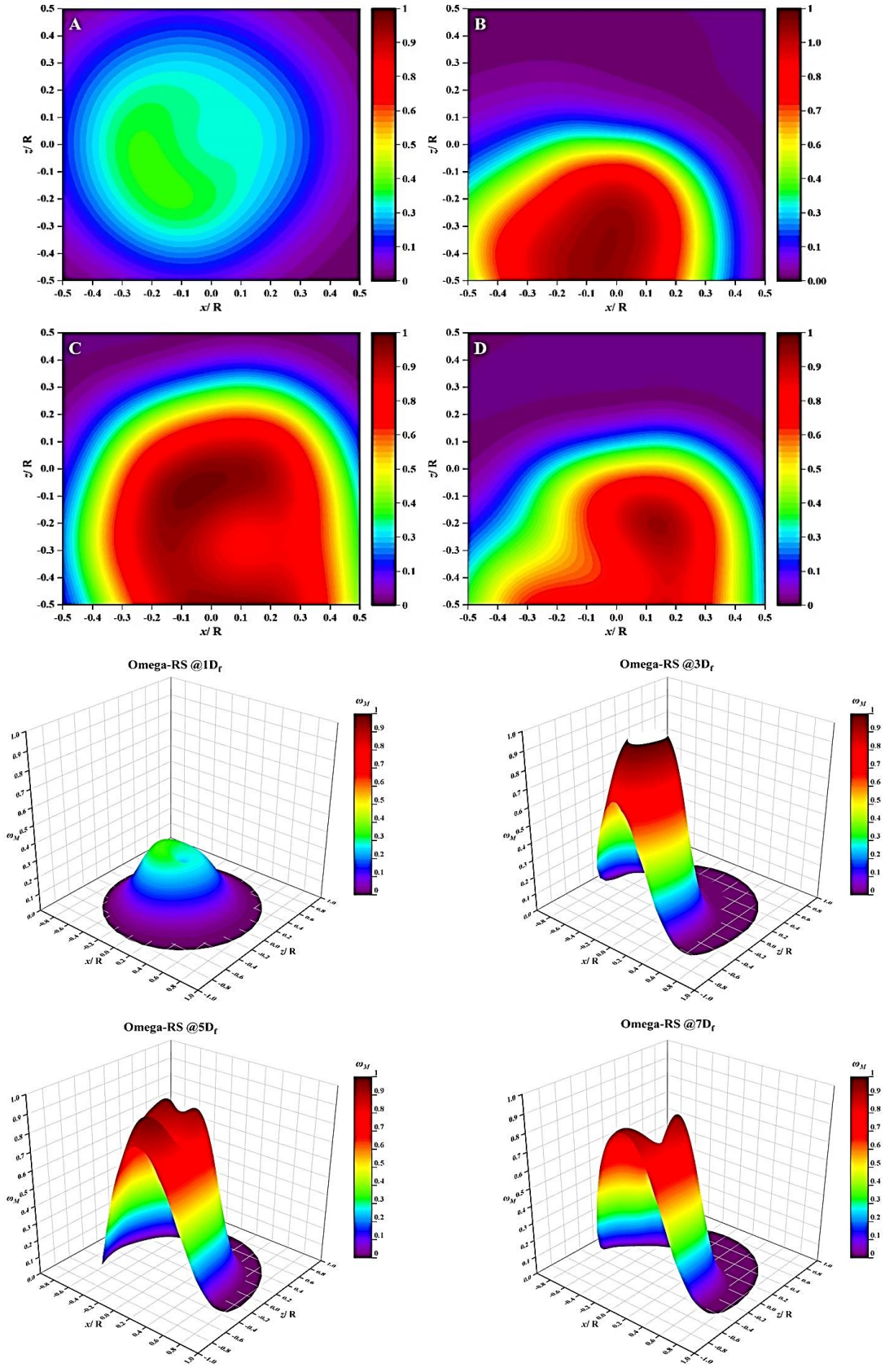

Figure 6-84: 2D (Top View) And 3D ω_M Contours Of Methane. A. 1D_f, B. 3D_f, C.5D_f, D. 7D_f. Omega-RS. S=1.07.

6.7 Reynolds stress turbulence models review

The effect of using Reynolds stress turbulence models on the results is clearly indicated for each swirl number. In addition, RSMs are mainly use for complicated fluids flow such as swirl flow (I. Ansys, 2011; CFX, 2018; Wasserman, 2016). Therefore, the main reason for this section is to sum up the influence of you using RSM on the swirling simulation to indicate the limitation for each RSM model as showing below:

A. First swirl number *S*=0.3

Generally, all the models have nearly same RMSE percentage at $1D_f$ and $3D_f$ where the effect of turbulent is high and dominate the flow zone. However, the error percentage gap among each model is slightly different at $5D_f$ and $7D_f$ where the effect of turbulent is decreases, while the effect of each model is increases. Moreover, Table 6-7 show the differences among each model where the average RMSE percentage for all location is nearly the same. However, the highlighted Omega-RS model have the lowest RMSE value which led to be used at this swirl strength i.e., this model is preferred to be implemented for such flow conditions. All together, RSMs show good agreement with the experiments data at this strength of swirl flow, specially at the last two location.

Table 6-7: RMSE Percent For RSMS At *S*=0.3

Model	RMSE				Average error percent
	Y/ D_f				
	1	3	5	7	
LRR-IP-RS	28.04%	26.64%	7.48%	4.31%	16.62%
SSG-RS	28.04%	26.96%	8.02%	3.65%	16.67%
Omega-RS	26.95%	26.50%	7.71%	3.88%	16.26%

B. Second swirl number *S*=0.58

The outcome of Reynolds stress turbulence models indicates the effect of each model on the simulation. For instance, LRR-IP-RS and SSG-RS models share nearly same error percentage at $1D_f$ i.e.., equivalent to 18%, while it is slightly less for Omega-RS which equal to 16%. Interestingly, all the models show better results comparing with the experiment's data than the first swirl number. The main reason behind that is because of the decreases of turbulent effect at different locations such as $1D_f$ and $7D_f$ as shown in Table 6-8. Moreover, Omega-RS have the lowest RMSE value among the models because of the ability of this model to conduct near wall affection. Generally, all the models can predict the swirl effects on the flow with

slightly different of error percent among each one of them. However, according to the results, the highlighted Omega-RS turbulence model is preferred at this swirl degree as shown in Table 6-8 below.

Table 6-8: RMSE Percent For RSMS At *S*=0.58

Model	RMSE Y/ D_f				Average error percent
	1	3	5	7	
LRR-IP-RS	18.34%	10.02%	9.28%	8.81%	11.61%
SSG-RS	18.00%	9.59%	9.02%	11.85%	12.11%
Omega-RS	16.94%	8.79%	8.89%	8.71%	10.83%

C. Third swirl number *S*=1.07

This part of swirling simulation is very significant as it's clearly showing the effect of each Reynolds stress turbulence models on the results due to high swirl degree. For instance, SSG-RS turbulence model have failed to predict the swirling phenomena at nearly all locations with an average error value equal to 40.49% as shown in Table 6-9. On the other hand, Omega-RS turbulence model show slightly better results than the previous model. However, the average error percentage remain high i.e., almost equal to 30% and equal to nearly 60% and 53% at certain locations such as $1D_f$ and $5D_f$, respectively. Conversely, the highlighted LRR-IP-RS show good agreement with experiment's data where the overall error percentage is equal to 14.72% only. Although this model shows high error percentage at $1D_f$ i.e., equivalent to 40%, the model shows better results at all the locations than the rest of RSMs outcomes. Therefore, this model is much preferred to be used for all swirl's degrees specially for high swirl flow as demonstrated in Table 6-9 below.

Table 6-9: RMSE Percent For RSMS At *S*=1.07

Model	RMSE Y/ D_f				Average error percent
	1	3	5	7	
LRR-IP-RS	40.87%	10.73%	4.28%	3.02%	14.72%
SSG-RS	11.26%	59.40%	52.81%	38.50%	40.49%
Omega-RS	32.15%	8.18%	56.82%	20.39%	29.39%

6.8 Effect of screws

This section focusing on the effect of screws on the flow symmetric structures. First, the previous Figure 5-6 show the location of screws inside the burner tube (cylinder) with a 120^{o} angle degree between each other. Moreover, these screws modelled as a solid wall with no slip wall conditions in the compactional domain. Therefore, they stand-in like solid body which can affect the flow path.

Furthermore, to cover the effect of screws on the symmetric in this study, another computational domain has been created without the screws. The new domain has the same dimension, boundary conditions and setup process as the previous one. In addition, the LRR-IP-RS turbulence model is applied to indicate this effect as it showed very good agreement with experiments data.

Therefore, a 2D and 3D Methane mixture contours has been utilized to present all the symmetric domain as shown in Figures 6-85 to 6-87. These figures have indicated the symmetric effect at S=0.3, S=0.58 and S=1.07 by showing the contour images for the solution domain with and without the screws. Interestingly, the results suggest that the existence of screws have a significate effect on symmetric. In another words, the screws increase the swirling strength in the simulation domain which led to create mor non-symmetric forms as showed in the previous results.

Furthermore, the author suggest that the simulation should have the screws inside the domain due to the existence of these screws in the original experiment. Also, the above figures indicate a minor different of Methane mass fraction values between the two cases. In addition, the experiment and author study selected locations $1D_f$, $3D_f$,$5D_f$ and $7D_f$ are applied in the front view of the experiment i.e., x, y coordinates where the results are slightly far from the screws effect. As a result, the current study is depending on the original experiments dimensions and lab conditions to assess the RANS turbulence models.

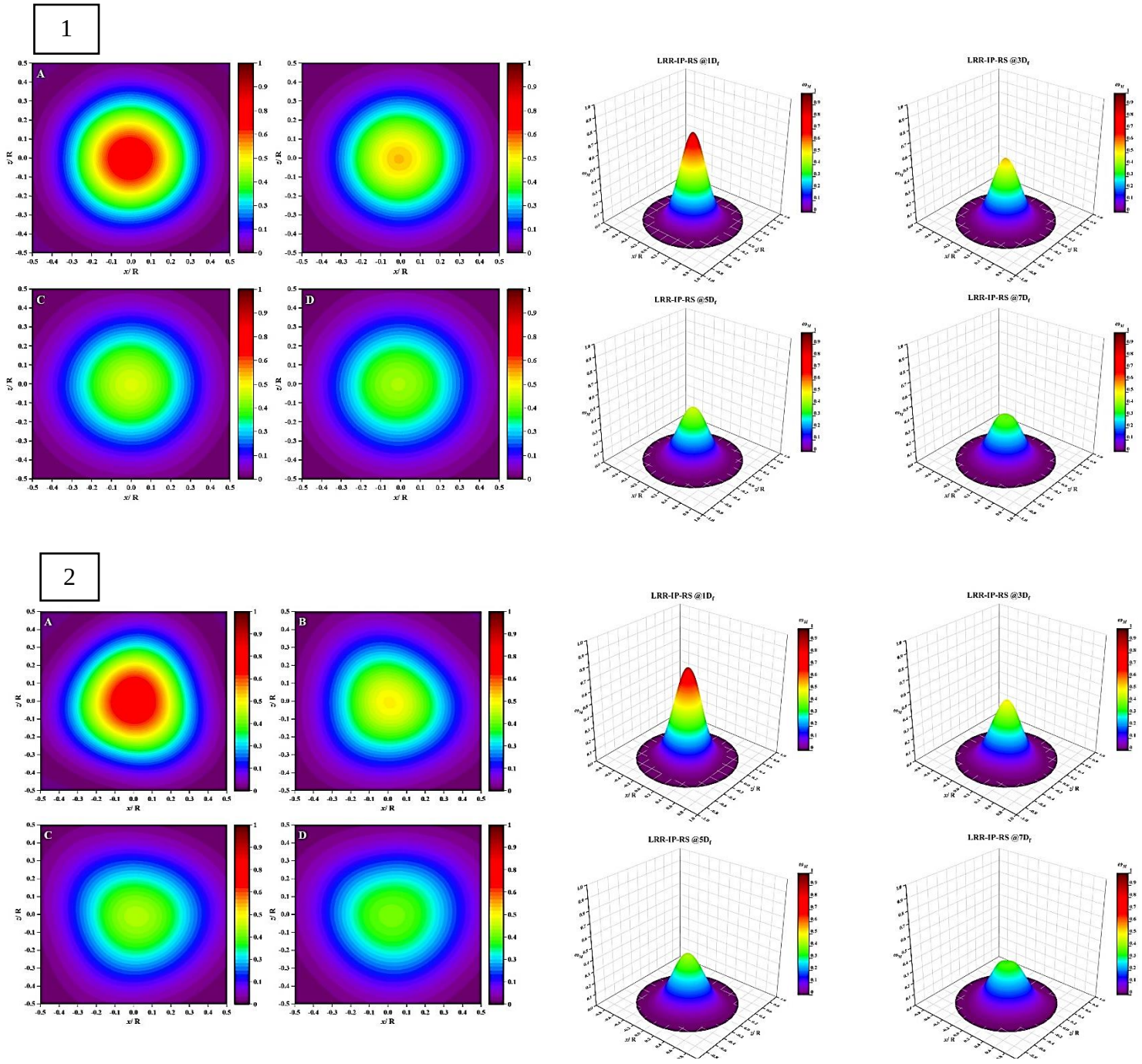

Figure 6-85: 2D (Top View) And 3D ω_M Contours Of Methane.

1. No Screws Simulation

2. With Screw Simulation

A. 1D$_f$, B. 3D$_f$, C.5D$_f$, D. 7D$_f$.

S=0.3, LRR-IP-RS

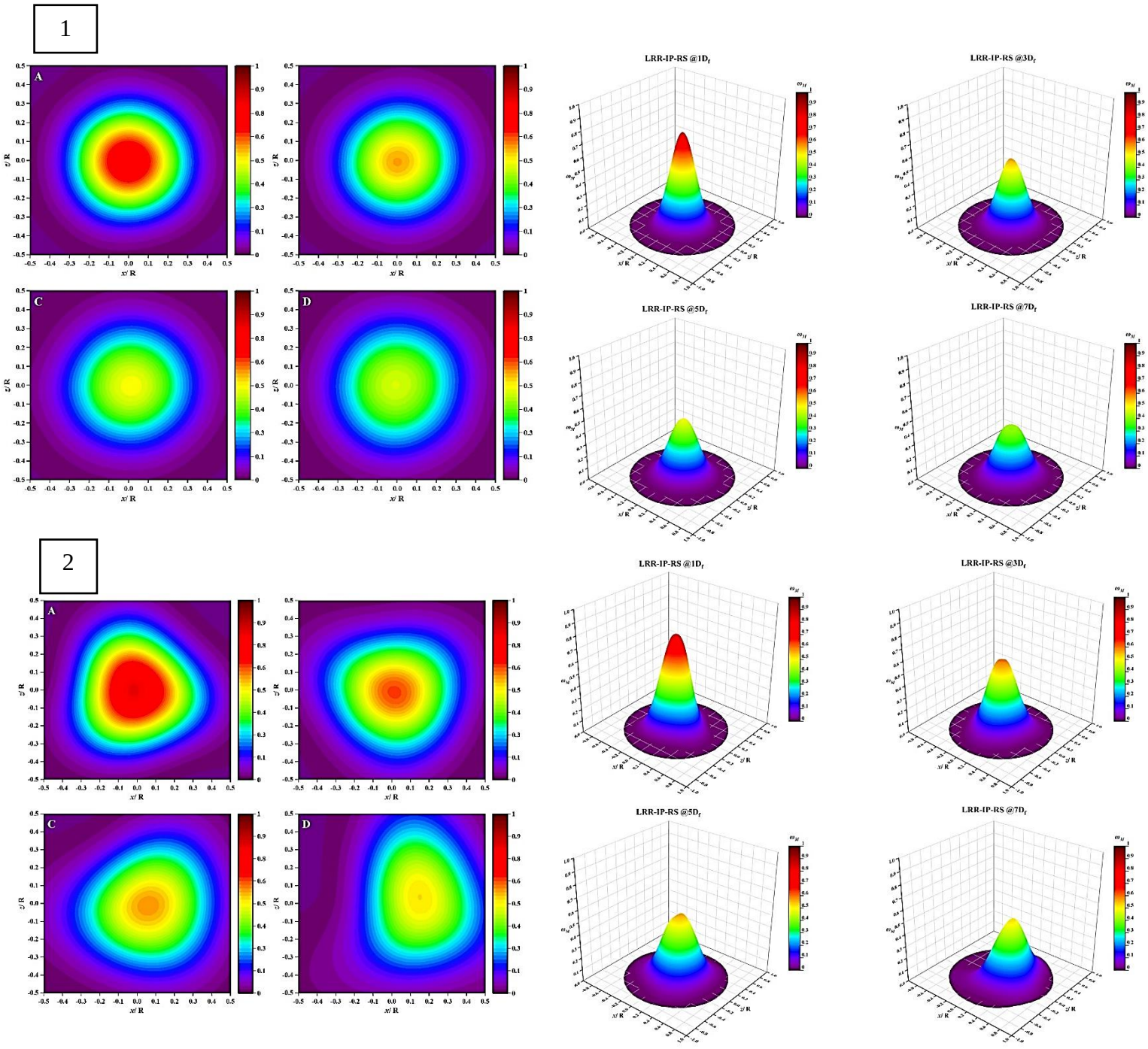

Figure 6-86: 2D (Top View) And 3D ω_M Contours Of Methane.

1. No Screws Simulation

2. With Screw Simulation

A. 1D$_f$, B. 3D$_f$, C.5D$_f$, D. 7D$_f$.

S=0.58, LRR-IP-RS

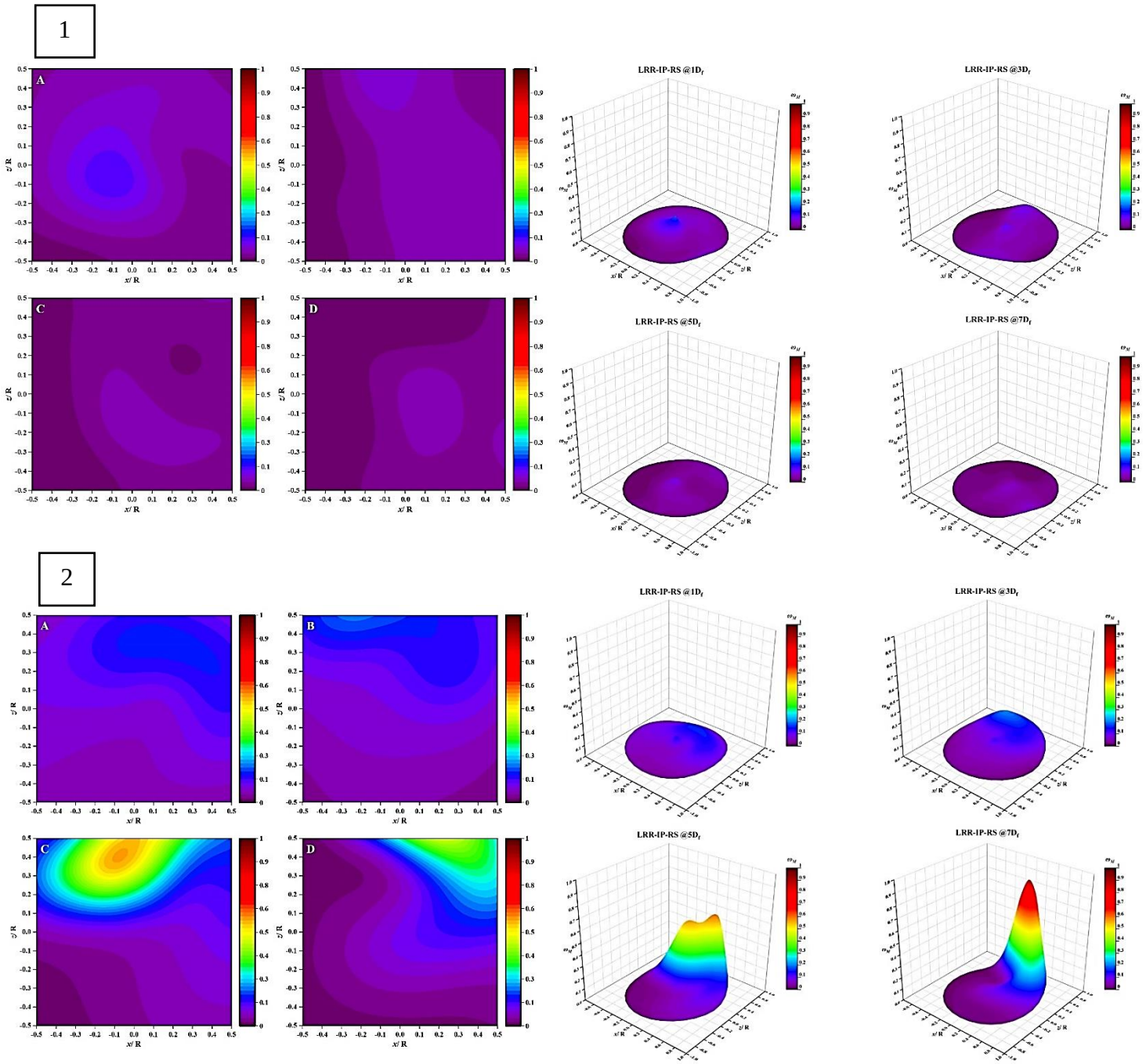

Figure 6-87: 2D (Top View) And 3D ω_M Contours Of Methane.

1. **No Screws Simulation**
2. **With Screw Simulation**

A. 1D$_f$, B. 3D$_f$, C.5D$_f$, D. 7D$_f$.

S=1.07, LRR-IP-RS

6.9 Effect of swirl

This section shows the effect of the swirl on the Methane volume fraction, velocity streamline and velocity vectors of the computational domain at all swirling numbers for LRR-IP-RS turbulence model only. Thus, Figures 6-84, 6-85 and 6-86 indicate Methane volume fraction along the domain in 2D X, Y plane at swirl number of 0.3, 0.58 and 1.07, respectively. The figures findings suggest that the swirl effect at S=0.3 has nearly no effect on the volume fraction streamline flow. However, the increases of swirl strength where S=0.58 specify a beginning of curvatures in the streamline which led to increase/decrease the volume fraction values at certain places. Moreover, at the highest swirling strength where S=1.07 the volume fraction almost disappears from the domain because of swirl impact that led to shift the fluid features out of the domain.

On the other hand, the velocity results of the Methane and Air are examined in this study to indicate the swirl effect. Figures 6-87, 6-88 and 6-89 display the velocity streamline and vectors for Methane at S=0.3, 0.58 and 1.07, respectively. And Figures 6-90, 6-91 and 6-92 show the velocity vectors of Air at S=0.3, 0.58 and 1.07 inside the domain. All the motioned figures show that the effect of swirl is nearly intangible at S=0.3, while it starts occurring when the swirling strength increases. For instance, at S=0.58 the velocity profiles have a spiral shape throughout computational domain where the recirculation zone starts appearing in the simulation due to the swirl effect. Furthermore, when the swirl reaches the maximum degree at S=1.07, both Air and Methane velocity vectors distribute all over the domain and the recirculation zone established. Interestingly, the velocity distribution is nearly divided in three directions as shown in Figures 6-89 and 6-92 due to the consequence of the screws. Lastly, Figure 6-93 show the effect of screws on the velocity vectors at S=0.58 by showing the flow once with screws, then without them. The previous figure explain that the existence of screws will increase the spinner of the air flow which can increase the swirl strength.

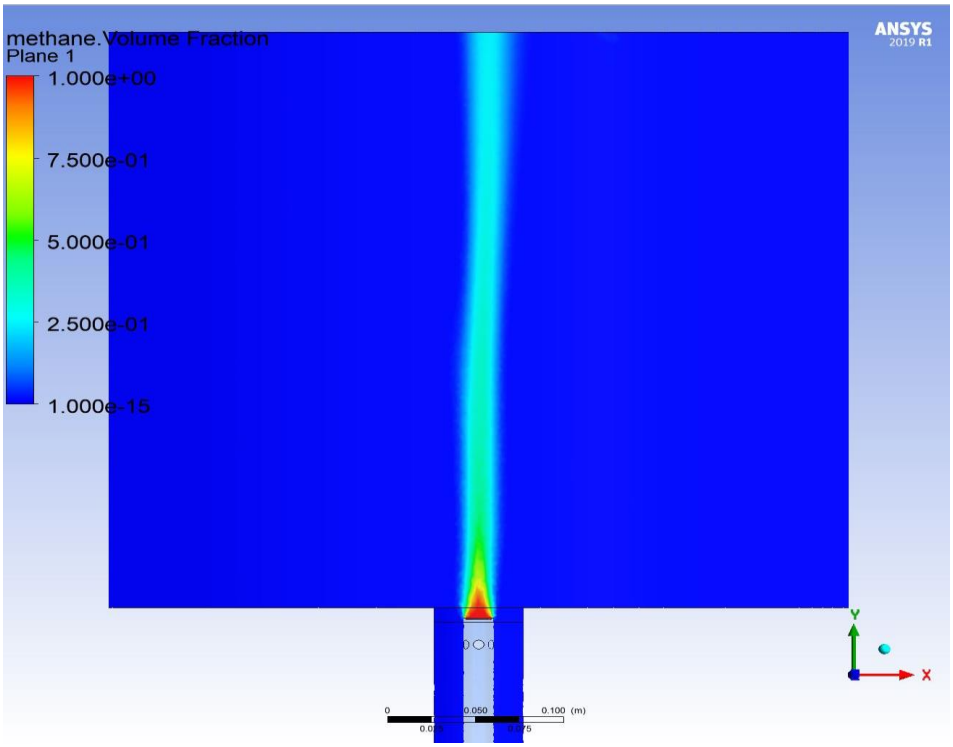

FIGURE 6-88: 2D (FRONT VIEW) METHANE VF. S=0.3, LRR-IP-RS.

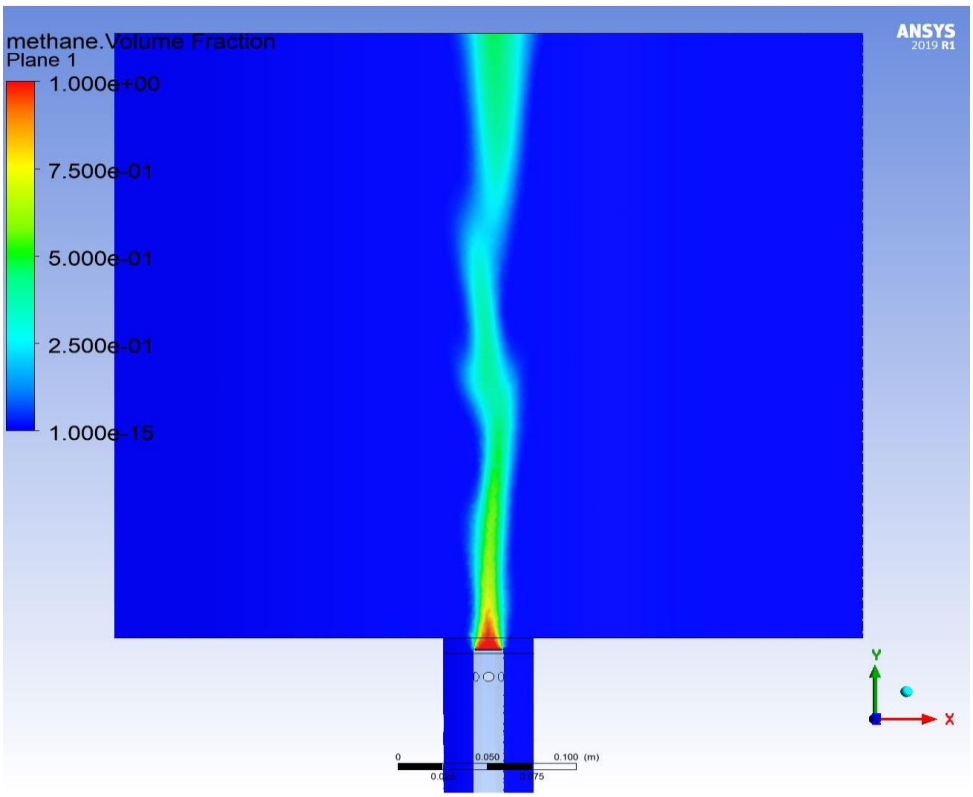

Figure 6-89: 2D (Front View) Methane VF. S=0.58, LRR-IP-RS.

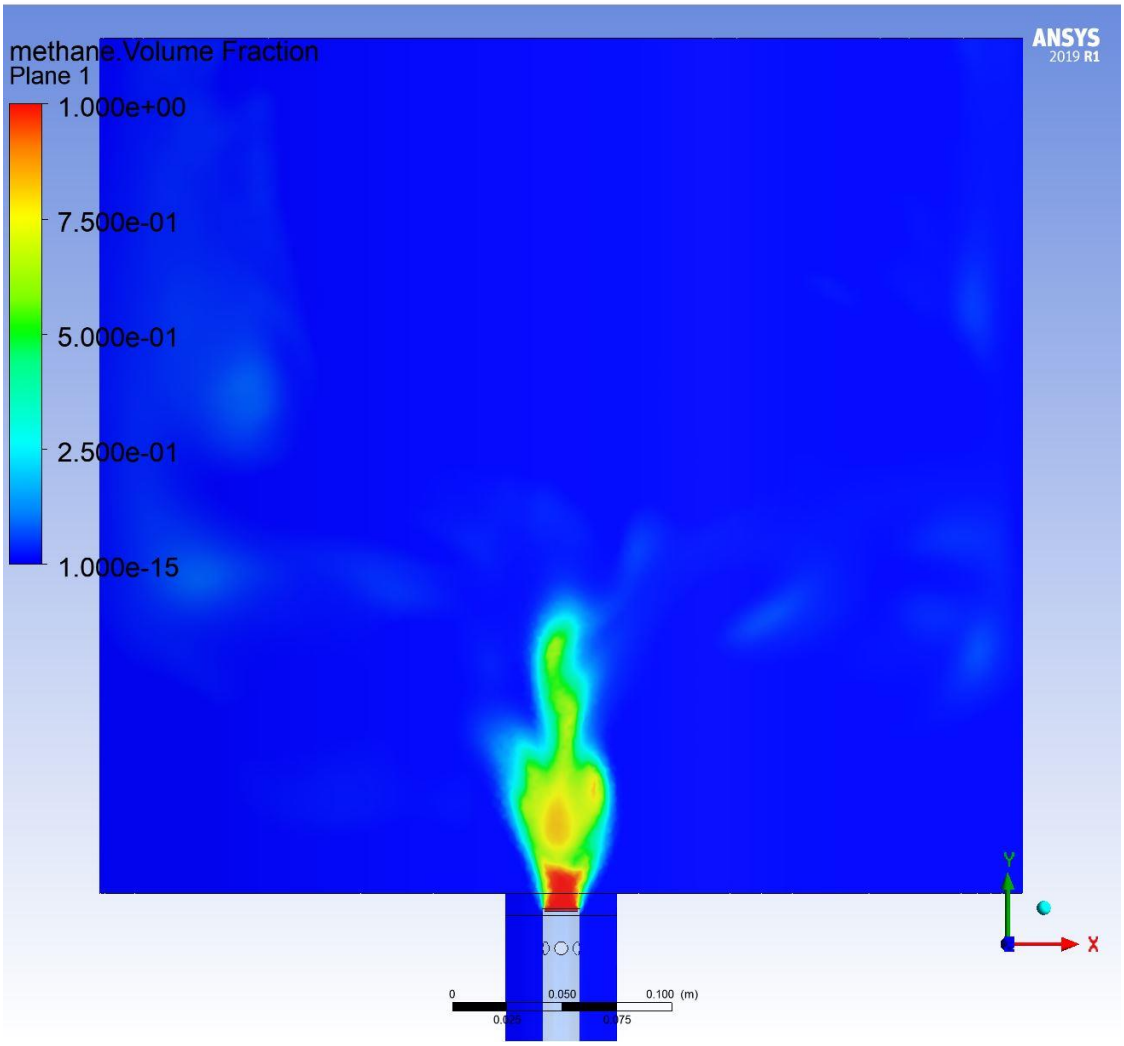

Figure 6-90: 2D (Front View) Methane VF. S=1.07, LRR-IP-RS.

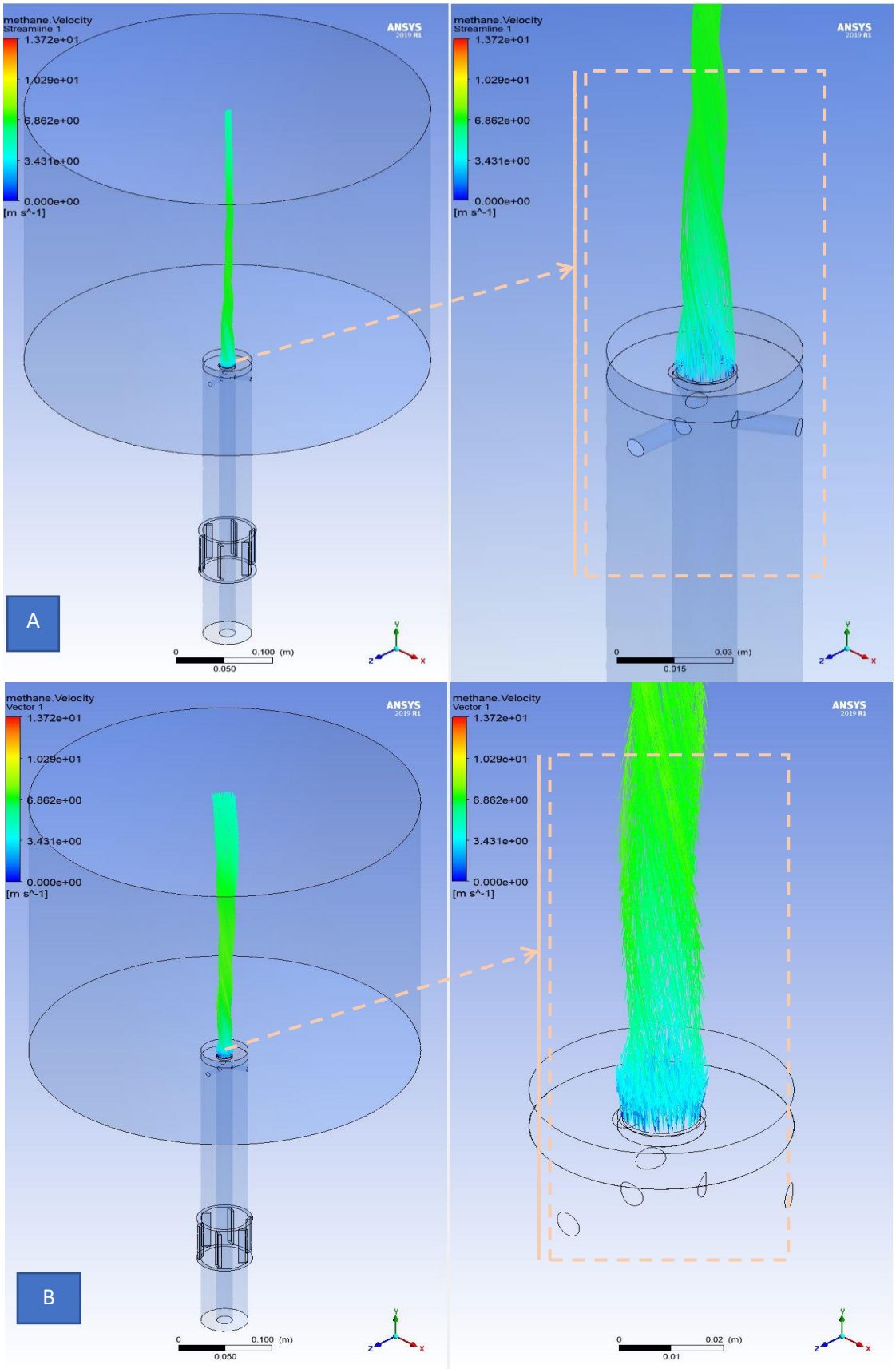

Figure 6-91: 3D Methane Velocity, A. Streamline, B. Vectors. S=0.3, LRR-IP-RS.

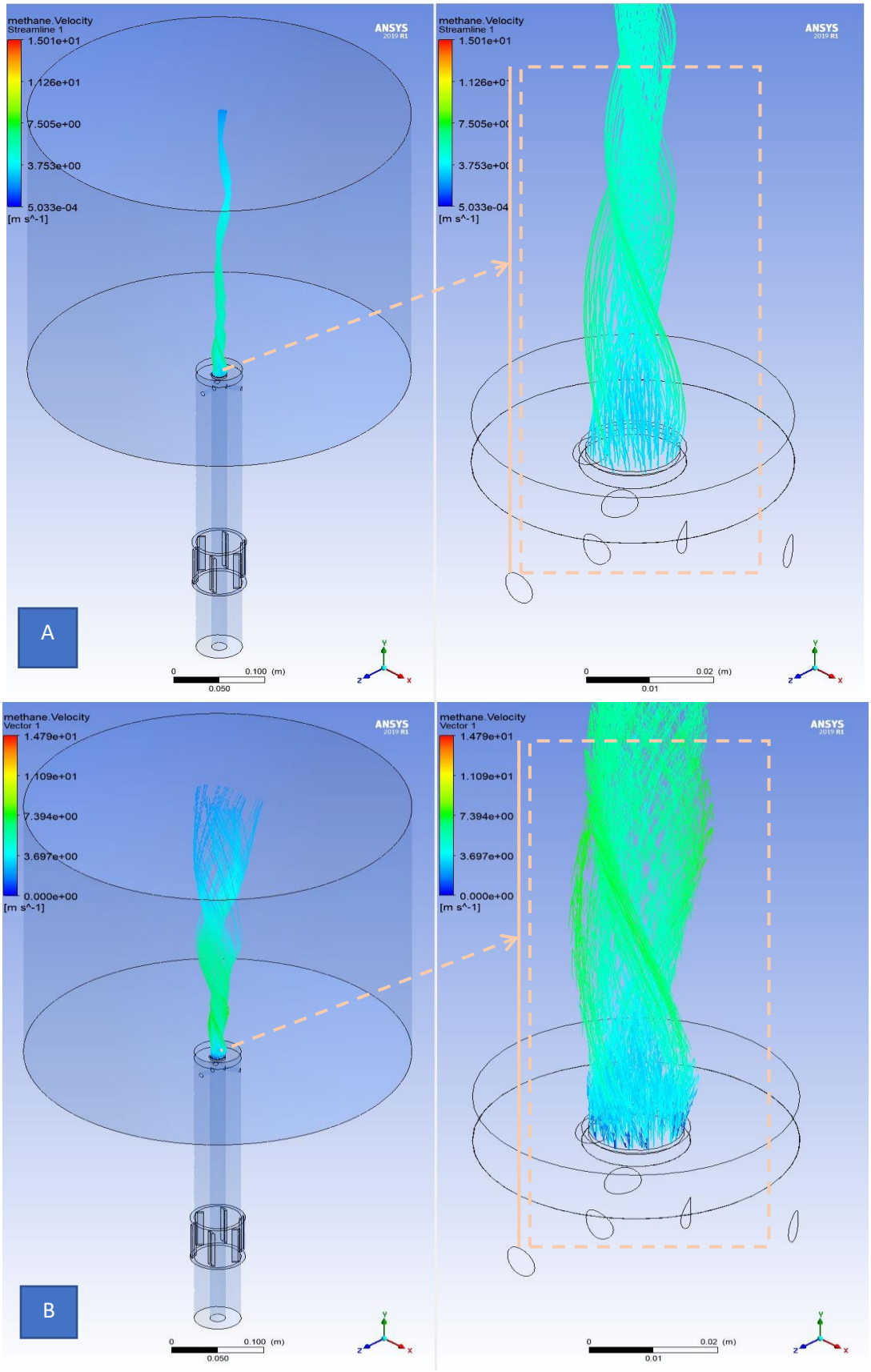

Figure 6-92: 3D Methane Velocity, A. Streamline, B. Vectors. S=0.58, LRR-IP-RS.

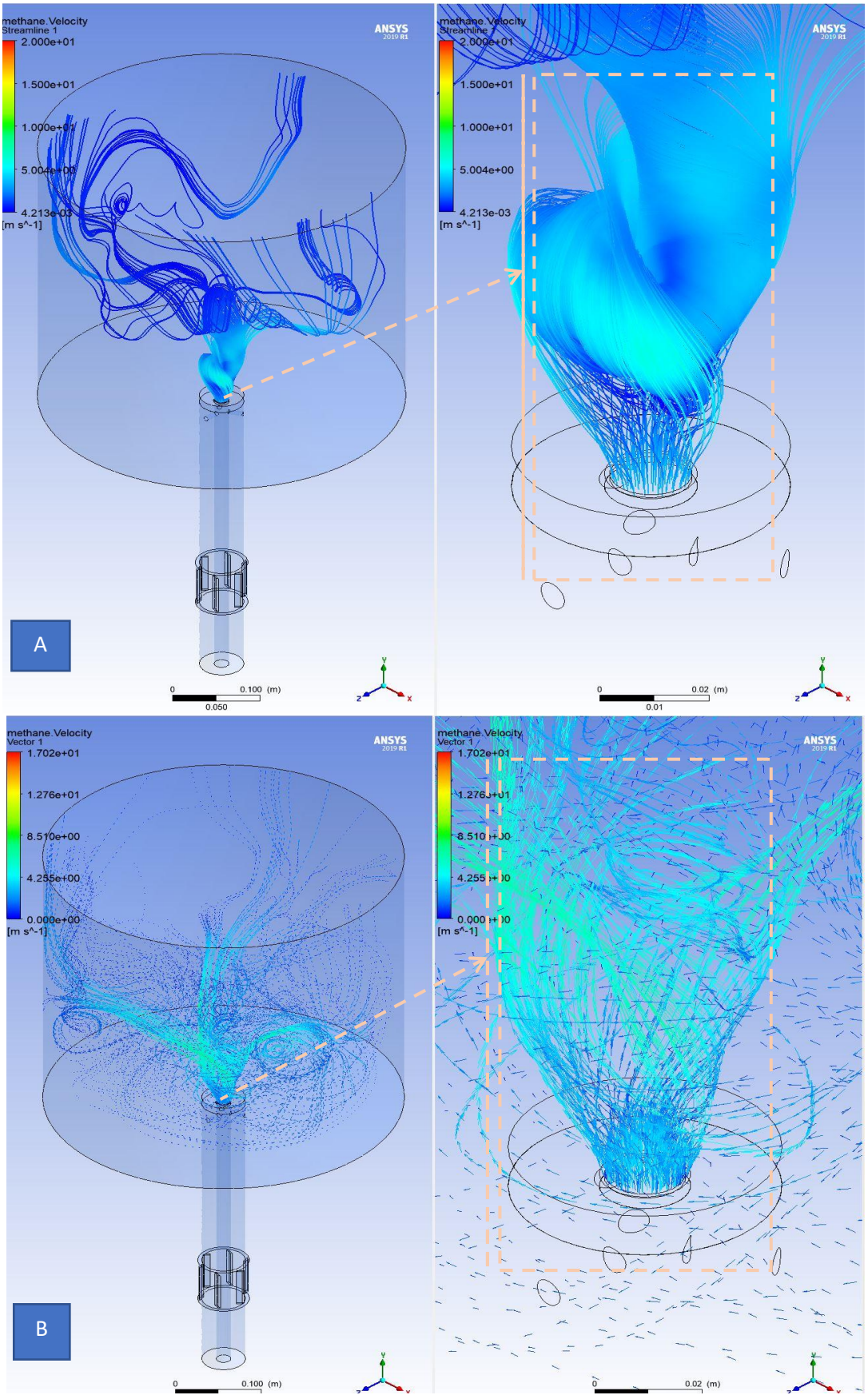

Figure 6-93: 3D Methane Velocity, A. Streamline, B. Vectors. S=1.07, LRR-IP-RS.

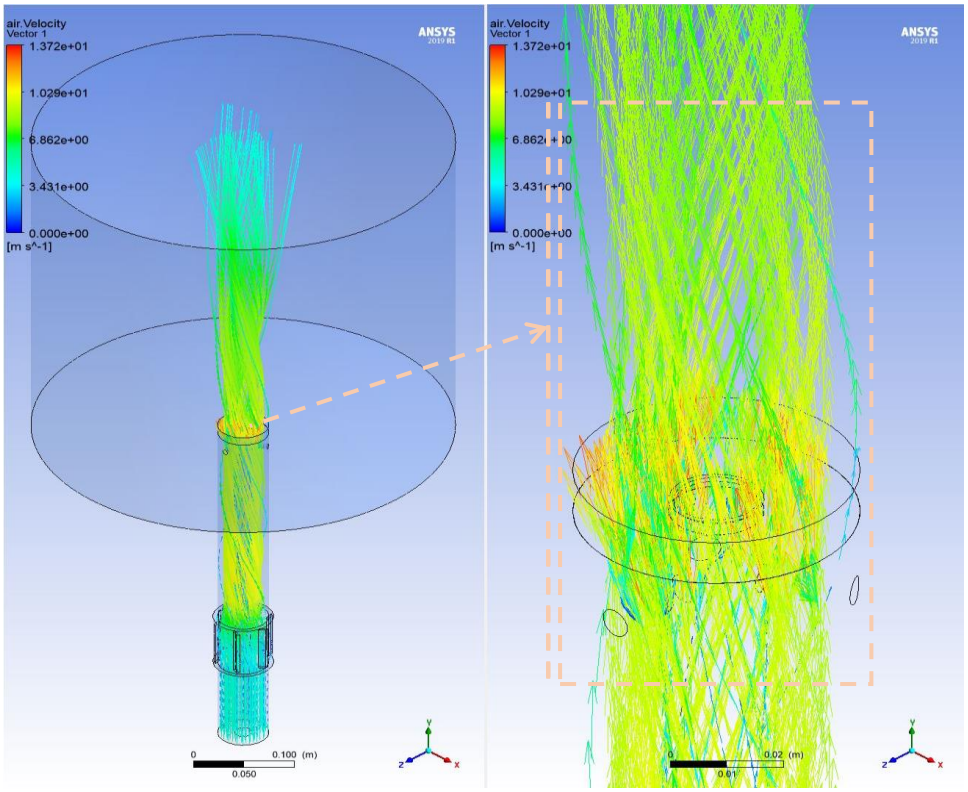

Figure 6-95: 3D Air Velocity Vectors. S=0.3, LRR-IP-RS.

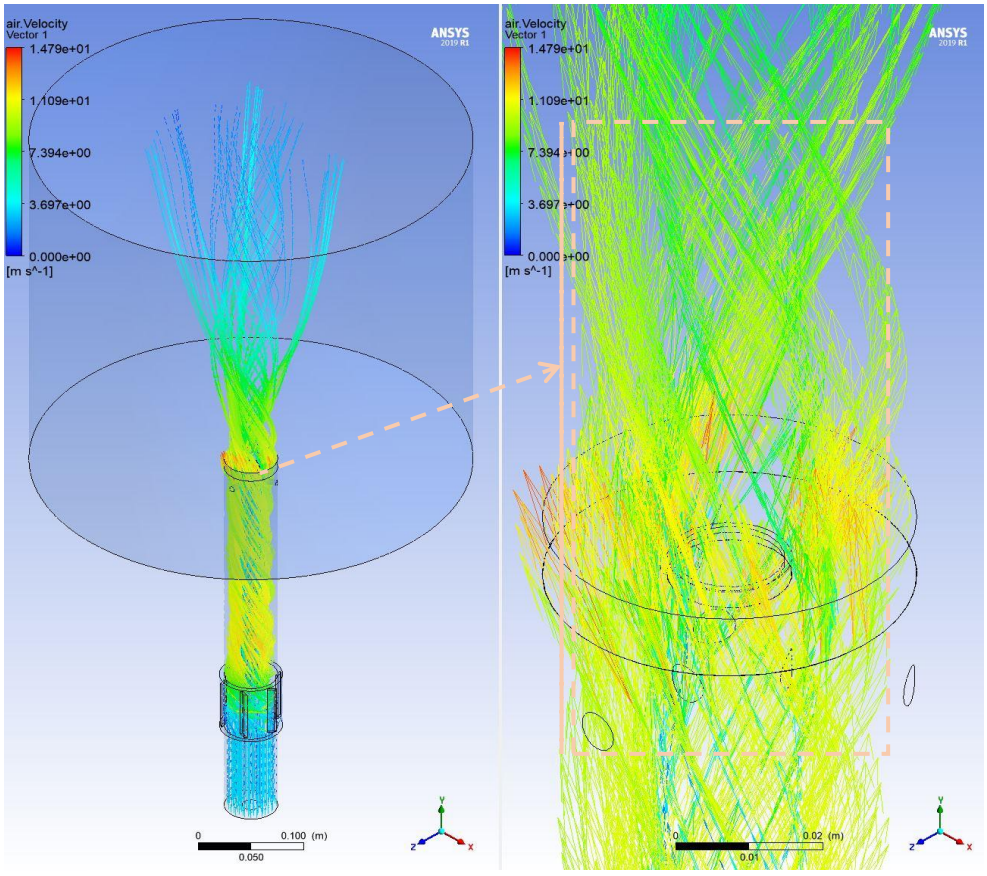

Figure 6-94: 3D Air Velocity Vectors. S=0.58, LRR-IP-RS.

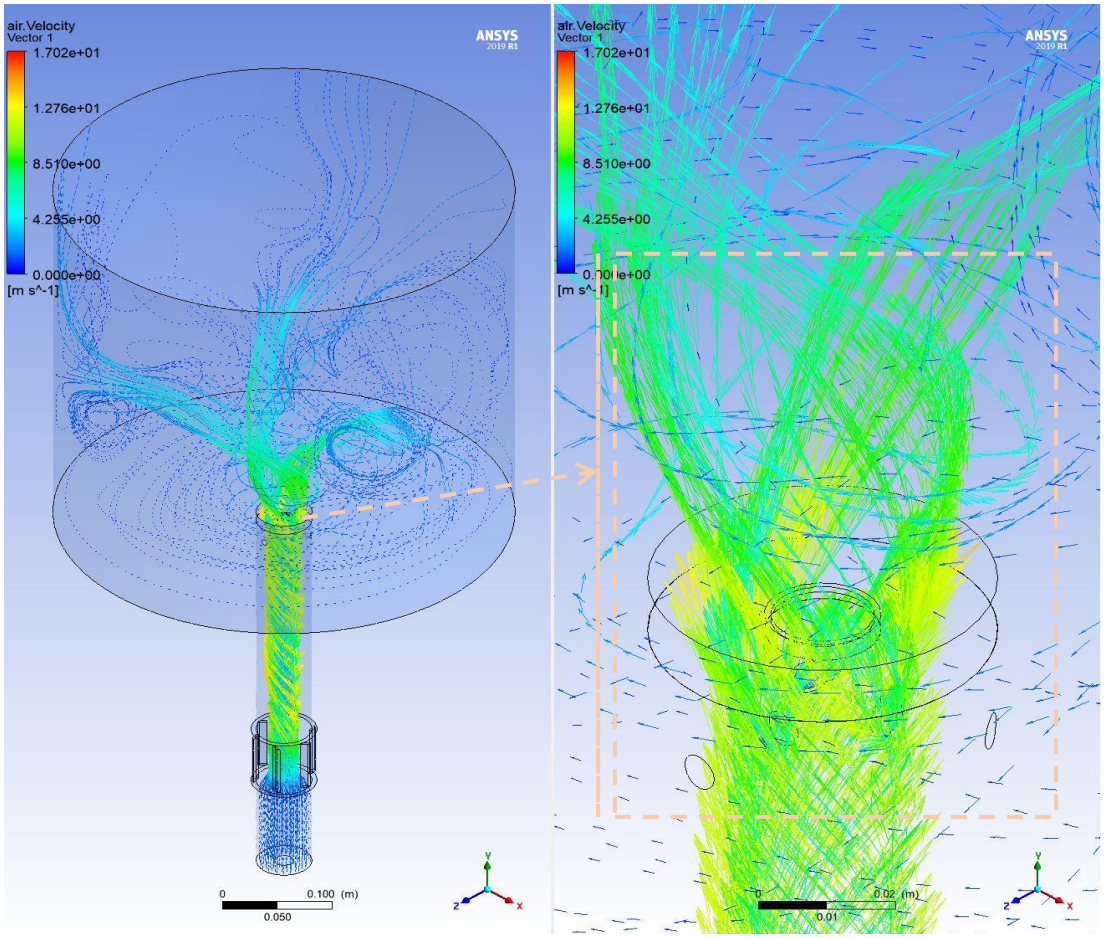

Figure 6-96: 3D Air Velocity Vectors. S=1.07, LRR-IP-RS.

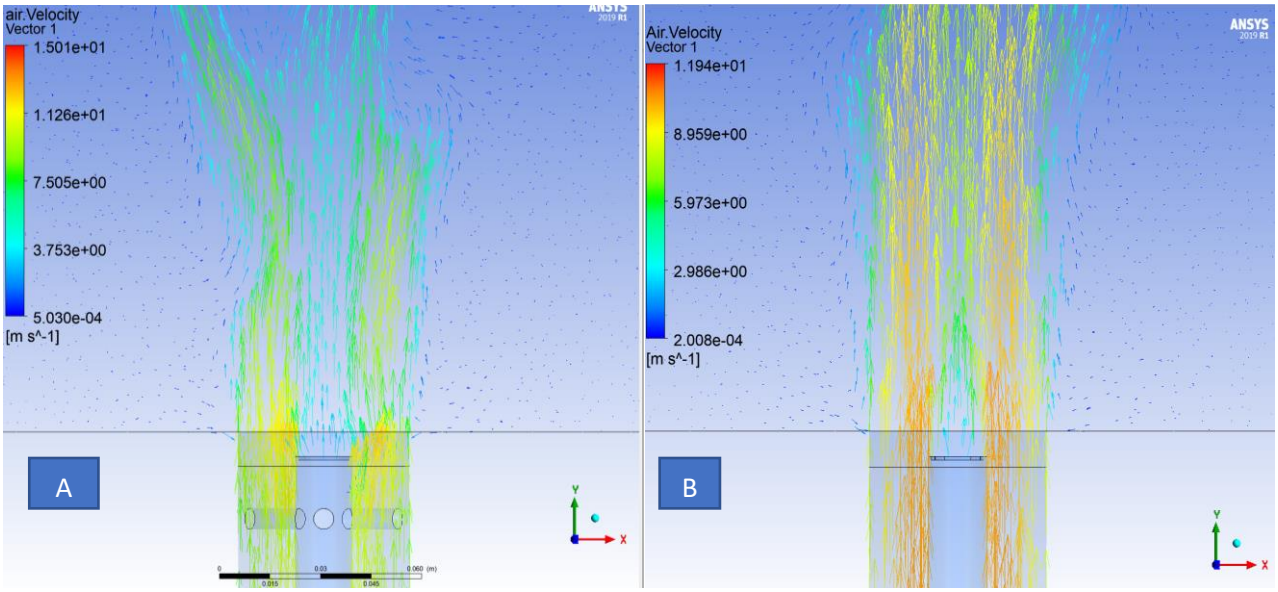

Figure 6-97: 2D Air Velocity Vectors. A. With Screws, B. Without Screws, S=0.58, LRR-IP-RS.

6.10 Effect of ANSYS-CFX

This section explains the effect of ANSYS-CFX on the grid type and quality. In another meaning, to explain the incompatibility between the element type of mesh and the simulation program. First, CFX is appropriate with three-dimensional mesh than the two-dimensional ones. In addition, it uses vertex-centred approach known as Finite Volume Method based on Elements while some programmes apply a cell-centred approach such as FLUENT. Therefore, CFX programme are not able to deal with cut-cell meshes and polyhedral mesh, otherwise, it applies the traditional tetra and hexa-mesh topologies as been showed in the sections 6.1.1, 6.2.1 and 6.4.1. On the other hand, the programme uses a CFX expression language known as CEL which make it very soft to define algebraic equations and monitor them during the run. Moreover, CFX is better than other simulation programme at certain type of flow physics research. For instance, turbomachinery problems are one of the main uses of CFX programme (Robin, 2018).

Chapter 7 CONCLUSION AND FUTURE WORK

7.1 Scope of work

The scope of this study was to investigate the applicability of turbulence modelling typically employed in RANS equations to model swirling flows by using the ANSYS-CFX simulation program. In addition, to indicate the appropriate turbulence module to use in swirling jet flow via comparing them with the previously published experimental data. Therefore, a general review of main components and background of turbulent jet has been established in chapter two. For instance, section 2.1 studied the flow characteristics of both planar and swirl jet turbulent flow while a planar jet flow review has been created to achieve the study's aim in section 2.2. In addition, sections 2.3 describe most of the numerical and experiment swirling studies related to this work.

Then, the theory behind the prediction and analysis of different numerical methods has been established in chapter three. For example, the background theory of Navier-Stoke equations detailed in section 3.1. Moreover, through sections 3.3 to 3.10, all the turbulence modelling along with RANS approach is comprehensively studied with a suitable equation's analysis for each numerical method. Chapter three conduct the limitations of each turbulence models used in this study along with CFD solving steps and a general explanation of the error and uncertainty.

On the other hand, two case studies of planar jet flow has been numerically investigated via applying 3D simulation procedure where a standard k-ε turbulence model is used, as shown in chapter four i.e., sections 4.1 and 4.2. The mentioned chapter proofed the ability of using CFX ANSYS simulation programme to predict planar jet flow which support the aim of this research.

Moving forward, chapter five establish a 3D numerical modelling of the main related-to-work experiment for swirling flow which can be seen in sections 5.1, 5.2 and 5.3. In chapter five, the process of transfer the experiment system into a numerical structure has been achieved where analysing of swirl flow occurred at different strengths levels. Then, Chapter six show the results and discussion of two planar cases explained in sections 6.1 and 6.2 while the outcome of swirling flow elucidated in sections 6.3 to 6.10.

Besides, various RANS turbulence models are applied in this study. For instance, three turbulence models based on two-equation phenomena known as eddy viscosity turbulence models are used, i.e.

1. Standard k-ε turbulence model
2. RNG k-ε turbulence model
3. Shear Stresses SST

Additionally, another three turbulence models based on Reynolds Stress Model RSM are used, i.e

1. The Standard Reynolds Stress Model RSM, as follow:

c) Launder, Reece and Rodi turbulence model (Isotropizatio of Production) (LRR-IP-RS)

d) Speziale, Sarkar and Gatski turbulence model (SSG-RS)

2. Omega-Based Reynolds Stress Model (Omega-RS)

The first three models have been selected due to their common use and the different approach for each on of them. For instance, RNG k-ε is mostly applied to indicate the effects of smaller scales of motion while the Shear Stresses SST is good foe the near-wall treatment. On another hand, the RSM models are usually used to model the complicated flow such as a swirl flow. Therefore, this study examined all the above models. The results suggest that the LRR-IP-RS turbulence model has the most accurate prediction among them.

7.2 Project's outcome

The main objective of this study was to investigate the ability of RANS turbulence models to model the swirl flow at different swirling number, using CFX. The following sub-sections discuss important aspects of the methods used and key insights from the results.

7.2.1 Verification and validation

The numerical error and uncertainty have been explained in section 3.9 which controlled using robust verification and validation methods. Therefore, errors and uncertainty have a certain aspect of CFD modelling, it is essential to develop accurate methods to improve the amount of confidence in its outcomes. The present study uses many methods to control the numerical error. For instance, 'CFX floating point error Floating point exception: Overflow' was minimised by using a double-precision flow solver within the commercial package.

Discretisation errors are an inevitable consequence of meshing and the only way to minimise them is to complete a mesh sensitivity study. The mesh independence study as explained in sections 4.1.3, 4.2.3 and 5.4 for two planar case study and the main swirling flow experiment. For the first case study, the selected mesh has an element size of 16 million with an average RMSE value of 0.73%. Then, the second case study selected with an element size of 8 million with an average RMSE value of 0.73% as well. In addition, the swirl numerical modelling has a mesh of 32 million and the average RMSE value was 1.56%. The previous meshes were selected after running through a filtration process which been explained in the mentioned sections before. Moreover, convergence error was reduced by running simulations until they had accurately converged, up until the residuals were completely constant and there were no errors due to unfinished convergence.

In terms of validation, one published planar case study was examined as shown in section 4.1 where the results showed very good agreement with the experimental and numerical data as explained in section 6.1. Then, second planar case study is applied using the same main swirl experiment but with planar jet flow conditions as explained in section 4.2, where the findings showed good agreement with the experiments data as explained in section 6.2.

7.2.2 Modelling approach

The computational domain for all cases created according to a logic mathematic process which explained in chapter four and five. However, a slightly larger domain is applied for tolerance purposes, and results showed sensible power predictions for all cases. In addition, a very fine mesh was required to successfully capture the flow behaviour for the planar and swirler flow. However, this was an extremely challenging process given that it required a numerical balance between sizes of the cells around and downstream of the jet to avoid any computational errors. For instance, the swirl modelling required a huge cell count up to 32 million which required substantial High-Performance Computer (HPC) resources to perform the runs. Dealing with such a fine mesh needed a huge computing effort for each run up to 10 days period via using the lab computers.

As mentioned in the previous sections, a CFX simulation using a RANS-based approach was employed in this study. Although this approach has limitations for complex flow phenomena, the $k-\varepsilon$ turbulence model show good agreement with the experimental data for both planar cases and the low and medium swirl flow strength S=0.3 and S=0.58. Moreover, RNG $k-\varepsilon$ and SST turbulence models show acceptable agreement with the experiments data

at the same swirl range. However, all the previous models have failed computing the swirl flow at high swirling strength S=1.07.

On another hand, the RSM turbulence models show very good prediction by indicating the existence of swirl effect. Unfortunately, the Omega-RS and SSG-RS models show over-predicted swirl effect compared to experimental results at the highest swirling strength S=1.07. However, LRR-IP-RS turbulence model show good agreement with experiments data even at high swirl strength flow.

7.3 Limitation

The major limitation of using CFD approach in this study is that only steady state simulations were performed. Although a good agreement with experimental results were achieved in planar jet flow along with the low and medium swirling flow, the impact of unsteady flow phenomena can only be examined with transient simulations. However, the main swirling experimental data were achieved with a mean value hypothesis with an average error percent of 10%.

In addition, the only mesh form has succussed in this study was with tetrahedral element form due to compatibility between the CFX solution approach and the mesh type, while many different types of element form had failed such as hexahedron as described in section 6.9. Moreover, a huge computing effort were needed to meet the mesh requirements specially at the near inlet area as the mesh element type have a tetrahedral form. This appeared because of the range of sizes in the geometry. With current computational resources, it was found difficult to increase the mesh size more than 32 million. As a result, a fine 3D tetrahedral mesh was implemented to provide meaningful data for the simulation domain.

Another limitation of this work is that effect of screws on the symmetric results. This effect has a large impact on the results at the RSM turbulence models only, as they were able to predict the swirl effect more than the eddy viscosity turbulence models, see section 6.7.

On another hand, the modulation of the swirling flow ‘especially at the highest swirl strength’ had many difficulties during the simulation run as it needs high computing resources with a long period to converged which is usually 12 days. Moreover, this study examined six turbulence models in total where each model is based on a certain equation and depending on variables, which means that the source of running difficulties may differ from one to another.

7.4 Contributions to knowledge

The main contributions to knowledge from this study help to extend the current understanding of turbulence modelling employed with the RANS equations to model the swirling flow. The current and previously published data in the open literature are still lacking and discrepancies between different studies exist. The contributions of the present work are summarised as follows:

1. Most of RANS turbulence models are not the best choice for high swirling flow modelling, the study shows a huge weakness of this model to predict the swirl flow effect. However, these models are good for low and medium degree of swirl flow, specially the RSM turbulence models.

2. The self-symmetric form affected particularly by the existence of screws inside the geometry of the burner. The screws have a significate impact on this type of results, and it is directly proportional to swirl flow degree. Moreover, the swirling flow number have a great effect on the turbulence level.

3. One of the most important findings of this study is that the diffusion effect on the scalar mixing process occur only with planar jet flow at low Reynolds number. While the turbulent mixing is the dominant process when the swirling flow take place at high Reynolds number.

7.5 Conclusion

The main goal of the present study was designed to determine the effect of using various RANS turbulence models to predict the swirling flow modulation. In another words, to study the swirling flow numerically and indicate the best applied model. Therefore, a three turbulence models based on eddy viscosity along with another three turbulence models based on Reynolds's stress equation were established in this study. A RANS-based CFD verification and validation study for planar and swirl jet flow formed to sustain this study. The following conclusions can be extracted from the present study.

First, the k-ε turbulence model showed very good agreement with the experiments data for two cases of the planar jet flow, where the error percent is 5.33% and 11% for the first and second case, respectively. Then, the swirl flow findings indicated that the selected turbulence models k-ε, RNG k-ε, Shear ST, LRR-IP-RS, SSG-RS and Omega-RS are recommended to apply for low swirl degree (S=0.3) with an approximate average error percent of 16% at each

one of them. In addition, the contours results denote a slightly non-symmetric effect due to existence of the swirl and the existence of the screws in the geometry, and the turbulence models were able to predict the change in the symmetric shape at each location at different level of prediction.

For medium swirl degree S=0.58, the study has found that generally both type of turbulence models was able to predict the flow with an approximate average error percent of 12%, however, the RSM models preferred to apply because of their ability of showing the influence of swirl degree on the scalar mixing process. Additionally, the contours indicate that the non-symmetric form is higher than the first swirling number because of the increasing in the swirl strength. However, the models show different level of computing this feature. For instance, two-equations based turbulence models predict a small non-symmetric shape at the last two locations. Though, the RMS turbulence models predict a large effect of non-symmetric structure. Therefore, the simulations findings conclude that the swirl flow influences the symmetric contour at high level when the swirl strength is 0.58.

One of the more significant findings to emerge from this study is that all the models has failed to predict the swirl flow at high swirl strength S=1.07, except the LRR-IP-RS model which show a good agreement with the experiment data with an average error percent of 14.72%. Furthermore, the two-equations based turbulence models predict a small non-symmetric shape through the computational domain because these models represent the flow like a planar flow at high velocity. Thus, the related contours of these models show high mixture fraction in all locations. Generally, all the RMS turbulence models predict a huge effect of non-symmetric structure due to the swirl force. However, Methane mass fraction is not correct specially in SSG-RS and Omega-RS turbulence model. Therefore, the RMS turbulence models can predict the high swirl effect on the symmetric structure more than the two-equations based turbulence models.

Alternatively, the zero-diffusion effect is studies in this work between the planar and swirl flow jet flow. The findings conclude that the diffusion process is dominated the scalar mixing at planar jet flow where the Reynolds number is relatively low. However, the turbulent mixing is the dominant process when the swirl occurred with the increasing of Reynolds number. Finally, the results suggest that the existence of screws have a significate effect on symmetric. In another words, the screws increase the swirling strength in the simulation domain which led to create mor non-symmetric forms as showed in the previous results.

7.6 Recommendations for future work

It is recommended that further research be undertaken in the following fields:

1. Since this study is on non-reacting flow, further numerical investigations are required to include the reacting swirl and planar jet flow due to its importantly in many industrial applications such as combustions chambers.
2. The results of this work can be used in another numerical investigation to increase the efficiency of the selected turbulence models by modifying the constant parameter for each model. In other words, one of the main effects on any turbulence model outcomes is the models' constants. Therefore, another study can use the current results to indicate a deep investigation of models' constants which can increase the efficiency of the turbulence models.
3. To investigate the symmetric regions at different swirl degrees, this work can be repeated for all models without applying the screws inside the geometry. Therefore, an overall understanding of flow behaviour can be conduct at different flow zones i.e., more than the current locations can be calculated.
4. One of the significant investigations for future work is via employing different numerical methods such as DNS and LES for the same experiment conditions. Thus, using the current results give a huge opportunity of contribution by comparing the results of each those methods with this work.
5. The current study couldn't include all the RANS turbulence models due to time limits. Therefore, including more RANS turbulence models is recommended for future work.

REFERENCES

Ahmed, S. A. (1998). Velocity measurements and turbulence statistics of a confined isothermal swirling flow. *Experimental Thermal and Fluid Science*, *17*(3), 256–264. https://doi.org/10.1016/S0894-1777(97)10039-5

Anderson Jr, J. D. (2010). Brief History of the Early Development of Theoretical and Experimental Fluid Dynamics. *Encyclopedia of Aerospace Engineering*.

Ansys, C. F. X. (2010). Release 11.0: ANSYS CFX-Solver theory guide. *ANSYS Inc., USA*.

Ansys, I. (2011). ANSYS FLUENT theory guide. *Canonsburg, Pa*, *794*.

Antonia, R A, & Bilger, R. W. (1973). An experimental investigation of an axisymmetric jet in a co-flowing air stream. *Journal of Fluid Mechanics*, *61*(4), 805–822.

Antonia, Robert A, Satyaprakash, B. R., & Hussain, A. (1980). Measurements of dissipation rate and some other characteristics of turbulent plane and circular jets. *The Physics of Fluids*, *23*(4), 695–700.

Antonia, Robert A, & Zhao, Q. (2001). Effect of initial conditions on a circular jet. *Experiments in Fluids*, *31*(3), 319–323.

Apte, S. V., Mahesh, K., Moin, P., & Oefelein, J. C. (2003). Large-eddy simulation of swirling particle-laden flows in a coaxial-jet combustor. *International Journal of Multiphase Flow*, *29*(8), 1311–1331. https://doi.org/10.1016/S0301-9322(03)00104-6

Ashgriz, N., & Mostaghimi, J. (2002). An introduction to computational fluid dynamics. *Fluid Flow Handbook*, *1*, 1–49.

Astronautics, A. I. of A. and. (1998). *AIAA guide for the verification and validation of computational fluid dynamics simulations*. American Institute of aeronautics and astronautics.

Babu, P., & Mahesh, K. (2005). Direct numerical simulation of passive scalar mixing in spatially evolving turbulent round jets. *43rd AIAA Aerospace Sciences Meeting and Exhibit*, 1121.

Bahrami, M. (2009). *Introduction and Properties of Fluids*.

Bakker, A. (2002). Lecture 1-Introduction to CFD Applied Computational Fluid Dynamics.

Fluent Inc.: Queens, NY, USA.

Bakker, A. (2003). Lecture 10-turbulence models applied computational fluid dynamics. *Power-Point Presentation*.

Balabel, A., & El-Askary, W. A. (2011). On the performance of linear and nonlinear k-ε turbulence models in various jet flow applications. *European Journal of Mechanics, B/Fluids*, *30*(3), 325–340. https://doi.org/10.1016/j.euromechflu.2010.10.006

Ball, C. G., Fellouah, H., & Pollard, A. (2012). The flow field in turbulent round free jets. *Progress in Aerospace Sciences*, *50*, 1–26.

Bašić, J. (2016). Turbulent History of Fluid Mechanics. *A Brief Essay, Research Gate*.

Basset, T., Viggiano, B., Barois, T., Gibert, M., Mordant, N., Cal, R. B., Volk, R., & Bourgoin, M. (2022). Entrainment, diffusion and effective compressibility in a self-similar turbulent jet. *ArXiv Preprint ArXiv:2201.02443*.

Batchelor, C. K., & Batchelor, G. K. (2000). *An introduction to fluid dynamics*. Cambridge university press.

Ben-Artzi, M., Croisille, J. P., & Fishelov, D. (2013). *Navier-Stokes equations in planar domains*. World Scientific.

Benim, A. C., Iqbal, S., Meier, W., Joos, F., & Wiedermann, A. (2017). Numerical investigation of turbulent swirling flames with validation in a gas turbine model combustor. *Applied Thermal Engineering*, *110*, 202–212.

Bisoi, M., Das, M. K., Roy, S., & Patel, D. K. (2017). Large eddy simulation of three-dimensional plane turbulent free jet flow. *European Journal of Mechanics-B/Fluids*, *65*, 423–439.

Bjorn, S. (2016, April 18). *What's The Difference Between FEM, FDM, and FVM?* https://www.machinedesign.com/3d-printing-cad/fea-and-simulation/article/21832072/whats-the-difference-between-fem-fdm-and-fvm

Cao, H. (2011). *Aerodynamics analysis of small horizontal axis wind turbine blades by using 2D and 3D CFD modelling*. University of Central Lancashire.

Carazzo, G., Kaminski, E., & Tait, S. (2006). The route to self-similarity in turbulent jets and plumes. *Journal of Fluid Mechanics*, *547*, 137.

Casey, M., Wintergerste, T., & Innotec, S. (2000). ERCOFTAC special interest group on quality and trust in industrial CFD. *Best Practices Guidelines*.

Celik, I. B. (1999). Introductory Turbulence Modeling. Lectures Notes. *West Virginia University Mechanical & Aerospace Engineering Dept*.

CFX, A. (2018). 19.1. *ANSYS CFX-Solver Theory Guide*.

Chambers, A. J., Antonia, R. A., & Browne, L. W. B. (1985). Effect of symmetry and asymmetry of turbulent structures on the interaction region of a plane jet. *Experiments in Fluids*, *3*(6), 343–348.

Chen, S., & Zhao, D. (2018). Numerical study of non-reacting flowfields of a swirling trapped vortex ramjet combustor. *Aerospace Science and Technology*, *74*(5), 81–92. https://doi.org/10.1016/j.ast.2018.01.006

Chernykh, G. G., Demenkov, A. G., & Kostomakha, V. A. (1998). Numerical model of a swirling momentumless turbulent wake. *Russian Journal of Numerical Analysis and Mathematical Modelling*, *13*(4), 279–288.

Chivaee, H. S. (2014). *Large eddy simulation of turbulent flows in wind energy*. DTU Vindenergi.

Chua, L. P., & Antonia, R. A. (1986). The turbulent interaction region of a circular jet. *International Communications in Heat and Mass Transfer*, *13*(5), 545–558.

Courant, R., Friedrichs, K., & Lewy, H. (1928). Über die partiellen Differenzengleichungen der mathematischen Physik. *Kurt Otto Friedrichs*, 53–95. https://doi.org/10.1007/978-1-4612-5385-3_7

Danaila, I., & Boersma, B. J. (2000). Direct numerical simulation of bifurcating jets. *Physics of Fluids*, *12*(5), 1255–1257.

Date, A. W. (2005). *Introduction to computational fluid dynamics*. Cambridge University Press.

De Farias Neto, S. R., Legentilhomme, P., Legrand, J., & De Farias Neto, S. R. (2001). Finite element simulation of mass transfer in laminar swirling decaying flow induced by means of a tangential inlet in an annulus. *Computer Methods in Applied Mechanics and Engineering*, *190*(35–36), 4713–4731. https://doi.org/10.1016/S0045-7825(00)00341-8

de Parias Neto, S. R., Legentilhomme, P., & Legrand, J. (1998). Finite-element simulation of laminar swirling decaying flow induced by means of a tangential inlet in an annulus. *Computer Methods in Applied Mechanics and Engineering*, *165*(1–4), 189–213.

Dixon, T. F., Truelove, J. S., & Wall, T. F. (1983). *Aerodynamic studies on swirled coaxial jets from nozzles with divergent quarls*.

Djenidi, L., & Antonia, R. A. (1997). Modeling of the Reynolds stress transport equation. *AIAA Journal*, *35*(3), 450–455. https://doi.org/10.2514/2.150

Dowling, D., & Dimotakis, P. (1988). On mixing and structure of the concentration field of turbulent jets. *1st National Fluid Dynamics Conference*, 3611.

Dowling, D. R. (1988). *Mixing in gas phase turbulent jets*. CALIFORNIA INST OF TECH PASADENA.

Dowling, D. R., & Dimotakis, P. E. (1990). Similarity of the concentration field of gas-phase turbulent jets. *Journal of Fluid Mechanics*, *218*, 109–141.

Eça, L., & Hoekstra, M. (2006). An Introduction To Cfd Code Verification Including Eddy-Viscosity Models. *European Conference on Computational Fluid Dynamics*, 1–13.

EidiAttarZade, M., Tabejamaat, S., Mani, M., & Farshchi, M. (2019). Numerically investigation of ignition process in a premixed methane-air swirl configuration. *Energy*, *171*, 830–841. https://doi.org/10.1016/j.energy.2019.01.005

Eldrainy, Y. A., Saqr, K. M., Aly, H. S., & Jaafar, M. N. M. (2009). CFD insight of the flow dynamics in a novel swirler for gas turbine combustors. *International Communications in Heat and Mass Transfer*, *36*(9), 936–941.

Elsner, J. W., & Kurzak, L. (1989). Semi-preserving development of a slightly heated free swirling jet. *Journal of Fluid Mechanics*, *199*, 237–255.

Emmons, H. W. (1944). *The numerical solution of compressible fluid flow problems*. HARVARD UNIV CAMBRIDGE MA.

Escue, A., & Cui, J. (2010). Comparison of turbulence models in simulating swirling pipe flows. *Applied Mathematical Modelling*, *34*(10), 2840–2849. https://doi.org/10.1016/j.apm.2009.12.018

Eymard, R., & Gallouët, T. (2010). Finite volume method. *Scholarpedia*, *5*(6), 9835.

Ezra, A. (2018). *Theory Of Jets*. Academia.Edu. https://www.academia.edu/22101358/2_THEORY_OF_JETS_2_1_Introduction_2_2_Overview_of_Jet_Flows_2_3_Structure_and_Development_of_a_Free_Jet_2_4_Factors_Influencing_Jet_Spread_2_5_Conclusion_2_1_Introduction

Facciolo, L. (2006). *A study on axially rotating pipe and swirling jet flows*. KTH.

Farokhi, S., Taghavi, R., & Rice, E. J. (1989). Effect of initial swirl distribution on the evolution of a turbulentjet. *AIAA Journal*, *27*(6), 700–706.

Feyedelem, M. S., & Sarpkaya, T. (1998). Free-and near-free-surface swirling turbulent jets. *AIAA Journal*, *36*(3), 359–364.

Freitag, M., Klein, M., Gregor, M., Geyer, D., Schneider, C., Dreizler, A., & Janicka, J. (2006). Mixing analysis of a swirling recirculating flow using DNS and experimental data. *International Journal of Heat and Fluid Flow*, *27*(4), 636–643. https://doi.org/10.1016/j.ijheatfluidflow.2006.02.020

García-Villalba, M., & Fröhlich, J. (2005). On the sensitivity of a free annular swirling jet to the level of swirl and a pilot jet. In *Engineering Turbulence Modelling and Experiments 6* (pp. 845–854). Elsevier.

Gazzah, M. H., Belmabrouk, H., & Sassi, M. (2004). A numerical study of the scalar field in turbulent round jet with co-flowing stream. *Computational Mechanics*, *34*(5), 430–437.

German, A. E., & Mahmud, T. (2005). Modelling of non-premixed swirl burner flows using a Reynolds-stress turbulence closure. *Fuel*, *84*(5), 583–594. https://doi.org/10.1016/j.fuel.2004.10.015

Gibson, M. M., & Launder, B. E. (1978). Ground effects on pressure fluctuations in the atmospheric boundary layer. *Journal of Fluid Mechanics*, *86*(3), 491–511.

Gilchrist, R. T., & Naughton, J. W. (2005). Experimental study of incompressible jets with different initial swirl distributions: mean results. *AIAA Journal*, *43*(4), 741–751.

Golub, V. V., & Polezhaev, Y. V. (2008). Jets. *A-to-Z Guide to Thermodynamics, Heat and Mass Transfer, and Fluids Engineering*. https://doi.org/10.1615/atoz.j.jets

Gopalakrishnan, R. N., & Disimile, P. J. (2018). *CFD Analysis of Twin Turbulent Impinging Axisymmetric Jets at Different Impingement Angles*.

Grinstein, F. F., & Young, T. R. (2006). SWIRLING JET SYSTEMS FOR COMBUSTION CONTROL. *Combustion Processes in Propulsion: Control, Noise, and Pulse Detonation*, *20*, 111.

Guo, H. F., Chen, Z. Y., & Yu, C. W. (2009). Simulation of the effect of geometric parameters on tangentially injected swirling pipe airflow. *Computers & Fluids*, *38*(10), 1917–1924.

Guo, T., Rau, M. J., Vlachos, P. P., & Garimella, S. V. (2017). Axisymmetric wall jet development in confined jet impingement. *Physics of Fluids*, *29*(2), 25102.

Gupta, A. K., Lilley, D. G., & Syred, N. (1984). Swirl flows. *Tw*.

Gupta, A., & Kumar, R. (2007). Three-dimensional turbulent swirling flow in a cylinder: Experiments and computations. *International Journal of Heat and Fluid Flow*, *28*(2), 249–261. https://doi.org/10.1016/j.ijheatfluidflow.2006.04.005

Gursul, I. (2004). Recent developments in delta wing aerodynamics. *The Aeronautical Journal*, *108*(1087), 437–452.

Halley, C. E., & Spall, R. E. (2000). An introduction of CFD into the undergraduate engineering program. *Age*, *5*, 1–10.

Hirsch, C. (2007). Introduction: An initial guide to cfd and to this volume. *Numerical Computation of Internal and External Flows*, 50034–50039.

Hogg, S., & Leschziner, M. A. (1989). Second-moment-closure calculation of strongly swirling confined flow with large density gradients. *International Journal of Heat and Fluid Flow*, *10*(1), 16–27. https://doi.org/10.1016/0142-727X(89)90050-7

Ilie, M. (2018). Numerical studies of turbulent swirling reacting flows using LES and URANS. *International Journal of Thermal Sciences*, *134*(August), 89–100. https://doi.org/10.1016/j.ijthermalsci.2018.07.045

Ishay, L., Bieder, U., Ziskind, G., & Rashkovan, A. (2017). Nozzle geometry effect on stratified layer erosion by vertical turbulent jet. *Journal of Nuclear Engineering and Radiation Science*, *3*(3).

Ismail-Zadeh, A., & Tackley, P. (2010). *Computational methods for geodynamics*. Cambridge University Press.

Jakirlić, S., Volkert, J., Pascal, H., Hanjalić, K., & Tropea, C. (2000). DNS, experimental and modelling study of axially compressed in-cylinder swirling flow. *International Journal of Heat and Fluid Flow*, *21*(5), 627–639. https://doi.org/10.1016/S0142-727X(00)00054-0

Jones, L. N. (2004). *Modelling of turbulent swirling flows*. University of Leeds.

Jones, W. P., Lettieri, C., Marquis, A. J., & Navarro-Martinez, S. (2012). Large eddy simulation of the two-phase flow in an experimental swirl-stabilized burner. *International Journal of Heat and Fluid Flow*, *38*, 145–158.

Kandakure, M. T., Patkar, V. C., & Patwardhan, A. W. (2008). Characteristics of turbulent confined jets. *Chemical Engineering and Processing: Process Intensification*, *47*(8), 1234–1245.

Khodabandeh, E., Moghadasi, H., Pour, M. S., Ersson, M., Jönsson, P. G., Rosen, M. A., & Rahbari, A. (2020). CFD study of non-premixed swirling burners: Effect of turbulence models. *Chinese Journal of Chemical Engineering*.

Kim, C. G., Kim, B. H., Bang, B. H., & Lee, Y. H. (2015). Experimental and CFD analysis for prediction of vortex and swirl angle in the pump sump station model. *IOP Conference Series: Materials Science and Engineering*, *72*(Forum 4). https://doi.org/10.1088/1757-899X/72/4/042044

Kinyua Kande, D. (2017). A CFD Analysis of Heat and Mass Transfer in greenhouses: An Introduction. *Mathematical Modelling and Applications*, *2*(2), 17. https://doi.org/10.11648/j.mma.20170202.11

Kolmogorov, A. N. (1991). The local structure of turbulence in incompressible viscous fluid for very large Reynolds numbers. *Proceedings of the Royal Society of London. Series A: Mathematical and Physical Sciences*, *434*(1890), 9–13.

Launder, Brian E. (1989). Second-moment closure: present… and future? *International Journal of Heat and Fluid Flow*, *10*(4), 282–300.

Launder, Brian Edward, Reece, G. J., & Rodi, W. (1975). Progress in the development of a Reynolds-stress turbulence closure. *Journal of Fluid Mechanics*, *68*(3), 537–566.

Launder, Brian Edward, & Spalding, D. B. (1983). The numerical computation of turbulent

flows. In *Numerical prediction of flow, heat transfer, turbulence and combustion* (pp. 96–116). Elsevier.

Lebarbier, C., Kockel, T. K., Fletcher, D. F., & Langrish, T. A. G. (2001). Experimental measurement and numerical simulation of the effect of swirl on flow stability in spray dryers. *Chemical Engineering Research and Design*, *79*(3), 260–268. https://doi.org/10.1205/026387601750281789

Li, X., Zhou, M., Zhang, J., & Xu, W. (2019). Numerical study of the velocity decay of offset jet in a narrow and deep pool. *Water*, *11*(1), 59.

Lienhard IV, J. H., & Lienhard, J. H. V. (2008). DOE fundamentals handbook: thermodynamics, heat transfer, and fluid flow. *Washington, DC: US Department of Energy*.

Lilley, D. G. (1976). Nonisotropic turbulence in swirling flows. *Acta Astronautica*, *3*(11–12), 919–933. https://doi.org/10.1016/0094-5765(76)90002-3

Liu, Z. H., Zheng, C. G., & Zhou, L. X. (2001). A second-order-moment-Monte-Carlo model for simulating swirling gas-particle flows. *Powder Technology*, *120*(3), 216–222. https://doi.org/10.1016/S0032-5910(01)00279-0

Loitsyanskii, L. G. (1966). *Mechanics of Liquids and Gases, Pergamon Press*. Oxford New York.

Lubbers, C. L., Brethouwer, G., & Boersma, B. J. (2001). Simulation of the mixing of a passive scalar in a round turbulent jet. *Fluid Dynamics Research*, *28*(3), 189.

Mansouri, Z., & Boushaki, T. (2018). Experimental and numerical investigation of turbulent isothermal and reacting flows in a non-premixed swirl burner. *International Journal of Heat and Fluid Flow*, *72*(October 2017), 200–213. https://doi.org/10.1016/j.ijheatfluidflow.2018.06.007

Mansouri, Z. M., Aouissi, M., & Boushaki, T. B. (2016). A numerical study of swirl effects on the flow and flame dynamics in a lean premixed combustor. *International Journal of Heat and Technology*, *34*(2), 227–235. https://doi.org/10.18280/ijht.340211

Manual, I. Q. (1999). Uncertainty Analysis in CFD and Guidelines for RANS codes. *Interim Recommended Procedure Prepared by Resistance Committee of 22nd ITTC*.

Margolin, L., & Plesko, C. (2019). Discrete regularization. *Evolution Equations & Control Theory*, *8*(1), 117.

Mehta, R. D., Wood, D. H., & Clausen, P. D. (1991). Some effects of swirl on turbulent mixing layer development. *Physics of Fluids A: Fluid Dynamics*, *3*(11), 2716–2724.

Mihailovic, D. T. (2012). Benoit Cushman-Roisin Thayer School of Engineering, Dartmouth College, Hanover, New Hampshire, USA Carlo Gualtieri Hydraulic and Environmental Engineering Department. *Fluid Mechanics of Environmental Interfaces*, 3.

Milosavljevic, V. D. (1993). Natural gas, kerosene and pulverised fuel fired swirl burners. *PhD Thesis, University of London*.

Miltner, M., Jordan, C., & Harasek, M. (2015). CFD simulation of straight and slightly swirling turbulent free jets using different RANS-turbulence models. *Applied Thermal Engineering*, *89*, 1117–1126.

Morrall, A., Quayle, S., & Campobasso, M. S. (2020). Turbulence modelling for RANS CFD analyses of multi-nozzle annular jet pump swirling flows. *International Journal of Heat and Fluid Flow*, *85*(July). https://doi.org/10.1016/j.ijheatfluidflow.2020.108652

Morsi, Y. S. M., & Clayton, B. R. (1986). Determination of principal characteristics of turbulent swirling flow along annuli: part 3: numerical analysis. *International Journal of Heat and Fluid Flow*, *7*(3), 208–222.

Mossad, R., & Ravinesh, C. (2015). Numerical modelling of the velocity field of a plane jet flow at moderate jet exit Reynolds numbers. *Proceedings of the 11th International Conference on CFD in the Minerals and Process Industries*.

Moukalled, F., Mangani, L., & Darwish, M. (2015). *The Finite Volume Method in Computational Fluid Dynamics: An Advanced Introduction with OpenFOAM® and Matlab*. Springer International Publishing. https://books.google.co.uk/books?id=GYRgCgAAQBAJ

Moureau, V., Domingo, P., & Vervisch, L. (2011). From Large-Eddy Simulation to Direct Numerical Simulation of a lean premixed swirl flame: Filtered laminar flame-PDF modeling. *Combustion and Flame*, *158*(7), 1340–1357. https://doi.org/10.1016/j.combustflame.2010.12.004

Murphy, S., Delfos, R., Pourquié, M. J. B. M., Olujić, Ž., Jansens, P. J., & Nieuwstadt, F. T. M. (2007). Prediction of strongly swirling flow within an axial hydrocyclone using two commercial CFD codes. *Chemical Engineering Science*, *62*(6), 1619–1635. https://doi.org/10.1016/j.ces.2005.10.031

Naji, H. (1986). The prediction of turbulent swirling jet flow. *International Journal of Heat and Mass Transfer*, *29*(2), 169–182.

Nakayama, Y. (2018). *Introduction to fluid mechanics*. Butterworth-Heinemann.

Niyogi, P., Chakrabartty, S. K., & Laha, M. K. (2006). *Introduction to computational fluid dynamics*. Pearson Education India.

Oefelein, J. C., Sankaran, V., & Drozda, T. G. (2007). Large eddy simulation of swirling particle-laden flow in a model axisymmetric combustor. *Proceedings of the Combustion Institute*, *31 II*, 2291–2299. https://doi.org/10.1016/j.proci.2006.08.017

Oljaca, M., Gu, X., Glezer, A., Baffico, M., & Lund, F. (1998). Ultrasound scattering by a swirling jet. *Physics of Fluids*, *10*(4), 886–898.

Örlü, R. (2006). *Experimental study of passive scalar mixing in swirling jet flows*. KTH.

Palm, R., Grundmann, S., Weismüller, M., Šarić, S., Jakirlić, S., & Tropea, C. (2006). Experimental characterization and modelling of inflow conditions for a gas turbine swirl combustor. *International Journal of Heat and Fluid Flow*, *27*(5), 924–936. https://doi.org/10.1016/j.ijheatfluidflow.2006.03.016

Pampaloni, D., Bertini, D., Puggelli, S., Mazzei, L., & Andreini, A. (2017). Methane swirl-stabilized lean burn flames: Assessment of scale-resolving simulations. *Energy Procedia*, *126*(201709), 834–841. https://doi.org/10.1016/j.egypro.2017.08.274

Park, S. H., & Shin, H. D. (1993). Measurements of entrainment characteristics of swirling jets. *International Journal of Heat and Mass Transfer*, *36*(16), 4009–4018.

Pedley, T. J. (1997). Introduction to fluid dynamics. *Scientia Marina*, *61*, 7–24.

Pinton, J. F., Plaza, F., Danaila, L., Le Gal, P., & Anselmet, F. (1998). On velocity and passive scalar scaling laws in a turbulent swirling flow. *Physica D: Nonlinear Phenomena*, *122*(1–4), 187–201. https://doi.org/10.1016/S0167-2789(98)00185-7

Pope, S. B. (2000). Turbulent flows. Turbulent Flows, by Stephen B. Pope. *ISBN*,

521591252, 806.

Qi, N., Wang, H., Zhang, K., & Zhang, H. (2010). Numerical simulation of fluid dynamics in the stirred tank by the SSG Reynolds Stress Model. *Frontiers of Chemical Engineering in China*, *4*(4), 506–514. https://doi.org/10.1007/s11705-010-0508-7

Qu, X., Sui, H., & Tian, M. (2016). CFD simulation of steam–air jet condensation. *Nuclear Engineering and Design*, *297*, 44–53.

Qu, X., Tian, M., Zhang, G., & Leng, X. (2015). Experimental and numerical investigations on the air–steam mixture bubble condensation characteristics in stagnant cool water. *Nuclear Engineering and Design*, *285*, 188–196.

Rajaratnam, N. (1976). *Turbulent jets*. Elsevier.

Reynier, P., & Minh, H. H. (1998). Numerical prediction of unsteady compressible turbulent coaxial jets. *Computers & Fluids*, *27*(2), 239–254.

Richardson, L. F. (1911). IX. The approximate arithmetical solution by finite differences of physical problems involving differential equations, with an application to the stresses in a masonry dam. *Philosophical Transactions of the Royal Society of London. Series A, Containing Papers of a Mathematical or Physical Character*, *210*(459–470), 307–357.

Roache, P. J. (1998). *Verification and validation in computational science and engineering* (Vol. 895). Hermosa Albuquerque, NM.

Robin, M. (2018). What Are the Differences Between. *Social Indicators Research*, 363–404. https://forum.ansys.com/discussion/1518/what-are-the-differences-between-cfx-and-fluent

Rosentrater, K. A., & Balamuralikrishna, R. (2005). Essential Highlights of the History of Fluid Mechanics. *Age*, *10*, 1.

Sahebjam, R., Kohan, K. F., & Gaskin, S. (2022). The dynamics of an axisymmetric turbulent jet in ambient turbulence interpreted from the passive scalar field statistics. *Physics of Fluids*, *34*(1), 15129.

Sakajo, T. (2001). Numerical computation of a three-dimensional vortex sheet in a swirl flow. *Fluid Dynamics Research*, *28*(6), 423–448. https://doi.org/10.1016/S0169-5983(01)00009-0

Samet, M., & Einav, S. (1988). Mean value measurements of a turbulent swirling-jet. *AIAA Journal*, *26*(5), 619–621.

Sanderse, B., Van der Pijl, S. P., & Koren, B. (2011). Review of computational fluid dynamics for wind turbine wake aerodynamics. *Wind Energy*, *14*(7), 799–819.

Sato, H., & Sakao, F. (1964). An experimental investigation of the instability of a two-dimensional jet at low Reynolds numbers. *Journal of Fluid Mechanics*, *20*(2), 337–352.

Schäfer, M. (2006). *Computational engineering: Introduction to numerical methods* (Vol. 321). Springer.

Schefer, R. W., Houf, W. G., & Williams, T. C. (2008). Investigation of small-scale unintended releases of hydrogen: momentum-dominated regime. *International Journal of Hydrogen Energy*, *33*(21), 6373–6384.

Schlichting, H. (1968). Boundary Layer Theory McGraw Hill Book Co. *New York*.

Shamami, K. K., & Birouk, M. (2008). Assessment of the Performances of RANS Models for Simulating Swirling Flows in a Can-Combustor. *The Open Aerospace Engineering Journal*, *1*(1), 8–27. https://doi.org/10.2174/1874146000801010008

Sharma, A. (2016). *Introduction to computational fluid dynamics: development, application and analysis*. John Wiley & Sons.

Shih, T.-H., Liou, W. W., Shabbir, A., Yang, Z., & Zhu, J. (1995). A new k-ϵ eddy viscosity model for high reynolds number turbulent flows. *Computers & Fluids*, *24*(3), 227–238.

Sloan, D. G., Smith, P. J., & Smoot, L. D. (1986). Modeling of swirl in turbulent flow systems. *Progress in Energy and Combustion Science*, *12*(3), 163–250. https://doi.org/10.1016/0360-1285(86)90016-X

Sommerfeld, M., & Qiu, H. H. (1993). Characterization of particle-laden, confined swirling flows by phase-doppler anemometry and numerical calculation. *International Journal of Multiphase Flow*, *19*(6), 1093–1127. https://doi.org/10.1016/0301-9322(93)90080-E

Speziale, C. G., Sarkar, S., & Gatski, T. B. (1991). Modelling the pressure–strain correlation of turbulence: an invariant dynamical systems approach. *Journal of Fluid Mechanics*, *227*, 245–272.

Stanley, S., Sarkar, S., & Mellado González, J. P. (2002). A study of the flow-field evolution

and mixing in a planar turbulent jet using direct numerical simulation. *Journal of Fluid Mechanics*, *450*, 377–407.

Steenbergen, W. (1995). *Turbulent pipe flow with swirl*. Citeseer.

Stein, O., & Kempf, A. (2007). LES of the Sydney swirl flame series: A study of vortex breakdown in isothermal and reacting flows. *Proceedings of the Combustion Institute*, *31 II*, 1755–1763. https://doi.org/10.1016/j.proci.2006.07.255

Stergiannis, N., Lacor, C., Beeck, J. V, & Donnelly, R. (2016). CFD modelling approaches against single wind turbine wake measurements using RANS. *Journal of Physics: Conference Series*, *753*(3), 32062.

Stetsyuk, V. (2014). *Experimental study of combustion and scalar mixing in swirling jet flows*. Imperial College London.

Toh, I. K., Honnery, D., & Soria, J. (2005). Velocity and scalar measurements of a low swirl jet. *Proc. 4th Australian Conf. Laser Diagnostics Fluid Mech. Comb*, 129–132.

Upp, E. L., & LaNasa, P. J. (2002). Types of Fluid Flow Measurement. In *Fluid Flow Measurement* (pp. 35–47). Elsevier. https://doi.org/10.1016/B978-088415758-8/50004-1

Versteeg, H. K., & Malalasekera, W. (2007). *An introduction to computational fluid dynamics: the finite volume method*. Pearson education.

Wasserman, S. (2016). Choosing the right turbulence model for your cfd simulation. *Engineering. Com].[En Línea]*, *22*.

Wegner, B., Maltsev, A., Schneider, C., Sadiki, A., Dreizler, A., & Janicka, J. (2004). Assessment of unsteady RANS in predicting swirl flow instability based on LES and experiments. *International Journal of Heat and Fluid Flow*, *25*(3), 528–536.

Wilcox, D. C. (1998). *Turbulence modeling for CFD* (Vol. 2). DCW industries La Canada, CA.

Woelke, M. (2007). Eddy Viscosity Turbulence Models emploed by Computational Fluid Dynamic. *Prace Instytutu Lotnictwa*, 92–113.

Wu, Y.-T., & Porté-Agel, F. (2012). Atmospheric turbulence effects on wind-turbine wakes: An LES study. *Energies*, *5*(12), 5340–5362.

Wygnanski, I., & Fiedler, H. (1969). Some measurements in the self-preserving jet. *Journal of Fluid Mechanics*, *38*(3), 577–612.

Xia, J. L., Smith, B. L., Benim, A. C., Schmidli, J., & Yadigaroglu, G. (1997). Effect of inlet and outlet boundary conditions on swirling flows. *Computers and Fluids*, *26*(8), 811–823. https://doi.org/10.1016/S0045-7930(97)00026-1

Xia, J. L., Yadigaroglu, G., Liu, Y. S., Schmidli, J., & Smith, B. L. (1998). Numerical and experimental study of swirling flow in a model combustor. *International Journal of Heat and Mass Transfer*, *41*(11), 1485–1491. https://doi.org/10.1016/S0017-9310(97)00239-1

Xiao, H., Luo, K., Jin, T., Wang, H., & Fan, J. (2020). Direct numerical simulation of turbulence modulation by premixed flames in a model annular swirling combustor. *Proceedings of the Combustion Institute*. https://doi.org/10.1016/j.proci.2020.06.272

Xiouris, C. Z., & Koutmos, P. (2012). Fluid dynamics modeling of a stratified disk burner in swirl co-flow. *Applied Thermal Engineering*, *35*, 60–70.

Yan, X., Ghodoosipour, B., & Mohammadian, A. (2020). Three-dimensional numerical study of multiple vertical buoyant jets in stationary ambient water. *Journal of Hydraulic Engineering*, *146*(7), 4020049.

Yang, S. L., Siow, Y. K., Peschke, B. D., & Tacina, R. R. (2003). Numerical study of nonreacting gas turbine combustor swirl flow using reynolds stress model. *Journal of Engineering for Gas Turbines and Power*, *125*(3), 804–811. https://doi.org/10.1115/1.1560706

Young, D. F., Munson, B. R., Okiishi, T. H., & Huebsch, W. W. (2010). *A brief introduction to fluid mechanics*. John Wiley & Sons.

Yue, Z. (1999). *Air jet velocity decay in ventilation applications*. KTH.

Zavila, O. (2012). Physical modeling of gas pollutant motion in the atmosphere. *Advances in Modeling of Fluid Dynamics*, 51–78.

Zhang, S., Law, A. W.-K., & Zhao, B. (2015). Large eddy simulations of turbulent circular wall jets. *International Journal of Heat and Mass Transfer*, *80*, 72–84.

Zhang, Y., & Vanierschot, M. (2021). Modeling capabilities of unsteady RANS for the

simulation of turbulent swirling flow in an annular bluff-body combustor geometry. *Applied Mathematical Modelling*, *89*, 1140–1154.

Zhao, Q. W., Chan, C. K., & Zhao, H. F. (2004). Numerical simulation of open swirl-stabilized premixed combustion. *Fuel*, *83*(11–12), 1615–1623. https://doi.org/10.1016/j.fuel.2004.02.003

Zheng, Y., Zhu, M., Martinez, D. M., & Jiang, X. (2013). Large-eddy simulation of mixing and combustion in a premixed swirling combustor with synthesis gases. *Computers & Fluids*, *88*, 702–714.

Zhou, L. X., Wang, F., & Zhang, J. (2003). Simulation of swirling combustion and NO formation using a USM turbulence-chemistry model. *Fuel*, *82*(13), 1579–1586. https://doi.org/10.1016/S0016-2361(03)00089-9

Zhou, X., Sun, Z., Durst, F., & Brenner, G. (1999). Numerical simulation of turbulent jet flow and combustion. *Computers & Mathematics with Applications*, *38*(9–10), 179–191.